

BODIL ELISABETH MONSEN

**IRON ORE CONCENTRATES-
OXIDATION AND REDUCTION**

Thesis submitted to the Division of Metallurgy, the Norwegian Institute of Technology, in partial fulfilment of the requirements for the Norwegian academic degree of Doctor of Engineering (dr. ing.)

DIVISION OF METALLURGY
THE NORWEGIAN INSTITUTE OF TECHNOLOGY
THE UNIVERSITY OF TRONDHEIM

December 1992

SUMMARY

This project was initiated because of the current interest in the Elkem Polar Process for reduction of ore fines. SINTEF and Elkem developed a laboratory scale reactor designed to simulate the Elkem Polar Process. This reactor was used in all prereduction experiments. The main intention of the present work has been to explain different reduction rates of iron ore concentrates by physical and chemical characterization of raw materials.

Oxidation of magnetite

Hematite and magnetite are the most common iron ore minerals, and both are included in the present investigation. Reduction of magnetite is known to be very slow compared to reduction of hematite. However, magnetite becomes an interesting iron ore mineral for the Elkem Polar Process after preoxidation to hematite. The process concept allows preoxidation in the heating unit, but maximum retention time will only be about 40 seconds.

Kinetics of magnetite oxidation was studied in the laboratory scale reactor to investigate the possibility of magnetite preoxidation in the heating unit of the Elkem Polar Process. Oxidation experiments were carried out in air at constant temperatures in the range 400-850°C for periods up to 60 seconds. The maximum conversion of Sydvaranger magnetite was 42% after 60 seconds at 850°C. Grain sizes in the range 74-100 μ m were used. Lower conversion was obtained using Kiruna and Minnesota magnetites.

These results indicate that, oxidation should be carried out in a separate unit and not in the heating unit of the Elkem Polar Process.

Topochemical growth of hematite with needles of hematite ahead of the topochemical front was observed. The rate of oxidation was found to follow the parabolic rate law, except during the initial period of 10 seconds or so. Best correlation was

II

achieved on the assumption of plane specimens, not spheres. The chemical reaction at the surface of each grain is probably rate controlling during the initial period. Otherwise, diffusion through a growing hematite layer is thought to be the slowest step.

Some magnetite was completely oxidized in another apparatus to produce material for subsequent reduction experiments. Sydvaranger super magnetite was oxidized for several hours in air at constant temperatures in the range 800-1250°C.

Individually oriented hematite crystals were formed in each grain. A gradual coarsening of the hematite crystals was observed for an increasing oxidation temperature. At the higher temperatures the hematite crystal size approached the grain size. The low temperature subgrain structure (800°C) is stable at the temperature at which it is formed, but not at higher temperatures.

The subgrain structures of oxidized samples were quantitatively characterized, using videoplan. Mean SBA values were measured. SBA is the ratio of the total length of subgrain boundaries within each grain and the grain section area. The mean SBA values were found to decrease steadily with increasing temperature.

Prereduction of hematite

Prereduction experiments were carried out at constant temperatures in the range 700-850°C for periods up to 60 seconds. Reduction gas mixtures of CO, CO₂ and H₂ and grain sizes in the range 63-90µm were used. The oxidizing potential of the reduction gas (%RO) and the content of hydrogen were varied in the ranges 20-50%RO and 0-45%H₂, respectively. Hematite concentrates from Brazil (2 types: angular and laminated), Guinea, Liberia, Canada and Norway (Rana) were included in the present investigation. Both preoxidation temperature and type

of hematite were found to be of importance for the rate of reduction.

The reduction of hematite to magnetite proceeds topochemically. Branches of magnetite/wüstite were observed along subgrain boundaries ahead of the topochemical front. This pattern is far more frequent in natural hematites than in preoxidized magnetite. Diffusion along subgrain boundaries seems to be easier in natural hematites than in preoxidized magnetite having comparable SBA values.

Wüstite starts forming in the magnetite pores, before the conversion of the hematite core is completed. Magnetite is reduced either uniformly (the whole grain volume participates) or quasi topochemically to wüstite. The front is most distinct during rapid reduction. Metallization proceeds mainly uniformly.

Prereduction of Sydvaranger magnetite proceeds at a higher rate after preoxidation at low temperatures (800-1050°C) than after preoxidation at elevated temperatures (1150-1250°C). The beneficial effect of low preoxidation temperatures is attributed to the subgrain structure. The initial reduction rate and the SBA value decrease gradually for increasing preoxidation temperature. Metallization is markedly retarded if the preoxidation temperature is raised from 1050 to 1150°C. The subgrain structure is markedly changed in the same temperature range. Iron nucleation may be enhanced by numerous active sites where subgrain interfaces intercept, or by vacancies, tiny cracks, defects, and foreign ions along the subgrain boundaries.

Natural hematite which contain grains made up of crystals, are reduced at a higher initial rate than those without substructure. However, the SBA values can not be used directly to predict reduction rates. Additional information about crystal shape and orientation is necessary. A laminated subgrain structure is reduced at the highest overall rate while anhedral subgrain structures (lack of crystal shape) are slowly reduced to wüstite

IV

and metal.

The laminated hematite from Brazil is reduced equally fast or even faster than magnetite preoxidized at low temperature. Tiny cracks along subgrain boundaries are probably created during rapid initial reduction, in which iron easily nucleates. Nucleation may have been enhanced by manganese on the subgrain boundaries.

The natural hematites from Guinea and Liberia, having anhedral subgrain structures, are reduced at a high initial reduction rate. The further reduction is equally slow, or even slower than the reduction of magnetite preoxidized at elevated temperature. Iron nucleation may have been retarded by aluminium, magnesium, silicon or chrome in the lattice.

The specific surface area is an important parameter for the initial reduction rate. Small variations in mean grain sizes and grain shapes, are of less importance. Magnetite contents in the natural hematite concentrates should be low, because magnetite reduces so slowly that magnetite can be considered to be inert during prerreduction.

PREFACE

The main part of this work has been carried out in the period 1987 - 1990 at the Division of Metallurgy at the Norwegian Institute of Technology (NTH). The work is made possible through a project scholarship from NTNF (Royal Norwegian Council for Scientific and Industrial Research) in the period 1987 - 1989, through financial support from Polarstål I/S (owned 50% by Elkem A/S and 50% by Norsk Jernverk A/S) in the period 1987 - 1988, and through a scholarship from NTH in the period 1. januar - 30. juni 1990. During the last mentioned period the author was affiliated to the Division of Metallurgy, the Norwegian Institute of Technology, but otherwise the author has been employed at SINTEF Metallurgy as a research engineer. The work was completed during summer 1991 - december 1992 with financial support from SINTEF¹.

Financial support in the way of numerous chemical analyses free of charge has also been given by Norsk Jernverk A/S (shut down in 1988) and later after its reorganization by MOLAB. Special thanks to P. Bernersen at MOLAB for the chemical analyses.

Thanks are also given to P. Storemyr who was engaged at the same project the two first years of the period. He was supposed to submit a thesis to the dr. ing. degree on the same main subject, emphasized on geological aspects of iron ores. Lack of financial support for two persons made him quit the project. However, the SIMS (Secondary Ion Mass Spectrometry) work in this report is mainly his credits.

I would like to express my gratitude to professor S. Olsen at the Norwegian Institute of Technology, Division of Metallurgy, for his supervision of this work. Special thanks go to dr. ing. L. Kolbeinsen at SINTEF Metallurgy, for his assistance in supervision and for his great support through fruitful discussions.

¹ SINTEF is a short term for The Foundation for Scientific and Industrial Research at the Norwegian Institute of Technology.

VI

T. Båsen (Elkem A/S) is acknowledged for his sincere interest in this work and for his ability to inspiration. Thanks also to T. Lindstad (SINTEF Metallurgy) who convinced me to go into this field. I do not regret.

Finally, thanks to all those who are not mentioned above, among the staff at SINTEF Metallurgy and at the Division of Metallurgy at the Norwegian Institute of Technology, for their assistance in several practical matters. Special thanks to the ones who helped me to carry gas containers down those three idiotic steps.

TABLE OF CONTENTS

	Page
SUMMARY	I
PREFACE	V
TABLE OF CONTENTS	VII
GEOLOGICAL AND MINERALOGICAL GLOSSARY	X
1 INTRODUCTION	1
1.1 Background	1
1.2 Aim of the present study	3
1.3 Experimental plan	4
2 GENERAL PRINCIPLES	6
2.1 Physical and structural properties	6
2.2 Phase diagrams	10
2.3 Chemical reactions	14
2.3.1 Reduction of hematite	14
2.3.2 The water-gas shift reaction (WGSR)	16
2.3.3 Methane formation	19
2.3.4 The Boudouard equilibrium	19
2.3.5 Cementite formation	21
2.3.6 Oxidation of magnetite	22
2.4 Why oxidation is necessary	22
3 MAGNETITE OXIDATION	24
3.1 Introduction	24
3.2 Previous work	25
3.2.1 Mechanism	26
3.2.2 Oxidation products	28
3.2.3 Grain refinement and recrystallization	30
3.2.4 Kinetics	33
3.3 Rate of oxidation	38
3.3.1 Experimental	38
3.3.2 Calculation of conversion	40
3.3.3 Results and discussion	41
3.3.4 Mathematical models	50
3.3.5 Concluding remarks	58

VIII

3.4	Complete oxidation	59
3.4.1	Choice of method	59
3.4.2	Experimental	60
3.4.3	Subgrain structure after complete oxidation	64
3.4.4	Concluding remarks	70
3.5	Characterization by videoplan	71
3.5.1	Introduction	71
3.5.2	Method	71
3.5.3	Results	74
3.5.4	Discussion	76
3.5.5	Concluding remarks	80
3.6	Conclusions	81
4	CHARACTERIZATION OF NATURAL HEMATITE CONCENTRATES	83
4.1	Introduction	83
4.2	Description of the iron ores	83
4.3	Sample preparation	89
4.4	Grain size distribution	89
4.5	Chemical analysis	92
4.6	Mineral phases by x-ray diffraction	95
4.7	Trace elements	100
4.8	Specific surface area	105
4.9	Subgrain structure	106
4.10	Grain shape	111
4.11	Porosity	114
4.12	Table of physical characteristics	116
5	PREREDUCTION	117
5.1	Introduction	117
5.2	Reduction kinetics	120
5.2.1	Physical models	120
5.2.2	Rate equations	121
5.2.3	The mass transfer coefficients	137
5.2.4	Physical factors affecting the reduction	145
5.2.5	Chemical factors affecting the reduction	159
5.3	Experimental	168
5.3.1	Raw materials	168
5.3.2	Equipment	168
5.3.3	Experimental procedure	173
5.4	Prereduction results: preoxidized Sydvaranger magnetite	176
5.4.1	Prereduction at 760°C	176
5.4.2	Effect of reduction temperature	178

5.4.3	Effect of gas composition	179
5.4.4	Effect of preoxidation temperature	180
5.5	Prereduction results: natural hematites	182
5.5.1	Prereduction at 760°C	182
5.5.2	Effect of reduction temperature	188
5.5.3	Effect of gas composition	190
5.6	Tables of main prereduction results	192
5.7	Discussion of method	194
5.7.1	Introduction	194
5.7.2	Accuracy of wet chemical analyses	195
5.7.3	Changing grain sizes	196
5.7.4	Material loss	200
5.7.5	Concluding remarks	204
5.8	Discussion of prereduction results: preoxidized magnetite	205
5.8.1	Introduction	205
5.8.2	The progress of reduction by optical microscope	205
5.8.3	Significance of differences in reduction rates	210
5.8.4	Possible reasons for the rate retarding effect	212
5.8.5	Concluding remarks	218
5.9	Discussion of prereduction results: natural hematites	220
5.9.1	Introduction	220
5.9.2	The progress of reduction by optical microscope	220
5.9.3	Reduction rates - significance and magnetite corrections	227
5.9.4	Effects of characteristic hematite properties	237
5.9.5	Concluding remarks	250
5.10	Comparisons of reduction rates of natural hematites and preoxidized magnetite	252
5.11	Conclusions	256
6	REFERENCES	258
	APPENDICES	272
A.1	Temperature curves from oxidation experiments in section 3.4	272
A.2	Calculated porosity after reduction	274
A.3	Experimental results from the prereduction experiments	276
A.4	Degree of oxidation with magnetite corrections	291

GEOLOGICAL AND MINERALOGICAL GLOSSARY

alteration: a change in the composition or texture of a rock occurring subsequent to its formation

anhedral (allotriomorphic): having a lack of crystal form

angular: grains with sharp edges

ankerite: variety of dolomite containing much iron,
 $\text{Ca}(\text{Fe}, \text{Mg}, \text{Mn})(\text{CO}_3)_2$

apatite: group of calcium phosphate minerals,
 $\text{Ca}_5(\text{F}, \text{Cl}, \text{OH}, 0.5\text{CO}_3)(\text{PO}_4)_3$

BIF: Banded Iron Formation

biotite: $\text{K}(\text{Mg}, \text{Fe})_3\text{AlSi}_3\text{O}_{10}(\text{OH}, \text{F})_2$, mineral in the mica group

boehmite: $\text{AlO}(\text{OH})$

calcite: CaCO_3 , calcium carbonate

chalcopyrite: CuFeS_2 , mineral with tetragonal structure

concentrates: ore treated by any process which retain valuable constituents and discard those of no commercial interest

chrysotile: fibrous silky serpentine $\text{Mg}_3\text{Si}_2\text{O}_5(\text{OH})_4$

cummingtonite: $(\text{Fe}, \text{Mg})_7\text{Si}_8\text{O}_{22}(\text{OH})_2$, may contain MnO

dolomite: $\text{MgO} \cdot \text{CaO} \cdot (\text{CO}_2)_2$, calcium magnesium carbonate

euhedral (idiomorphic): having the proper crystal shape

epidote: a group of minerals, generally $\text{Ca}_2(\text{Al}, \text{Fe})_3\text{Si}_3\text{O}_{12}(\text{OH})$

ferrodolomite: $\text{Ca}(\text{Mg}_{0.5}\text{Fe}_{0.5})(\text{CO}_3)_2$

gibbsite: $\text{Al}(\text{OH})_3$, aluminum hydroxide

goethite: $\text{FeO} \cdot \text{OH}$, a mineral of iron hydrogen oxide

granular: consisting of granules (small grains, as sugar)

grunerite: $\text{Fe}_7\text{Si}_8\text{O}_{22}(\text{OH})_2$, a variety of amphibole

hematite: common iron ore, $\alpha\text{-Fe}_2\text{O}_3$, rhombohedral lattice

hornblende: mineral $(\text{Ca}, \text{Na})_{2-3}(\text{Mg}, \text{Fe}, \text{Al})_5(\text{Si}, \text{Al})_8\text{O}_{22}(\text{OH})_2$

hypogene: formed by generally ascending solutions (opposed to supergene)

ilmenite: $\text{FeO} \cdot \text{TiO}_2$

itabirite: iron ore composed of alternate layers or laminations of metamorphosed hematite, magnetite, or martite and quartz

- kaolin:** clay containing kaolinite as its principle constituent
- kaolinite:** hydrous aluminum silicate $\text{Al}_2\text{Si}_2\text{O}_5(\text{OH})_4$
- jaspilite:** a compact siliceous rock rich in hematite and resembling jasper (an opaque cryptocrystalline quartz)
- maghemite:** $\gamma\text{-Fe}_2\text{O}_3$, spinel with structure similar to magnetite
- magnetite:** magnetic iron ore, Fe_3O_4 , inverse spinel (cubic)
- marble:** the metamorphosed equivalent of carbonate rocks
- martite:** pseudomorph hematite, formed from magnetite
- metamorphic grade:** the relative intensity of metamorphism, low m.g. implies low pressures and temperatures
- metamorphism:** a pronounced change in the constitution of a rock caused by pressure, heat, and moisture that results in a more compact and crystalline condition of the rock
- metasomatic:** relating to important changes in the chemical composition as well as mineral comp. and texture of rock
- meteoric water:** water which falls as rain or snow
- mica:** group of hydrous aluminosilicate minerals with a sheetlike crystal structure, $\text{K}_2\text{O}\cdot 3\text{Al}_2\text{O}_3\cdot 6\text{SiO}_2\cdot 2\text{H}_2\text{O}$
- protore:** metalliferous material before it becomes ore
- pseudomorph:** with characteristic outward form of another mineral
- pyrite:** FeS_2 , cubic crystals
- rutil:** TiO_2 , tetragonal crystals of titanium oxide
- schist:** a metamorphic crystalline rock with a closely foliated structure that readily is cleaved in approx. parallel planes
- siderite:** ferrous carbonate, FeCO_3 , containing 48% Fe
- specular:** having a smooth reflecting surface or metallic lustre
- subhedral (hypidiomorphic):** a textural term implying that some grains show crystal contours, others are irregular
- supergene:** deposited or enriched by downward moving solutions
- synmetamorphic:** deposit metamorphic changed at the same time as the rocks in which it occurs
- taconite:** a low grade, hard, sedimentary ore, mainly magnetite and a silicious gangue
- tabular:** having a flat surface
- talc:** $3\text{MgO}\cdot 4\text{SiO}_2\cdot \text{H}_2\text{O}$

1 INTRODUCTION

1.1 Background

The reason why this project was initiated was the actuality of the Elkem Polar Process for reduction of iron, manganese, chrome, and titanium fines (Båsen and Ephithite, 1988). Although most of the work done so far has focused on iron ore prereduction, the Elkem Polar Process is designed to reduce ore fines to pig iron, steel, FeNi, FeMn, FeCr, etc.. The steel process is shown in figure 1.1. The original process concept includes a calcining unit for cheap coal. In separate units ore fines are dried, preheated and prereduced during pneumatic transport in a reducing gas from Elkem's electric furnaces, and introduced directly into the respective smelts. In each step gas and concentrate are concurrent, but the different steps are arranged to be counter current for optimum energy benefit, referring to figure 1.2.

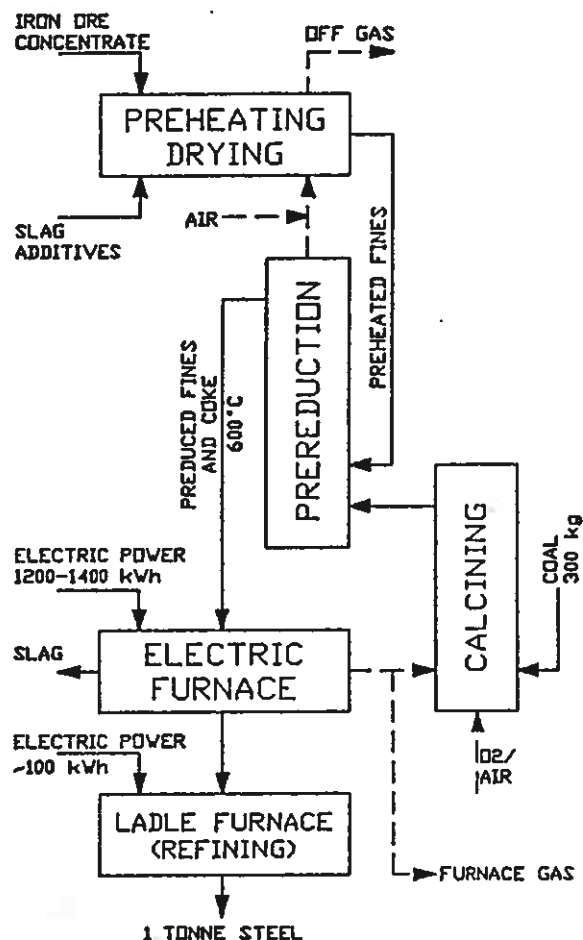


Fig. 1.1 The steel process (Båsen and Ephithite, 1988)

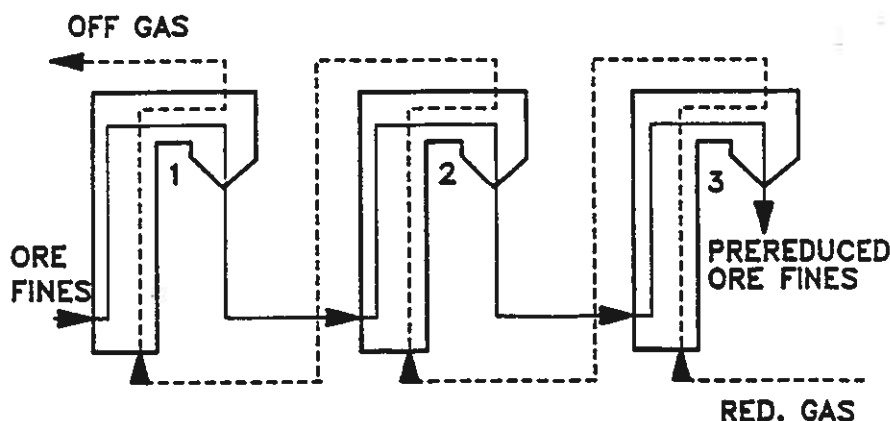


Fig. 1.2 Prereduction unit, 3 steps (Kolbeinsen et al., 1988)

Because the Elkem Polar Process is based on pneumatic transport, only limited time will be available for prereduction. High reduction rates are essential for the benefit of the prereduction unit.

The Elkem Polar Process lower the production price of pig iron both by optimal energy use and cheap raw materials (Båsen and Ephithite, 1988). There will be no need for pellet or sinter plants.

SINTEF and Elkem developed a laboratory scale reactor designed to simulate the Elkem Polar Process. It has been described by Kolbeinsen, Lindstad and Grøntvedt (1988 and 1989). This reactor provides a convenient means to study gas/solid reactions. Positive results from prereduction experiments encouraged Elkem to build a pilot plant in collaboration with Norsk Jernverk A/S at their facilities in Mo i Rana in northern Norway to test parts of the concepts of the Elkem Polar Process. Drying, heating, and prereduction of hematite fines from Rana was conducted. Calcining of cheap coal was also carried out.

Båsen, Ephithite, and Floa (1989) concluded from the gathered results that prereduction should take place in one or two steps preferably without calcining of coal. In this way 20-25% of the ore oxygen content is removed. Actual pilot plant experiments gave a retention time of 12 s for fines in one prereduction unit. During these 12 seconds, 8% of the oxygen was removed from the hematite concentrate. Reduction gas from the electric reduction furnace at Norsk Jernverk A/S was used and coal calcining was excluded. Experiments carried out in a modified model of the pilot plant have indicated the possibility of extending the retention time to 40 seconds. Båsen, Ephithite, and Floa (1989) also conclude that there is good agreement between the results from the laboratory scale reactor and the pilot plant. Smelting of fines is possible and has been carried out at New Zealand Steel and in the laboratory, but further experiments are required.

1.2 Aim of the present study

Hematite (Fe_2O_3) and magnetite (Fe_3O_4) are among the most common iron ore minerals. The reduction rate of magnetite is known to be very slow compared to the reduction rate of hematite. Experiments carried out in the previously mentioned laboratory scale reactor by Baumann (1985), Storemyr (1986 b), and Steinmo (1986), have verified that magnetite concentrates are too slowly reduced to be used directly in the Elkem Polar Process.

However, magnetite becomes an interesting iron ore mineral for the Elkem Polar Process after preoxidation to hematite. The process concept allows oxidation in the heating unit, but maximum retention time will be the same as in the prereluction unit (40s). Preoxidation should be carried out in a separate unit if oxidation is not fairly complete within 40s. Partial oxidation is not sufficient for rapid prereluction (Monsen et al., 1988).

It is considered to be a great advantage for the Elkem Polar Process if initial reduction rates for different natural hematite concentrates could be predicted by raw material characterization.

Oxidation conditions may influence on the reduction rates. Predictions of reduction rates of differently oxidized magnetite by characterization of subgrain structure of preoxidized samples should also be an advantage for the Elkem Polar Process.

The aim of the present work can be divided in three parts:

The first is to explain different reduction rates of naturally occurring hematite by physical and chemical characterization of raw materials.

The second is to investigate the possibility of preoxidation of magnetite in the heating unit of the Elkem Polar Process by studying oxidation kinetics for magnetite.

The third is to investigate a possible influence of the preoxidation temperature on the reduction rates of completely oxidized magnetite concentrates. Different reduction rates should be explained by characterization of preoxidized samples.

1.3 Experimental plan

Hematites from Brazil (2 types), Guinea, Liberia, Canada and Norway have been selected for comparing reduction rates. A narrow fraction (63-90) μm of the hematite fines is to be used in the prereduction experiments (see chapter 5) and the same fraction is to be characterized in chapter 4. Actual parameters are mineral phases, grain size distribution, specific surface area, subgrain structure, grain shape, and trace elements.

The progress of reduction will be studied in the previously mentioned laboratory scale reactor developed by SINTEF and Elkem. Hematite samples will be exposed to moderate temperatures (700-850°C) for periods up to 60 seconds in gas mixtures of H_2 , H_2O , CO and CO_2 , according to an experimental plan shown in table 1.1.

Table 1.1. Experimental plan for hematite reduction.

Temperature (°C)					RO ¹⁾ (%)			H ₂ in inlet gas (%)					Reduction time (s)						
700	730	760	800	850	20	35	50	0	15	25	35	45	12	20	30	35	40	50	60
		x			x						x		x	x	x		x	x	x
		x				x					x		x	x		x			x
		x					x				x		x	x		x			x
		x			x			x						x					
		x					x		x					x					
		x					x			x				x					
		x			x						x			x					
		x	x								x			x					
x							x				x			x					
	x						x				x			x					
			x				x				x			x					
				x			x				x			x					

1) RO (%) = The oxidizing potential of the reduction gas
Equilibrium phases at 760°C: Fe (20%RO), Fe_{1-y}O (35 and 50% RO)
%RO = %H₂O + %CO₂

The gas mixture is equilibrated by means of a Ni-catalyst for the water-gas shift reaction (WGS). The inlet gas mixture consists

of H₂, CO, and CO₂. Temperature, oxidizing potential of the reduction gas (%RO, referring to formula 1.1), and hydrogen content will be varied, but kept constant during each experiment.

$$\%RO = \%H_2O + \%CO_2 \quad (1.1)$$

Methods chosen to investigate the progress of reduction are wet chemical analyses of the prereduced samples and studies in optical microscope on polished surface specimens of selected samples. Differences in rates of reduction are to be related to properties characteristic of the hematite fines.

Sydvaranger magnetite concentrate with >99% magnetite is commercially available. This concentrate is chosen both for the studies of oxidation rate in section 3.3, and for the preoxidation experiments (complete oxidation, see section 3.4).

The laboratory scale reactor developed by SINTEF and Elkem is well suited for the studies of rate of oxidation at temperatures below 850°C. Oxidation will be carried out at 400-850 °C in air for 15, 30, and 60s, referring to section 3.3. Chemical analysis and microscopy will be used to study the progress of oxidation.

Another method, described in section 3.4, was chosen for preoxidation of material for subsequent reduction. Magnetite concentrate is oxidized to hematite at 8 different temperatures ranging from 800°C to 1250°C, referring to section 3.4. The subgrain structures of these preoxidized samples ("artificial" hematites) are characterized by videoplan in section 3.5. The results of prereduction experiments with the preoxidized magnetite are given in section 5.4, while the different reduction rates are discussed in section 5.8.

The rates of reduction for "artificial" and natural hematites will be compared in section 5.10. Differences will, if possible, be related to characteristic properties.

2 GENERAL PRINCIPLES

2.1 Physical and structural properties

This section deals with the physical and structural properties of the minerals hematite and magnetite and the reduction products wüstite and iron. Table 2.1 gives a brief review of the actual modifications, their existence and physical and structural properties.

Table 2.1 Physical and structural properties.

Name	Formula	Structure	Density 1) (g/cm ³)	Iron content (wt%)
Hematite	α -Fe ₂ O ₃	rhombohedral	5.24	70.0
Maghemite	γ - "	cubic, spinel	-	
Magnetite	Fe ₃ O ₄	cubic, inverse spinel	5.18	72.4
Wüstite	Fe _{1-y} O T>560°C	cubic, NaCl type	5.7	74.4- 76.9
Iron:	Fe ²⁾	cubic:	7.86	100
Ferrite	α -Fe T<912°C	body-centred		
Austenite	γ -Fe 912<T<1394°C	face-centred		
	δ -Fe 1394<T<1539°C	body-centred		

1) Weast: "Handbook of chemistry and physics", 1981-1982.

2) Transformation temperatures: Cubberly et al.: "Metals Handbook", 1979.

Hematite is the highest oxidation state of iron and forms the most abundant and important ore of iron. Different modifications exist (α and γ) of which α -Fe₂O₃ is the one abundant in ores. A third modification, β -Fe₂O₃, has also been produced under very special conditions. β -Fe₂O₃ has a cubic structure.

α -Fe₂O₃ crystallizes in the rhombohedral system of the Al₂O₃ type. The unit cell contains 18 oxygen ions arranged in a close-packed hexagonal lattice with the ferric ions (Fe³⁺) in octahedral coordination between them. As indicated in figure 2.1 only ²/₃ of the octahedral spaces are occupied by Fe³⁺, the remaining ¹/₃ are vacant. The (0001) plane is also shown in figure 2.1. Each oxygen ion is shared between four octahedra.

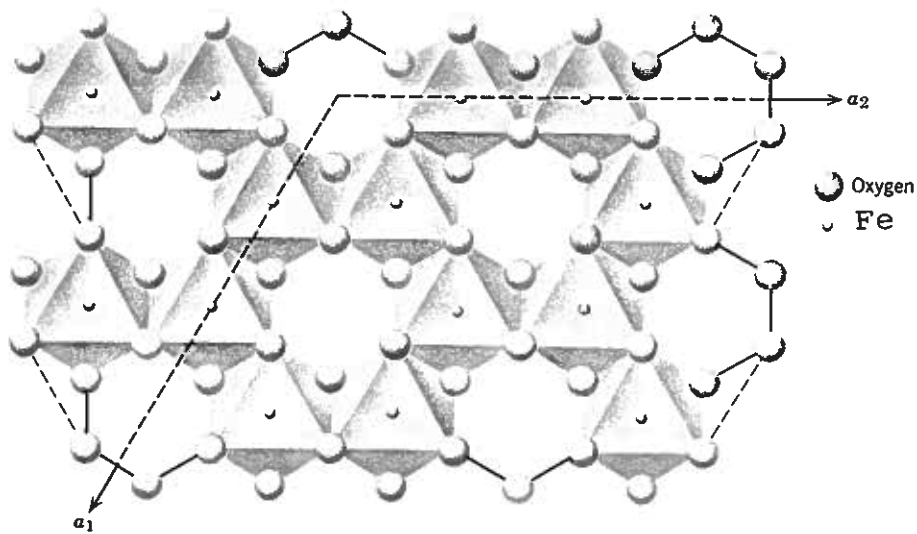


Fig. 2.1 Structure of hematite, $\alpha\text{-Fe}_2\text{O}_3$, with one octahedron vacant for every two octahedra with Fe^{3+} in centre, (Hurlbut and Klein, 1977).

Hematite crystals are usually tabular on (0001), as shown in figure 2.2b, and both thick and thin plates are common (Hurlbut and Klein, 1977). The thin plates may be grouped in rosettes (iron roses). More rarely crystals are distinctly rhombohedral and twinned on (0001) and (1011). Hematite crystals may also be micaceous and foliated (specular).

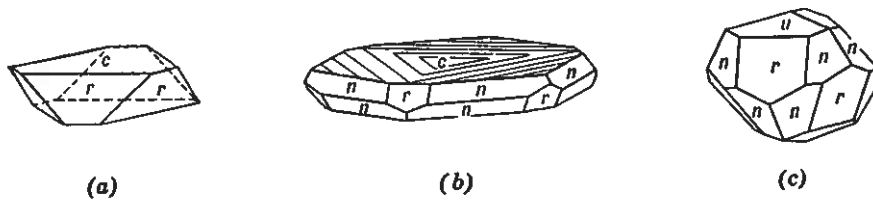


Fig. 2.2 Hematite crystals (Hurlbut and Klein, 1977).

$\gamma\text{-Fe}_2\text{O}_3$ is a spinel with an increased concentration of vacancies in the octahedral positions. The lattice structure of this modification of hematite has great similarities with the magnetite lattice. $\gamma\text{-Fe}_2\text{O}_3$ is called maghemite and it is also magnetic. Maghemite may be produced by oxidation of magnetite, but only under quite specific conditions. Water is thought to stabilize the structure.

Magnetite ($\text{Fe}^{2+}\text{O}\cdot\text{Fe}^{3+}_2\text{O}_3$) crystallizes in the cubic, inverse spinel, lattice. The oxygen ions form a face-centred cubic lattice while the smaller iron ions are distributed in the interstices.

The unit cell contains 32 oxygen atoms and 24 iron ions. A photograph of a model of the magnetite structure is shown in figure 2.3. In an ideally ordered lattice the iron ions occupy 8 of the 64 tetrahedral possible positions (mainly vacancies) and 16 of the 32 octahedral positions. The sixteen octahedral positions are occupied by 8 Fe^{3+} and 8 Fe^{2+} , while the remaining 8 Fe^{3+} are in the tetrahedral positions.

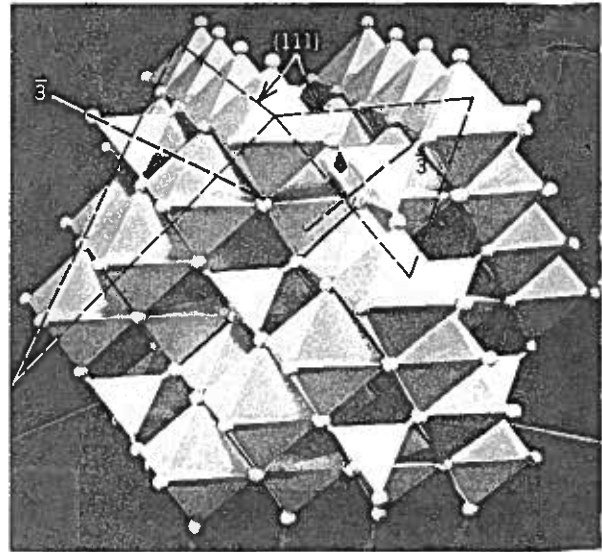


Fig. 2.3 The magnetite structure, inverse spinel, from Hurlbut and Klein (1977).

Deviations from this ideal inverse spinel structure occur in that octahedral and tetrahedral vacancies may be occupied and vice versa. Disorder plays an important part in the iron ions diffusion in the magnetite lattice. Easy interchange of charge between Fe^{2+} and Fe^{3+} in octahedral positions gives rise to high electrical conductivity. Magnetite is also strongly magnetic. At elevated temperatures ($>900^\circ\text{C}$) the magnetite structure is able to incorporate an excess of the trivalent iron ions.

Magnetite is frequently found as octahedral crystals, occasionally twinned on (111). Dodecahedrons occur more rarely, referring to figure 2.4, (Hurlbut and Klein, 1977).

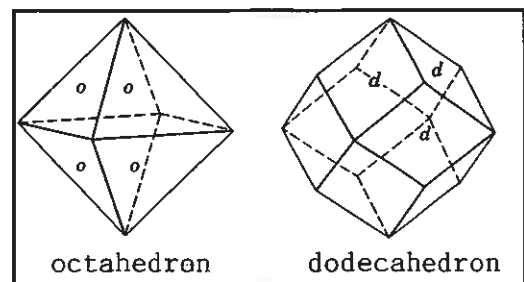
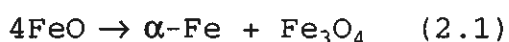


Fig. 2.4 Magnetite crystals (Hurlbut and Klein, 1977).

Wüstite crystallizes in the cubic NaCl lattice. The oxygen sublattice is largely occupied in the face-centred (close-packed) positions while the smaller iron ions are arranged in the octahedral interstices. Iron is to be considered as deficient as the formula Fe_{1-y}O indicate. The letter y in Fe_{1-y}O denotes the proportion of vacant iron ion lattice positions relative to the available number of iron lattice-points. The range of existence for wüstite is fairly large, but does not include stoichiometric FeO ($0.046 < y < 0.168$, Barin et al., 1977). The concentration y of the vacancies is dependant on the oxygen pressure and the temperature.

Electrical neutrality is maintained by the substitution of trivalent iron ions for divalent iron ions, equal to double the number of vacancies. The structure is illustrated in figure 2.5, indicating the easy diffusion of iron ions in the wüstite lattice because of the vacancies.

Wüstite is unstable below 570°C , where it decomposes into $\alpha\text{-Fe}$ and Fe_3O_4 .



However, wüstite can easily be maintained as a metastable phase by quenching.

Iron in its pure liquid state freezes at 1539°C and crystallizes to $\delta\text{-Fe}$ in a body-centred cubic lattice. On cooling the lattice changes to a face-centred cubic structure at 1394°C . This iron modification is called austenite ($\gamma\text{-Fe}$) and is stable down to 912°C , where the structure rearranges again to a body-centred cubic form, named ferrite ($\alpha\text{-Fe}$).

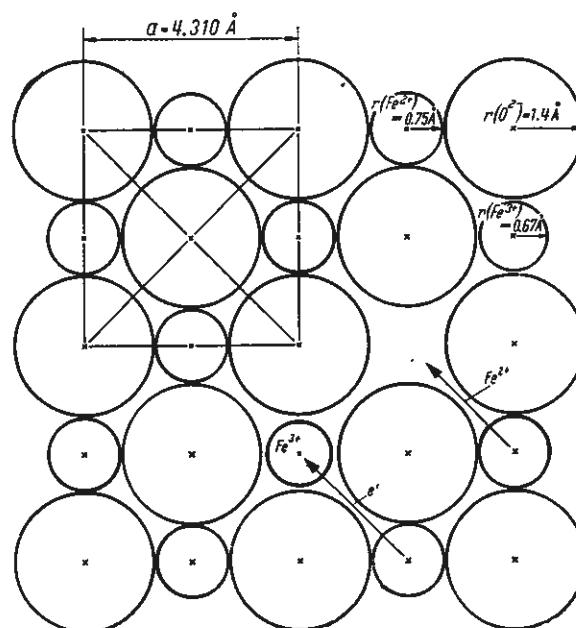


Fig. 2.5 (100)-plane of Fe_{1-y}O with an iron ion vacancy and 2Fe^{3+} . Big ions are oxygen and small ions are iron (Bogdandy and Engell, 1971).

Iron is magnetic, but loses its magnetism during heating above 771°C (magnetic transformation temperature: Cubberly et al.: "Metals Handbook", 1979.)

Iron may dissolve carbon in the presence of CO/CO₂ gas mixtures. The body-centred cubic structure of ferrite has a maximum solubility of approximately 0.025% carbon at about 723°C, while the face-centred cubic structure of austenite may dissolve almost 2% carbon.

2.2 Phase diagrams

The thermodynamically stable phases in the iron-oxygen system are given in the binary diagram in figure 2.6. The diagram is mainly

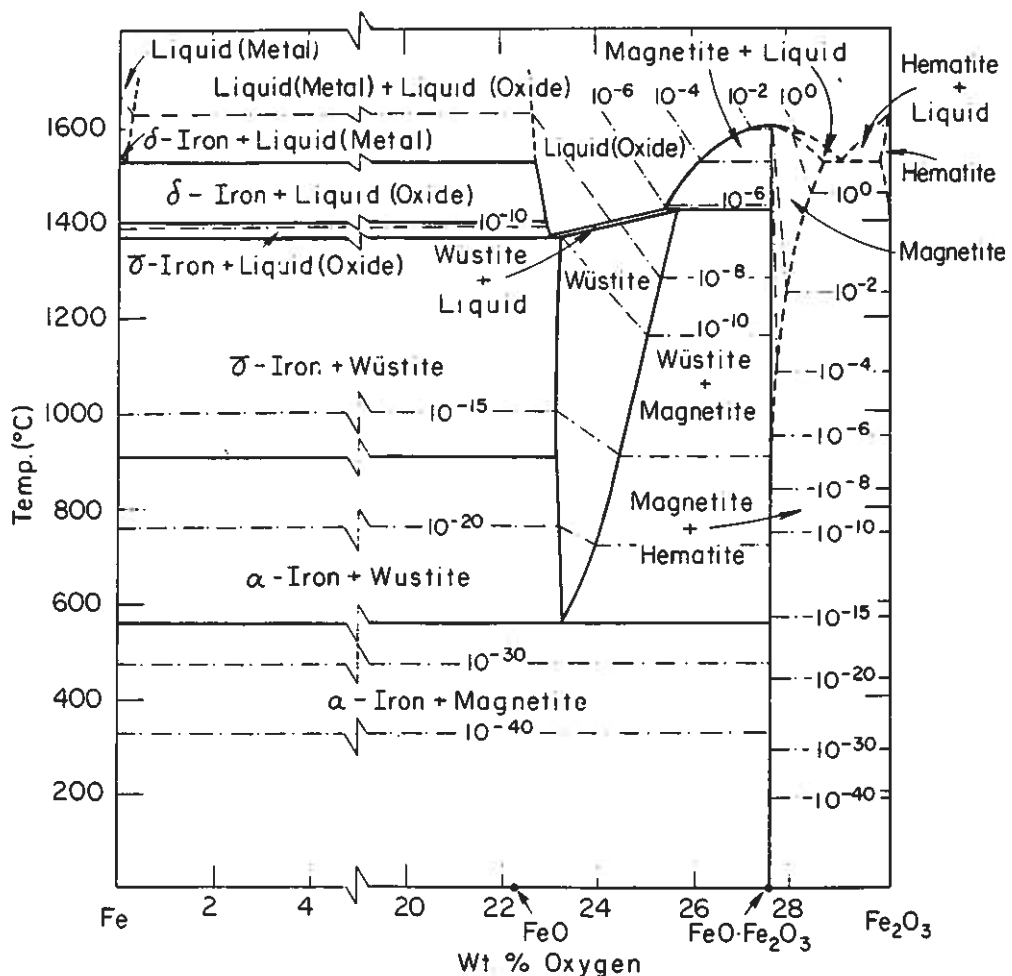


Fig. 2.6 The iron-oxygen system (Levin, Robbins, and McMurdie, 1969). Dash-dot lines are O₂ isobars.

based on the original measurements of Darken and Gurry (1946), in the form given by Muan (1958), and presented by Levin, Robbins, and McMurdie in "Phase diagrams for ceramics" (1969).

Figure 2.7 shows the regions of stability for iron, wüstite, magnetite, and hematite. The diagram was prepared by Bogdandy and Engell (1971) by using mean values for ΔH and ΔS from thermodynamical tables. The narrow stability region of wüstite decreases continuously as the temperature falls and disappears at 570°C.

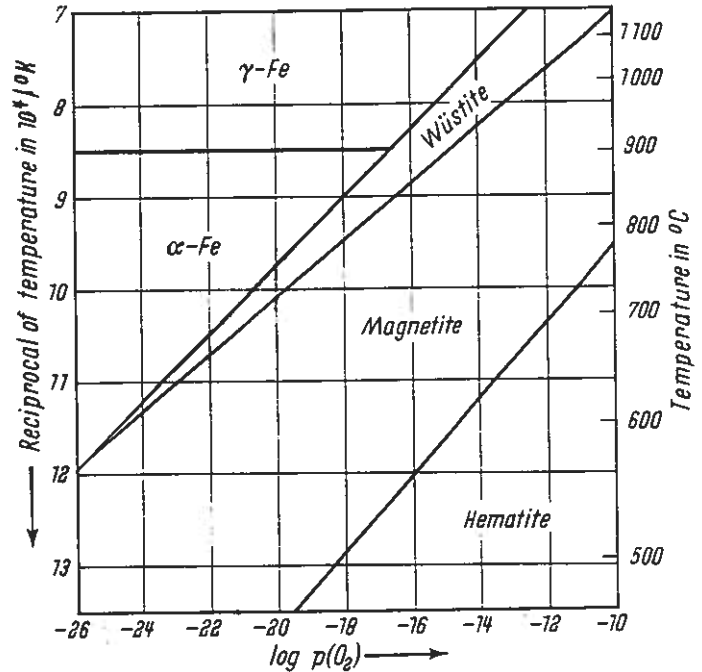


Fig. 2.7 Thermochemically stable regions for Fe, $Fe_{1-y}O$, Fe_3O_4 , and Fe_2O_3 (Bogdandy and Engell, 1971).

A closer look into the wüstite phase domain in the iron-oxygen system is taken in figure 2.8. The diagram shows the dependence of the vacancy concentration y in $Fe_{1-y}O$ on both temperature and oxygen pressure. The diagram was constructed by Bogdandy and Engell (1971) from the results obtained by several authors.

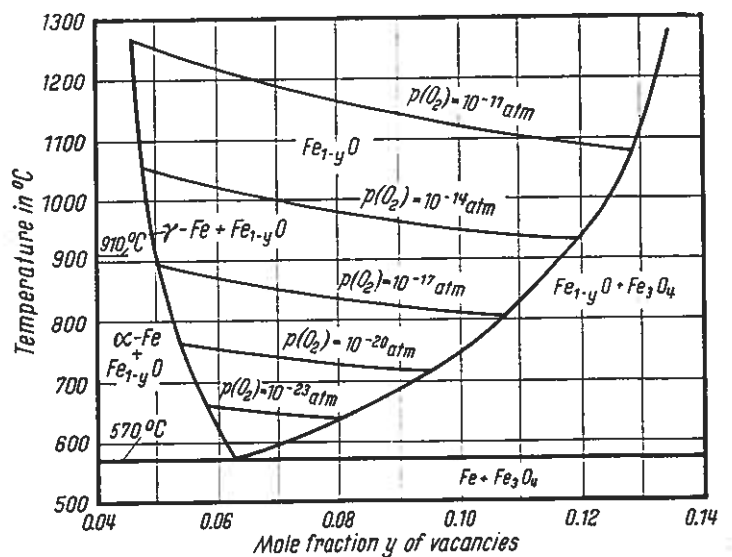


Fig. 2.8 The $Fe_{1-y}O$ phase domain with O_2 isobars in the Fe - O_2 system (Bogdandy and Engell, 1971).

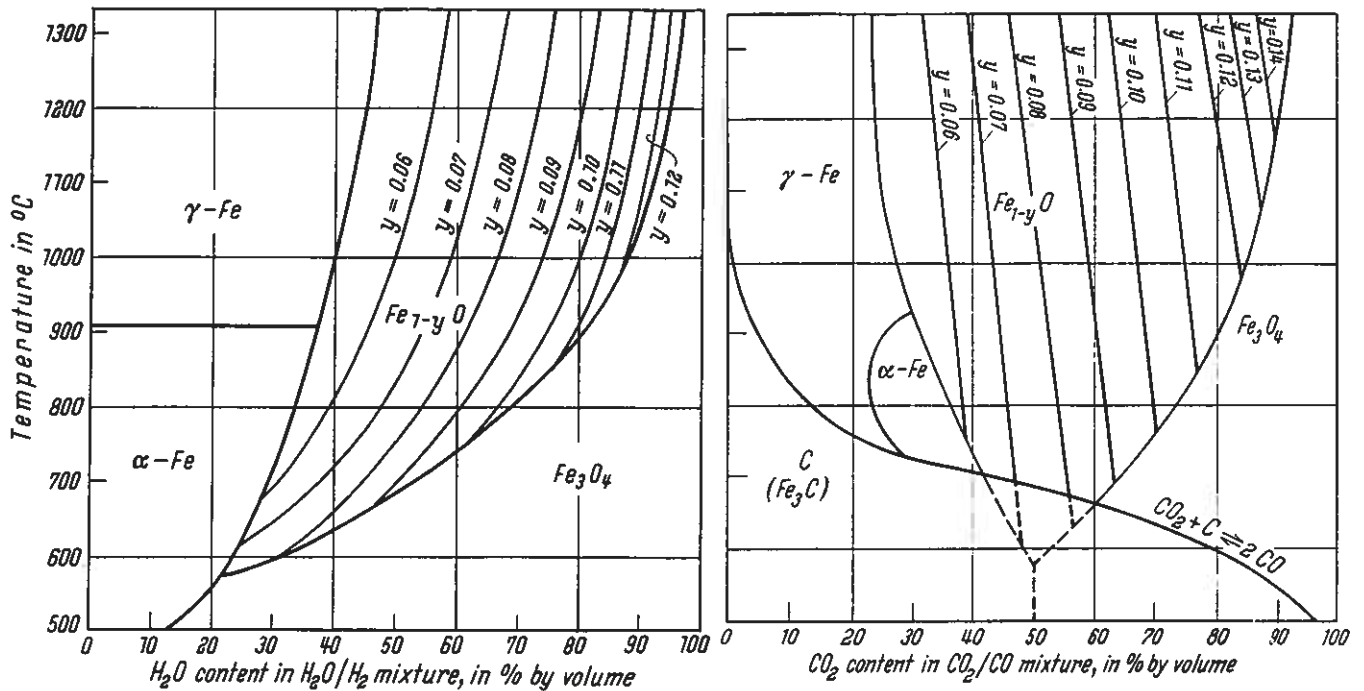


Fig. 2.9 Baur-Glaessner diagrams showing the equilibria between iron, wüstite, magnetite and:

- H₂/H₂O
- CO/CO₂ and C(s), $P(\text{CO}) + P(\text{CO}_2) = 1 \text{ atm.}$

The equilibria between iron, wüstite, magnetite and a H₂/H₂O gas mixture are shown in figure 2.9a while figure 2.9b shows the equilibria between the same solid phases in addition to carbon and a CO/CO₂ gas mixture (Bogdandy and Engell, 1971). Such equilibrium diagrams are generally known as Baur-Glaessner diagrams.

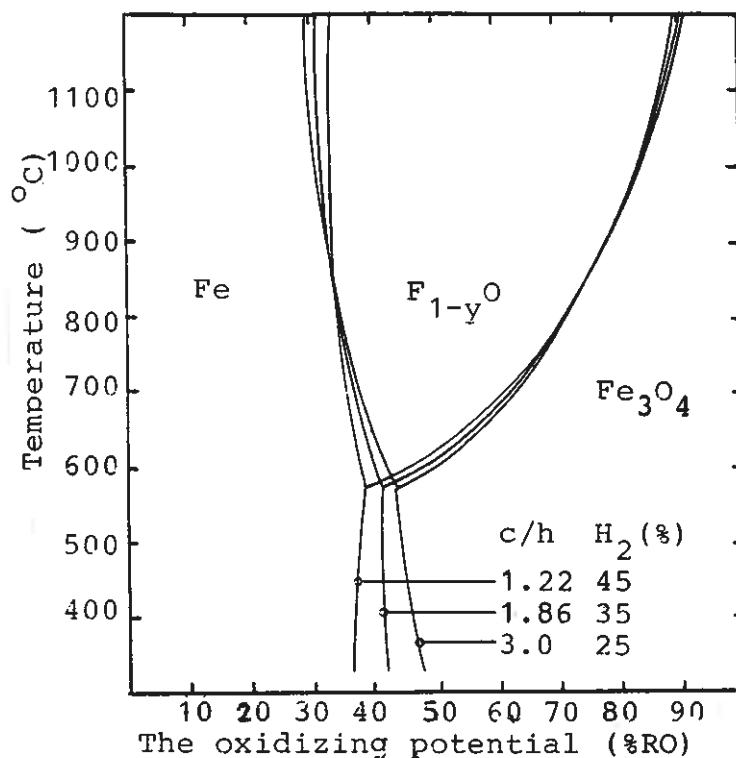
The two diagrams are fairly similar and the characteristic shape of the phase boundaries of the wüstite phase, the "fork", may be recognized in both.

The equilibrium line for the Boudouard reaction: $2\text{CO}(\text{g}) = \text{CO}_2(\text{g}) + \text{C}(\text{s})$ is also drawn in the diagram in figure 2.9b. Below this line the CO/CO₂ gas mixture is supersaturated on carbon and carbon deposition is possible.

To avoid carbon deposition, according to figure 2.9b, the temperature should not fall below 760°C and 685°C with 20% and

50% CO₂ (%RO) in the reducing gas, respectively. These limits have been carefully watched in the present work in the reduction experiments without hydrogen in the reduction gas. The reduction experiments are carried out in the temperature range 700-850°C and the content of CO₂ in the inlet reduction gas never falls below 20%.

However, in most of the reduction experiments, the reduction gas is a mixture of CO, CO₂, H₂, and H₂O. A diagram which combines the two diagrams is therefore very useful. Such a Baur-Glaessner diagram is shown in figure 2.10. The diagram was constructed by Dr. L. Kolbeinsen, as explained in his thesis (Kolbeinsen, 1982) and reported by Grøntvedt et al. (1986) and Kolbeinsen et al. (1988, 1989). The diagram is drawn for constant relations



between carbon and hydrogen bearing species in the reduction gas in accordance with formula 2.2. The oxidizing potential of the reduction gas (%RO) is defined according to formula 2.3.

$$\frac{c}{h} = \frac{P_{CO} + P_{CO_2}}{P_{H_2} + P_{H_2O}} \quad (2.2)$$

$$\%RO = \frac{P_{H_2O} + P_{CO_2}}{P_{H_2O} + P_{CO_2} + P_{H_2} + P_{CO}} \cdot 100\% \quad (2.3)$$

The relative thermodynamical stability of the phases Fe, Fe_{1-y}O , and Fe_3O_4 in the temperature range 700-850°C is insignificantly changed in the c/h range 1.22-3.0, corresponding to 45%-25% H_2 in the reduction gas.

The iron-carbon phase diagram is given in figure 2.11 as presented by Rosenqvist (1985) on the basis of the work by Smith (1946). Only the thermodynamically stable phases are shown.

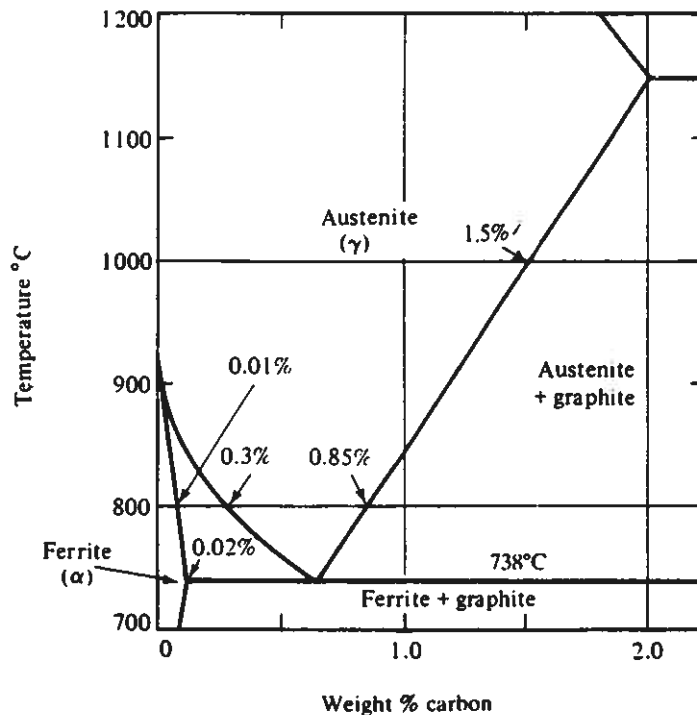
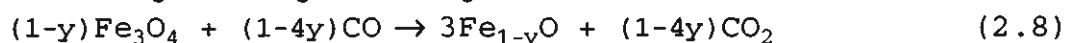
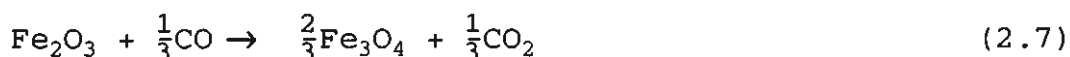
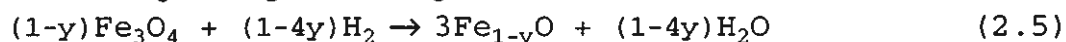


Fig. 2.11 The iron-carbon system showing the thermodynamically stable phases. (Rosenqvist, 1985).

2.3 Chemical reactions

2.3.1 Reduction of hematite

Reduction of Fe_2O_3 (hematite) to iron proceeds over the lower oxides Fe_3O_4 (magnetite) and Fe_{1-y}O (wüstite). The reduction reactions for reduction of hematite with the two reducing gases H_2 and CO are shown in the following. Other reducing gases (e. g. natural gas) have not been considered in the present work.



Calculations of ΔH_r° and ΔG_r° for the reactions 2.4-2.9 are presented in table 2.2. The calculations are based on JANAF Thermochemical Tables (1985) and $y=0.053$ in Fe_{1-y}O ($\text{Fe}_{0.947}\text{O}$).

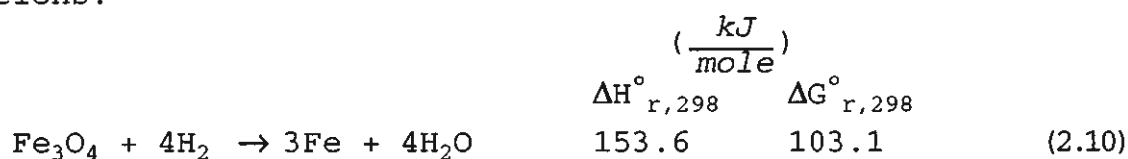
Table 2.2. Thermodynamical data calculated from JANAF Thermochemical Tables (1985).

Equation no. ¹	(kJ/equation)			
	$\Delta H_{r,298}^\circ$	$\Delta G_{r,298}^\circ$	$\Delta H_{r,1033}^\circ$	$\Delta G_{r,1033}^\circ$
2.4	-2.7	-11.0	-3.0	-31.6
2.5	72.1	48.0	48.4	-0.9
2.6	24.4	16.6	15.7	6.5
2.7	-16.1	-20.5	-14.5	-32.3
2.8	39.7	25.4	21.2	-2.5
2.9	-16.7	-12.1	-18.8	4.5

1) $y = 0.053$ in equations 2.5, 2.6, 2.8, and 2.9.

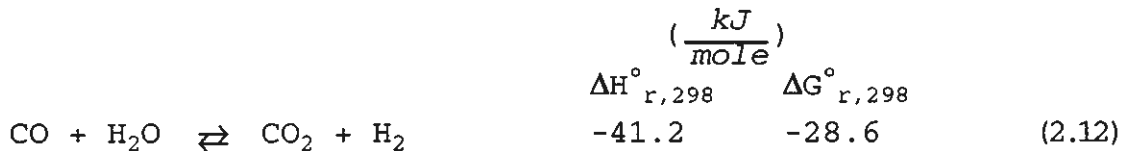
Both H_2 - and CO -reduction of hematite to magnetite are exothermal reactions, while reduction of magnetite to wüstite are endothermal reactions. The final reduction of Fe_{1-y}O to iron with H_2 is endothermic while reduction with CO is exothermic. Enthalpy and free energy of reaction at 760°C (1033°K) are incorporated in table 2.2 because most of the reduction experiments are carried out at that temperature.

Fe_{1-y}O is unstable at temperatures below 570°C . At these low temperatures magnetite reduces directly to iron according to the equations:



2.3.2 The water-gas shift reaction (WGSR)

When reduction is carried out with mixtures of the reduction gases H_2 and CO , the WGSR has to be taken into account:



The WGSR does not change the oxidizing potential of the reduction gas, but merely shifts the oxygen atom between the two reducing gases, H_2 and CO . Reduction rates are higher for reduction by H_2 than by CO and even small additions of H_2 to CO/CO_2 mixtures have a reaction promoting effect, referring also to chapter 5. Bogdandy and Engell (1971, pages 200-202) conclude in their literature survey that $Fe_{1-y}O$ is reduced largely by H_2 in gas mixtures and a major use for the CO is to regenerate H_2 by the WGSR. In this way the WGSR is thought to play an important role in iron ore reduction with gas mixtures.

According to Bogdandy and Engell (1971) there is also a general agreement in the literature that the rate-determining stage of the water-gas shift reaction is the transfer of adsorbed oxygen (adsorbed on a catalyst) to the CO in reaction 2.12b.



This was later confirmed by Meschter and Grabke (1979). They found an activation energy of 124.7 kJ/mole for the WGSR on a $Fe_{1-y}O$ surface. They also confirm that the WGSR needs a catalyst to be effective at temperatures of iron ore reduction. Karim and Mohindra (1974), among others, also found that the WGSR did not reach equilibrium conditions within a reasonable residence time below 730°C in homogeneous uncatalysed combustion systems.

The WGSR is a reaction of considerable industrial importance and

frequently used in conjunction with the production of hydrogen via the nickel catalysed steam reforming of hydrocarbons. The effluent from the steam reformers is passed to a series of water-gas shift reactors which are operated at lower temperatures in order to shift the equilibrium of reaction (2.12) to the right. In the first stage at intermediate temperatures (315-485°C) the water-gas shift reaction catalyst is based on iron oxide-chromium oxide compositions. In the second stage at still lower temperatures (175-350°C) the catalyst of choice is based on copper oxide - zinc oxide. This information and further descriptions of commercial catalysts can be found in "Catalytic processes and proven catalysts" by Thomas (1970). Grenoble et al. (1981) have investigated the catalytic effect of several alumina-supported metals on the WGSR at 300°C and found the turnover number (rate per surface metal atom) to decrease in the order: Cu, Re, Co, Ru, Ni, Pt, Os, Au, Fe, Pd, Rh, and Ir. In the present work a nickel based catalyst is chosen to provide water-gas shift equilibrium prior to reduction in the reactor.

All the constituents in iron ore reduction are catalysts, but metallic iron is held to be a much better catalyst than the iron oxides. According to Grabke (1965 and 1967) the rate constants for oxygen exchange according to reaction (2.12b) are $1.5 \cdot 10^{-9}$ and $2.5 \cdot 10^{-7}$ for wüstite and iron, respectively, at 800°C for a ratio of $\text{CO}_2/\text{CO} = 0.5$. Turkdogan and Vinters (1972) found that the rate of dissociation or formation of H_2O or CO_2 on the iron surface is about an order of magnitude greater than that on the surface of Fe_{1-y}O . They also conclude that even in the presence of porous metallic iron, gas reactions participating in the water-gas shift equilibrium are slow at temperatures below 1000°C.

As earlier pointed out, the rate determining step in the WGSR is the transfer of oxygen from the catalyst to the CO. The same step is rate determining in CO-reduction of Fe_{1-y}O (Grabke, 1965). This immediately implies that the WGSR on Fe_{1-y}O cannot take place more quickly than Fe_{1-y}O reduction with CO. To

understand the increase in reduction rate of Fe_{1-y}O by addition of even slight amounts of H_2 to CO/CO_2 mixtures, the catalytic effect of iron on the WGSR must be remembered. The reduction takes place at the oxides, but the regeneration of the hydrogen by the WGSR takes place at the iron. These two reactions must be connected by diffusion of one of the participants in the reaction. The optimal conditions occur at the boundary metal/oxide/gas.

The equilibrium constant (k_w) for the WGSR is given by:

$$k_w = \frac{P_{\text{CO}_2} \cdot P_{\text{H}_2}}{P_{\text{CO}} \cdot P_{\text{H}_2\text{O}}} = \exp\left(-\frac{\Delta G_{r,T}^\circ}{RT}\right) \quad (2.13)$$

A formula for rough calculations of k_w is given by Bogdandy and Engell (1971, page 39) for the temperature range 600 - 1100°C:

$$\log k_w = -1.6 + 1800/T \quad (^\circ\text{K}) \quad (2.14)$$

However, for accurate calculations the values of k_w must be found from the values of $\Delta G_{f,T}^\circ$ for the components as given in thermochemical tables. These accurate values of k_w are given in table 2.3 for the temperatures which are actual in the present work. The free energy of the reaction (2.12) is calculated from JANAF Thermochemical Tables (1985). From the same thermodynamical data it is found that $k_w = 1$ at 823°C.

Table 2.3 Equilibrium constant (k_w) for the WGSR (2.12), calculated from $\Delta G_{r,T}^\circ$ according to formula 2.13.

Temperature		$\Delta G_{r,T}^\circ$ ¹ (kJ/mole)	k_w
(°C)	(°K)		
700	973	-3.888	1.6169
730	1003	-2.923	1.4196
760	1033	-1.984	1.2598
800	1073	-0.733	1.0856
850	1123	+0.811	0.9169

1) Calculated from JANAF Thermochemical Tables (1985)

2.3.3 Methane formation

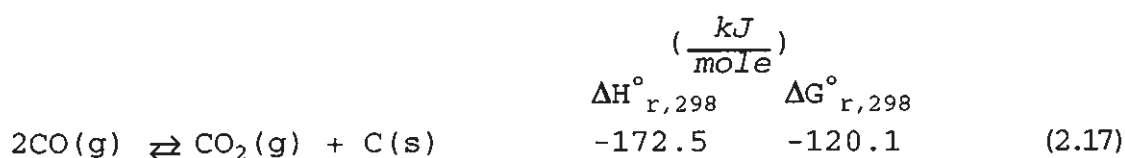
Undesired reactions in gas mixtures of CO/H₂/CO₂/H₂O, such as formation of methane (CH₄), are theoretically possible by the reactions:



Nickel has a catalytic effect on these two reactions (Thomas, 1970). Formation of CH₄ is favoured at low temperatures, elevated pressures and low contents of H₂O and CO₂, respectively. However, the opposite reactions, formation of H₂ and CO, are applied in the reforming of natural gas on a nickel based catalyst with steam and CO₂ at temperatures in the range of 650-1000°C at 3-40 atm. The ratio of steam or CO₂ (moles) to hydrocarbons (atoms) is here 2-6, or higher. These conditions leave 0.1-2.0% CH₄ unreacted (Thomas, 1970). At lower pressure and high contents of CO₂ it is not to be expected any significant formation of CH₄, even for intermediate temperatures (700-850°C) and in the presence of a nickel catalyst. Formation of methane in the gas phase is neglected in the present work for the above mentioned reasons. In the absence of a Ni-catalyst Hara (1976) found that the amount of CH₄ is lower than 1% where the CO-concentration is lower than 30%.

2.3.4 The Boudouard equilibrium

The Boudouard equilibrium has to be taken into account:



Formation of carbon (graphite) from the reduction gas is dependant on temperature, total pressure, and partial pressure

of CO and is likely to happen at low to moderate temperatures and at elevated pressures of CO.

The experimental conditions in the present work have been chosen to avoid carbon deposition because this reaction changes the gas composition in an uncontrollable manner. The oxidizing potential of the reduction gas (%RO) increases with increasing carbon deposition. Carbon deposition will also damage the nickel catalyst.

The decomposition of CO in the homogeneous gas phase takes place so slowly that it is of no real importance for the reduction of ores (Bogdandy and Engell, 1970). Supersaturated reduction gas with respect to graphite may therefore exist, even at rather low temperatures. However, iron is an active catalyst for CO dissociation while cementite (Fe_3C) is considered to be a poor catalyst (Walker et al., 1959, Ruston et al., 1969, Turkdogan and Vinters, 1974, and Olsson and Turkdogan, 1974). Nickel catalysts are also highly active for this undesirable reaction (Thomas, 1970).

The presence of H_2 or H_2O can markedly enhance the rate of carbon deposition under certain conditions (Walker et al., 1959, Turkdogan and Vinters, 1974, Olsson and Turkdogan, 1974, Kolesnik and Pierre, 1980, and Towhidi and Szekely, 1983). Kolesnik and Pierre (1980) try to explain these experimental evidences by suggesting a possible formation of an intermediate complex $(\text{CHO})^*$ on the catalytic surface. They found that there is an optimum content of H_2O in CO- H_2O mixtures which provides the maximum rate of carbon deposition at each temperature in the temperature range 430-590°C. It is possible to consider the influence of H_2O in association with the influence of H_2 by taking the water-gas shift reaction into account. Hydrogen is thought to play the active part of the two in carbon deposition. Towhidi and Szekely (1983) found a maximum rate of carbon deposition to occur between 500°C and 600°C, when reducing hematite pellets in $\text{H}_2/\text{CO}/\text{N}_2$ gas mixtures. Above 900°C no carbon deposition was observed. The

presence of N_2 appeared to retard the deposition process.

The critical temperature region for carbon deposition is extended to higher temperatures as the hydrogen content of the gas mixture (CO/H_2) is increased (Walker et al., 1959). For increasing H_2 -content and in the presence of an iron catalyst they found that the temperature increased at which the maximum rate of carbon deposition occurred, from about $528^\circ C$ (99.2% CO -0.8% H_2) to $630^\circ C$ (80.1% CO -19.9% H_2). Increasing the hydrogen content in the gas also markedly increased the total amount of carbon which was formed before catalyst deactivation occurred. A spent catalyst consisted primarily of cementite.

2.3.5 Cementite formation

Cementite (Fe_3C) may be formed by reaction of iron or its oxides and a reduction gas supersaturated with respect to graphite (carbon activity greater than unity):

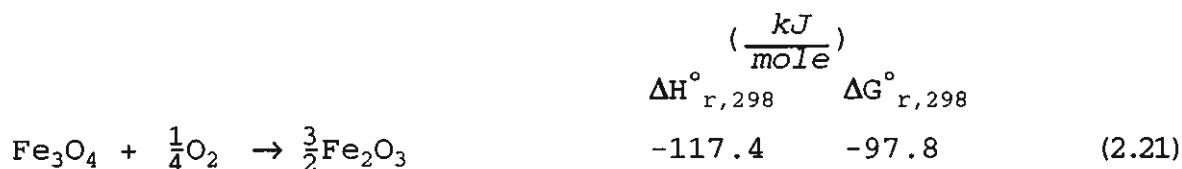


Because cementite is thermodynamically unstable with respect to graphite, the reactions 2.18 - 2.20 are to be regarded as metastable equilibria (Rosenqvist, 1985). Formation of cementite from wüstite and magnetite is only possible below $700^\circ C$.

Towhidi and Szekely (1983) found, however, in a structural examination of their partially reacted hematite pellets that the carbon deposited was in the form of elemental carbon rather than cementite. These experiments were carried out in $CO/H_2/N_2$ -mixtures in the temperature range 500 - $1200^\circ C$. Turkdogan and Vinters (1974) have pointed out that if carbon is converted into cementite this could inhibit or at least hinder further carbon deposition since cementite is not a catalyst for CO decomposition.

2.3.6 Oxidation of magnetite

Oxidation of magnetite takes place according to equation 2.21.



Oxidation of magnetite is an exothermal reaction which might well take place at room temperature from a thermodynamical point of view (negative $\Delta G^\circ_{r,298}$). The kinetics of the oxidation process is unfavourable at low temperatures. Hence, large magnetite deposits are present in nature. The kinetics of the oxidation process will be discussed in chapter 3. Thermodynamical data for the oxidation reaction 2.21 are given in table 2.4 for the temperatures actual in the present work.

Table 2.4 Thermodynamical data for oxidation of magnetite¹.

Temperature		$\Delta H^\circ_{r,T}$	$\Delta G^\circ_{r,T}$
(°C)	(°K)	(kJ/mole)	(kJ/mole)
400	673	-118.7	-73.3
600	873	-123.1	-59.3
700	973	-120.9	-52.1
800	1073	-119.2	-45.1
850	1123	-119.0	-41.7
900	1173	-118.8	-38.3
1000	1273	-118.5	-31.4
1050	1323	-118.4	-28.0
1100	1373	-118.2	-24.6
1150	1423	-117.9	-21.2
1200	1473	-117.7	-17.8
1250	1523	-117.4	-14.4

1) Calculated from JANAF Thermochemical Tables (1985)

2.4 Why preoxidation is necessary

As previously pointed out in section 1.2, the reduction rate of magnetite is too slow to be used directly in the Elkem Polar Process. The slow reduction rate of magnetite compared to hematite was confirmed in experiments performed in the previously mentioned

laboratory scale reactor by Baumann (1985), Storemyr (1986 b), and Steinmo (1986). These authors used reduction gas mixtures of H_2 , CO , and CO_2 , and grain sizes in the range 50-100 μm .

Figure 2.12 shows some results from reduction of magnetite and hematite, obtained by Steinmo (1986). The initial degree of oxidation¹ of the magnetite was 88.7%, while it was close to 100% for the hematite. After reduction for 60 seconds, the magnetite is insignificantly reduced, while the hematite is considerably reduced. The inlet content of H_2 was 15%.

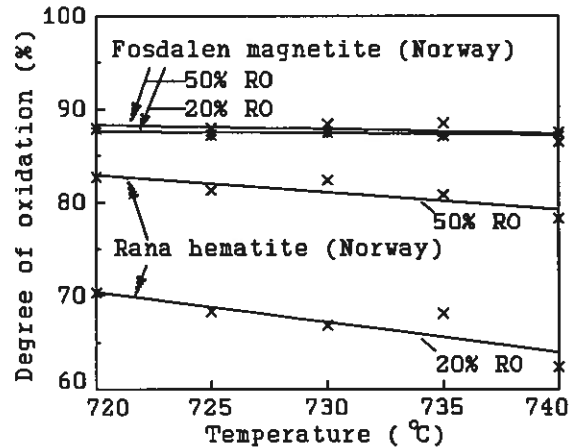


Fig 2.12 Magnetite and hematite reduced for 60s.

The degree of oxidation was only slightly lowered during reduction of different magnetite ores (Storemyr, 1986 b). The results after 60 seconds reduction at 800°C and 35% RO (35% H_2 , inlet gas) were:

Fosdalen magnetite from Norway:	88.7% → 87.2%	degree of oxidation
Sydvaranger magnetite	88.7% → 88.0%	"
Kiruna magnetite from Sweden:	88.9% → 86.9%	"

The oxygen ions form a closed-packed hexagonal structure in hematite and a face-centred cubic structure in both magnetite and wüstite. The slow reduction of magnetite compared to hematite, may be explained by the fact that no structural change in the oxygen lattice takes place during reduction of magnetite to wüstite, while the oxygen atoms have to undergo a severe readjustment during reduction of hematite. The readjustment results in volume increase, which tends to open up the structure, facilitating the subsequent reduction.

Edstrøm (1953) found that there was 4-5% shrinkage due to nucleation and growth of iron crystals when natural magnetite crystals were reduced to iron by CO at 1000°C. He found a volume increase of 25% for the reduction of hematite to magnetite and a volume increase of 7-13% for the next reduction step to wüstite. The overall volume increase was 25-27%, due to metal sintering.

1) Degree of oxidation (OX%), a measure for the oxygen content compared to pure hematite: $OX = 100 \cdot (1.5 \cdot Fe^{3+} + Fe^{2+}) / 1.5 \cdot Fe^{tot}$

3 MAGNETITE OXIDATION

3.1 Introduction

As previously pointed out, reduction of magnetite is too slow to be used directly in the Elkem Polar Process. However, the reduction rate is considerably increased by oxidation of magnetite to hematite prior to the reduction.

The Elkem Polar Process concept allows oxidation in the heating unit. The concept is based on pneumatic transport of iron ore concentrates. A realistic estimate for the maximum retention time would be about 40 seconds. If oxidation is fairly complete within 40-60 seconds at moderate temperatures, magnetite concentrates may be used directly in this process without any process modifications. In this way the costs of both the usual agglomeration step and an ordinary oxidizing unit will be avoided. However, if oxidation is far from completion a separate oxidizing unit will be necessary. The rate of oxidation is for this reason very important.

The rate of oxidation is investigated in the temperature range 400-850°C (see section 3.3). The previously mentioned laboratory scale reactor developed by SINTEF and Elkem was chosen for simulation of oxidation during pneumatic transport of concentrates. The laboratory scale reactor has a maximum operating temperature of 850°C limited by its steel quality. Because of material loss during the experiments, a practical limit of 60 seconds is set for the length of each experiment. The main purpose of these experiments, is to study the rate of oxidation at different temperatures, and not to complete the oxidation. The rate of oxidation at elevated temperatures (>1000°C) is also of interest, but experiments at these temperatures have not been carried out in the laboratory scale reactor. A high oxidation temperature would also require some modifications of the original concept of the Elkem Polar Process.

Another method, described in section 3.4, was chosen for preoxidation of material for subsequent reduction experiments. It is important that the oxidation is completed to eliminate the retarding effect of magnetite inclusions on the reduction rate. Material for reduction tests was oxidized at constant temperature in the temperature range 800-1250°C. A qualitative description and photographs of grain sections of the preoxidized samples are given in section 3.4. The subgrain structure of these preoxidized samples are characterized by videoplan in section 3.5. A quantitative measure for the subgrain structures is developed.

3.2 Previous work

Most of the previous work on oxidation of magnetite has been carried out on pellets because of their industrial importance. Ball et al. (1973) concluded from a literature review that the oxidation mechanism of magnetite cannot be considered to be completely explained. A two step mechanism was considered to be most probable, the first of which was rapid whilst the second was slow.

With "artificially" made magnetites (usually made by precipitating magnetite from a solution), the first step did proceed at temperatures below 400°C with the formation of $\gamma\text{-Fe}_2\text{O}_3$ (maghemite). In the second step $\gamma\text{-Fe}_2\text{O}_3$ was transformed to $\alpha\text{-Fe}_2\text{O}_3$ (hematite). With natural magnetites, the mechanism of the first step is a source of controversy, but the second step definitely resulted in the formation of $\alpha\text{-Fe}_2\text{O}_3$. Differences in the behaviour of various magnetites during the first step of oxidation were attributed to differences in specific surface areas and to different diffusion rates of ferric ions (Fe^{3+}). Diffusion of ferric ions can be affected by dislocations, vacancies, and the presence of trace elements.

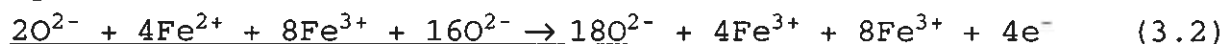
The main processes during oxidation of unfluxed pellets made from magnetite concentrates can be described as oxidation of each

magnetite grain and subsequent recrystallization (reorientation and grain growth). Oxidation in the present work is carried out using magnetite concentrates. The main processes during oxidation of pellets and concentrates will be very much the same. Hence, this review of previous work includes oxidation of pelletized materials. Relevant topics are oxidation mechanism, products, grain refinement and recrystallization, and oxidation kinetics. These topics are intimately mixed, but are tentatively separated here.

3.2.1 Mechanism

Bentell and Mathisson (1978) found that oxidation at 800°C took place by solid-gas reaction throughout the whole volume of a comparatively porous pellet made from magnetite concentrate. After some time the reaction speed decreased significantly as the magnetite grains were covered by a thin layer of hematite. The temperature was too low to permit a fast diffusion of ferrous ions through the hematite shell. The growth continued slowly in the most favourable planes. Bentell and Mathisson describe the growth of the characteristic hematite laminae as follows:

At low temperatures oxidation of the magnetite depends only upon the diffusion of Fe^{2+} and the Fe^{3+} ions in the magnetite because of the limited mobility of the oxygen ions and the high degree of stoichiometry in the hematite structure. A continuous film of hematite around the magnetite grains would prevent further oxidation. A schematic description of the oxidation process is shown in figure 3.1 and stoichiometrically described in equations 3.1 and 3.2.



Reaction 3.1 results in production of oxygen ions and in the consumption of electrons. The oxygen ions do not diffuse into

the magnetite, but remain at the surface of the grain. (Diffusion of oxygen ions is only possible to a small extent along the hematite-magnetite boundary.) The electrons originate from the Fe^{2+} ions which have diffused from the central part of the magnetite grain to the surface.

Most of the resulting Fe^{3+} ions return to the most

favourable surface sites of the hematite crystal and are intercalated with local oxygen ions from the magnetite. In the beginning the growth is parallel to the close packed planes in the magnetite, and the (111) planes are transformed to (1000) planes in the hematite. The distance between the close packed planes is greater in hematite than in magnetite, which implies that there is no space available for new (111) planes and so the perpendicular growth is halted. Later the supersaturation of oxygen ions and Fe^{3+} ions between the laminae increases to an extent, which makes the driving force sufficient to allow lateral growth. At increased temperatures, diffusion of Fe^{2+} through any hematite layer is also possible.

An important detail concerning the transformation of the lattice at the hematite magnetite boundary is the occurrence of stresses, owing to the fact that the distances between the oxygen ions in the close packed planes are shorter in the hematite than in the magnetite. The distances between the ions are 5.04 and 5.94 Å, respectively. However, the distance between these planes is greater in the hematite than in the magnetite, 6.87 compared to 4.85 Å. The lattice disturbance probably causes the transportation not only of iron ions but also of oxygen ions along the interface where the defects in the lattice are greatest. Stresses may cause microcracks.

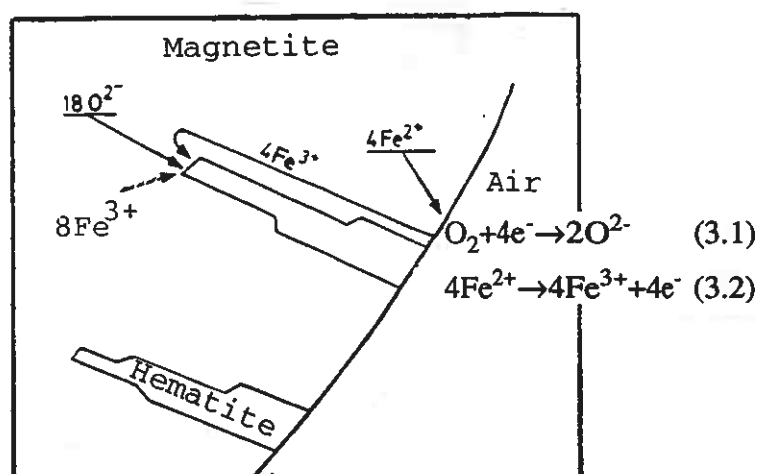
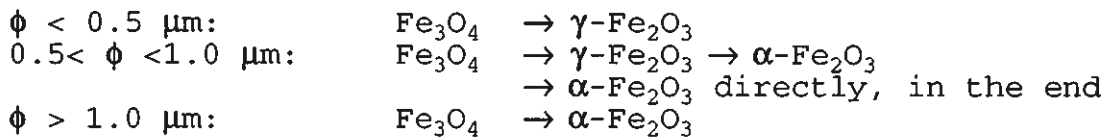


Fig. 3.1 Surface oxidation, Bentell and Mathisson (1978)

3.2.2 Oxidation products

Gilliot, Rousset, and Dupre (1978) investigated the influence of crystallite size on the oxidation kinetics of artificial magnetite in the temperature range 80-600°C. The artificial magnetite was made by precipitating magnetite from a solution. The investigation was carried out for crystallite sizes with diameters (ϕ) between 0.01-1.5 μm . The oxidation product was dependant on crystallite size and the influence of size could be accounted for in terms of structure and stresses at the crystal lattice level. Their findings are summarized below.



For intermediate sizes ($0.5 < \phi < 1.0 \mu\text{m}$), $\gamma\text{-Fe}_2\text{O}_3$ forms at the beginning of the reaction, followed by $\alpha\text{-Fe}_2\text{O}_3$ forming from $\gamma\text{-Fe}_2\text{O}_3$. $\alpha\text{-Fe}_2\text{O}_3$ forms directly from the unoxidized core towards the end of the reaction.

Some authors are of the opinion that $\gamma\text{-Fe}_2\text{O}_3$ is formed from artificial magnetite and $\alpha\text{-Fe}_2\text{O}_3$ is formed from natural magnetite. Artificial magnetite usually have a large specific surface and small grain sizes, which lead to the formation of $\gamma\text{-Fe}_2\text{O}_3$, according to Gilliot et al. (1978). Natural magnetites usually have larger grain sizes. According to the same authors, the comparatively larger grain sizes promote the formation of $\alpha\text{-Fe}_2\text{O}_3$. Other authors claim that stabilizing impurities initially present in Fe_3O_4 , or traces of H_2O , promote formation of $\gamma\text{-Fe}_2\text{O}_3$. However, in most of these works there appear to be a lack of control with grain sizes.

Because of the disagreements in the literature, concerning the oxidation products at low temperatures, some examples from earlier works will be given.

Twenhofel (1927) found that $\gamma\text{-Fe}_2\text{O}_3$ (called oxidized magnetite), formed by oxidation of artificial magnetite, always converted to

α -Fe₂O₃ above 500°C. This conversion from γ - to α -Fe₂O₃ occurred at 800°C for natural magnetite. Prolonged oxidation did always result in transformation from γ - to α -Fe₂O₃.

DeBoer and Selwood (1954) made γ -Fe₂O₃ from artificial magnetite by oxidation at 230-300°C in air. They found the transformation of γ - to α -Fe₂O₃ to take place at 350-500°C and measured the activation energy of the transformation. The activation energy decreased with increasing severity of the heat treatment. They concluded that water stabilizes the γ -Fe₂O₃. They also concluded that alumina stabilizes the γ -Fe₂O₃ structure, lanthana decreases its stability, while gallia has no effect.

The results of David and Welch (1956) supported the view that water is essential for the stability of maghemite. They found that maghemite contained water which could not be removed without destroying the spinel structure. They suggested that the structure is stabilized by OH⁻ replacing some of the O²⁻ in the spinel lattice. These conclusions or suggestions are based on their experiments with artificial magnetites, one precipitated from solution and dried in steam and another produced by reacting hematite with iron at 960°C in argon atmosphere for 6 hours. The latter gave only α -Fe₂O₃ on oxidation (185-370°C). The oxidation was very slow and not completed after 30 hours. Precipitated magnetite, which prior to oxidation was dried at temperatures between 250 and 850°C in argon, gave γ -Fe₂O₃ on oxidation in the temperature range 180-500°C. At higher drying temperatures α -Fe₂O₃ was formed, but traces of α -Fe₂O₃ were also detected at the lower oxidation temperatures. The temperature of the first appearance of α -Fe₂O₃ was dependent on the temperature of pretreatment. Wet magnetite precipitate, which was oxidized without drying, gave diffuse x-ray patterns. Hence, magnetite and a possible γ -Fe₂O₃ phase could not be distinguished.

These previous findings may be regarded as a confirmation of the importance of grain size on the product of oxidation. If water is removed from artificial magnetite by heating, grain growth occurs, and the oxidation product may change from γ - to α -Fe₂O₃.

3.2.3 Grain refinement and recrystallization

Cooke and Stowasser (1952) studied isothermal oxidation of magnetite pellets ($\phi = 0.75$ inch) made of Mesabi magnetite concentrate in the temperature range 300-1400°C. During oxidation hematite was formed from magnetite by a process of **grain refinement**. No physical disintegration was observed. Because certain crystallographic directions within any one magnetite crystal are preferentially oxidized, a single crystal of magnetite eventually became a number of independently oriented crystals of hematite. At temperatures around 500-600°C the resulting structure was relatively stable, and prolonged heating at these temperatures did not change the orientation or size of the hematite crystals. At higher temperatures, however, the hematite crystals did grow, and what was originally a single crystal of magnetite became a single crystal of hematite.

Just as crystal growth (reorientation) occurs within a hematite grain, also does grain growth occur throughout the mass of a pellet. Cooke and Stowasser found that the small grains were absorbed by the larger, until a network of equally axed hematite grains were established throughout the pellet.

There is a striking increase in grain size at elevated temperatures, especially above 1300°C, referring to figure 3.2 by Cooke and Stowasser. The two authors used analytical grade hematite with an original particle size of $\phi=0.8\mu\text{m}$. Heat treatment for 30 minutes at 1100, 1200, 1300, and 1400°C resulted in an average grain size of 6, 7, 20, and 400 μm , respectively, referring to figure 3.2

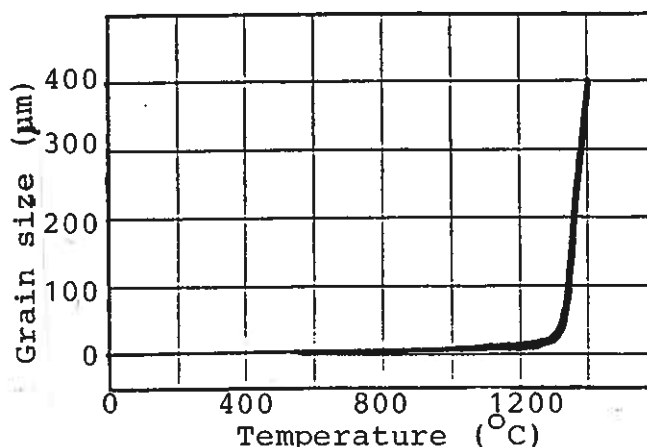


Fig. 3.2 Grain growth of hematite (Cooke and Stowasser, 1952)

The early observations by Cooke and Stowasser (1952), concerning crystal growth and grain growth of hematite, are supported by other authors. Ulvensøen et al. (1991) found that each hematite grain was made up of several crystals after isothermal oxidation of magnetite concentrate in a bed (height of bed was 3 mm), instead of using pellets. A small increase in the crystal size within each grain was observed for an increasing oxidation temperature in the range 800-1050°C.

Callender (1962) oxidized fine grained artificial magnetite. He observed that the hematite grains formed during oxidation of pellets at 850°C, were larger than the original magnetite grains. Large hematite grains were found to consist of several small crystals and recrystallization had commenced. Between 850°C and 1180°C the grains continued to grow. Between 1180°C and 1250°C a distinct change in structure occurred, the fine interstitial hematite was replaced by a compact mass of equiaxial crystals.

The importance of temperature on the hematite grain size was emphasized by Bentell and Mathisson (1978). They observed that the surface of indurated pellets was characterized by small hematite grains with different orientations of crystal axis, while in the centre of the same pellet the hematite grains were bigger. Because oxidation is an exothermal reaction, the temperature is increased in the pellet cores in so-called "isothermal" experiments. Hence, the central part of the pellets is oxidized at a significantly higher temperature than the surface.

Olsen and Malvik (1989) believe that large grain hematite is formed from recrystallized magnetite because recrystallization of magnetite occurs during heating in nitrogen atmosphere. They found that fine grained, randomly oriented hematite crystals were formed during isothermal oxidation of pellets at temperatures below approximately 1000°C. At higher temperatures groups of large grained equiaxial hematite were formed.

Cooke and Stowasser (1952) actually measured the core and surface temperature of the pellets, the core temperature being the

higher. The temperature difference was 54°C, if the pellets were brought up to the reaction temperature (1120°C) in a nitrogen atmosphere and then oxidized in O₂. The temperature difference was 104°C, if heating and oxidation (at 1020°C) both were carried out in O₂. The authors presumed that the lower temperature difference when heating in nitrogen was caused by slow magnetite oxidation due to recrystallization of magnetite, and also by the lowered permeability effected by slag formation. The temperature difference was only 10°C, if heating and oxidation (at 1090°C) were carried out in air. Papanastassiou and Bitsianes (1973) reported the maximum temperature rise within any one pellet to be 35-40°C during oxidation in air.

The above presumptions by Cooke and Stowasser, concerning recrystallization of magnetite followed by slow oxidation, have been verified by several authors. Papanastassiou and Bitsianes (1973) found that the rate of oxidation in air at 1000°C was slower for pellets preheated in N₂ atmosphere at 1250°C, due to magnetite recrystallization. Fitton and Goldring (1966) observed grain growth of magnetite at temperatures above 1250°C. Magnetite in pellet cores recrystallized and the original shape of the Sydvaranger concentrate particles was lost. Oxidation was also slow because gas diffusion was halted by smelt formation.

Grain growth of magnetite particles was also observed by Cooke and Ban (1952) during isothermal heat treatment of pellets in an inert atmosphere (N₂ or He). They found that magnetite grains in pellets did tend to form bonds already at 900°C. At about 1000°C, grain growth commenced at the expense of the fine magnetite particles (spatially separated), probably due to a transfer of magnetite through a slag (gangue) phase.

To conclude, previous findings seem to confirm that hematite is formed from magnetite by a process of grain refinement. The independently oriented hematite crystals are relatively stable at 500-600°C, but grow at higher temperatures. There is a striking increase in hematite grain size above 1300°C. Magnetite may recrystallize prior to oxidation, which will retard the subsequent oxidation, and probably affect the hematite grain size.

3.2.4 Kinetics

Papanastassiou and Bitsianes (1973) investigated initial oxidation rates for pellets made of two different magnetite concentrates. Below 420°C, a surface type of chemical reaction with activation energy of about 37 kcal/mole was initially rate controlling. The experimental rate constants (k) were calculated according to the formula 3.4. The specific surface areas (S_g) of the actual concentrates, taconite and relatively pure Missouri magnetite, were 12140 and 5350 cm²/g, respectively.

$$\frac{dn_o}{dt} = \frac{4\pi R_o^3}{3} \delta_b \cdot S_g \cdot k \cdot c_b \quad \left(\frac{\text{gmole } O_2}{s} \right) \quad (3.4)$$

dn_o/dt = rate of fractional weight gain (compared to theoretical)
 R_o = pellet radius (cm)
 S_g = specific surface area (cm²/g)
 δ_b = pellet density (g/cm³)
 c_b = concentration of oxygen in gas phase (g mole/cm³)

$$\text{Taconite: } k = 3.49 \cdot 10^4 \exp\left(\frac{-34.3}{RT}\right) \quad \frac{\text{cm}}{s} \quad (3.5)$$

$$\text{Missouri: } k = 3.47 \cdot 10^6 \exp\left(\frac{-39.4}{RT}\right) \quad \frac{\text{cm}}{s} \quad (3.6)$$

Above 420°C, mass transfer through the gaseous boundary layer dominated the initial reaction rate and was the controlling step with an activation energy of 2.5 kcal/mole. The flow rate used, 1100 cm³/min (0.07 m³/h), was said to be well above the critical flow rate needed for the oxidation experiments. However, in my opinion this low flow rate could be the reason for the dominance of gas film resistance during initial oxidation above 420°C.

Later on, at 1000-1200°C, diffusion through a growing product layer dominated the overall reaction rate. At intermediate temperatures (600-900°C) there was a mixed control, both chemical and mass transfer control. Uniform pellet porosity was achieved by a special method and the porosity was 35% in all these experiments. In other experiments, the pellet porosity was varied in the range 22-42% and found to be important for the rate of oxidation.

The oxygen potential is one of the major factors influencing the rate of reaction, according to Zetterström (1950), Edström (1957), and Papanastassiou and Bitsianes (1973).

Ball, Buttler, and Ratter (1966) oxidized pellets ($\phi = 0.38-0.5$ inch) in air in the temperature range 200-840°C. They measured the weight gain (y%) during oxidation and found y to obey formula 3.7 where k_1 and k_2 are rate constants and t is time. This model is used in corrosion studies. The formula was derived by Evans (1960), on the assumption that the pores in the material are blocked by formation of fresh hematite. k_1 is in fact an asymptotic value of the weight increase (y), which can never be exceeded.

$$y = k_1 (1 - e^{-k_2 \cdot t}) \quad (3.7)$$

Their weight gain - time curves are very similar to those reported by Zetterström (1950). The rate of oxidation falls off rapidly and the % oxidation approaches a value which appears to be very temperature dependant. Figure 3.2 shows a theoretical curve for the oxidation, compared to the experimental results. The values of k_1 and k_2 were selected to give the best fit.

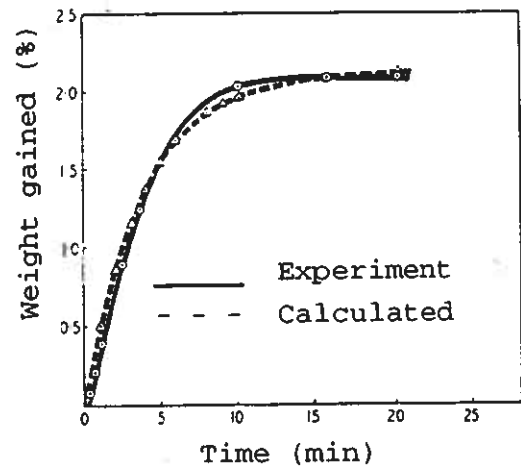


Fig. 3.3 Oxidation curve for magnetite (Ball et al., 1966)

Ball et al. could not find any relationship between k_2 and temperature but the value of k_1 did steadily increase with temperature. From Arrhenius plots, between $\log k_1$ and T^{-1} , the activation energy was calculated both for their own results and for the oxidation data of Zetterström. Some of the Arrhenius plots appeared to fall into two distinct parts with different slopes. As shown in table 3.1, all activation energies were low, especially low for artificial magnetite, which may indicate a physical rather than a chemical rate control.

Table 3.1 Activation energy (E), calculated by Ball et al. (1966), for oxidation of magnetite pellets.

Data of Ball, Buttler, and Ratter			Zetterström, 400-1000°C	
Magnetite type	Temperature (°C)	E (kcal/mole)	Magnetite type	E (kcal/mole)
Artificial	210-520	1.1	Artificial	0.4
Sydvaranger	280-840	5.6	Aurora ¹	7.3
Gellivare D	240-440	2.0	Scrub oaks	5.1
	440-560	6.2		
Jaspilite	200-320	10.6	Babbite ¹	5.1
	320-560	1.1	Shasta	5.8

1) Magnetic concentrate from taconite, an intimate association of magnetite and a siliceous gangue.

Mazanek et al. (1973) found the rate of oxidation in air to obey formula 3.7 in the temperature range 200-1000°C. Contrary to Ball et al., they obtained a temperature dependence for both rate constants, and used k_2 instead of k_1 in the calculations of activation energies from Arrhenius plots. For pellets made of artificial magnetite they obtained low activation energies (0.3-6,7 kcal/mole) in accordance with those reported by Ball et al.. Arrhenius plots for pellets made of natural magnetite concentrate (Fosdalen) did not show any linear relation between $\log k_2$ and T^{-1} . The authors concluded that the mechanism and kinetics of the oxidation are dependant on the type and origin of the magnetite. They presumed that the temperature of its formation and crystallization is decisive for the oxidation.

The rate of growth of hematite on magnetite have also been measured by Davies, Simnad, and Birchenall (1951), using a thermogravimetric method, and found to be diffusion controlled in oxygen atmosphere at temperatures between 800 and 1000°C. They did not use pellets, but flat specimens (0.75·0.5·0.1 inch) which were produced by oxidizing iron in water. The rate of oxidation gave a parabolic relationship between weight gain and time, suggesting diffusion control, since an interface reaction controlled process would manifest itself in an linear rate law. Approximate values for the parabolic rate constant were derived from the straight portions of the plot of weight gain (W) per area (A) (g/cm^2) versus $\text{time}^{1/2}$. The parabolic rate constant is

defined by formula 3.8.

$$\frac{W}{A} = k \cdot t^{\frac{1}{2}} \quad (3.8)$$

800°C:	k = 4.5 · 10 ⁻⁵	g/(cm ² ·min ^{1/2})
900°C:	k = 1.5 · 10 ⁻⁴	"
950°C:	k = 1.3 · 10 ⁻⁴	"
988°C:	k = 3.0 · 10 ⁻⁴	"

From these values of the parabolic rate constant, the activation energy was calculated to E = 101 kJ/mole (24 kcal/mole) in an Arrhenius plot.

Himmel, Mehl, and Birchenall (1953) measured the self diffusion coefficient (D) for iron in magnetite and in hematite. Natural hematite crystals from Minas Geraes in Brazil were cut in rectangular parallelepiped (0.75·0.5·0.24 inch). They found D to be near independent of crystallographic direction in hematite.

Self diffusion coefficient (D) for iron in hematite:

1000°C:	D=1.0·10 ⁻¹⁴ cm ² /s	1217°C:	D=2.0·10 ⁻¹² cm ² /s	parallel to c-axis
"	D=1.0·10 ⁻¹⁴ "	"	D=1.6·10 ⁻¹² "	perpendicular "

D for iron in magnetite: 800°C: D=10⁻¹¹ cm²/s

Because the rate of iron diffusion in magnetite is several orders of magnitude higher than in hematite, the mechanism of initial oxidation proposed by Bentell and Mathisson (1978) is plausible.

An Arrhenius plot gave an activation energy of about 100 kcal/mole for self-diffusion of iron in hematite. Since only two temperatures were included in the investigation, Himmel et al. have pointed out that the high value of 112 kcal/mole reported by Lindner (1952) tentatively must be accepted.

Himmel et al. calculated a parabolic scaling constant from D at 1000°C and compared it to the parabolic rate constant found by Davies et al. (1951), the latter being two orders of magnitude higher. They concluded that iron is not the only mobile

component in $\alpha\text{-Fe}_2\text{O}_3$. The lack of agreement between calculated and experimentally determined rate constants was attributed to transport predominately by oxygen ions or oxide ion vacancies.

Edström (1957) studied the mechanism and kinetics of oxidation of magnetite pellets ($\phi=5\text{-}32$ mm) with 32% porosity at 1230°C and found oxidation to be topochemical and the rate of oxidation to obey the parabolic rate law for spheres (equation 3.10). The parabolic rate law is derived from Fick's 1. law and lead to the formulas 3.9 and 3.10 for parallelepiped and spheres, respectively.

$$\begin{array}{l} x = \text{depth oxidized} \\ R = \text{pellet radius} \\ t = \text{time} \\ k = \text{rate constant} \end{array} \quad x^2 = k \cdot t \quad (3.9)$$

$$\frac{x^2}{2} - \frac{x^3}{3R} = k \cdot t \quad (3.10)$$

The time required to obtain a given oxidation percentage was proportional to the square of the pellet diameter and the rate of oxidation was more than 10 times faster in oxygen than in air.

$$\begin{array}{l} k = 0.72 \text{ mm}^2/\text{min} = 1.2 \cdot 10^{-4} \text{ cm}^2/\text{s} \text{ in air,} \\ k = 8.6 \text{ mm}^2/\text{min} = 1.4 \cdot 10^{-3} \text{ cm}^2/\text{s} \text{ in oxygen} \end{array} \quad R = 10.5\text{-}15 \text{ mm}$$

Edström concluded that pore diffusion, and not solid state diffusion, was responsible for the inward transport of oxidizing agent, because the rate constant was hundreds of times higher than for oxidation by solid diffusion of iron through hematite.

To conclude, the rate controlling mechanism at temperatures above 1000°C is pore diffusion, according to Edström (1957) and Papanastassiou and Bitsianes (1973). Most authors (Davies et al., 1951, Ball et al., 1966, Mazanek et al., 1973) find that diffusion is rate controlling also at lower temperatures, and not the chemical reaction. Papanastassiou and Bitsianes (1973), however, suggest chemical control during initial oxidation below 420°C and mixed control at intermediate temperatures ($600\text{-}900^\circ\text{C}$).

3.3 Rate of oxidation

3.3.1 Experimental

The rate of oxidation was studied under isothermal conditions in the temperature range 400-850°C. The experiments were carried out in air for periods of up to 60 seconds. An ordinary quality of Sydvaranger magnetite concentrate was used in most of the experiments. A few experiments at 600 and 850°C were also carried out using other magnetite concentrates. The fractions 74-100 μm of the concentrates were oxidized, if not otherwise indicated. Chemical analyses of the actual magnetite fractions are given in table 3.2.

Table 3.2 Chemical analyses¹ of magnetites.

	Weight %		
	Sydvaranger	Kiruna ²	Minnesota
Fe ^{tot}	65.2	71.1	57.4
Fe ²⁺	22.3	23.7	21.0
Fe ₃ O ₄	90.1	98.3	79.3
SiO ₂	8.6	0.8	16.1
TiO ₂	<0.01	0.23	-
Al ₂ O ₃	<0.1	<0.1	0.11
MnO	0.09	0.07	0.26
CaO	0.3	0.3	0.80
MgO	0.3	0.1	1.30
P	0.019	0.052	0.024
S	0.13	-	-
CO ₂	0.11	-	-
Sum	<99.8	<100.0	97.9

1) Analyzed at Norsk Jernverk A/S.

2) Exception: Fraction analyzed was 53-100 μm .

The previously mentioned laboratory scale reactor, developed by SINTEF and Elkem, was used for oxidation of the concentrates. This equipment provides an excellent means of bringing small particles in thorough contact with gas. Because of the high speed of air (3.5 m³/h) and the small samples, each particle will always experience fresh air, which at the same time removes the excess heat evolved during oxidation. Hence, the particles are isothermally oxidized. The rate of diffusion through the gas film around each particle is regarded to be of no significance.

The reactor was most frequently used in reduction experiments. It is thoroughly described in the chapter 5, section 5.3.2, and shown in the figures 5.26 and 5.27. The Ni-catalyst, shown in figure 5.26, was removed from the apparatus before the oxidation experiments were carried out. The main principles, however, will be repeated here.

Magnetite concentrate samples (0.5 g) were blown with argon into the reactor, shown in figure 3.4. The reactor is placed inside a furnace together with heating coils for the gas. During oxidation, centrifugal forces keep the particles rotating inside the reactor, while the oxidizing gas leave the reactor. There will always be a loss of material because some particles will follow the off gas. A process computer provided automatic valve operations and the necessary time control. After oxidation, the samples were purged out

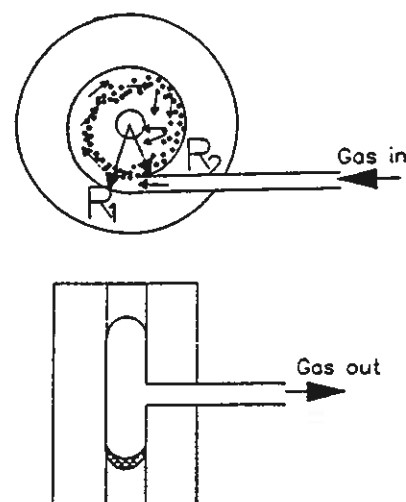


Fig. 3.4 Reactor
R₁₋₂=25-22mm

of the reactor using nitrogen and collected in a filter outside the furnace where they were cooled in purging argon gas for 20 seconds. Several (5-19) single samples were collected in the filter to get enough material for one sample. The total sample was split in two parts for different purposes.

Wet chemical analyses were carried out by Norsk Jernverk A/S using one part of each sample (1 g). The total amount of Fe (Fe^{tot}) and Fe²⁺ were determined in separate analyses. The methods are described in section 5.3.3. Fe³⁺ was calculated: Fe³⁺ = Fe^{tot} - Fe²⁺.

Polished surface specimens were made by moulding samples in epoxy. After hardening, the specimens were alternating polished and cleaned. The last polish was on a 1 μm NAP-cloth.

A Reichert MeF3 optical microscope from Leica in Austria with equipment for photographing was used to study polished surfaces.

3.3.2 Calculation of conversion

Previous works on oxidation kinetics are mainly based on the continuous gravimetric method, referring to section 3.2.4. The conversion is reported as a fractional weight increase. The fractional weight increase (y) is the ratio of the measured weight increase (ΔW_i) and the weight increase for complete oxidation (ΔW_{\max}).

The present work is based on a completely different principle. Samples are oxidized in batches and the results are based on chemical analyses of both Fe^{tot} and Fe^{2+} of each batch after oxidation at desired temperatures. The remaining content of magnetite (mt) may be calculated according to formula 3.11 for each sample. In the formulas 3.11 - 3.14, M is the molecular weight. The subscripts denote the actual materials.

$$mt(\%) = \frac{Fe^{2+}(\%) \cdot M_{mt}}{M_{Fe}} \quad (3.11)$$

The weight% of hematite (hm) in each sample is calculated according to formula 3.12. The weight% of Fe^{3+} in hematite is the difference between the total weight% of iron and the weight% of iron in magnetite. Weight% of iron in magnetite is $3 \cdot Fe^{2+}(\%)$, since the formula for magnetite can be written as $Fe^{2+}O \cdot Fe^{3+}_2O_3$.

$$hm(\%) = \frac{Fe^{\text{tot}}(\%) - 3 \cdot Fe^{2+}(\%)}{M_{Fe}} \cdot \frac{M_{hm}}{2} \quad (3.12)$$

For an easy comparison of this method with the usual gravimetric method, the conversion calculated from chemical analyses can be presented in the usual way, as a fractional weight increase (y).

$$\Delta W_i(\%) = \frac{Fe^{\text{tot}}(\%) - 3 \cdot Fe^{2+}(\%)}{M_{Fe}} \cdot \left(\frac{M_{hm}}{2} - \frac{M_{mt}}{3} \right) \quad (3.13)$$

$$\Delta W_{\max}(\%) = \frac{Fe^{\text{tot}}(\%)}{M_{Fe}} \cdot \left(\frac{M_{hm}}{2} - \frac{M_{mt}}{3} \right) \quad (3.14)$$

$$y\% = \frac{\Delta W_i(\%)}{\Delta W_{\max}(\%)} \cdot 100\% = \frac{(Fe^{\text{tot}}(\%) - 3 \cdot Fe^{2+}(\%))}{Fe^{\text{tot}}(\%)} \cdot 100\% \quad (3.15)$$

3.3.3 Results and discussion

Results

Chemical analyses and calculated conversions (y%) are given in table 3.3. The ordinary quality of Sydvaranger magnetite was used in most of the experiments. Through a fairly simple process this concentrate reaches a high purity, >99% magnetite, so-called Sydvaranger super magnetite, which was used in a few experiments.

Table 3.3 Conversion to hematite during isothermal oxidation in air. Fraction 53-150 μm of Sydvaranger super was used, and fractions 74-100 μm of the other magnetites.

Sample	Temp. (°C)	Time (s)	Analyses		Calculations ¹		
			Fe ^{tot} (%)	Fe ²⁺ (%)	Magnetite (Mt) ² (%)	Hematite (Hm) ³ (%)	y ⁴ (%)
Sydvaranger	400	15	65.3	21.5	89.1	1.1	1.2
		30	65.3	20.8	86.0	4.3	4.6
		60	65.0	20.6	85.5	4.5	4.8
	600	15	65.8	20.0	82.9	8.2	8.8
		30	65.3	20.1	83.5	7.0	7.5
		60	65.0	20.0	82.9	7.2	7.7
		60	67.2	20.3	84.0	9.2	9.6
	700	15	65.0	19.8	81.9	8.2	8.9
		30	66.0	19.5	80.8	10.7	11.4
		60	68.3	18.5	76.7	18.2	18.7
		60	68.0	19.4	80.3	14.1	14.5
	800	15	67.5	17.6	73.1	20.9	21.6
		30	68.0	16.6	68.9	25.9	26.6
		60	68.5	15.5	64.3	31.5	32.1
	850	15	67.5	15.9	65.8	28.4	29.4
		30	67.0	15.0	62.2	31.5	32.8
60		68.5	13.4	55.5	40.5	41.4	
60		68.5	13.1	54.4	41.6	42.5	
Kiruna	600	60	71.0	21.8	90.2	8.2	8.1
		60	71.0	21.6	89.7	8.7	8.6
	850	60	70.8	16.0	66.3	32.5	32.2
Minnesota	600	60	60.8	18.3	75.7	8.6	9.9
	850	60	61.8	14.5	60.1	26.1	29.6
Sydv. super	600	60	72.5	22.5	93.3	7.2	6.9
	850	60	72.0	14.3	59.1	41.8	40.6

1) Calculations were carried out with 2 decimals in the analyses

2) $Mt(\%) = M_{mt} \cdot Fe^{2+}(\%) / M_{Fe} = 231.54 \cdot Fe^{2+}(\%) / 55.85$

3) $Hm(\%) = M_{hm} \cdot (Fe^{tot}(\%) - 3 \cdot Fe^{2+}(\%)) / (2 \cdot M_{Fe}) = 159.69 \cdot (Fe^{tot} - 3 \cdot Fe^{2+}) / (2 \cdot 55.85)$

4) $y(\%) = \text{Conversion}(\%) = 100\% \cdot (Fe^{tot}(\%) - 3 \cdot Fe^{2+}(\%)) / Fe^{tot}(\%)$

The progress of oxidation may more easily be studied in figure 3.5 for the ordinary quality of Sydvaranger magnetite. The rate of oxidation is rather high during the first 15 seconds, especially at the higher temperatures, 800 and 850°C. During this period the surface of the particles are covered with hematite. The conversion is nearly 30% after 15 seconds at 850°C. The rate of oxidation levels off, and the conversion has only reached 42% after 60 seconds at 850°C.

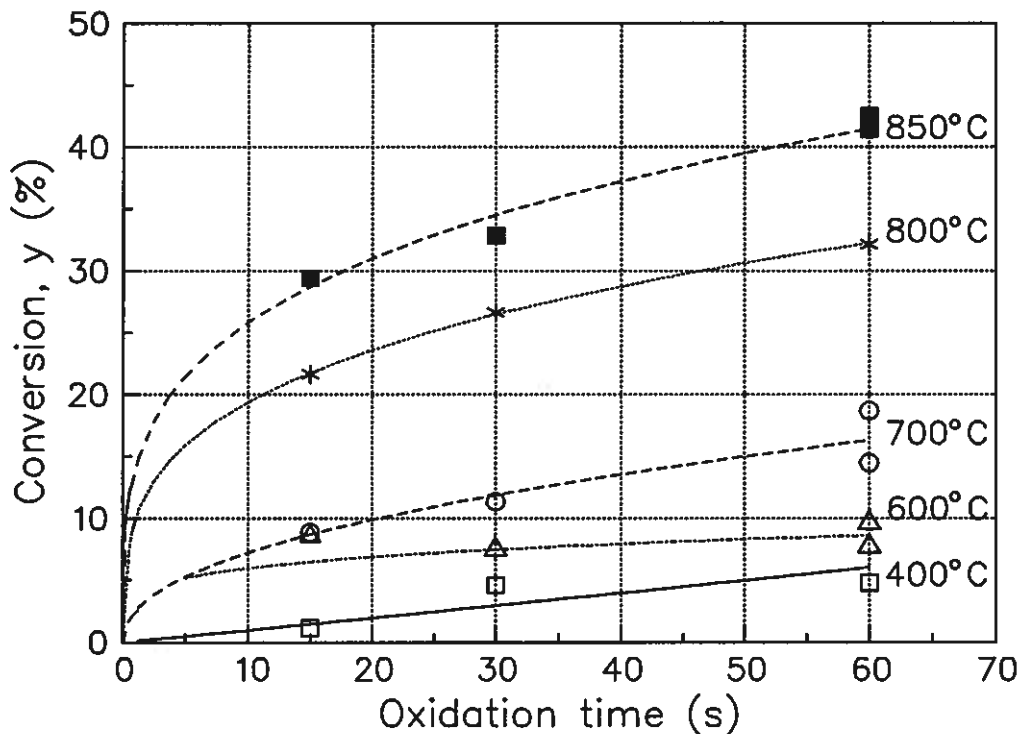


Fig. 3.5 Isothermal oxidation in air of the fraction 74-100 μm of Sydvaranger magnetite (ordinary quality).

The curves in figure 3.5 were not drawn by hand, but by a program called Freelance. A power function ($y\% = k_1 \cdot t^{k_2}$) was chosen, where k_1 and k_2 are constants and t is the oxidation time in seconds. The program calculated k_1 and k_2 in such a way that the curves gave the closest fit to the experimental values. The formulas and the correlation factors (R^2) for the curves are given below.

$$400^\circ\text{C}: \quad y\% = 0.089 \cdot t^{1.03} \quad R^2=0.771 \quad (3.16)$$

$$600^\circ\text{C}^1: \quad y\% = 3.69 \cdot t^{0.206} \quad R^2=0.357 \quad (3.17)$$

$$700^\circ\text{C}: \quad y\% = 2.52 \cdot t^{0.456} \quad R^2=0.888 \quad (3.18)$$

$$800^\circ\text{C}: \quad y\% = 10.05 \cdot t^{0.285} \quad R^2=0.999 \quad (3.19)$$

$$850^\circ\text{C}: \quad y\% = 14.02 \cdot t^{0.265} \quad R^2=0.962 \quad (3.20)$$

1) The point (15s, 8.8%) at 600°C is excluded

The curves correlate well with the experimental values at the highest temperatures, but not at the lowest temperatures.

Figure 3.6 shows a grain cross section of the ordinary Sydvaranger quality after 60 seconds oxidation at 850°C in air. Hematite is white and magnetite is grey. The oxidized layer appears to be rather compact. Oxidation proceeds mainly topochemically, but with needles of hematite ahead of the topochemical front.

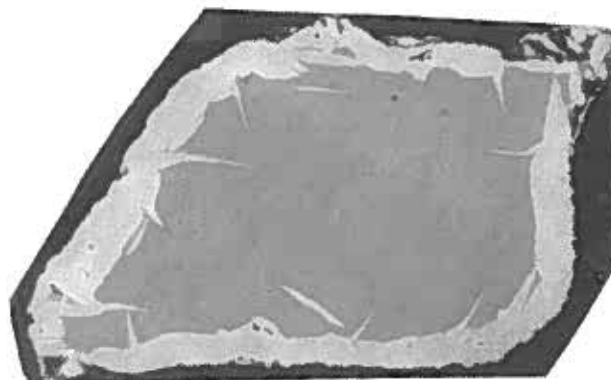


Fig. 3.6 Oxidized Sydvaranger grain, 850°C for 60s.

According to Bentell and Mathisson (1978) these needles are parallel to the close packed planes in magnetite, and the (111) planes in magnetite are transferred to (1000) planes in hematite.

Initially, the chemical reaction is thought to be rate controlling. During the first 15 seconds, the rate controlling mechanism appears to change and diffusion through a growing hematite layer is believed take over. Diffusion would be expected to be rate controlling, especially at the higher temperatures, where chemical reactions usually are rapid. At the lowest temperature, 400°C, the rate of oxidation could be chemically controlled. The best fit to the experimental values was a linear approach, referring to equation 3.16 and figure 3.5, although correlation was not good ($R^2=0.771$).

The rate of oxidation is not increased by using other natural magnetite qualities, referring to figure 3.7. After 60 seconds oxidation at 850°C, the Sydvaranger magnetite obtains the highest conversion (only 41-42%). The conversions of the ordinary Sydvaranger quality and the Sydvaranger super quality are approximately equal. The conversions of the different magnetite qualities after 60 seconds at 600°C can be considered to be equal, within the limits of experimental uncertainties.

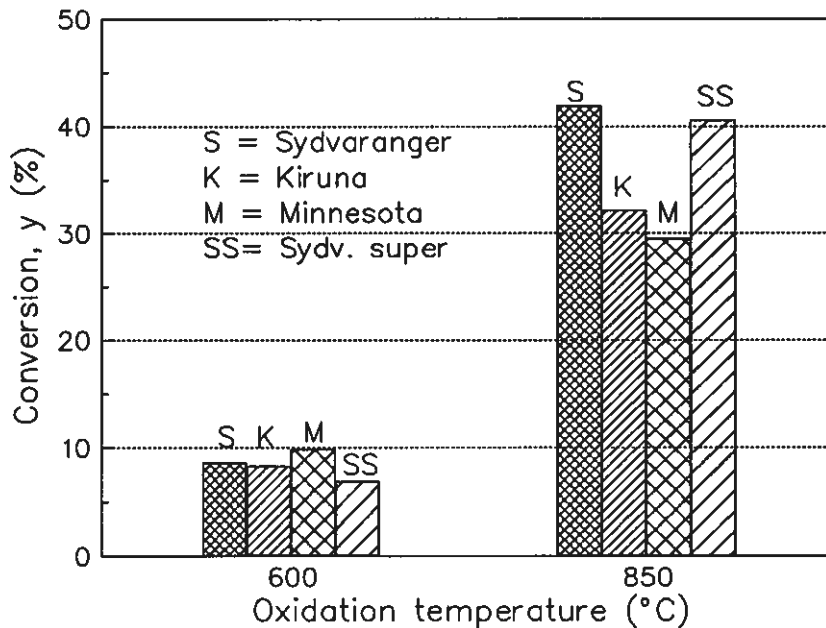


Fig. 3.7 Conversion after isothermal oxidation of different magnetites in air. Fraction 53-150 μm was used for Sydvaranger super, and 74-100 μm for the others. Oxidation time: 60 seconds.

The conversions of Minnesota and Kiruna magnetite, however, are about 10% lower than for Sydvaranger magnetite at 850°C. The reasons for this may be several. Some factors affecting the rate of oxidation, which may differ for the different qualities, are mentioned: grain size distribution, grain shape, porosity, vacancy concentration, and foreign ions in the magnetite lattice.

Oxidation product

The oxidation product is probably $\alpha\text{-Fe}_2\text{O}_3$ at all temperatures. $\alpha\text{-Fe}_2\text{O}_3$ was verified in polarized light in optical microscope by identifying the reflections of the anisotropic $\alpha\text{-Fe}_2\text{O}_3$. Contrary, the cubic structure of $\gamma\text{-Fe}_2\text{O}_3$ is isotropic in all directions. From the previous work by Gilliot et al. (1978), it would be expected that $\alpha\text{-Fe}_2\text{O}_3$ is formed, even at low temperatures, due to the large grain sizes (53-150 μm).

Discussion of method

The method in the present work has both advantages and drawbacks. The exact content of hematite and magnetite of each sample may be determined for each batch. The small particles are brought

into close contact with oxidizing gas. The rate of diffusion through the gas film around each particle may be regarded to be of no significance. Each particle will always experience fresh reaction gas because of the high gas flow rate compared to the small samples. At the same time the surplus gas removes the heat evolved during oxidation and provides isothermal oxidation.

However, the method is not continuous and many experiments are required to draw a precise curve showing the course of oxidation. Some material is lost during oxidation. This material loss may be selective. Particles may be lost because of their density (f. ex. low density of SiO_2), size, or shape. However, since both Fe^{tot} and Fe^{2+} of each sample are analyzed a loss of material due to low density is not thought to be significant for the calculated conversion. The density of hematite and magnetite are rather close, 5.24 and 5.18 $\text{g}\cdot\text{cm}^{-3}$, respectively. Hence, selective material loss due to different density is not expected.

There is a possibility for grinding of particles in contact with reactor walls. "Dust" from the particle surface in the form of hematite may be blown out with the gas. The conversion will in this case be higher than determined by the chemical analyses. The maximum fault will be limited to the material loss.

The particles get a thermal shock both on heating and cooling, which might cause cracks and size degradation. Thermal shocks on cooling will not have any effect on the calculated conversion. Size degradation due to thermal shocks on heating might cause material loss, especially of the smaller grain sizes. The remaining smaller particles may get an increased oxidation rate.

Material is mainly lost during the first 15 seconds. The mean material loss was about 32%, except at 400°C and in one experiment at 600°C (15 s). The mean material loss in these experiments was 67% and 75%, respectively, about twice as high as in the other experiments. The reason was a leakage which was later repaired.

The loss of material during oxidation was about 33% for the ordinary quality of Sydvaranger magnetite after 60 seconds at 850°C, while it was only 17% for Sydvaranger super magnetite. If hematite was the only material lost, maximum conversion would have been about 75% and 58%, respectively. Small leakages are thought to be the main reason for the different material losses. Leakages are thought to cause a uniform material loss, which should not have any significant effect on the calculated conversion. The main difference between the two concentrates is in their quartz contents, which are not thought to affect the rate of oxidation.

The content of Fe^{tot} (%) is supposed to decrease during oxidation, but by comparing table 3.3 and 3.2, an increase frequently can be observed for the ordinary quality of Sydvaranger magnetite. This may be explained by selective material loss of f. ex. SiO_2 during oxidation. Iron from the reactor walls is not thought to be the iron source. Prior to the oxidation experiments, the reactor was opened and metallized particles from previous reduction experiments were removed. The reactor walls were polished.

Discussion of accuracy of chemical analyses

Referring to table 3.3, four oxidation experiments were carried out twice. These parallel experiments (runs) were carried out for 60 seconds. The mean values of the calculated conversion and the deviations are presented below. The deviations increase from 1.3% of the conversion at 850°C to 13% at 700°C.

<u>Sydvaranger (ordinary):</u>	<u>deviation in % of y%:</u>
600°C: $y\% = (8.7 \pm 1.0)\%$	11%
700°C: $y\% = (16.6 \pm 2.1)\%$	13%
850°C: $y\% = (42.0 \pm 0.6)\%$	1.3%
<u>Kiruna:</u>	
600°C: $y\% = (8.4 \pm 0.3)\%$	3.6%

Standard deviations (STD) of the chemical analyses of Fe^{tot} and Fe^{2+} are reported in chapter 5. The following standard

deviations were found in prereduction experiments (different runs):

$$\begin{aligned} \text{Fe}^{\text{tot}} &= 69-76\% \pm 0.3 \\ \text{Fe}^{2+} &= 23\% \pm 0.7 \end{aligned}$$

Maximum deviation in the conversion may be calculated from the above standard deviations, being the difference between maximum and mean conversion. Maximum conversion is found using the lower value of Fe^{2+} (-STD) and the higher value of Fe^{tot} (+STD) in formula 3.15. Maximum deviation so calculated is dependant on the degree of conversion, referring to table 3.4. The table shows the maximum deviation, calculated for the ordinary quality of Sydvaranger magnetite after oxidation for 60 seconds. For the higher conversions at 800-850°C, maximum deviation is 8-10% of the conversion, which is acceptable.

Table 3.4 The conversion of Sydvaranger magnetite after 60 seconds oxidation, and calculated maximum deviation.

Oxidation temperature (°C)	Conversion ± max. deviation (Y%)	Max. deviation in % of conversion
400	4.8 ± 3.7	75 %
600	8.6 ± 3.6	42 %
700	16.6 ± 3.4	21 %
800	32.1 ± 3.4	10 %
850	41.5 ± 3.3	8 %

The deviations observed in the parallel oxidation experiments are low, compared with maximum deviations calculated from STD of the chemical analyses.

Maximum deviation for the conversion of Sydvaranger magnetite at 400°C, is large, about 75% of the conversion. At 600°C, the calculated conversion after 15 seconds is higher than after 30 seconds. It is also higher than the mean value of the conversion after 60 seconds. This point at 15 seconds is excluded in the further work for several reasons: it seems to be out of range, large maximum deviation (42% of the conversion), and a large loss of material (75%) during oxidation.

Comparisons with previous works

Interpretations of oxidation curves previously reported, give an indication whether oxidation rates in the present work are faster than those obtained for pellets. Comparison after only 1 minute conversion gives only a rough measure, because experiments with pellets have been carried out for at least half an hour. The conversion obtained for pellets after one minute of isothermal oxidation in air varies considerably. Several authors, Sæverud (1984) and others, have pointed out the rate retarding effect of bentonite additions to pellets.

Sæverud (1984) oxidized pellets made of Sydvaranger super concentrate without bentonite addition. The conversion obtained by Sæverud after one minute of isothermal oxidation in air is compared with results obtained in the present work, see below. At 400°C the conversion was appreciably higher for pellets, probably due to the smaller grain sizes. About 80% of the materials used for pelletizing are usually grains smaller than 45µm. The grain sizes used in the present work are much larger. At higher temperatures, Sæverud obtained about 30% conversion after one minute at both 750°C and 900°C, while the conversion was 12% higher (42%) at 850°C in the present work.

	Sæverud (1984)	Present work
400°C:	23%	4.8%
600°C	28%	8.7%
750°C	30%	-
800°C	-	32%
850°C	-	42%
900°C	30%	-

A lower conversion, was obtained by Zetterström (1950) for pellets made of different natural magnetite concentrates. The conversion after one minute in air at 800°C varied from 13 to 17% for these concentrates. Bentell and Mathisson (1978) obtained a conversion of 30% at 800°C for dolomite fluxed pellets, fairly close to 32% obtained in the present work.

These findings indicate that oxidation at 800-900°C proceeds somewhat slower in pellets. If the whole volume of the pellet participates in the reaction, the rate of oxidation would be expected to be much higher for pellets due to the smaller grain

sizes. The results indicate that pore diffusion in the macroscopic pellet pores contributes weakly to the overall resistance. Pore diffusion in the growing hematite layer in each grain appear to be the rate controlling mechanism.

Estimates for complete oxidation

Recrystallization of magnetite retards oxidation, referring to section 3.2.3. Recrystallization has to be taken into account when extrapolating to higher temperatures, or to prolonged residence times. If the time at temperature is short (f.ex. 20-40 seconds), recrystallization probably may be neglected.

Recrystallization of magnetite prior to oxidation is not expected to retard oxidation in the present experimental work, because:

- heating time is short
- the reaction temperature is too low
- the reaction time is too short.

The particles are heated during the transport to the reactor. The transport time is about 1/10 second.

Calculations of the time needed for complete oxidation ($y=100\%$) from the formulas 3.19 and 3.20 give 52 and 28 minutes at 800 and 850°C, respectively. As the experimental work is limited to the first minute of oxidation, these calculations are far outside the experimental range.

The following conversions were obtained after oxidation of pellets made of natural magnetite concentrates in air:

Papanastassiou et al. (1973)	:	100%	after	4 min.	at	1000°C
Sæverud (1984)	:	95%	after	6 min.	at	900°C
"	:	92%	after	6 min.	at	1100°C
Mazanek et al. (1973)	:	96%	after	8 min.	at	900°C
Zetterström (1950)	:	98%	after	11 min.	at	1000°C

Since 95-100% conversion is achieved for pellets within 4 minutes at 1000°C or within 6 minutes at 900°C, concentrates should reach the same conversion sooner, since oxidation appears to proceed somewhat slower in pellets. However, the results indicate that oxidation will not be completed (95-100%) in the heating unit of the Elkem Polar Process, using air. Recrystallization probably retards oxidation at 1100°C, referring to the results by Sæverud.

Enriched air

The rate of oxidation is increased if the oxidation is carried out in oxygen instead of in air, according to Edström (1957), Zetterström (1950) and Papanastassiou and Bitsianes (1973).

Papanastassiou and Bitsianes (1973) obtained high conversions in air at reasonable temperatures. Oxidation of Missouri magnetite pellets, having a uniform porosity of 42%, gave the following conversions after one minute at 1000°C:

60% using air
70% using 30% O₂
85% using 40% O₂
100% using 60% O₂.

Complete oxidation within 40 seconds was achieved at 1000°C for concentrations of O₂ at and beyond 80%.

Oxidation in enriched air in the Polar Process is an economic question, which will not be considered here. Since complete oxidation within 40 seconds can be obtained for pellets at 1000°C using 80%O₂, it should also be possible for concentrates during pneumatic transport.

3.3.4 Mathematical models

The present experimental work is limited both in temperature and in time of oxidation. Anyway, an effort is made to suit a physical and mathematical model to the experimental results obtained for the ordinary Sydvaranger quality. If the model describes well what actually takes place, the model may predict the lower temperature limit for complete oxidation in air within 40 seconds. The activation energy will indicate whether the rate of oxidation is controlled by chemical reaction or by diffusion in the pores.

The temperature dependence of the rate constants (k) can be expressed by formula 3.21.

$$k = k_0 \cdot e^{-\frac{E}{R \cdot T}} \quad (3.21)$$

The activation energy (E) is calculated from the slope of an Arrhenius plot between $\ln k$ and T^{-1} . The temperature independent constant k_0 is found from the cut of the y-axis at $\ln k_0$.

Pore blockage model

Ball et al. (1966) and Mazanek (1973) found the weight gain during oxidation to obey formula 3.22, referring to section 3.2.4. k_1 and k_2 are rate constants, and t is time. The value of k_1 is the asymptotic value of the conversion. The model is used in corrosion studies. The model is derived on the assumption that the diffusion in the product layer is halted because the pores are blocked by the fresh hematite produced. Ball et al. found the appearance of the conversion-time curves to be very similar to those reported by Zetterström (1950). The rate of oxidation decreased and the conversion approached a value which appeared to be very temperature dependant.

$$y\% = k_1 (1 - e^{-k_2 \cdot t}) \quad (3.22)$$

In the present work, good correlation between formula and experimental values were not obtained at the higher temperatures, see figure 3.8. The model describes well the experimental results at 400-700°C, within the experimental accuracy.

The k_2 -values may be derived from the slope of the straight line in a plot between $\ln(k_1 - y)$ and oxidation time

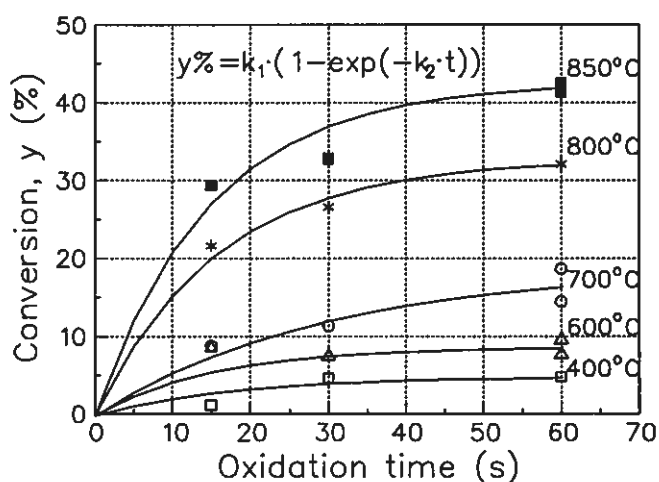


Fig. 3.8 Isothermal oxidation of Sydvaranger magnetite. Model: $y\% = k_1(1 - \exp(-k_2 t))$.

the straight line in a plot between $\ln(k_1 - y)$ and oxidation time

as shown in figure 3.9. The values for k_1 and k_2 are given in table 3.5. The higher k_1 -values obtained in the experiments by Sæverud (1984), may be explained by the smaller grains used in pellets compared with the grain sizes used in the present work.

Table 3.5 Constants in the formula 3.22.

Temp. (°C)	k_1 (%)	k_2 (s ⁻¹)
400	5.0	0.0569
600	8.8	0.0673
700	18.9	0.0342
800	32.8	0.0635
850	42.6	0.0678

Sæverud (1984) obtained by experiments:

400°C: $k_1=50\%$

600°C: $k_1=75\%$

900°C: $k_1=97\%$

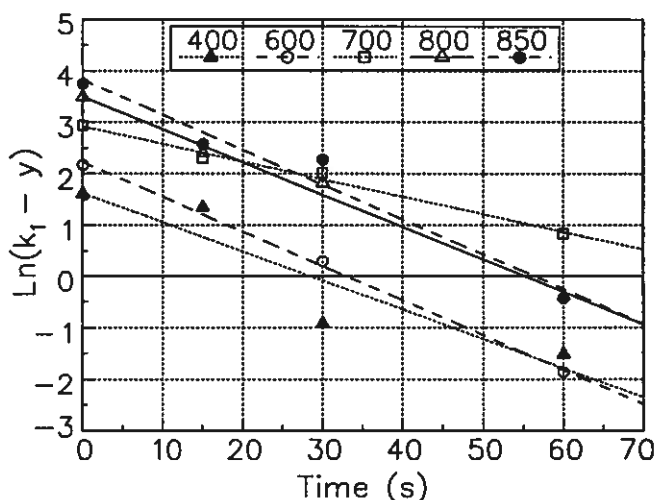


Fig. 3.9 Model: $y\% = k_1(1 - \exp(-k_2t))$. Finding k_2 from the slopes.

An Arrhenius plot for k_1 is shown in figure 3.10. The activation energy for k_1 was found to be 29.6 kJ/mole (7.1 kcal/mole) from the Arrhenius plot, for the temperature range 400-850°C. Correlation coefficient for the straight line was 0.903. This activation energy is rather close to the one obtained by Ball et al.

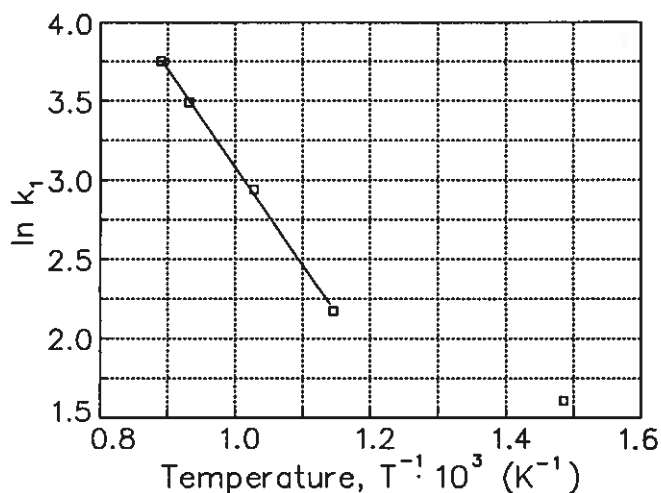


Fig. 3.10 Arrhenius plot for k_1 . Model: $y\% = k_1(1 - \exp(-k_2t))$.

(1966) for Sydvaranger magnetite, 5.6 kcal/mole, using the same model. A higher correlation factor for the straight line in figure 3.10 is obtained, $R^2=0.999$, if the k_1 -value at 400°C is excluded. An activation energy of 51.1 kJ/mole (12.2 kcal/mole) is calculated for the temperature range 600-850°C. The latter value gives a better approach to the experiments in the present work, due to the low accuracy of the calculated conversion after oxidation at 400°C. The low activation energy indicate that

diffusion is the rate controlling mechanism.

Formula 3.23 is derived for k_1 and is utilized for extrapolations to higher temperatures.

$$k_1 = 10224 \cdot e^{-\frac{51.14(kJ/mole)}{R \cdot T}} \quad (3.23)$$

A mean value for k_2 ($0.058 \pm 0.016 s^{-1}$) in the temperature range 600-850°C is applied in the extrapolation. 40 seconds in air is found to be sufficient for complete oxidation above a temperature of about 1086°C. Deviations in k_2 contribute to diminish the accuracy of the extrapolation. $k_2 = 0.074 s^{-1}$ gives 1071°C and $k_2 = 0.042 s^{-1}$ gives 1118°C.

Ball et al. (1986) found no correlation between k_2 and temperature. The latter is supported by the present work, as an Arrhenius plot for k_2 showed no correlation for the straight line ($R^2 = 0.0016$).

Complete oxidation is not obtained for values of k_1 below 100%. However, other experiments in section 3.4 have shown that oxidation is complete at 800°C after 24 hours. As the correlation between the experimental values and the model is not too good for the curves at and above 800°C, a better model should be used, at least at the higher temperatures.

Conventional diffusion models

Two diffusion models are derived from Fick's 1. law on the assumption that diffusion is rate controlling. Both are called the parabolic rate law and are derived on the assumptions of plane specimens (or parallelepiped) and spheres, respectively. These models are expressed by the equations 3.24 and 3.25, where k_1 is a rate constant and t is time.

$$\text{plane specimens: } y\% = k_1 \cdot \sqrt{t} \quad (3.24)$$

$$\text{spheres: } 1 - (1-y)\frac{2}{3} = k_1 \cdot t \quad (3.25)$$

The models, derived by anticipating that oxidation does not contribute to volume changes, lead to the expressions 3.26 and 3.27 (x = oxidized depth, R = sphere radius, h = specimen height)

$$\text{plane specimens: } \frac{x}{h} = y \quad (3.26)$$

$$\text{spheres: } \frac{x}{R} = 1 - (1-y)^{\frac{1}{3}} \quad (3.27)$$

The equations 3.24 and 3.25, can be derived from the formulas 3.9 and 3.10 in section 3.2.4, by inserting equations 3.26 and 3.27, respectively.

The rate constants (k_1), being the slope of the straight lines shown in figures 3.11 and 3.12, are found by linear regression analyses.

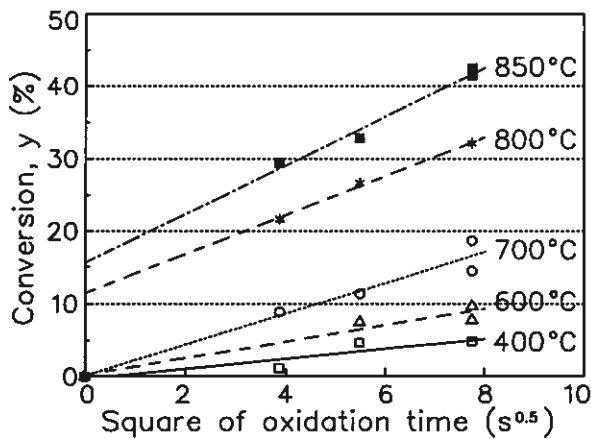


Fig. 3.11 Diffusion model, plane specimens (3.24).

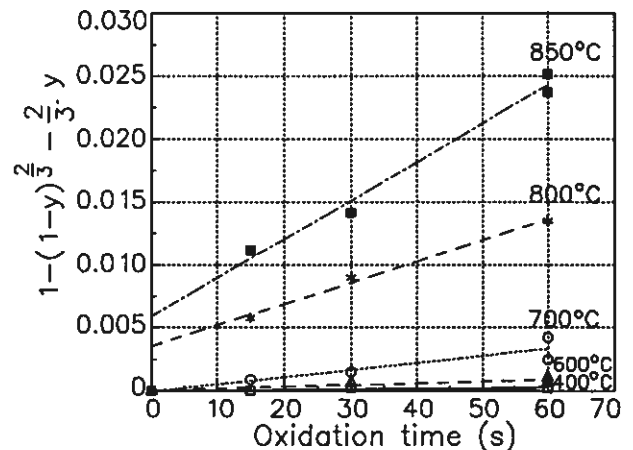


Fig. 3.12 Diffusion model, spheres (3.25).

Diffusion is not initially rate controlling at 800 and 850°C, because the curves cut the y -axes above zero. In the initial 10 seconds or so the chemical reaction at the surface of each particle is thought to be rate controlling.

The values for k_1 , the cut of the y -axes (a), and the correlation coefficients for the straight lines in figures 3.11 and 3.12, are given in table 3.6. The parabolic rate law for plane specimens correlates the better of the two models. Correlation is best at the highest temperatures. The models are compared in figure 3.13.

Table 3.6 Coefficients in the two diffusion models.

Temp. (°C)	Plane specimens model (3.24)			Sphere model (3.25)		
	k_1 (%·s ^{-0.5})	a (%)	R ²	$k_1 \cdot 10^5$ (s ⁻¹)	$a \cdot 10^3$	R ²
400	0.679	0	0.835	0.48	0	0.775
600	1.124	0	0.941	1.39	0	0.822
700	2.123	0	0.953	5.59	0	0.854
800	2.687	11.48	0.995	16.83	3.526	0.991
850	3.356	15.70	0.977	30.64	5.918	0.983

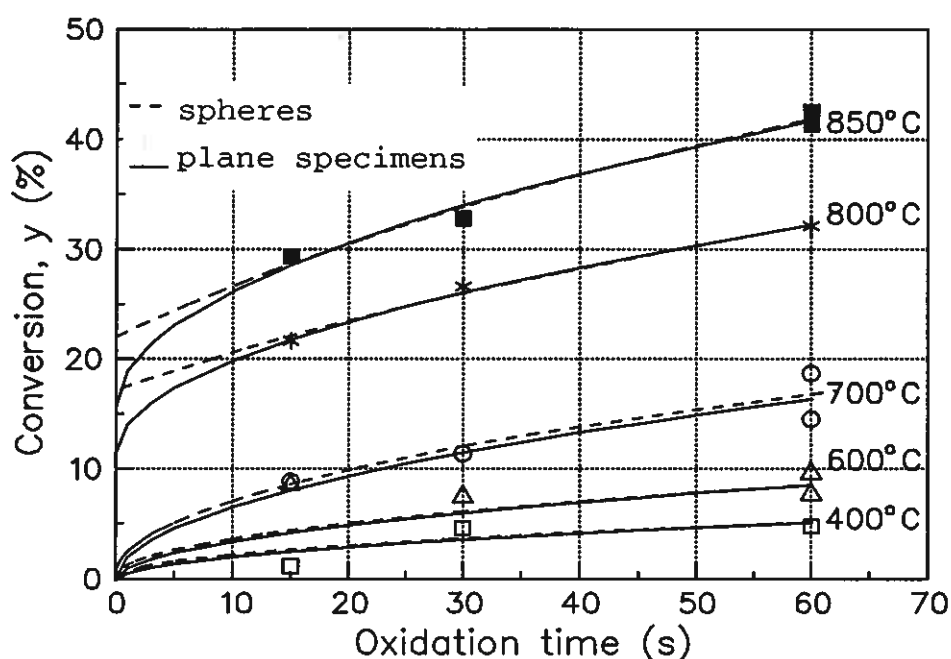


Fig. 3.13 Comparison of two diffusion models for isothermal oxidation of Sydvaranger magnetite (74-100 μ m)

Figure 3.13 shows that both models fit well with the experimental work, but neither of them apply for the initial oxidation up to about 10 seconds or so at temperatures above and at 800°C. Both models correlate better than the model $y = k_1(1 - \exp(-k_2 \cdot t))$, with the experimental results above 700°C, except during the first 10 seconds.

The activation energy was calculated from Arrhenius plots for both models, shown in figures 3.14 and 3.15. It was found to be 34.2 kJ/mole (8.1 kcal/mole) according to the parabolic rate law for plane specimens and 99.7 kJ/mole (23.7 kcal/mole) for spheres. k_1 at 400°C was excluded in the calculations for the same reasons, as previously mentioned.

General equations for k_1 in the two diffusion models are derived from the Arrhenius plots.

$$\text{plane specimens: } k_1 = 131.46 \cdot e^{-\frac{34.23 \text{ (kJ/mole)}}{R \cdot T}} \left(\frac{\%}{\sqrt{s}} \right) \quad (3.28)$$

$$\text{spheres: } k_1 = 12.68 \cdot e^{-\frac{99.72 \text{ (kJ/mole)}}{R \cdot T}} \quad (s^{-1}) \quad (3.29)$$

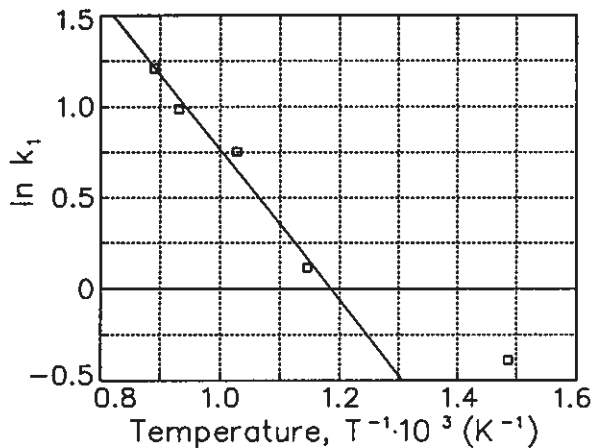


Fig. 3.14 Arrhenius plot, $R^2=0.976$
Diffusion model,
plane specimens (3.24).

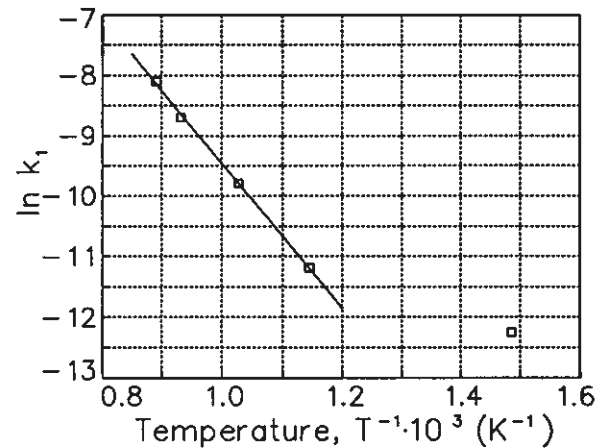


Fig. 3.15 Arrhenius plot $R^2=0.999$
Diffusion model,
spheres (3.25).

The activation energy deviates with a factor of nearly 3 for the two diffusion models, although both are low, indicating diffusion control. Himmel et al. (1953) found the activation energy for diffusion of iron in hematite to be about 100 kcal/mole while it was 55 kcal/mole for diffusion of iron in magnetite. According to these authors, and because of the low activation energy derived for both diffusion models, solid state diffusion of iron is not thought to be rate controlling.

Selection of a model

The rather big discrepancy between the two diffusion models in calculated activation energies shows the importance of the selected model. A selection between these two models is rather difficult because the experimental work is limited. The highest correlation coefficients (R^2) for 4 of the 5 curves, were obtained using the parabolic rate law for plane specimens. Both models correlate better than the pore blockage model, $y\% = k_1(1 - \exp(-k_2 \cdot t))$, with the experimental results above 700°C, except

during the first 10 seconds. Hence, the parabolic rate law for plane specimens is selected. A shape factor have been determined for preoxidized Sydvaranger magnetite in section 3.5. It was found to be 0.66 ± 0.03 , indicating deviations from the spherical shape, which partly supports the selection.

The low activation energy of 34.2 kJ/mole (8.1 kcal/mole), which was obtained for plane specimens, is fairly close to that obtained by Ball et al. (1966) for Sydvaranger pellets in the temperature range 280-840°C. They found $E=5.6$ kcal/mole, using the pore blockage model (3.21). The activation energy obtained in the present work by use of the latter model was 12.1 kcal/mole, in the temperature range 600-850°C.

Davies et al. (1951) and Edström (1957) found the oxidation to obey the parabolic rate law for plane specimens and spheres (pellets), respectively. Davies et al. obtained an activation energy of 24 kcal/mole, which is somewhat higher than the present findings, using the same model. Davies et al. used flat specimens produced by oxidizing iron in water. Magnetite so produced could be denser than the natural magnetite grains, implying slower diffusion.

For calculating the lowest temperature necessary for complete oxidation within 40 seconds based on the selected model, a temperature dependence for a (the cut of the y-axis in Fig. 3.11) must be assumed. As only two points exist, extrapolation to higher temperatures is rather uncertain. However, complete oxidation in air may be achieved within 40 seconds at temperatures above 1118°C, according to the selected model.

To conclude, in the present work the chemical reaction at the surface of each grain is rate controlling during the initial period of about 10 seconds at the higher temperatures. Diffusion in micropores or cracks in hematite and/or diffusion of oxygen along the hematite needles at the hematite/magnetite interface are thought to be rate controlling after the initial period. The experimental work is too limited to distinguish between diffusion or chemical rate control at 400°C.

3.3.5 Concluding remarks

Isothermal oxidation in air for maximum 60 seconds for an ordinary quality of Sydvaranger magnetite (74-100 μ m) has been carried out in the temperature range 400-850°C. Maximum conversion obtained was 42.0%, after 60 seconds at 850°C. A few experiments were performed with Kiruna and Minnesota magnetites, for which the conversion obtained under equal conditions were approximately 10% lower.

Topochemical growth of hematite with needles of hematite ahead of the topochemical front was observed.

The rate of oxidation for the ordinary quality of Sydvaranger magnetite follows the parabolic rate law in the temperature range 400-850°C, except during the initial period of 10 seconds or so. Best correlation is obtained on the assumption of plane specimens. The chemical reaction at the surface of each grain is thought to be rate controlling during the initial period. Otherwise, diffusion in micropores or cracks in hematite and/or diffusion of oxygen along the hematite needles at the hematite/magnetite border is thought to be rate controlling.

The activation energy was found to be 34.2 kJ/mole (8.1 kcal/mole) in the temperature range 600-850°C, according to the parabolic rate law for plane surfaces. According to the parabolic rate law for spheres the activation energy was found to be nearly the triple.

A model based on the assumption that the pores in the material are blocked by the fresh hematite produced, was also found to correlate well with the experimental data at and below 700°C.

The results indicate that, oxidation should be carried out in a separate unit and not in the heating unit in the Elkem Polar Process, provided that oxidation is to be carried out using air at temperatures below 1100°C.

3.4 Complete oxidation

3.4.1 Choice of method

Complete oxidation of magnetite to hematite is carried out to produce the necessary amounts of material for subsequent studies of reduction kinetics. The prereduction experiments require 50-100 g oxidized material of the fraction 63-90 μ m. It is important that the oxidation is brought to completion to eliminate the rate retarding effect of magnetite inclusions.

Isothermal and complete oxidation are important premises for the following reduction experiments. The results reported in section 3.3 have shown that the oxidation at temperatures below 700°C is too slow to be of practical interest. Oxidation should be carried out in a large temperature interval, 800-1300°C, to detect any effect of preoxidation temperature on the reduction rate.

Different oxidation methods were considered; the previously mentioned laboratory scale reactor used to study reaction kinetics, a fluidized bed apparatus, or plainly a crucible or a tray in a muffle furnace. Reduction experiments require larger quantities of oxidized material than what is practically produced in the laboratory scale reactor. This reactor does neither satisfy the need for prolonged residence time nor the demand for temperatures above 850°C, but it does satisfy the claim of isothermal oxidation. Isothermal oxidation is not possible in a crucible, and is difficult in a fluidized bed.

The method chosen was oxidation on a large tray (a plate) in a ceramic furnace with devices for gas inlet and outlet. The temperature of a heat resistant steel plate will be uniform and provide an equal temperature for all the particles, provided that the concentrate is distributed in a rather thin layer on the plate. In this case the excess heat evolved during oxidation will be transported out with the off gas.

3.4.2 Experimental

Oxidation procedure and materials

The magnetite used was a very pure concentrate from Sydvaranger. The quality was so-called Sydvaranger super concentrate. The results of chemical analysis, carried out by MINPRO (Swedish Mineral Processes AB), and size analysis are given below.

<u>Element basis:</u>	<u>Oxide basis:</u>	<u>Size distribution:</u>
Fe: 71.9 %	Fe ₃ O ₄ : 99.36%	-106 μm: 99.0%
Mn: 0.11 %	MnO ₂ : 0.17%	- 75 μm: 87.9%
Si: 0.11 %	SiO ₂ : 0.24%	- 53 μm: 61.8%
P : 0.005%	<u>Sum : 99.77%</u>	- 45 μm: 46.3%
S : 0.003%		- 38 μm: 24.6%

Approximately 20% of the concentrate was in the size range 63-90μm, which was the actual fraction for the reduction experiments. To minimize the heat evolved during oxidation, only the necessary amount of material was applied in the isothermal oxidation experiments. For this reason the magnetite concentrate was sieved wet on a 63μm sieve. The +63μm fraction was dried at 110°C and sieved on a 90μm sieve. In each oxidation experiment 150 g of the fraction 63-90μm was uniformly distributed on a steel tray in a 0.5 mm thick layer.

Two different furnaces were used. Oxidation in the temperature range 800-1100°C was carried out in furnace 1, shown in figure 3.16. This furnace was best suited, but could not be used above 1100°C. Oxidation in the temperature range 1150-1250°C was carried out in furnace 2, illustrated in figure 3.17.

Heating and cooling were carried out in nitrogen atmosphere. The quality used was nitrogen grade 2. Maximum contents of impurities according to specifications are given below.

Nitrogen grade 2:

N ₂	≥ 99.99%
O ₂	≤ 40 ppm
H ₂ O	≤ 21 ppm
Ar	≤ 30 ppm

The rate of heating in furnace 1 was 600°C/h and 200°C/h during the last 100°C below oxidation temperature. Heating was carried

out in a flow of N_2 ($1 \text{ m}^3/\text{h}$). The temperature was allowed to stabilize for about 10 minutes before oxidation was started. The heating rate in furnace 2 was also $600^\circ\text{C}/\text{h}$ during the first hour, but later as fast as possible. The temperature lagged behind the program. In order to reach the desired temperature, the flow of N_2 was reduced from $1 \text{ m}^3/\text{h}$ to $0.5\text{-}0.3 \text{ m}^3/\text{h}$ towards the end of the heating period. Total heating time was about 5 hours in furnace 2 while maximum heating time in furnace 1 was 2.5 hours.

Oxidation was carried out for 3 hours in air at each of the temperatures 900 ± 7 , 1002 ± 5 , 1050 ± 5 , 1104 ± 7 , 1150 ± 5 , 1195 ± 7 , and $1244\pm 7^\circ\text{C}$, and for 24 hours at $799\pm 5^\circ\text{C}$. The oxidation temperature was kept constant within the limits indicated. Temperature curves for each experiment are given in Appendix A.1.

Oxidation in the temperature range $799\text{-}1104^\circ\text{C}$ was carried out in furnace 1 while air was purged at an initial rate of $2.5 \text{ m}^3/\text{h}$. After 1 minute, the flow rate was reduced. Minimum flow rate was $1.1 \text{ m}^3/\text{h}$. The samples were in this way supplied with enough O_2 for complete oxidation during the first 25 seconds.

Oxidation in the temperature range $1150\text{-}1244^\circ\text{C}$ was carried out in furnace 2 while air was purged at a rate of $0.2 \text{ m}^3/\text{h}$. During the first 5 minutes enough O_2 was supplied for complete oxidation. At 1150°C , the flow rate was $1.0 \text{ m}^3/\text{h}$ during the first minute.

Furnaces

Furnace 1 is shown in figure 3.16. Maximum operating temperature was 1100°C . The heating element was 4.2 kW. Each of the four gas inlet tubes has 10 holes ($\phi_i = 4 \text{ mm}$) to secure a uniform gas distribution. The tray ($550\cdot 400\cdot 30 \text{ mm}$) containing the sample was placed directly on the insulation block. The furnace was controlled by a temperature control unit. The control temperature was measured 10 cm above the sample.

Two temperatures were recorded. The first temperature was measured directly in the sample with a calibrated thermocouple,

type Chromel-Alumel. The thermocouple (0.5 mm in diameter) was inserted into the furnace between the washer and the flange. The temperature correction relative to a reference thermocouple was -1.9°C and -0.5°C at 600°C and 1000°C , respectively. The calibration uncertainty was calculated to $\pm 2.5^{\circ}\text{C}$. The temperature was recorded with a data logger and reported without temperature correction. The second temperature recorded was measured approximately 10 cm above the sample.

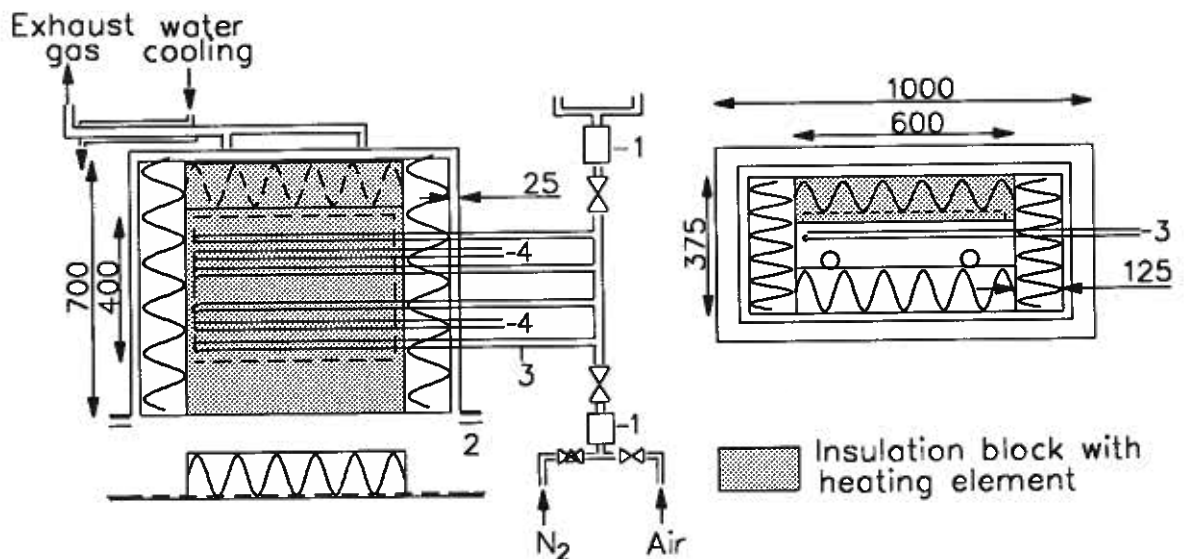


Fig. 3.16 Furnace 1

- 1 Flowmeter
- 2 Chesterton 191 - washing, 2.4 mm thick
- 3 Tubes of Canthal ($\phi_1=10$ mm) each with 10 holes ($\phi_2=4$ mm) uniformly distributed for gas inlet.
- 4 Tubes of Canthal ($\phi_1=3$ mm) for thermocouples.

Furnace 2 is a ceramic chamber furnace with inner dimensions 610·830·540 mm, and shown in figure 3.17. Maximum operating temperature was 1300°C . A special equipment was constructed to control the atmosphere above the sample during the experiments. The gas inlet is easily seen from the figure. The gas outlet was plainly between the cover and the tray periphery. The temperature was measured with a thermocouple, type Pt/Pt10%Rh, which was inserted directly in the sample in the centre of the tray and the temperature was recorded with a data logger. A temperature control unit did control the furnace.

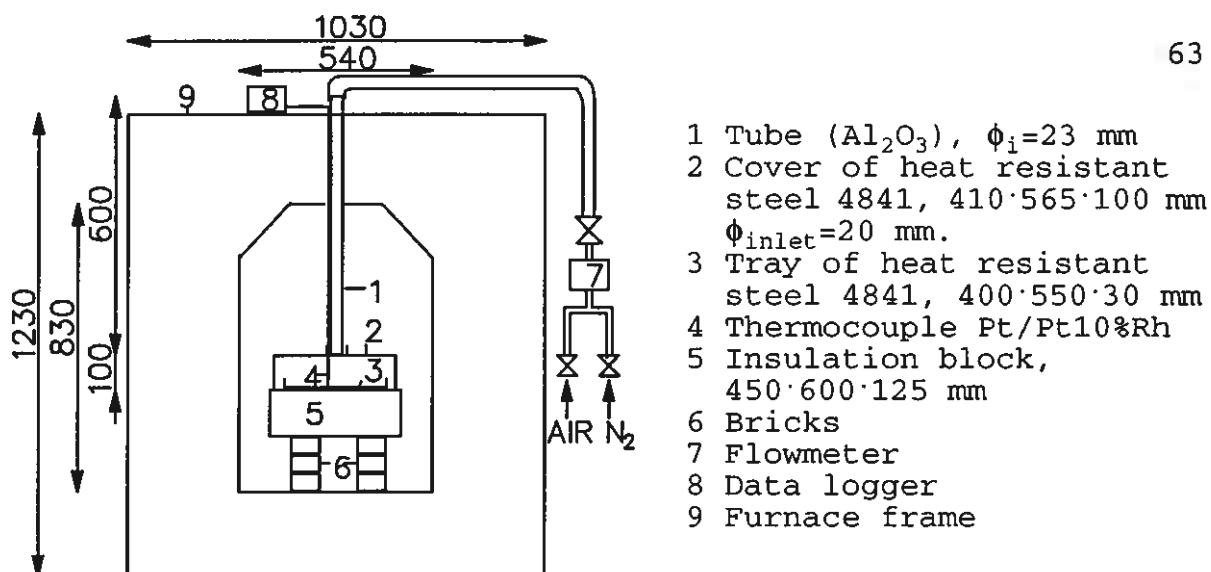


Fig. 3.17 Furnace 2 (Scandia)

Sample preparation after oxidation

Some sintering occurred during oxidation, the more the higher the temperature. The samples were alternately ground and sieved until each sample was $-90\mu\text{m}$. Sieving at $63\mu\text{m}$ was first performed dry and then wet. The fractions $63-90\mu\text{m}$ were dried at 110°C and kept for prereduction experiments. Samples for wet chemical analyses and polished surface specimens were split from this fraction before wet sieving.

Wet chemical analyses were carried out by MOLAB. The total amount of Fe (Fe^{tot}) and Fe^{2+} were determined in two separate analyses. Fe^{tot} was determined by making a solution of 0.5 g sample in HCl. The solution was reduced by SnCl_2 . Fe^{2+} was determined in another 0.5 g sample by reduction by NaHCO_3 in HCl without access to air. Indicator and an acid solution were added to the cold solutions before both were titrated with $\text{K}_2\text{Cr}_2\text{O}_7$.

Polished surface specimens were made by moulding the powder in a two component epoxy (Epofix). After 8-12 hours hardening, the specimens were alternatingly polished and cleaned. As a last step the surface was polished on a $1\mu\text{m}$ NAP-cloth.

A german Leitz Wetzlar Microscope with equipment for photographing was used to look at and take pictures of polished surfaces, both in reflected and polarized light.

3.4.3 Subgrain structure after complete oxidation

The samples of Sydvaranger super magnetite concentrate were completely oxidized at the different temperatures. Wet chemical analyses gave $\text{Fe}^{2+} < 0.2\%$ for all the oxidized samples, which implies that the magnetite content is below 0.28%. The detecting limit is 0.2% for Fe^{2+} by wet chemical analysis. Hence, traces of magnetite in the grain cores of the "artificial" hematite (preoxidized magnetite) can not be detected by wet chemical analysis.

The subgrain structures of representative grains of the preoxidized magnetite samples are presented in the figures 3.18 and 3.19. The samples are named S1-S8 for an increasing temperature from 799°C (S1) to 1244°C (S8). The photos were taken in optical microscope using polarized light. In polarized light, the individual orientations of hematite crystals appear in each grain. In reflected light, the grain sections shown on the photos look uniformly white.

Magnetite inclusions, which have a brownish-greyish appearance in reflected light, were only observed in a few grain cores of the samples S1 and S8, approximately in 1 of 100 grains and in 1 of 500 grains, respectively. All the samples are said to be completely oxidized as their magnetite contents are well below the detecting limit by wet chemical analyses.

The higher the temperature of oxidation the coarser are the individual hematite crystals formed in each grain. There is a gradual coarsening, which is easily detected at the higher temperatures in the temperature range 1104-1244°C, referring to figure 3.19. There is also a gradual coarsening in the lower temperature interval, referring to figure 3.18, but this is not so easy to observe from photos. When the polarizer, or the specimens, are rotated in the microscope, however, other individually oriented hematite crystals appear, the more the lower the oxidation temperature.

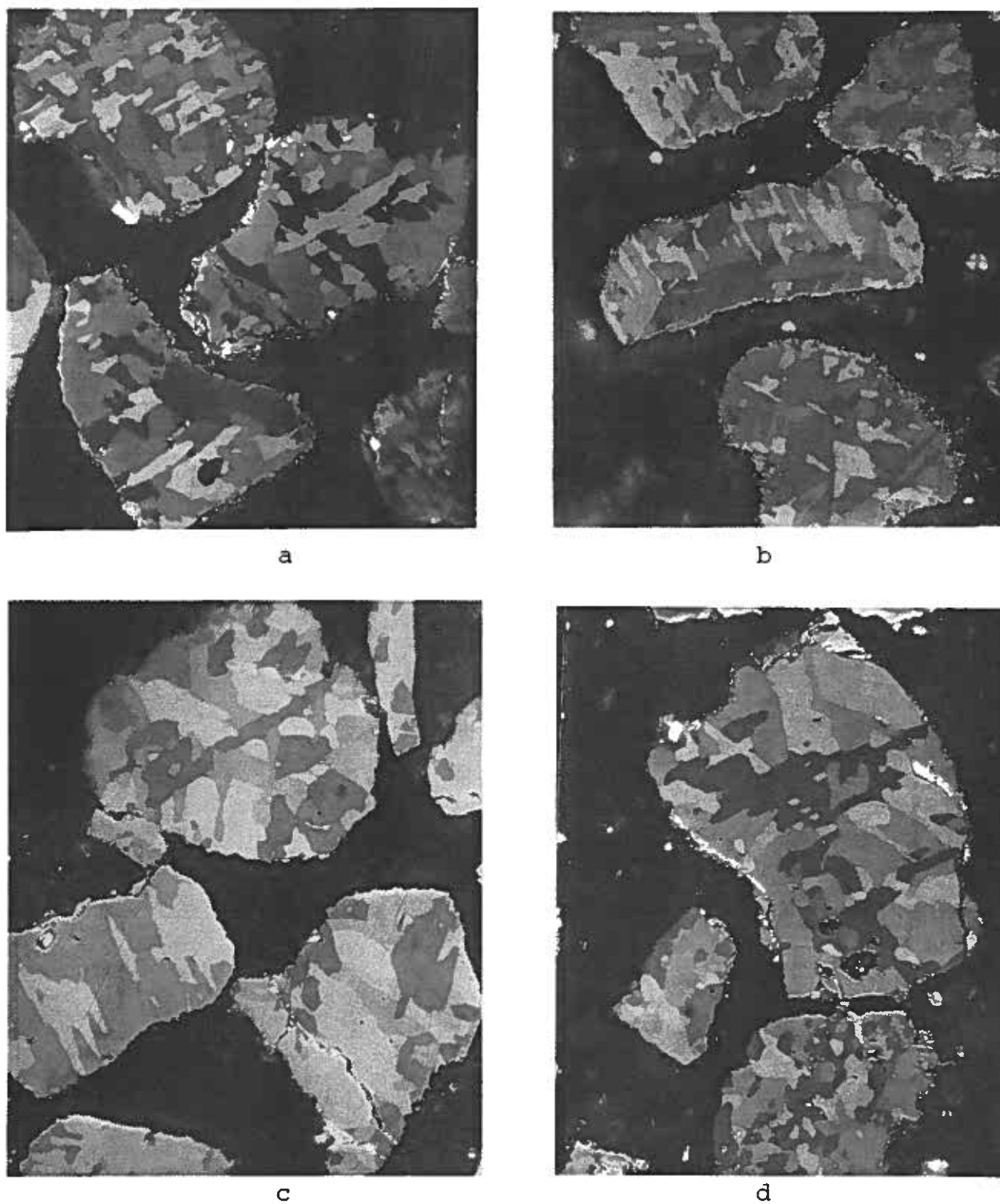


Fig. 3.18

Subgrain structures of Sydvaranger super magnetite after isothermal oxidation in air.

- | | | |
|--------|---------------------------|--------------|
| a) S1: | 799 \pm 5 $^{\circ}$ C | for 24 hours |
| b) S2: | 900 \pm 7 $^{\circ}$ C | for 3 hours |
| c) S3: | 1002 \pm 5 $^{\circ}$ C | for 3 hours |
| d) S4: | 1050 \pm 5 $^{\circ}$ C | for 3 hours |



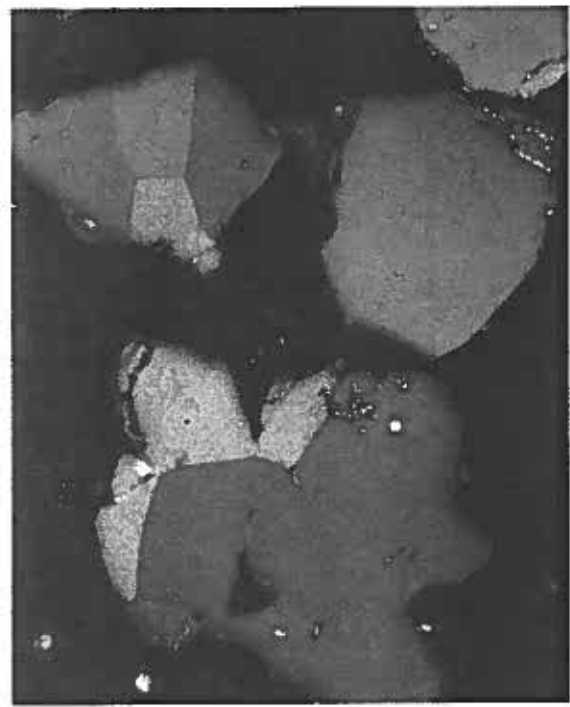
a



b



c



d

10 μm

Fig. 3.19

Subgrain structures of Sydvaranger super magnetite after isothermal oxidation in air for 3 hours.

a) S5:	1104±7°C
b) S6:	1150±5°C
c) S7:	1195±7°C
d) S8:	1244±7°C

Ulvensöen et al. (1991) did also notice a small increase in the crystal size of individually oriented hematite crystals for an increasing oxidation temperature in the range 800-1050°C.

For the high temperature forms, S7 and S8, shown in figure 3.19 c and d, the subgrain structure from one grain cross section to another may vary. For these samples the subgrain size, which is the size of the individually oriented hematite crystals, approaches the grain size. The way the grains are cut, in the centre, or at the sides, parallel to c-axes or in an angle to the c-axes, becomes more important as the subgrain size approaches the grain size.

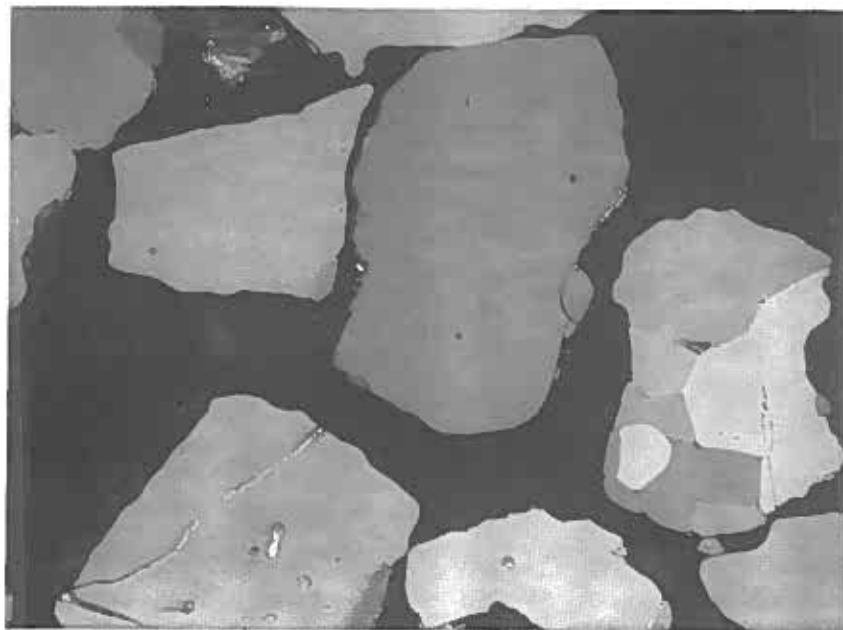
The subgrain structure seems to be formed by a process of grain refinement, in accordance with observations by Cooke and Stowasser (1950). During oxidation certain crystallographic directions within any one single magnetite crystal are preferentially oxidized and a single crystal of magnetite eventually becomes a number of independently oriented crystals of hematite. Preferential growth of hematite was observed during oxidation, referred to in section 3.3 and shown in figure 3.6 as needles of hematite ahead of the topochemical front. In the beginning the growth is parallel to the close packed planes in magnetite and the (111) planes in magnetite is transferred to (1000) planes in hematite, according to the oxidation mechanism presented by Bentell and Mathisson (1978).

Callender (1962) observed a gradual grain growth between 850°C and 1180°C when oxidizing pellets of fine grained magnetite, but between 1180°C and 1250°C a distinct change in structure occurred. Fine interstitial hematite was replaced by a compact mass of equiaxial crystals. An abrupt change in the subgrain structure has not been detected in the present work.

The subgrain structure at 800°C, referring to sample S1 in figure 3.18 a, is relatively stable at 800°C. This sample was oxidized for 24 hours (to ensure complete oxidation at this rather low temperature) compared to 3 hours for the others. In spite of the

prolonged time at temperature, the sample S1 has the finest subgrain structure (each grain section consists of several more individually oriented hematite crystals). This is in accordance with the findings of Cooke and Stowasser (1952), who found that the resulting hematite structure was relative stable at low temperatures, around 500-600°C.

The low temperature subgrain structure is not stable at higher temperatures, referring to figure 3.20. The figure shows the low temperature subgrain structure of S1 (799°C for 24 hours) after additional heat treatment at 1250°C in air for 7 hours. The subgrain structure of S1 has changed markedly. The individually oriented hematite crystals in each grain have recrystallized. The crystal size is approaching the grain size. The appearance of the subgrain structure resembles the high temperature subgrain structure of sample S8, which was oxidized at 1244°C for 3h and shown in figure 3.19 d. The change in subgrain structure indicate that the hematite crystal size at each temperature approaches a characteristic crystal size, from which further changes take place very slowly. The present observations are in accordance with the findings of Cooke and Stowasser (1952).



10 μm

Fig. 3.20 Subgrain structure of S1 (799°C for 24 hours) after further heat treatment in air at 1250°C for 7 hours.

During heating in nitrogen there is a possibility of solid state reaction between the tray and the magnetite with formation of wüstite, but this reaction is very slow and no sintering between the plate and the oxidized material was observed.

The samples may oxidize during heating in nitrogen. Maximum content of O_2 in the nitrogen gas was 40 ppm, according to specifications. As the heating period in furnace 1 was maximum 2.5 hours and the nitrogen flow rate was $1 \text{ m}^3/\text{h}$, each sample was supplied with maximum 0.0045 mole oxygen during this period. If every O_2 molecule reacted with Fe_3O_4 , a maximum of 2.8% of the magnetite in each 150 g sample would oxidize during heating.

However, the actual conversion taking place during heating is probably far less. Oxidation is slow at the lower temperatures, below 600°C . Further, the gas flow rate is rather high compared to slow diffusion of oxygen in the bulk gas. In addition, the actual content of O_2 in the nitrogen gas is in most cases far below the guaranteed maximum content of 40 ppm.

Referring to section 3.2.3, magnetite probably recrystallizes during heating in nitrogen, especially at elevated temperatures. Cooke and Ban (1952) found that magnetite grains in pellets did tend to form bonds already at 900°C .

The subgrain structure observed in the present work at the higher temperatures may have been formed from recrystallized magnetite. However, similar subgrain structures were observed for preoxidized Sydvaranger super magnetite samples which were not preheated in an inert atmosphere. Hence, the hematite subgrain structure formed at each temperature is not significantly dependant on whether the magnetite has recrystallized or not prior to oxidation. Sydvaranger magnetite were oxidized in crucibles by introducing them directly into a hot furnace at 850 , 1050 , and 1150°C . The hematite crystal size of these samples were perhaps a little coarser than those heated in nitrogen at the respective temperatures of oxidation, and there were also

greater variation from grain to grain. The reason for this is the lack of temperature control during oxidation of batches of 0.5 kg in crucibles. A temperature increase is to be expected because of the exothermal heat evolved.

The subgrain structure formed at the higher temperatures could have been formed from a fine subgrain structure by recrystallization of hematite. It could also have been formed directly at the higher temperatures.

3.4.4 Concluding remarks

Complete oxidation of Sydvaranger super magnetite concentrate (63-90 μ m) was achieved after isothermal oxidation in air for 24 hours at 799°C or for 3 hours at 900°C, 1002°C, 1050°C, 1104°C, 1150°C, 1195°C, and 1244°C, respectively.

Individually oriented hematite crystals were formed in each grain, probably by a process of grain refinement. A gradual coarsening of the hematite crystals was observed for an increasing oxidation temperature. At the higher temperatures the hematite crystal size approached the grain size.

The low temperature subgrain structure (800°C) is stable at the temperature at which it is formed, but not at higher temperatures. The results indicate that there is a characteristic hematite crystal size at each temperature.

3.5 Characterization by videoplan

3.5.1 Introduction

Complete oxidation of Sydvaranger super magnetite concentrate (63-90 μ m) was carried out in the temperature range 800-1250°C as previously described in section 3.4. In the same section is also given a qualitative description and photographs of the different subgrain structures obtained after 3 hours (or 24 hours) isothermal oxidation.

The main purpose in this section is to characterize the subgrain structure of these completely oxidized samples by a quantitative measure. A quantitative measure is developed, which may be useful for the subsequent studies of reduction kinetics. A shape factor is also measured.

3.5.2 Method

Quantitative characterization of the three-dimensional subgrain structures and grain shapes were carried out using planar two-dimensional sections.

A Videoplan 2 Image Processing System, Kontron Image Analysis Division, with a Sanyo Camera Adopter and a Leitz Wetzlar Microscope, were used. Measurements were carried out directly on polished surface specimens at a magnification of 2520 in the microscope.

Subgrain structure

Characterization of subgrain structure was based on the anisotropic structure of hematite. By rotating either the polarizer, the analyzer, or the sample 90°, the light intensity of the crystals will vary from zero to maximum. Photographs of the subgrain structures were not used in the characterization because all the subgrains do not necessarily appear on the photographs. For this reason, the measurements were performed

directly on the polished surface specimens in polarized light in the microscope. The polarizer of the microscope was rotated so that all the individually oriented hematite crystals in each grain were detected.

Several measurements may be carried out. Examples are:

- the average hematite subgrain diameter in proportion to average grain diameter (diameter of a sphere with the same area as the subgrain or grain in section)
- the average hematite subgrain diameter
- the major or minor axis of the hematite subgrain in proportion to the major or minor axis of the grain
- the major or minor axis of subgrains
- an average number of subgrains per grain area in section
- the average subgrain area in proportion to the grain area in section.

Results can be reported as mean values or as size distributions.

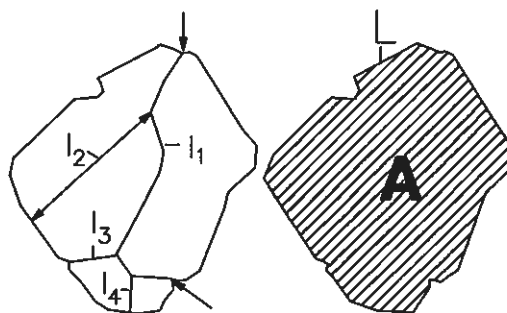
However, to detect a possible influence of the subgrain structure on the reduction rate, the characterization should be carried out with this in mind. In the present work the subgrain boundaries are regarded as preferable reduction paths where diffusion of reduction gas and/or diffusion in the solid state more easily are accomplished. The total area of the subgrain interfaces in proportion to the grain volume would be the most interesting measure. On two-dimensional planar sections a convenient measure is the ratio of the entire length of the internal subgrain boundaries and the grain section area.

The following parameters were measured for each grain cross section:

Area: A (μm^2)

Periphery (perimeter): L (μm)

Subgrain boundaries: $\sum_{i=1}^n l_i$ (μm)



The area was measured by the computer from the drawing of the grain cross section. For each polished surface specimen 10 representative grains were measured this way, if not otherwise indicated.

From these measurements the ratio of the entire length of the internal subgrain boundaries to the grain section area (SBA) was calculated for each grain section according to formula 3.30.

$$SBA = \frac{\sum_{i=1}^n l_i}{A} \quad (\mu m^{-1}) = 10^6 \cdot \frac{\sum_{i=1}^n l_i}{A} \quad (m^{-1}) \quad (3.30)$$

From these separate SBA calculations an average value, \overline{SBA} , was derived for a number of grains.

If the subgrains are uniformly distributed in each grain and the subgrain boundaries are uniformly distributed in each grain section, the two-dimensional measure in equation 3.30, if averaged for a number of grain sections, will be an adequate measure. A true measure for the total internal subgrain interfaces in proportion to the grain volume is probably not obtained from the two-dimensional measurements. However, the two-dimensional measures are well suited for comparing different subgrain structures.

Shape factor

Numerous shape parameters have been proposed, but only a few are practical. By far the most frequently used planar shape parameter is the one in equation 3.31 (Exner, Metals Handbook, 1984). This shape factor was applied in the present work.

$$\text{Shape factor: } \psi = \frac{4 \cdot \pi \cdot A}{L^2} \quad (3.31)$$

For a spherical particle, $\psi=1$, and for any other shape, $0 < \psi < 1$. Highly elongated grains as well as highly rugged perimeters (large surface areas) yield low shape factors. To differentiate between these aspects of shape, additional measurements are necessary.

For an accurate statistical calculation of the shape factor, 50-100 grains should have been measured. However, a mean value for at least 10 grains will give an indication of the degree of surface ruggedness or deviation from the spherical size. The shape factor was calculated separately for each grain and the mean value was calculated for a number of grains.

Standard distribution

The mean value (\bar{x}) of SBA and ψ were calculated and reported along with the standard deviation (STD) according to formula 3.32 (n=10 if not otherwise indicated).

$$STD = \frac{\sqrt{\sum_{i=1}^n (x_i - \bar{x})^2}}{n - 1} \quad (3.32)$$

There is a 68% probability for a value x_i to be within the range $\bar{x} \pm STD$.

3.5.3 Results

The subgrain structures of Sydvaranger super magnetite concentrate (63-90 μ m) after isothermal oxidation in air for 3 hours in the temperature range 900-1250°C, and for 24 hours at 799°C, were qualitatively described in section 3.4. The results from the characterization of these subgrain structures by videoplan, are presented in figure 3.21. For simplicity, this curve is called the SBA curve. There is a gradual decrease in the mean SBA values for an increasing temperature. At each temperature the average SBA value for 10 grains and the standard deviation are shown in the figure.

The figure 3.21 illustrates the gradual coarsening of the subgrain structure for an increasing temperature. There is no abrupt changes in the structure as previously pointed out and

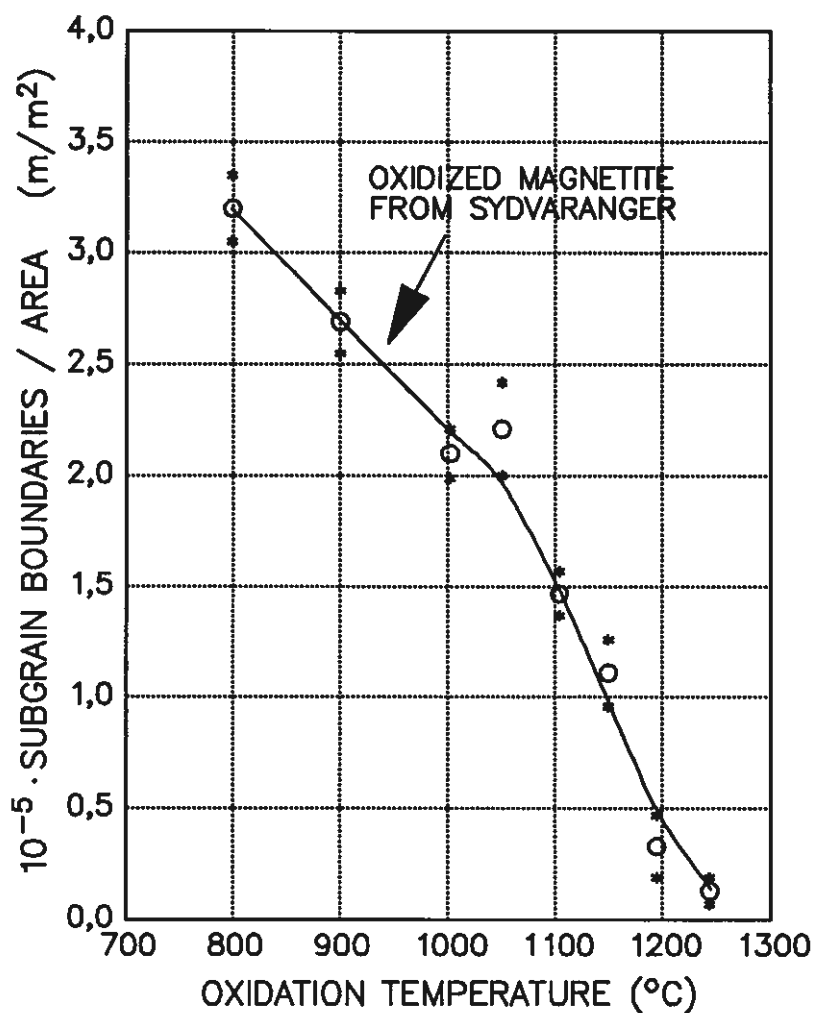


Fig. 3.21 SBA curve for preoxidized magnetite, showing the effect of oxidation temperature on the subgrain structure after 3 hours (24h/800°C).

discussed in section 3.4. However, there is a shift in the slope of the SBA curve at 1050°C. Above this temperature the coarsening of the individually oriented hematite crystals is more pronounced. At elevated temperatures the SBA value approaches zero, implying that the subgrain size approaches the grain size.

The exact measurements of the average SBA values and the shape factors, and the standard deviations, are given in table 3.7. According to the rather low shape factors, particle shapes either deviate significantly from the spherical shape and/or their surface are rugged. The shape factor appears to be independent of the oxidation temperature in the temperature range 800-1250°C.

This indicate that the observed coarsening of subgrain structure for an increasing temperature, does not contribute to any exterior changes in the surface or in the shape of the particles. The average value, 0.66 ± 0.03 , for the 80 grains could as well be reported. The high number of grains makes this value an acceptable statistical average.

Table 3.7 Average SBA values and shape factors $\bar{\psi}$ measured by videoplan¹, for preoxidized Sydvaranger magnetite, completely oxidized at different temperatures.

Sample	Oxidation in air		$\overline{\text{SBA}}$	$\bar{\psi}$
	Temperature (°C)	Time (hours)	(m/m ²)	Shape factor
S1	799±5	24	$(3,20 \pm 0.15) \cdot 10^5$	0.66 ± 0.03
S2	900±7	3	$(2.69 \pm 0.14) \cdot 10^5$	0.67 ± 0.02
S3	1002±5	3	$(2.10 \pm 0.11) \cdot 10^5$	0.73 ± 0.03
S4	1050±5	3	$(2.21 \pm 0.21) \cdot 10^5$	0.63 ± 0.03
S5	1104±7	3	$(1.47 \pm 0.10) \cdot 10^5$	0.62 ± 0.02
S6	1150±5	3	$(1.11 \pm 0.15) \cdot 10^5$	0.66 ± 0.03
S7	1195±7	3	$(0.33 \pm 0.14) \cdot 10^5$	0.66 ± 0.04
S8	1244±7	3	$(0.13 \pm 0.06) \cdot 10^5$	0.62 ± 0.03

1) 10 grains were measured on each polished surface.

3.5.4 Discussion

The figures 3.22-3.25 show the 10 individual measurements of the total length of the internal subgrain boundaries in each grain and the respective grain area in section for the eight samples. Different grain areas arise mainly because the grains are differently cut. Some are cut in the centre and some at the sides. Linear regression analyses give straight lines which intercept the y-axes close to origo, implying that the subgrain interfaces are uniformly distributed in each grain. This indicates a uniform temperature throughout each grain during oxidation.

If there is a large number of subgrains in each grain, it will be sufficient to measure 10 grains. This will be the case for the low temperature forms (S1-S5) also shown in the figures 3.18a-d

and 3.19a. The photos look perhaps similar, but additional subgrain boundaries will appear if the polarizer is rotated, especially for the samples S1 and S2. The accuracy of the measurements is acceptable for all these samples (S1-S5). The standard deviations in percentage of the mean SBA values are excellent, only 5%, for the samples S1, S2, and S3, and below 10%, for the all samples S1-S5, referring to table 3.7.

Correlation coefficients (R^2) for the regression lines are given in the figure texts. A correlation coefficient between 0.8 and 1.0 is usually accepted as an excellent linear approach. This is achieved for the samples S1, S2, S3, and S5, which implies that the subgrain boundaries are uniformly distributed in the grain sections.

An exception is the low correlation factor for the sample S4 ($R^2=0.64$), which still is acceptable for a linear approach. This regression line intercepts the y-axis at $127\mu\text{m}$, indicating an increased number of subgrains towards the grain surface. As the other samples show no such trends, the subgrain boundaries may be considered to be uniformly distributed in the grain sections.

The bad linear approach for S6 ($R^2=0.22$) may be explained by an unfortunate choice of grains of approximately equal grain area in section. The standard deviation in percentage of the average SBA value is 13,5%, still acceptable.

The grain orientation before cutting is growing more important for an increasing subgrain size. Variations in subgrain structure from one grain section to another are observed for the high temperature samples, S7 and S8, presented in the figures 3.19 c-d, 3.24, and 3.25. To maintain the accuracy for the two samples, for which the subgrain size approaches the grain size, the number of grains included in the investigation should be increased. Instead only representative grains are measured. These considerations explain the bad correlation coefficients for the samples S7 and S8. It does also explain the large standard deviations in percentage of the average SBA values, 42% and 46%, respectively.

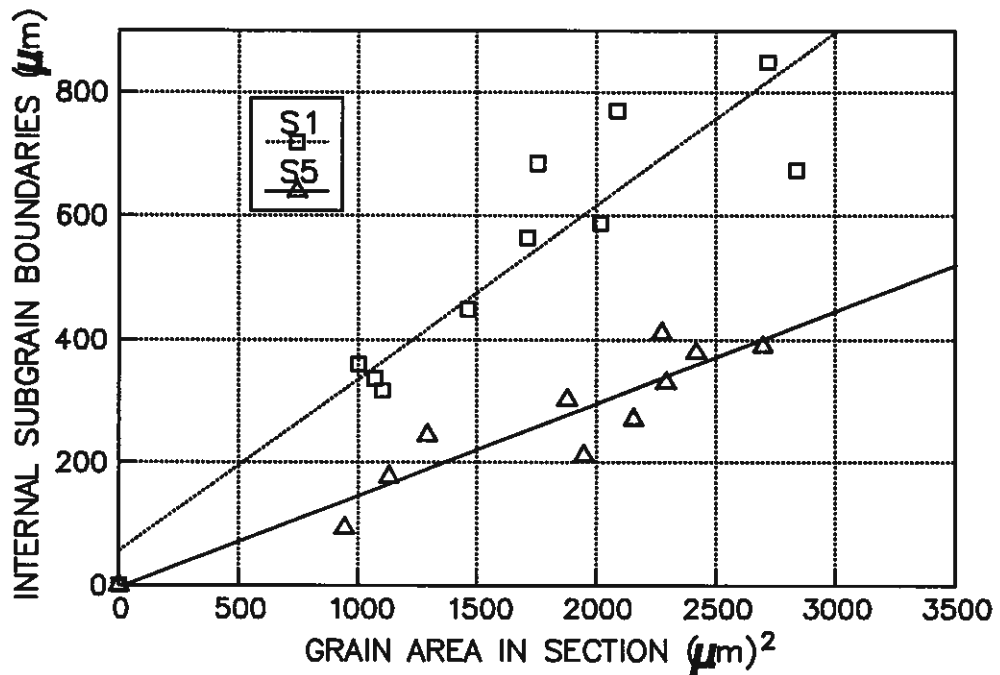


Fig. 3.22 Linear regression analysis of the internal subgrain boundaries and grain area in section for samples oxidized at 799°C (S1) and 1104°C (S5).

$$S1: y = 0.281 \cdot x + 55 \quad (\mu\text{m}) \quad R^2 = 0.87$$

$$S5: y = 0.150 \cdot x - 4 \quad (\mu\text{m}) \quad R^2 = 0.88$$

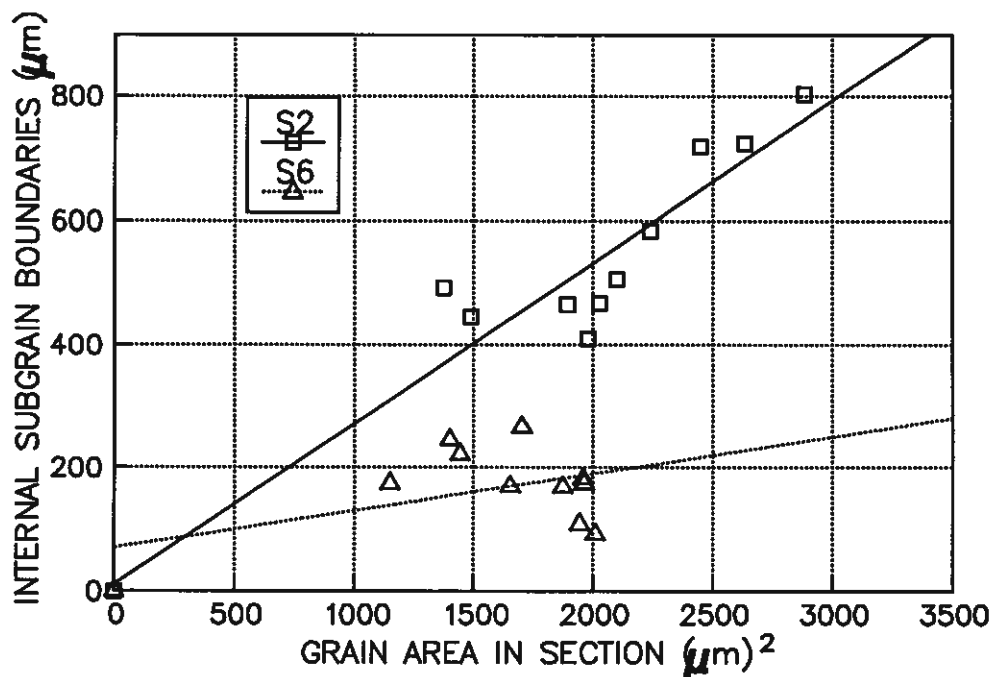


Fig. 3.23 Linear regression analysis of the internal subgrain boundaries and grain area in section for samples oxidized at 900°C (S2) and 1150°C (S6).

$$S2: y = 0.261 \cdot x + 11 \quad (\mu\text{m}) \quad R^2 = 0.90$$

$$S6: y = 0.006 \cdot x + 70 \quad (\mu\text{m}) \quad R^2 = 0.22$$

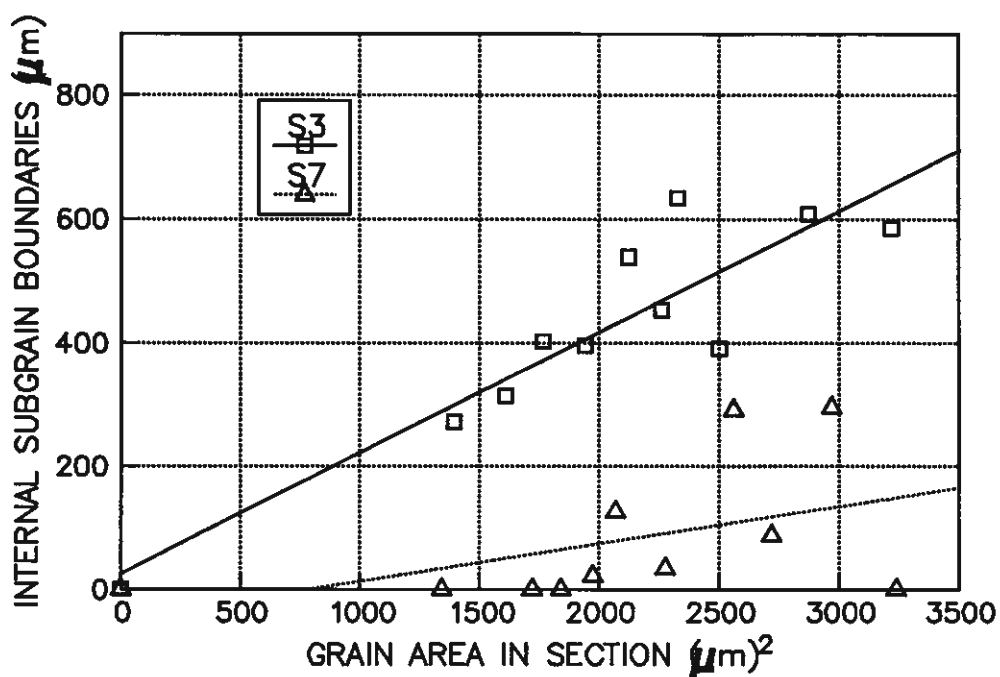


Fig. 3.24 Linear regression analysis of the internal subgrain boundaries and grain area in section for samples oxidized at 1002°C (S3) and 1195°C (S7).
 S3: $y = 0.196 \cdot x + 26$ (μm) $R^2 = 0.83$
 S7: $y = 0.060 \cdot x - 47$ (μm) $R^2 = 0.22$

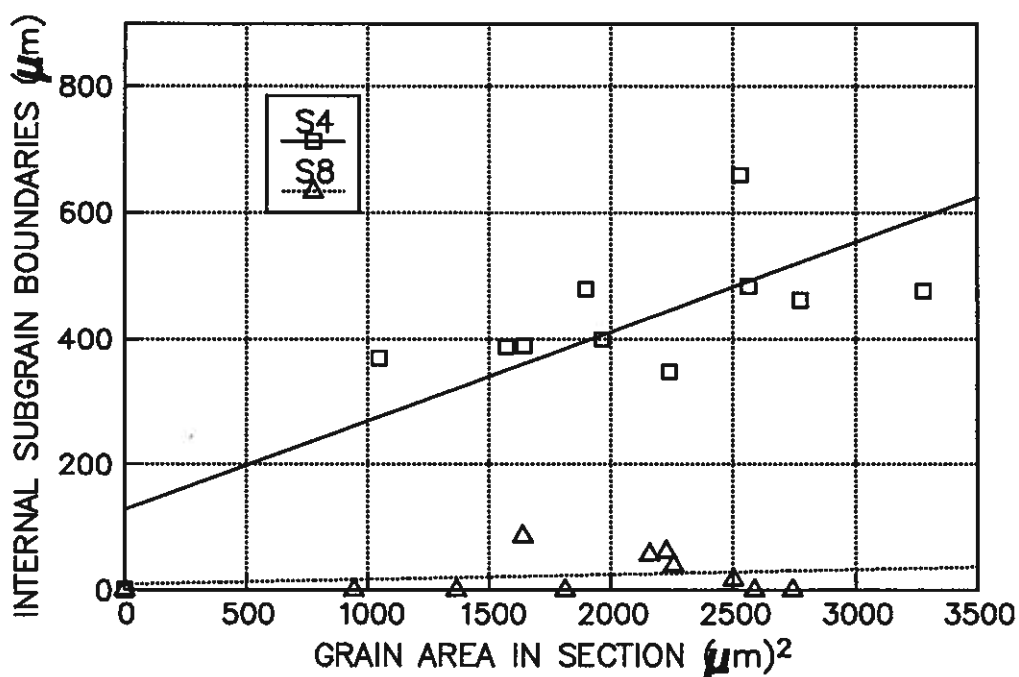


Fig. 3.25 Linear regression analysis of the internal subgrain boundaries and grain area in section for samples oxidized at 1050°C (S4) and 1244°C (S8).
 S4: $y = 0.142 \cdot x + 127$ (μm) $R^2 = 0.64$
 S8: $y = 0.008 \cdot x - 9$ (μm) $R^2 = 0.04$

3.5.5 Concluding remarks

The subgrain structures of preoxidized Sydvaranger super magnetite concentrate (63-90 μ m) were quantitatively characterized by videoplan measurements. The ratio of total length of subgrain boundaries and the grain section area, SBA, was measured. Average SBA values were derived for 10 grains of each of the samples S1 - S8.

The mean SBA values were found to steadily decrease with an increasing oxidation temperature from $(3.20 \pm 0.15) \cdot 10^5$ at 799°C to $(0.13 \pm 0.06) \cdot 10^5$ m/m² at 1244°C, shown by the SBA curve. The slope of the curve changes at 1050°C. Above this temperature the coarsening of the individually oriented hematite crystals is more pronounced.

The subgrain interfaces were found to be uniformly distributed in the grains, indicating a uniform temperature throughout each grain during oxidation.

The standard deviation in percentage of the average SBA measurements were below 10% for S1-S5 (5% for S1-S3). Above an average SBA value of $(1-1.5) \cdot 10^5$ m/m² the characterization method has the necessary sensitivity to differentiate between subgrain structures. At elevated temperatures, however, the subgrain size approaches the grain size, the direction of the grain cut gains importance, causing a high percentage standard deviation for S7 (42%) and S8 (46%).

A shape factor was measured to 0.66 ± 0.03 . The results indicate that the shape factor is independent of the oxidation temperature in the temperature range 800-1250°C. Hence, the observed coarsening of subgrain structure with temperature does not contribute to exterior changes in the particles surface or shape.

3.6 Conclusions

Isothermal oxidation experiments in the range 400-850°C were carried out in the laboratory scale reactor for periods of up to 60 seconds, using air. Maximum conversion, 42.0%, was obtained for an ordinary quality of Sydvaranger magnetite (74-100 μ m) after 60 seconds at 850°C. Lower conversions were obtained using Kiruna and Minnesota magnetites.

The activation energy for Sydvaranger magnetite was found to be 34.2 kJ/mole (8.1 kcal/mole) in the temperature range 600-850°C, according to the parabolic rate law for plane surfaces.

The results indicate that, oxidation should be carried out in a separate unit and not in the heating unit of the Elkem Polar Process.

Topochemical growth of hematite with needles of hematite ahead of the topochemical front was observed.

The rate of oxidation for Sydvaranger magnetite follows the parabolic rate law, except during the initial period of 10 seconds or so. Best correlation is obtained on the assumption of plane specimens, not spheres. The chemical reaction at the surface of each grain is probably rate controlling during the initial period. Otherwise, diffusion through a growing hematite layer is thought to be the slowest step.

A model based on the assumption that the pores in the material are blocked by the fresh hematite produced, was also found to correlate well with the experimental data at and below 700°C.

Some magnetite was completely oxidized, using another apparatus, to produce material for subsequent reduction experiments. Sydvaranger super magnetite concentrate (63-90 μ m) was oxidized for several hours in air at constant temperatures in the range 800-1250°C.

Individually oriented hematite crystals were formed in each grain, probably by a process of grain refinement. A gradual coarsening of the hematite crystals was observed for an increasing oxidation temperature. At the higher temperatures the hematite crystal size approached the grain size. The low temperature subgrain structure (800°C) is stable at the temperature at which it is formed, but not at higher temperatures.

The subgrain structures of the completely oxidized samples were quantitatively characterized, using videoplan. SBA values were measured. SBA is the ratio of total length of subgrain boundaries within each grain and the grain section area. Average SBA values were derived for 10 grains of each sample.

The mean SBA values were found to decrease steadily with an increasing oxidation temperature, shown by the SBA curve. The slope of the curve changes at 1050°C. Above this temperature the coarsening of the individually oriented hematite crystals is more pronounced.

The characterization method has high reproducibility and the necessary sensitivity to differentiate between subgrain structures. At elevated temperatures, the subgrain size approaches the grain size, the direction of the grain cut gains importance, causing a high percentage standard deviation.

4 CHARACTERIZATION OF NATURAL HEMATITE CONCENTRATES

4.1 Introduction

It is considered a great advantage if initial reduction rates for different natural hematite concentrates could be predicted by raw material characterization. For this reason hematite concentrates from the whole world have been included in the present investigation. A characterization of these concentrates is given in this chapter. The results from prereduction experiments with the same concentrates are given in chapter 5.

A narrow fraction (63-90 μm) of the concentrates is used in the prereduction experiments both because this fraction is most convenient for our laboratory scale reactor and because comparison should be carried out for approximately equal grain sizes. The same fraction (63-90 μm) is characterized in this chapter. Actual parameters are mineral phases, grain size distribution, specific surface area, subgrain structure, grain shape, and trace elements.

4.2 Description of the iron ores

Hematite is the dominating iron oxide in the mineral assemblage of hematite ores. The 6 different hematite concentrates, which are characterized in the present investigation, are made from hematite ores situated in 5 different countries, Brazil, Liberia, Guinea, Canada, and Norway. Simple short terms are used for simplicity, based on country, type, mine, or company. Each of these ores is in the following described below the heading of the respective country. The short terms are written in braces in the headings. Descriptions of these ores among others are also found in a report written by P. Storemyr (1986a).

The hematites and the short terms used are shown in table 4.1.

Table 4.1 Short terms for the hematite concentrates.

Short term	Country	District, mine	Company	Received type
MBA	Brazil	Minas Gerais, Aguas Claras	MBR ¹	Lumps. Angular
MBL	"	"	MBR ¹	Lumps. Laminated
GUL	Guinea	Nimba Range	Lamco	Washed fines
LIL	Liberia	"	"	"
CCL	Canada	Wabush, Carol Lake	IOC ²	Pellet feed
RHP	Norway	Rana	Rana Gruber A/S	Hematite fines ³

1) Mineracoes Brasileiras Reunidas

2) Iron Ore Company of Canada

3) Taken from the dryer of Elkems Polar Process equipment in Mo i Rana

Brazil (MBA and MBL)

The second largest iron ore producer in Brazil is MBR (Mineracoes Brasileiras Reunidas) (Cooke and Bailey, 1987). The company runs several hematite mines and produces both fines for pelletizing, sinter fines, and lumps. We have received lumps of two different types from Aguas Claras Mine in the Minas Gerais district. These are named angular and laminated hematite. The company's output of lumpy ore was 2.9 mill. tonnes in 1985, that is 21% of MBR's total output (Cooke and Bailey, 1987). According to Caracas (private communication with the MBR company, 1987) the hematite is both granular and specular and occurs in compact, platy and powdery varieties.

The high-grade hematite deposits of Minas Gerais occur in the Cauè Itabirite which is a metamorphosed chemical sediment consisting mainly of banded hematite and quartz of Precambrian age (BIF). It is generally agreed that the hematite has replaced quartz to form large ore bodies of extraordinary purity.

The following description of the ore was given by Caracas (1987):
 "The Aguas Claras ore is a tabular lens of high-grade hematite and is made up of essentially soft hematite. The mine is 1650 m long, on average 250 m wide, and lies in a 200-350 m thick section of the Cauè Formation. Conformably enclosed in the soft hematite body there are lenses and beds of mixed and hard hematite, up to 30 m thick. It is believed that most of the soft ore was formed through supergene alteration of dolomitic itabirite frequently found to the south-east of the mine."

Dorr (1964, 1965) investigated the nature and origin of the iron ores of Minas Gerais and defined the following expressions:

high-grade hematite ore: ore containing more than 66% Fe on average and less than 1.5% water of crystallization
soft high-grade hematite: porous ore, density varies to as low as 3 g/cm³
hard high-grade hematite: dense and compact ore, density varies to more than 5 g/cm³ in the best.

Dorr concluded that all the significant high-grade hematite ores in the region are hypogene (contrary to supergene) in origin, formed by synmetamorphic metasomatic replacement of quartz in itabirite by hematite derived from the iron formation itself. Transportation of iron to and quartz from the formation was by fluids at high temperatures (350-600°C) and pressures. According to the opinion of Dorr, most high-grade soft ores were formed from the hard, but porous, high-grade hematite by supergene leaching of hematite.

Two-three generations of hematite occur in the ore (Dorr, 1965). The specular ore being the older and the granular ore the younger. Ore minerals include hematite (martite) with minor amounts of magnetite, goethite and maghemite (Caracas, 1987). Constituents other than hematite in the high-grade hematite ores are minor amounts of magnetite, quartz, gibbsite or boehmite, talc, kaolin, chrysotile, and probably apatite (Dorr, 1965). MBL (termed laminated) is the specular and MBA (termed angular) the granular ore, from the appearance of handpieces and lumps.

Liberia and Guinea (LIL and GUL)

The Nimba Range is a mountainous area in the border region between Liberia and Guinea in West Africa. Lamco operates iron mines on both sides of the border. The products being lumps (62.5% Fe), fines (64.3% Fe), and DR concentrate (66.7% Fe) (Cooke and Bailey, 1987). We have received washed fines from both Liberia and Guinea. About 97-98% of the washed fines was coarser than 63 μ m and 94-95% was coarser than 90 μ m. The company's output of washed fines was 6.7 mill. tonnes in 1985, which was 86% of their total output (Cooke and Bailey, 1987).

In the following a description is given of the high-grade hematite ores and their origin according to Berge (1974, 1977):

"The Main Orebody of the Nimba Range, northeast Liberia, was formed by alteration of grey itabirite (magnetite and quartz) of the Precambrian age Nimba Itabirite. The banded iron formation of the Nimba Itabirite is chemical sediments subsequently folded and metamorphosed, mainly an iron silicate formation, but with grey itabirite to northeast where the Main Orebody is located. The Main Orebody consists of hard, medium-hard and soft high-grade hematite (locally termed blue ores) and has a dual origin. **Hard** and **medium-hard** ores were formed through synmetamorphic alteration of the grey itabirite at moderate metamorphic temperature and pressure. **Soft** ores were formed from blue itabirite (hematite and quartz) through leaching of silica by postmetamorphic meteoric waters. The blue itabirite was formed by local oxidation of the grey itabirite. Elsewhere along the Nimba Range close to the surface there is goethite-martite brown ore formed by supergene leaching of silica from itabirite. Blue and brown ores are blended during mining and processing.

The blue ores of the Main Orebody consists almost entirely of anhedral hematite and martite with quartz as the only significant impurity. Anhedral hematite is by far the most common form of hematite, martite is of secondary importance, while specular hematite and goethite are rare in the blue ores. Both anhedral

hematite and martite have been developed by oxidation of magnetite. Remnants of magnetite are present in some few grains of hematite. Martite is distinguished from anhedral hematite by the extinction pattern of grain cross sections in polarized light in optical microscope.

Hard and medium-hard ore is compact, cemented or not, with a porosity of about 30% and a dominance of **anhedral hematite**. **Soft ore** has a dominance of **martite** with some quartz and reacts on handling as a sand.

Martite extinction pattern is characterized by a cross-hatched network of dark and light stripes at angles forming octahedra (lamellas).

Anhedral hematite extinction pattern shows an irregular patchwork of dark and light spots which form an anhedral mosaic."

Canada (CCL)

Carol Lake mine is situated in the Wabush iron ore district in the southwestern part of the Labrador province and is operated by the Iron Ore Company of Canada (IOC). The company owns several mines and the output in 1985 was 9.0 mill. tonnes of Carol Lake pellets and 5.4 mill. tonnes of Carol Lake concentrates (Cooke and Bailey, 1987). We have received Carol Lake pellet feed, of which approximately 25% is coarser than 63 μm and 13% is coarser than 90 μm .

The Upper Wabush Iron Formation consists 80% of specular hematite-quartz schist, the remaining being banded to massive magnetite-quartz rocks, while the Lower Iron Wabush Formation consists of quartz-carbonate-iron silicate schist and quartz-magnetite rock (Klein, 1966). Klein states that most Upper Wabush Iron Formation outcrops show little or no weathering.

The Wabush Iron Formation is of late Precambrian age and is thought to have deposited as a well banded chemical sediment which later has undergone regional mechanical and thermal metamorphose (Klein, 1966). According to Klein minimum pressure conditions have been approximately 600-1000 MPa (6000-10000 bar) and the maximum temperature has been below about 600°C. The mechanical metamorphism produced tight, overturned folds and

minor faulting. Accordingly the thermal metamorphism caused recrystallization of the original hematite, magnetite, and chert, to coarser grained specular hematite, magnetite, and quartz, along with reactions between chert and carbonates. The sedimentary textural features are still preserved.

The minerals present are mainly specular hematite which is medium to coarse grained and flaky in habit, magnetite, quartz, ferrodolomite-ankerite, and cummingtonite-grunerite (Klein, 1966).

Norway (RHP)

Rana mines is situated in Dunderlandsdalen at Mo i Rana and is run by the company Rana Gruber A/S, previously owned by Norsk Jernverk A/S. Both hematite and magnetite concentrates are produced. The company runs Ørtfjell and Storforshei mines and output in 1985 was 1.3 mill. tonnes concentrates (Cooke and Bailey, 1987). A hematite concentrate of the same quality as used in the Polar Process pilot plant in Mo i Rana in 1988 was applied in the present work. About 61% of this concentrate was coarser than 90 μm and 80% was coarser than 63 μm .

The ores are banded, metamorphic, of sedimentary origin, and occur in a sequence of marble and mica schists (Bugge, 1948). The banded structure is due to thin alternating bands of quartz and hematite or magnetite, the band heights being a few mm to more than one cm. Such banded iron formations constitute a characteristic common type (BIF), but they are generally of Precambrian age. The deposits of Dunderlandsdalen are younger, both a late Precambrian (800-900 mill. years) and a Cambrian-Silurian (408-570 mill. years) age have been suggested (Bugge, 1978). Whether they may be classified in this group or not is a question of controversy.

The hematite is usually specular, the lamellas being 0.1-1.0 mm long and 0.01 mm thick, but granular hematite, 0.2-1.0 mm across, occurs in minor amounts in small stringers in the ore (Bugge, 1978). The lamellas are always cleaved along the basal facies

(0001) (Bugge, 1948). Polysynthetic twins along (10 $\bar{1}$ 0) are common and these have probably been formed during deformation (Bugge, 1948). The gangue minerals of the hematite- and magnetite-dominated ores are quartz, calcite, epidote, biotite, green hornblende, grunerite, and a fluor-carbonate apatite with a MgO:CaO ratio of 1:10, while sulphur is present in pyrite and chalcopyrite in subordinate amounts (Bugge, 1978). In some hematite grains Bugge (1948) observed very small oriented lamellas of probably rutil or ilmenite.

4.3 Sample preparation

The hematites were used as received without further concentration. Lumps from Brazil were crushed. Large quantities (5-20kg) of each concentrate were screened, because only 2-20% of each concentrate was in the actual 63-90 μ m fraction. About 0.5kg was enough for further work. The 63-90 μ m fraction was also wet sieved on the 63 μ m screen and dried at 110°C. All the samples used for characterization of hematite concentrates were split from the 63-90 μ m fraction, if not otherwise indicated.

Polished surface sections were made by moulding these samples (split from the 63-90 μ m fraction) in epoxy. After hardening, the specimens were alternating polished and cleaned. The last polish was on a 1 μ m NAP-cloth.

4.4 Grain size distribution

Although the 63-90 μ m fractions have been sieved both dry and wet on the 63 μ m sieve, the size cut at 63 μ m was not efficient. Screen analyses of samples split from the 63-90 μ m fraction are shown in figure 4.1 and in table 4.2, and particle size distributions measured by sedigraph are shown in figure 4.2. In fact, 18-50% of the fractions passes the 61 μ m screen, and 32-50% of the fractions have equivalent spherical diameter less than 60 μ m. Efficient size cutting of large quantities, 5-20kg, is difficult.

The samples were oxidized for one hour in air at 800°C (heating and cooling were slow) before the measurements by sedigraph were carried out. This was done to avoid agglomeration of magnetite grains during settling, which will be registered as coarse particles. Magnetite grains may agglomerate due to their magnetic properties. Before measuring, the samples were also treated with ultra high frequency waves for 15 minutes. The effect of heat treatment on grain size was controlled by screen analyses, which are reported in table 4.3 and in figure 4.3. The changes are negligible. CCL have become a little coarser, while the other samples have become a little finer.

The cumulative mass percent less than the reported equivalent spherical diameter was calculated from the particle settling rate in a solution of 50% glycerol. The calculations are based on the mean density of each concentrate, which is reported in section 4.11. The accuracy of the grain size distributions by screen analysis is considered to be better than by sedigraph, since the concentrates contain hematite, magnetite, quartz, etc., which have different densities and settling rates. The mean grain size (d_{50}), of which 50 weight% is coarser, is ranging from about 61 μm for RHP to 82 μm for GUL, based on screen analysis.

Table 4.2 Screen analysis of the fractions 63-90 μm .

Sieve size (μm)	Cumulative % through sieve					
	RHP	GUL	LIL	MBA	MBL	CCL
104	100.0	100.0	100.0	99.4	99.9	100.0
74	62.5	32.0	45.1	60.2	44.3	51.2
61	50.4	17.7	29.7	44.5	30.4	31.9
45	4.6	0.0	0.0	0.9	0.3	0.1

Table 4.3 Screen analysis of the fractions 63-90 μm after heat treatment in air at 800°C (1h).

Sieve size (μm)	Cumulative % through sieve					
	RHP	GUL	LIL	MBA	MBL	CCL
104	100.0	100.0	100.0	100.0	100.0	100.0
74	66.1	34.8	49.1	64.8	50.8	49.1
61	49.2	17.4	30.9	48.1	31.1	30.9
45	4.0	0.0	0.0	1.8	1.6	0.1

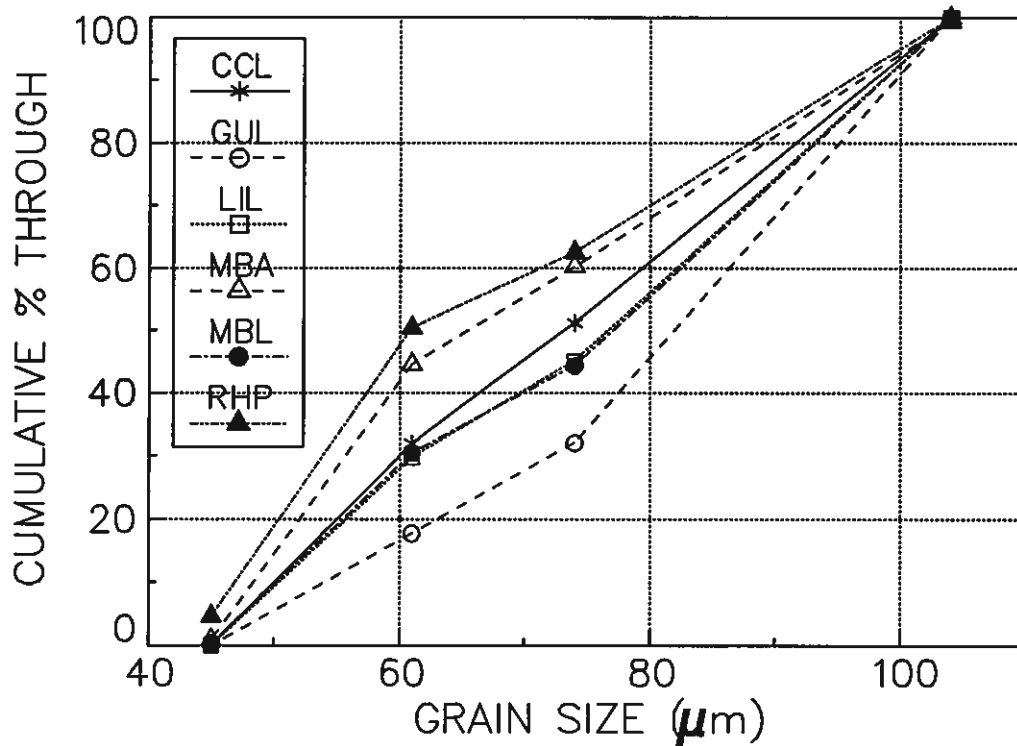


Fig. 4.1 Grain size distributions of the fractions 63-90µm of the hematite concentrates, measured by screen analysis.

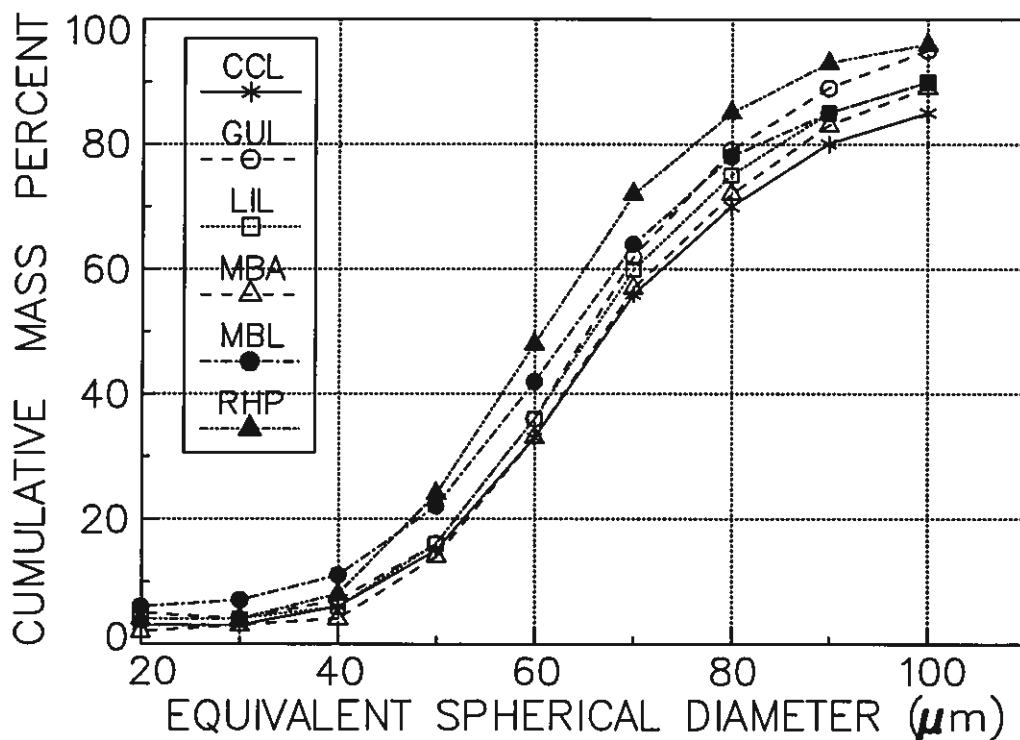


Fig. 4.2 Particle size distributions, measured by sedigraph, of the fractions 63-90µm of the hematite concentrates after heat treatment at 800°C for 1 hour.

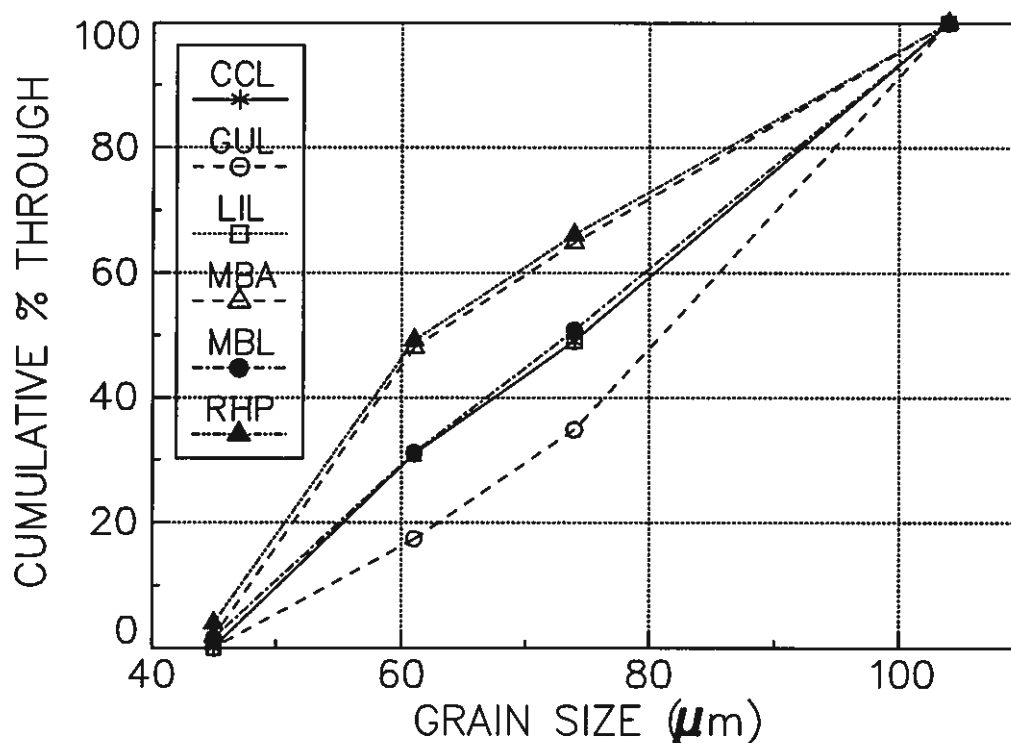


Fig.4.3 Grain size distributions of the fractions 63-90 μm of the hematite concentrates after heat treatment in air at 800 $^{\circ}\text{C}$ (1h), measured by screen analysis.

4.5 Chemical analysis

Chemical analyses of the 6 hematite concentrates, fraction 63-90 μm , were carried out at MOLAB and are presented in table 4.4. The table shows that all the concentrates have a high content of hematite. Especially high-grade are MBL, LIL, GUL, and MBA with 98.9, 98.4, 98.2, and 96.1% hematite, respectively.

Traces of magnetite are present in all the concentrates. CCL has a high magnetite content, 19.1%, while RHP contains 7.1%. Observations in optical microscope confirm these findings. Magnetite is present as separate grains in the concentrates CCL and RHP, while in MBL, MBA, GUL, and LIL the magnetite is present as inclusions in hematite. The lowest content of magnetite was found in MBL (0.4%).

Table 4.4 Chemical analysis of hematite concentrates, fraction 63-90 μ m.

	MBL (%)	MBA (%)	LIL (%)	GUL (%)	CCL (%)	RHP (%)
Fe ^{tot} 1	69.5	69.9	70.0	69.6	64.6	66.9
Fe ²⁺ 1	0.1	0.9	0.4	0.3	4.6	1.7
Fe ³⁺ (calc.) ²	69.4	69.0	69.6	69.3	60.0	65.2
Hematite (calc.) ³	98.9	96.1	98.4	98.2	72.6	88.4
Magnetite " ³	0.4	3.7	1.7	1.2	19.1	7.1
SiO ₂	0.01	0.51	0.44	0.63	5.4	1.83
TiO ₂	0.01	n.d.	n.d.	n.d.	< 0.10	0.89
Al ₂ O ₃	0.43	0.05	0.03	0.09	< 0.1	0.73
MnO	n.d.	n.d.	n.d.	n.d.	0.11	0.14
CaO	n.d.	n.d.	n.d.	n.d.	0.4	0.67
MgO	n.d.	n.d.	n.d.	n.d.	0.1	0.13
SO ₂ ⁴	n.a.	n.a.	n.a.	n.a.	0.022	0.018
C, total ⁴	n.a.	n.a.	n.a.	n.a.	0.58	0.08
CO ₂ ⁴	n.a.	n.a.	n.a.	n.a.	0.42	n.a.
P ₂ O ₅	0.027	0.110	0.057	0.043	n.a.	0.032
Sum oxides	99.8	100.5	100.6	100.2	<98.8	100.0

1) Determined by wet chemical analysis (referring to section 3.4.2)

2) $Fe^{3+} = Fe^{tot} - Fe^{2+}$

3) Assumption: Fe²⁺ is contained only in magnetite and Fe³⁺ is present in either hematite or magnetite: Fe³⁺ in hematite = Fe³⁺ - 2·Fe²⁺

4) Determined in a LECO-apparatus.

n.d. not detected

n.a. not analyzed

The contents of SiO₂ are high in CCL and RHP (5.4 and 1.8%, respectively), low in MBA, GUL, and LIL (about 0.5%), and especial low in MBL (0.01%). According to the previous description of the different ores, SiO₂ is probably mainly present as quartz in all the concentrates.

TiO₂ in RHP (0.89%) is probably present as ilmenite or rutil lamellas in the hematite grains as previously proposed by Bugge (1948). Traces of TiO₂ were also detected in MBL and CCL.

The reported content of Al₂O₃ is 0.7% in RHP and 0.43% in MBL, while the other concentrates contain less than 0.1%. According

to the literature referred to in section 4.2, Aluminium is probably present in mica (biotite), epidote, or hornblende in RHP, but in gibbsite/boehmite or kaolin in MBL.

Sulphur were detected as SO_2 in CCL and RHP, and is probably present in pyrite (FeS_2) and/or chalcopyrite (CuFeS_2). Bugge (1978) mentioned these minerals in the mineral assemblage of the Rana hematite/magnetite.

Phosphorous was found in all the hematite concentrates apart from CCL, in which phosphorous was not analyzed. Phosphorous is probably present in apatite, $\text{Ca}_5(\text{F,Cl,OH},0.5\text{CO}_3)(\text{PO}_4)_3$. According to literature referred to in the description of the ores, section 4.2, apatite is present in the mineral assemblage of MBA, MBL, and RHP. MBA has the highest level of P_2O_5 (0.11%) and MBL the lowest content (0.027%), contributing to approximately 0.27% and 0.07% apatite at a maximum, respectively.

CaO , MgO , and MnO were only detected in RHP and CCL. Some CaO is contained in apatite. The remaining content of CaO , MgO , and MnO in CCL and RHP are partly contained in carbonates because these concentrates contain carbon, 0.08% and 0.58%, respectively.

According to Klein (1966), the main gangue minerals in CCL are ferrodolomite-ankerite and cummingtonite-grunerite. If all the detected CO_2 (0.42%) in CCL is contained in ferrodolomite, $\text{Ca}(\text{Mg}_{0.5}\text{Fe}_{0.5})(\text{CO}_3)_2$, this would contribute to approximately 1.0% ferrodolomite. The remainder being 0.1% CaO , 0.1% MnO , and 0.47% free carbon.

In RHP about 0.04% CaO and 0.004% MgO are contained in apatite, according to the description of the flour-carbonate apatite by Bugge (1978). CaO , and MgO may be contained in calcite, biotite, hornblende, and/or epidote, in accordance with the observations by Bugge (1978), but the presence of dolomite-ankerite is also possible. Manganese may substitute for magnesium in dolomite-ferrodolomite-ankerite, but may also be contained in magnetite and hematite.

Typical uncertainties of the analyses are given in table 4.5.

Table 4.5 Typical uncertainties of the analyses.

	Conc. range (%)	Uncertainty (%)
Fe ^{tot}	60-68	±0.1
Fe ²⁺	0.5-15	±0.05-0.20
SiO ₂	1-7	±0.1-0.2
TiO ₂	0.2-0.8	±0.02-0.05
C	-	±0.01
S	-	±0.005
P	0.01-0.03	±0.002
Al ₂ O ₃	0.5-1.5	±0.05-0.10

The calculations of hematite and magnetite are based on the assumption that the complete amount of Fe²⁺ is present in magnetite and Fe³⁺ is contained in either hematite or magnetite. If some of the samples have other iron containing minerals, for example goethite (FeO·OH), ferrodolomite (CaMg_{0.5}Fe_{0.5}(CO₃)₂), siderite (FeCO₃), or iron silicates, the calculated amount of magnetite and hematite in table 4.4 should be adjusted accordingly. The hematite content of MBA is for example a little lower than indicated in table 4.4 because traces of goethite (which also contain Fe³⁺) were detected in optical microscope on a polished surface specimen.

4.6 Mineral phases by x-ray diffraction

Powder x-ray diffraction analyses (XRD) were carried out at NTH (the Norwegian Institute of Technology). An automatic powder diffractometer system from Phillips (PW 1700) was used at 40 kV and 20 mA. The x-ray source was Cu K_α radiation with 2 wavelengths, 1.54060 and 1.54439 Å. The samples were split from the fractions 63-90µm. They were not further crushed.

The diagrams are presented in figure 4.4a and 4.4b. The angle in degrees (2θ) on the abscissa in the diagrams is related to the d-spacing in the mineral crystals in accordance with Bragg's law given in formula 4.1 for the wavelength of the Cu K_{α} radiation ($\lambda=1.54060 \text{ \AA}$) where n is an integer.

$$n \cdot \lambda = 2 \cdot d \cdot \sin\theta \quad (4.1)$$

The detected minerals were mainly hematite in all the samples and minor amounts of magnetite in CCL and RHP. Quartz (SiO_2) was detected in CCL, RHP, and in GUL (traces). Quartz is probably present in small amounts below the detecting level also in MBA and LIL, referring to the chemical analyses. A few small peaks in the diagram of MBA indicate that traces of magnetite and goethite may be present. This is confirmed by chemical analysis and in optical microscope.

Traces of dolomite-ferrodolomite-ankerite were detected in CCL and RHP, based on the observed main peaks at $d=2.89$. Ferrodolomite is probably present in CCL (about 1% is possible, referring to section 4.5) in accordance with the observations by Klein (1966). About 0.6% dolomite may be present in RHP, if carbon is mainly contained in dolomite. According to Bugge (1948), calcite is common in the Rana hematite-magnetite ores. Calcite, however, has its main peak at $d=3.03$, which is a little too far from the observed peak at $d=2.89$. The d-values of the main peaks of dolomite, ferrous dolomite, and ankerite are 2.89, 2.90, and 2.90, respectively.

Traces of siderite (FeCO_3) were probably detected in CCL, based on another small peak at $d=2.78$. Siderite has its main peak at $d=2.795$ while the other peaks are 35% of the main peak, or less.

The peak at $d=4.81$ in MBL indicates that traces of gibbsite, $\text{Al}(\text{OH})_3$, are present. This is supported by chemical analysis. $\text{Al}_2\text{O}_3 = 0.43\%$ may as well be reported as $\text{Al}(\text{OH})_3 = 0.66\%$. A similar peak is observed in the diagram for GUL. Chemical

analysis gave $\text{Al}_2\text{O}_3 = 0.09\%$ or $\text{Al}(\text{OH})_3 = 0.14\%$ and support this observation, although contents as low as 0.1% are usually not detected by x-ray diffraction analyses.

The minerals detected by XRD are shown in table 4.6. Referring to the chemical analyses in section 4.5, the calculated content of some of the minerals are included in the table.

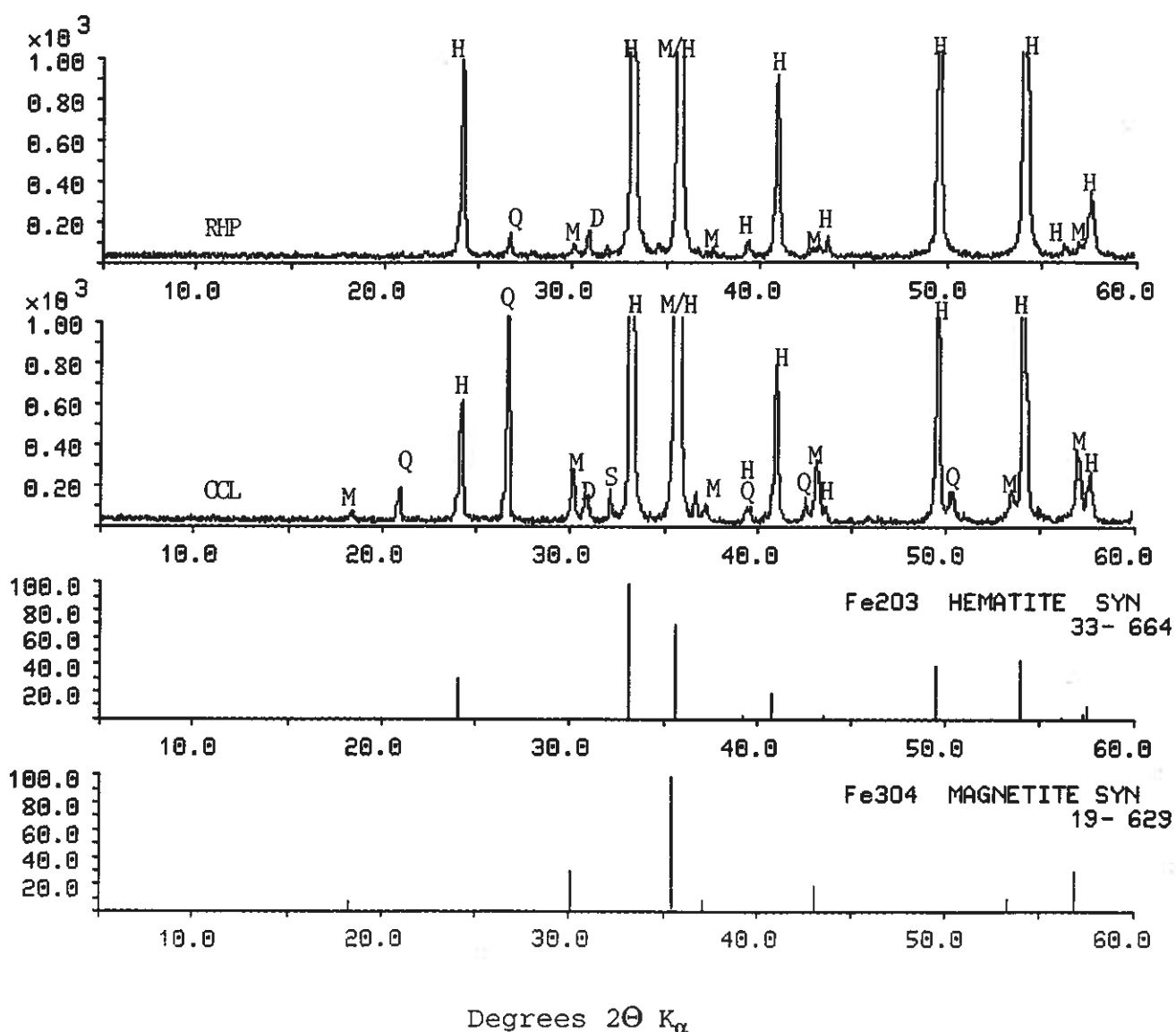


Fig. 4.4a X-ray diffraction diagrams of fraction 63-90 μm of the hematite concentrates RHP and CCL.
 H=Hematite M=Magnetite D=Dolomite/ankerite/
 Q=Quartz S=Siderite ferrodolomite

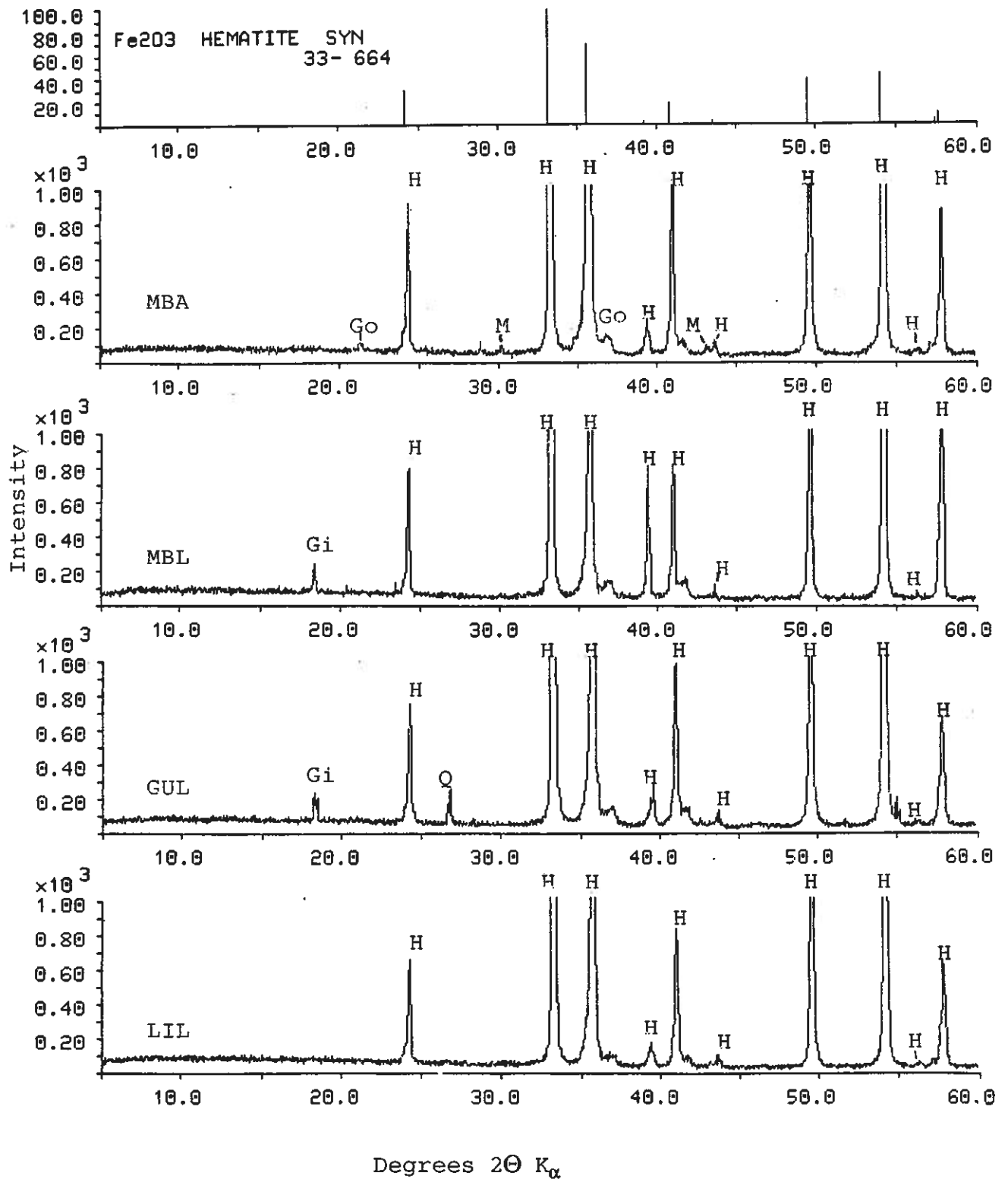


Fig. 4.4b X-ray diffraction diagrams of fraction 63-90 μ m of the hematite concentrates MBA, MBL, GUL, and LIL.
H=Hematite Gi=Gibbsite Q=Quartz
M=Magnetite Go=Goethite

Table 4.6 Minerals detected by XRD (xx and x¹).
The amounts are calculated from chemical analyses.

	Hematite 2) (%)	Magnetite 2) (%)	Quartz (%)	Gibbsite (%)	Goethite (%)	Ferro-/ Dolomite (%)	Siderite (%)
MBA	xx 96.1	x 3.7	0.5		x		
MBL	xx 98.9	0.4	0.0	x 0.7			
GUL	xx 98.2	1.2	x 0.6	x 0.1			
LIL	xx 98.4	1.7	0.4				
CCL	xx 72.6	xx 19.1	xx 5.4			x	x
RHP	xx 88.4	x 7.1	x 1.8			x 0.6	

- 1) xx identification by strong peaks
x traces, weak peaks
- 2) The content is calculated on the assumption that Fe²⁺ is contained only in magnetite and Fe³⁺ is contained in either hematite or magnetite. Fe³⁺ in hematite = Fe³⁺-2·Fe²⁺

The magnetite content is an important parameter in the characterization of the hematites. Minor amounts of magnetite in hematite is difficult to detect by XRD, because the second strongest peak of hematite coincides with the main peak of magnetite (see figure 4.4a). As previously mentioned, magnetite is present as separate grains in CCL and RHP and as inclusions in hematite in MBL, MBA, LIL, and GUL. According to the chemical analyses, all the concentrates contain some Fe²⁺. Other Fe²⁺-containing phases than magnetite have not been detected in the four last mentioned concentrates. Hence, the calculated contents of magnetite in tables 4.4 and 4.6 are correct for MBA, MBL, GUL, and LIL within the uncertainty of the determination of Fe²⁺.

The reason why magnetite was not detected by XRD in GUL, LIL, and MBL may be because the amount is below the detecting level or because the x-ray radiation did not reach the magnetite in the grain cores.

The calculated amounts of magnetite in RHP and CCL, on the other hand, are probably too high. In these concentrates other Fe²⁺-containing minerals have been detected. An estimation of the amounts of these minerals will be rather uncertain. In CCL traces of ferrodolomite and siderite were detected by XRD.

Pyrite or chalcopyrite are probably also present in small amounts below the detecting level. In RHP ferrodolomite-ankerite or dolomite have been detected by XRD. According to chemical analyses there is also a possibility for the presence of both ilmenite, pyrite or chalcopyrite, biotite, and hornblende, but in small amounts below the detecting level by XRD.

Rough estimates have been made for the contents of Fe^{2+} which may be contained in other minerals than magnetite. The estimates were less than about 0.55% Fe^{2+} in CCL (contained in siderite and pyrite) and less than 0.63% Fe^{2+} in RHP (contained in ilmenite and pyrite). These estimates were derived on the assumptions that the complete amounts of CO_2 and SO_2 detected in CCL are present in siderite and pyrite, respectively, and that the complete amounts of TiO_2 and SO_2 in RHP are present in ilmenite and pyrite, respectively.

Minor amounts of magnetite and maghemite ($\gamma\text{-Fe}_2\text{O}_3$) are difficult to distinguish both by x-ray diffraction analysis and in optical microscope.

4.7 Trace elements

Secondary Ion Mass Spectrometry (SIMS) is a sensitive technique for measuring trace elements in micro areas of material surfaces. The technique, equipment, procedure, and results were well described in a report by Storemyr (1989) where also a survey of the SIMS-literature was given. The semi - quantitative and the qualitative SIMS analyses were all conducted at Chalmers Institute of Technology in Gothenburg in Sweden using a Cameca IMS 3F instrument. Primary ions of O_2^+ with an energy of 5.5 keV and a primary current of 800 nA were bombarded on the samples. The main results of the 15 trace elements analyzed are presented in table 4.7.

Except the sample called RANA, the 5 other hematite concentrates

were taken from the 63-90 μ m fractions. RANA is from the same ore as RHP. The fraction 54-100 μ m of RANA was applied. Chemical analysis of RANA is given in the foot note in table 4.7.

Only 3-6 point analyses, usually on different grains, were conducted for each concentrate. The grains were embedded in indium - foil to ensure a good conducting "matrix". No polishing was involved. To obtain good results, a well controlled quantitative procedure should be applied. Several spot analyses should be carried out on one or different grains to get good statistical mean values since trace elements are not homogeneously distributed in the hematite lattice (Storemyr, 1989). Unfortunately the SIMS quantitative procedure followed was not accurate since only 3-6 point analyses were carried out for each concentrate. Hence, the results can only be regarded as semi-quantitative.

The quantitative procedure followed was based on RSF (Relative Sensitivity Factors) values for standard glass samples with known concentrations. Iron was used as an internal reference element. Matrix effects may affect the quantification as different matrices (glass and hematite) lead to different rates of sputtering. The SIMS results are included in the present investigation, despite the fact that they are rather uncertain. They may be used to compare the level of each trace element in the different concentrates to each other.

Table 4.7 shows that the variation for an element from ore to ore is usually less than two orders of magnitude. The concentration of each element is in mole ppm.

The semi-quantitative SIMS analyses of the hematite concentrates are compared with the chemical analyses in table 4.8. The absolute levels of trace elements are not accurate, because the calculations were based on RSF-values for standard glass samples while the different matrices, glass compared to hematite, may cause unequal sputtering rates of the different elements. In the

Table 4.7 Semi-quantitative SIMS analysis of hematite concentrates (Storemyr, 1989).

Element	Cal ¹	Element concentration (mole ppm)					
		MBL	MBA	LIL	GUL	CCL	RANA ²
Na	3	6	20	40	35	40	0.1
Mg	1.3	15	85	90	190	12	11
Al	1.5	1350	3300	1800	5000	1250	2800
Si	1.5	760	5100	2900	125	20	25
K	3.5	6	15	10	75	< 0.05	< 0.02
Ca	1.8	6	80	70	11	< 0.25	< 0.45
Sc	1.8	< 1ppm	< 1ppm	< 1ppm	< 1ppm	< 1ppm	< 1ppm
Ti	1.8	270	120	110	30	85	2850
V	1.3	100	50	15	30	44	200
Cr	1.4	150	16	240	23	10	95
Mn	1.2	430	215	245	265	100	65
Co	1.2	2	2	4	6	< 1	2
Ni	1.3	7	15	20	35	35	5
Cu	1.7	< 5	< 5	< 6	< 5	< 3	< 40
Zn	2	50	25	< 6	< 8	25	< 300

- 1) Calibration uncertainty factor. A factor of 1 is a quite certain analysis while a factor of 2.0 means that there is a 100% uncertainty. The factors have been obtained when comparing RSF-values measured in different SIMS-laboratories.
- 2) Chemical analysis: Fe^{tot}: 68.6%, Fe²⁺: 0.8%, SiO₂: 0.8%, TiO₂: 0.75%, Al₂O₃: 0.3%, MnO: 0.08%, CaO: 0.1%, MgO: 0.1%.

calculations it is assumed 100% hematite matrices, which is approximately correct for the concentrates MBL, MBA, GUL, and LIL, but which may be too high for CCL and RANA.

In most cases lower contents of the different oxides are detected by SIMS than by chemical analyses, referring to table 4.8. This may reflect that these oxides are contained in separate inclusions and not in the hematite lattice. In some cases the SIMS analyses give the highest values, which may indicate an uneven distribution of the respective elements in the hematite lattice. The SIMS analyses provide poor statistical results for unevenly distributed elements, since only 3-6 point analyses were carried out for each concentrate. Too high levels by SIMS analysis may indicate that the elements are present in tiny

Table 4.8 Semi-quantitative SIMS analysis of hematite concentrates compared to chemical analysis.

		(weight%)					
		MBL	MBA	LIL	GUL	CCL	RANA
SiO ₂	chemical	0.01	0.51	0.44	0.63	5.4	0.8
	SIMS	0.057	0.38	0.22	0.0094	0.0015	0.0019
	SIMS/chem.	5.7	0.7	0.5	0.01	0.0003	0.002
TiO ₂	chemical	0.01	n.d.	n.d.	n.d.	< 0.10	0.75
	SIMS	0.027	0.012	0.011	0.0030	0.0085	0.29
	SIMS/chem.	2.7	-	-	-	>0.09	0.4
Al ₂ O ₃	chemical	0.43	0.05	0.03	0.09	< 0.1	0.3
	SIMS	0.086	0.21	0.11	0.32	0.080	0.18
	SIMS/chem.	0.2	4.2	3.8	3.5	>0.8	0.6
MnO	chemical	n.d.	n.d.	n.d.	n.d.	0.11	0.08
	SIMS	0.038	0.019	0.022	0.023	0.0089	0.0058
	SIMS/chem.	-	-	-	-	0.08	0.07
CaO	chemical	n.d.	n.d.	n.d.	n.d.	0.4	0.1
	SIMS	0.0004	0.006	0.005	0.0008	0.00002	0.00003
	SIMS/chem.	-	-	-	-	0.00004	0.0003
MgO	chemical	n.d.	n.d.	n.d.	n.d.	0.1	0.1
	SIMS	0.0008	0.004	0.005	0.01	0.0006	0.0006
	SIMS/chem.	-	-	-	-	0.006	0.006

n.d.: not detected

inclusions which are not homogeneously distributed. Too high levels may also have been caused by matrix effects.

Two concentrates are much lower in K and Ca than the others, RANA and CCL, but according to bulk chemical analyses the CaO-contents of the same two concentrates are the higher. This indicates that Ca is distributed in the hematite grains or in finely distributed apatite in the hematite grains in MBA, MBL, GUL, and LIL, whereas Ca is mainly found in separate inclusions as for example in dolomite-ferrodolomite in RANA and CCL.

The same relation is also observed for the elements Mg and Mn for the two concentrates CCL and RANA. According to bulk chemical analyses the contents of both MgO and MnO are approximately 0.1% in CCL and RANA (and RHP) while MgO and MnO were not detected in the other concentrates. However, the same two concentrates have the lowest level of Mg and Mn according to the SIMS analysis. Mg and Mn are probably mainly contained in separate inclusions

in CCL and RANA (and RHP), in for example dolomite-ankerite, while these elements probably are mainly distributed in the hematite lattice in the other samples. The Mn concentration is about twice as high in MBL as in GUL, LIL, and MBA. The Mg concentration is 6-12 times lower.

According to chemical analyses, the highest contents of SiO_2 were found in CCL (5.4%), RHP (1.83%), and GUL (0.63%). XRD proved this SiO_2 to be quartz. According to the SIMS analyses, however, the concentrates CCL, RANA, and GUL have the lowest level of Si (20, 25, and 125 mole ppm, respectively). Once more Si is thought to be distributed in the hematite lattice in relatively high concentrations in MBA (5100 mole ppm), LIL (2900 mole ppm), and MBL (760 mole ppm), but it may also be contained in finely divided inclusions, while it is mainly found in separate quartz grains or large inclusions in the other concentrates.

RANA has by far the highest content of TiO_2 of the concentrates according to chemical analyses (0.75%) and does also have an order of magnitude higher level of Ti (2850 mole ppm) according to SIMS analyses. The second highest Ti concentration, about twice as high as in MBA and LIL, is found in MBL (270 mole ppm). TiO_2 was found to be 0.01% by chemical analysis. Only 85 mole ppm Ti was detected by SIMS in CCL, although Ti was verified also by chemical analysis.

Other elements as Na, Co, Ni, Cu, and Zn are present at low concentration levels. The Na level is especially low in RANA. Aluminum, however, is present at comparatively high concentration levels in all the concentrates according to the SIMS analysis. There does not seem to be any relation between the amounts of Al detected by chemical analyses and the concentration levels found by SIMS, but the amounts are of comparable sizes for CCL and RANA. This may reflect a homogeneous distribution of Al for these two concentrates and an uneven distribution for the others.

The concentration of Cr was found to be about an order of magnitude higher in LIL, MBL, and RHP (240, 150, and 95 mole ppm,

respectively) than in the other concentrates.

Ion micrographs of 2 grains of the RANA hematite (Storemyr, 1989) confirm that elements as Na, Mg, Mn, Ca, and Si are concentrated in separate inclusions on the grain surfaces. Some Mg, Mn, and Si, are also homogeneously distributed in the grains. Al, Sc, Ti, and Cr are homogeneously distributed in the grains, but Al shows depletion along a few "lineaments" where there is also an increased concentration of Cr, Ti, and V. The concentration level of Ti differ for the two grains.

4.8 Specific surface area

The specific surface areas of the six hematite concentrates were measured by the BET isothermal adsorption method. Krypton was used instead of nitrogen because small specific surface areas were expected to be found. Specific surface area of hematite spheres with a specific gravity of 5.24 g/cm^3 and a diameter of $63 \text{ }\mu\text{m}$, can be calculated to $0.018 \text{ m}^2/\text{g}$. The measurements were carried out with a Carlo Erba Sorptomatic 1800, which was evacuated to $p < 10^{-4} \text{ mmHg}$ at 150°C for one hour before measuring. The BET method is described in textbooks about heterogenous catalyses, for example the textbook by Satterfield (1980). The results are given in table 4.9 and in figure 4.5. The standard deviation of such measurements is $\pm 5\%$.

Table 4.9 Specific surface area of $63\text{-}90\text{ }\mu\text{m}$ fractions.

	Specific surface area (m^2/g)
GUL	0.73 ± 0.04
MBL	0.50 ± 0.03
LIL	0.37 ± 0.02
MBA	0.34 ± 0.02
CCL	0.22 ± 0.01
RHP	0.057 ± 0.003 0.061 ± 0.003

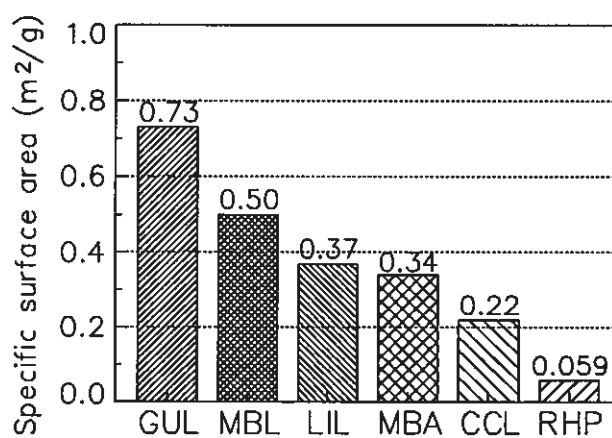


Fig. 4.5 Specific surface area

Surface areas of GUL and MBL are about 40 and 28 times larger than calculated, respectively, while those of LIL and MBA are approximately 20 times larger. The most striking feature is the small surface area of RHP compared to the others ($0.059 \text{ m}^2/\text{g}$, only 3 times larger than calculated). The specific surface area of RHP was measured twice and the obtained values, 0.057 and $0.061 \text{ m}^2/\text{g}$, lie within the said standard deviation.

Although the shape of the particles deviates from the shape of a sphere, surface ruggedness is probably the main reason for the large surface areas of GUL, MBL, LIL and MBA. The surfaces of these concentrates look rugged in the stereo microscope, while the surfaces of RHP and CCL look smooth and rather smooth, respectively. The samples contain pores and/or cracks, except perhaps RHP, referring to the photos of grain sections in section 4.9. Pores are dominating in the grains of GUL and LIL and pores are present in MBL, too. Some cracks are observed in all the samples, but MBL has the most.

The presence of undersize will contribute to a slightly larger surface area. About 50% of RHP is $-61\mu\text{m}$, and only 18% of GUL, referring to the screen analyses in section 4.4.

4.9 Subgrain structure

Subgrain structures of natural hematites are presented in figures 4.6 and 4.7. All photos were taken in a Leitz Wetzlar optical microscope in polarized light on polished sections. Only pure hematite grains are shown on the photos. The different white to grey to dark shadows represent the subgrains or twin planes which appear in polarized light because of the anisotropic structure of hematite.

The grains of CCL do not have any subgrains, as shown in figure 4.6a. The subgrain size equals the grain size. According to Klein (1966) maximum temperature during metamorphism at the formation of the ore was approximately 600°C and minimum pressure

was 600-1000 MPa (6000-10000 bar). In section 3.4 the effect of oxidation temperature on the subgrain structure of hematite is demonstrated for hematite oxidized from Sydvaranger magnetite. The grains of the 63-90 μm fractions were shown to consist of several subgrains at the lowest oxidation temperature (800°C). The fact that CCL (63-90 μm) has no such subgrains, although the formation temperature probably did not exceed 600°C, may reflect the prolonged time at temperature or the extreme pressure conditions during the formation. The lack of subgrain structure of CCL can also indicate that this ore was not formed from magnetite, in accordance with Klein's theory of its formation, as previously described in section 4.2.

The majority of the grains of RHP are rather equal to the grains of CCL, but some RHP grains have twin planes as shown in figure 4.6b. Twins are common and have probably been formed during deformation (Bugge, 1948).

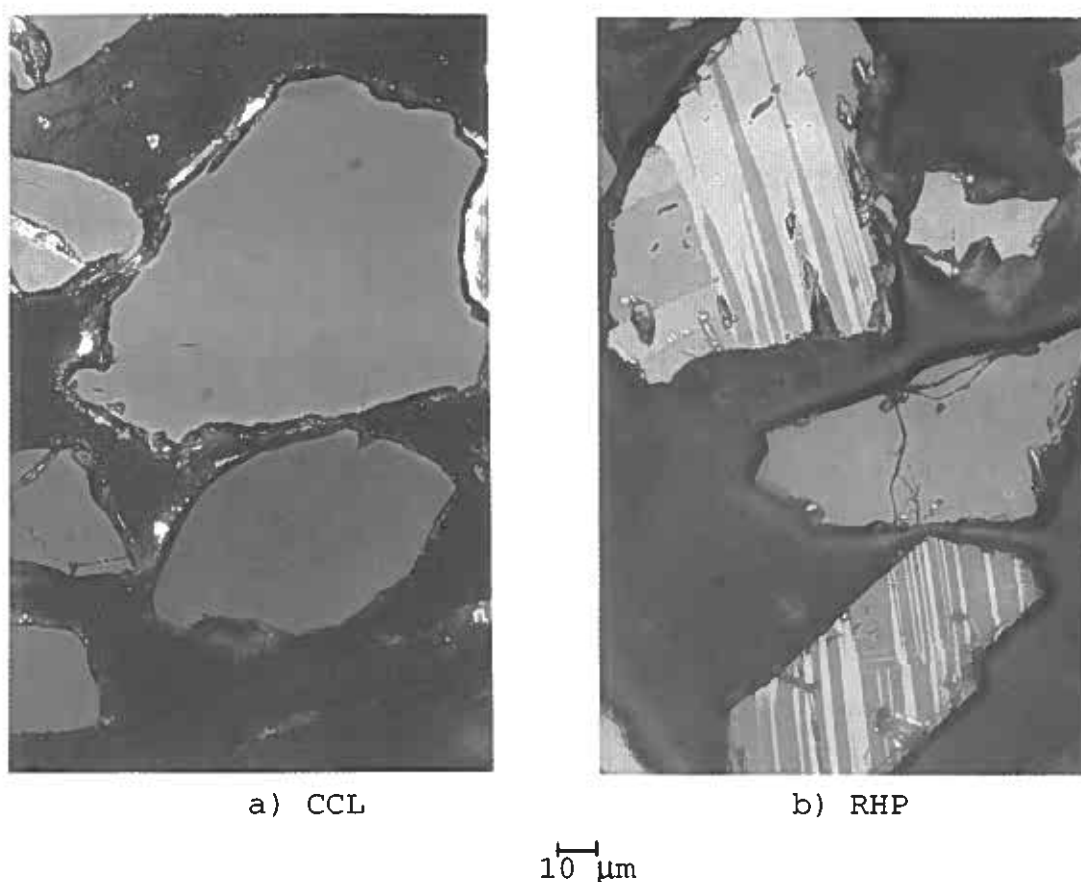
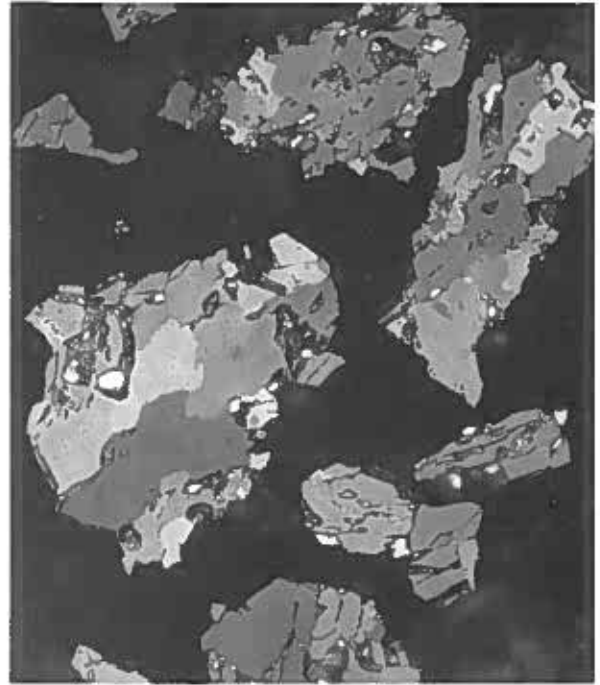


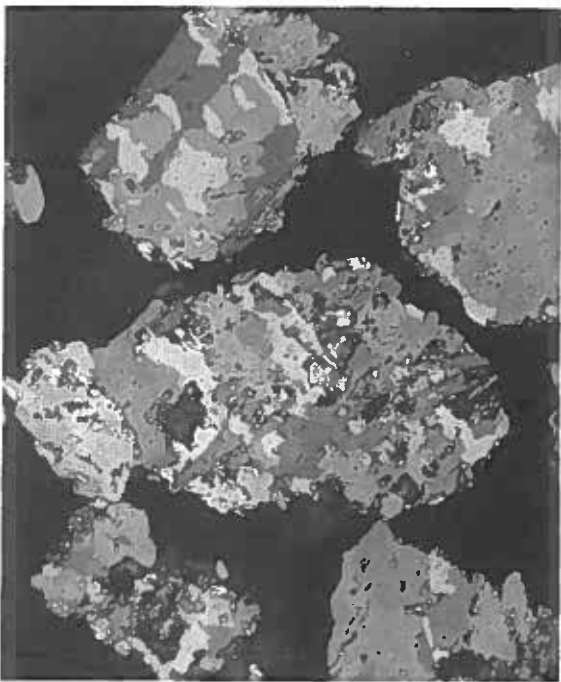
Fig. 4.6 Subgrain structure of CCL and RHP in polarized light.



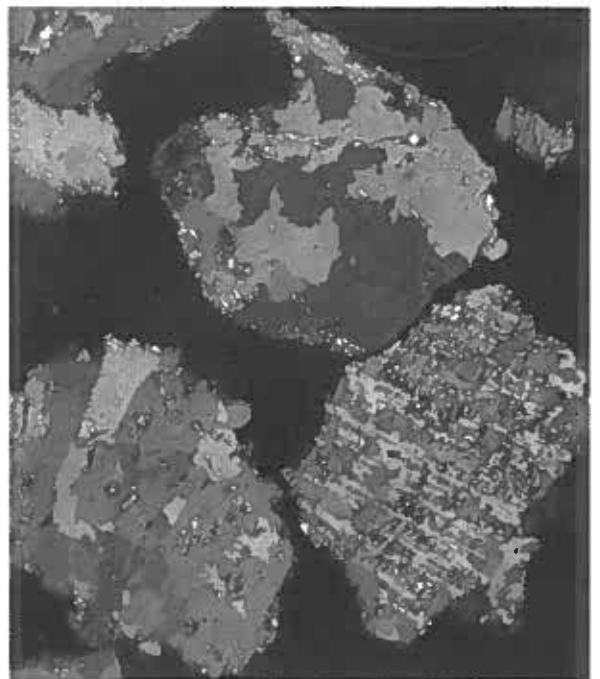
a) MBL



b) MBA



c) LIL



d) GUL

10 μm

Fig. 4.7 Subgrain structure of MBL (a), MBA (b), LIL (c) and GUL (d) in polarized light.

The subgrain structures of MBL, MBA, LIL, and GUL are shown in figure 4.7. Each of these grains consists of several subgrains. The subgrains of LIL and GUL have mainly an anhedral structure (lack of crystal shape), but a few grains have a martitic extinction pattern as shown in the grain to the right in figure 4.7d. LIL and GUL have probably been formed by oxidation of magnetite (grey itabirite) according to Berge (1974 and 1977). These concentrates do also show subgrain structures similar to those observed when oxidizing magnetite in section 3.4.3, but the anhedral shapes of the subgrains are far more common.

The subgrain shapes of MBL and MBA are more well developed than for LIL and GUL, and may be characterized as subhedral to euhedral. MBL has probably the best developed subgrain crystal shape of the two. This ore is also the older.

The impression of the subgrain structure was visualized by measuring the sum of internal subgrain boundaries divided by the grain area in section (SBA) on 10 grains, if not otherwise indicated. The measuring method and the videoplan used were described in greater detail in section 3.5.2. The mean values and the standard deviation ($\pm(\sum(x_i-x)^2)^{1/2}/(n-1)$, according to a standard distribution) are given in table 4.10.

Table 4.10 Subgrain structure of hematite concentrates, measured by videoplan¹

Polished surface specimens of (fraction 63-90 μ m)	SBA (m/m ²)
GUL	(1.48 \pm 0.19)*10 ⁵
MBL	(1.05 \pm 0.16)*10 ⁵
LIL	(0.97 \pm 0.09)*10 ⁵
MBA	(0.56 \pm 0.13)*10 ⁵
RHP ²	(0.46 \pm 0.18)*10 ⁵
CCL	0

- 1) 10 grains were measured on each polished surface, except on RHP for which 14 grains were measured.
- 2) Boundaries between twin planes, only.

From the table it is seen that GUL have the highest SBA value, while MBL has the second highest. The SBA value is of course zero for CCL because its subgrain size equals the grain size. The SBA measure for RHP is an exception as the boundaries measured are boundaries between twin planes. For this sample the investigation was expanded to 14 grains, because of variation from grain to grain. Some grains have several twin planes, some have only one, but the majority has none. In calculating the standard deviation for RHP, n is used instead of $n-1$. All the same, the standard deviation is rather huge, 39% of the value.

The standard deviations for the others are 9-23% of the values. Compared with equal SBA values for preoxidized magnetite in section 3.5.3, the standard deviations are approximately of comparable sizes, except for GUL. The standard deviation for GUL is twice as high (13%) as for S5 (oxidized at 1104°C).

Naturally one would expect a larger standard deviation for natural hematites than for carefully oxidized magnetite, since the conditions they have been exposed to may vary within the same ore both with respect to temperature and pressure.

The results are summarized in figure 4.8, where the subgrain structure of natural hematite concentrates are compared with the SBA curve for preoxidized magnetite (described in section 3.5).

Referring to figure 4.8, all natural hematites have rather low SBA values, corresponding to elevated oxidation temperatures (1100°C or above) for preoxidized magnetite. Since natural hematites have been exposed to high pressures and a prolonged time at temperature, the temperature axis of the SBA curve should not be used to predict a maximum temperature which the natural hematites have been exposed to. Effects of pressure and a prolonged time at temperature on the subgrain structure have not been studied in the present work. In addition some of these hematites may not have been formed from magnetite.

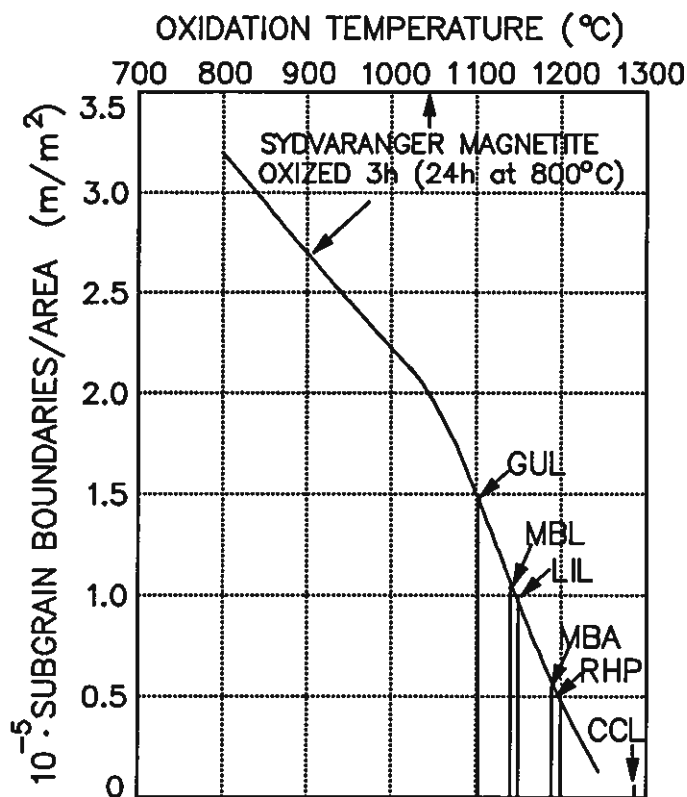


Fig. 4.8 Subgrain structure of natural hematite concentrates compared to the SBA curve for preoxidized magnetite.

4.10 Grain shape

The grain shape was characterized by a shape factor and an elongation factor, which are not independent variables.

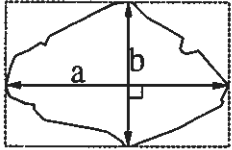
The shape factor (ψ) was measured by videoplan on polished surface specimens according to the method described in section 3.5.2 and defined according to formula 3.31 where A is the grain area in section and L is the periphery.

$$\text{Shape factor: } \psi = \frac{4 \cdot \pi \cdot A}{L^2} \quad (3.31)$$

According to this formula the shape factor of a sphere with a smooth surface is 1. All other shapes, including rugged surfaces, have shape factors below 1.

The shape factor is a combined measure for both the actual grain shape and the surface ruggedness. Both large specific surface areas and elongated particles give low shape factors.

The elongation of the particles was for this reason measured separately. The ratio of the particle length (major axis, a) to the width (minor axis, b) was measured and here called the elongation factor as defined by formula 4.2. The elongation factor is a true measure of shape.

$$\text{Elongation factor} = \frac{a}{b} \quad (4.2)$$


The diagram shows an irregular, roughly oval-shaped particle enclosed in a dashed rectangular box. Two perpendicular double-headed arrows are drawn across the particle. The horizontal arrow is labeled 'a' and represents the major axis (length). The vertical arrow is labeled 'b' and represents the minor axis (width). A small square symbol at the intersection of the two arrows indicates they are perpendicular.

The shape factor and the elongation factor were measured for 10 grains on each polished surface, except on RHP for which 14 grains were measured. The average values and the standard deviations are reported in table 4.11 for the six hematites.

Table 4.11 Elongation factor and shape factor

Samples	Elongation factor	Shape factor
RHP	2.2 ± 1.0	0.55±0.03
CCL	2.0 ± 0.9	0.58±0.05
MBL	1.7 ± 0.5	0.44±0.05
MBA	1.5 ± 0.4	0.43±0.04
LIL	1.5 ± 0.2	0.46±0.04
GUL	1.3 ± 0.4	0.50±0.04

The deviation from a sphere with a smooth surface is rather large for all the hematites, the shape factors being between 0.43 and 0.58. The standard deviations are ±(5-11)% of the values. For comparison, the shape factor for oxidized magnetite was found to be 0.66±0.03 in section 3.5.3.

Referring to the elongation factors in table 4.11, the concentrates RHP, CCL, and MBL contain the most elongated particles. As previously mentioned, these ores are all called specular in the literature (section 4.2). CCL and RHP have the highest mean elongation factors (2.0-2.2). The grain shapes of the two have a wide distribution, shown by the large standard deviations, $\pm 0.9-1.0$.

MBA, LIL, and GUL have low elongation factors, 1.3-1.5, being more spherical. These ores have been described as granular (MBA) and anhedral in the literature. These elongation factors have low standard deviations, $\pm 0.2-0.4$.

A graphical presentation of the shape factors and the elongation factors is given in the figures 4.9 and 4.10, respectively. The shape factor and the elongation factor are not independent variables. A schematic relation between grain shapes, elongation factors and shape factors is shown in figure 4.11.

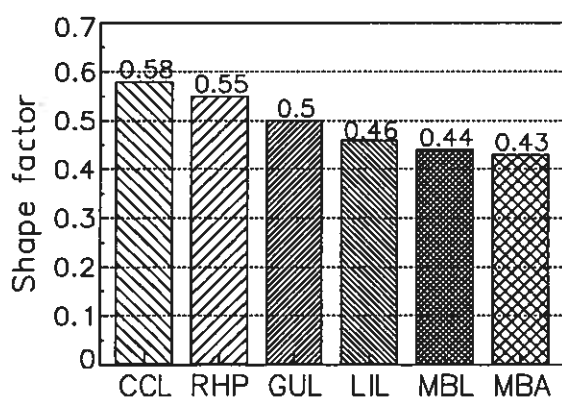


Fig. 4.9 Mean shape factor of natural hematite concentrates

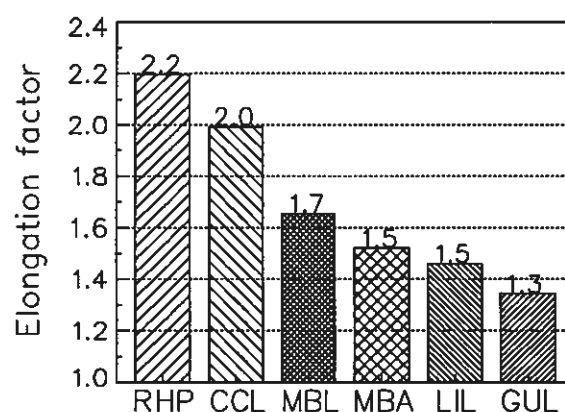


Fig.4.10 Mean elongation factor of the hematite concentrates.

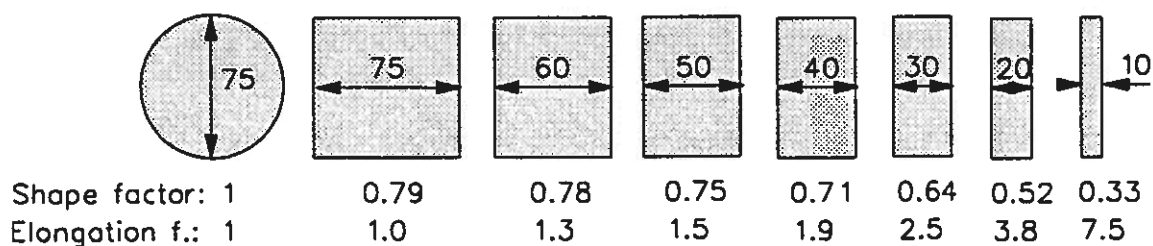


Fig. 4.11 Schematic relation between grain shape and factors.

The concentrates have smaller shape factors than what is expected from their elongation factors, because their rugged grain surfaces also result in small shape factors. Elongated grains have small shape factors, as shown in figure 4.11, but small shape factors do not necessarily imply elongated grains. Grains with highly rugged surfaces have relatively long perimeters (L) compared to the area in section (A), also resulting in small shape factors. The very small shape factors of MBA, MBL, LIL and GUL (0.43-0.50) can mainly be attributed to their large specific surface areas. Small differences between these mean shape factors, in the range of the standard deviations, $\pm 0.03-0.05$, can be disregarded.

The shape factors of RHP and CCL (0.55-0.58) are in fact rather small, which may largely be attributed to the elongated grains of the two concentrates, since their grains have rather smooth surfaces. Specific surface areas, elongation factors and shape factors are presented together with other physical characteristics in table 4.13 in section 4.12.

4.11 Porosity

Estimates of the closed pore volume in the grains of each concentrate were derived from the measured densities compared with theoretical densities based on chemical analyses. Open porosity of ore lumps was calculated from measured bulk density.

Mean densities of the concentrates were measured in a Beckman, Air Comparison Pycnometer, model 930. Each sample (50 g) was split from the 63-90 μm fraction. The samples were not crushed before the measurements. The results are shown in table 4.12.

The mean density of CCL is much lower than for the other concentrates. This can be explained by its high content of SiO_2 (5.4%). Specific gravity of SiO_2 is only 2.65 g/cm³, while specific gravity of hematite and magnetite is 5.24 and 5.18 g/cm³, respectively. Accordingly, the density of RHP is second lowest because of its second highest SiO_2 content (1.8%).

The density is lower than theoretical for the high-grade concentrates, too, indicating the presence of closed pores and cracks. From the chemical analyses (and XRD analyses) of MBL, MBA, GUL, and LIL, a theoretical density of approximately 5.22 g/cm³ was calculated. Estimates for their closed pore volumes were made and found to be about 1% for MBL and MBA and about 2% for GUL and LIL, referring to table 4.12. Correspondingly, RHP was found to contain about 0.7% of closed pores or cracks. An estimate for CCL is not reported, because the chemical analysis of CCL only reaches 98.8%, and because a high content of foreign minerals makes an estimate very uncertain.

Open porosity of handpieces or ore lumps was calculated according to formula 4.3 in which ρ_c is the density of the concentrates. The weight of 3-4 lumps of each ore was recorded. The volume was determined in mercury by measuring the weight increase on submerging each lump. The bulk density (ρ_b) of the lumps were calculated. The results are included in table 4.12.

$$\text{Open porosity: } \frac{\frac{1}{\rho_b} - \frac{1}{\rho_c}}{\frac{1}{\rho_b}} \cdot 100\% \quad (4.3)$$

Table 4.12 Porosity and density of concentrates and lumps

	Concentrates		Lumps	
	Density (ρ_c) (g/cm ³)	Closed porosity (%)	Bulk density (ρ_b) (g/cm ³)	Open porosity (%)
MBL	5.15	1	5.01 ± 0.03	2.7 ± 0.6
MBA	5.17	1	5.00 ± 0.08	3.3 ± 1.6
GUL	5.10	2	3.75 ± 0.03	26.5 ± 0.6
LIL	5.13	2	3.34 ± 0.05	34.9 ± 0.9
CCL	4.89	-	4.51 ± 0.05	7.8 ± 1.0
RHP	5.07	0.7	-	-

The high open porosity of the ore lumps of GUL and LIL (26.5 and 34.9%, respectively), is in accordance with the description of the ores in section 4.2. Hard and medium-hard ores were reported to have about 30% porosity and a dominance of anhedral hematite.

Contrary, the ores of MBA and MBL are massive with only about 3% open porosity. This is in accordance with the description in section 4.2 of the hard high-grade hematite ores in Brazil. Hard high-grade hematite was described as dense and compact ore. Bulk density could reach 5 g/cm³ at the best.

The higher contents of closed pores in the grains of LIL and GUL (having about 2% closed porosity) than in the grains of the other concentrates (1% or less), are reasonable from the high porosity of the lumps (25-35%).

4.12 Table of physical characteristics

Table 4.13 presents the main physical characteristics of the natural hematite concentrates, which previously have been discussed in this chapter.

Table 4.13 Physical characteristics of the hematite concentrates.

Physical properties	Concentrate					
	MBL	MBA	LIL	GUL	RHP	CCL
Specific surface area (m ² /g)	0.50	0.34	0.37	0.73	0.059	0.22
Mean grain ¹ size d ₅₀ (μm)	77	66	77	82	61	73
Shape factor	0.44	0.43	0.46	0.50	0.55	0.58
Elongation factor	1.7	1.5	1.5	1.3	2.2	2.0
SBA · 10 ⁻⁵ (m/m ²)	1.05	0.56	0.97	1.48	0.46 ²	0
Closed grain porosity (%)	1	1	2	2	0.7	-
Grain or subgrain shape	specular laminated euhedral	granular euhedral-subhedral	anhedral	anhedral	specular	specular

- 1) Mean grain size by screen analysis; the size of which 50 weight% is coarser
 2) Boundaries between twin planes, only

5 PREREDUCTION

5.1 Introduction

This chapter deals only with **gaseous** reduction of hematite. As previously pointed out in chapter 1, it is considered a great advantage for the Elkem Polar Process if (initial) reduction rates for hematite concentrates could be predicted by raw material characterization. Reduction kinetics is here studied both for natural hematite concentrates and for "artificial" hematite concentrates made by complete oxidation of Sydvaranger magnetite at different temperatures. A possible influence of the preoxidation conditions on the reduction rate is also investigated. The natural hematites have been characterized in chapter 4 and the "artificial" hematites have been described in sections 3.4 and 3.5. Since reduction rates of the different hematite concentrates should be compared for equal grain sizes, only fraction 63-90 μ m of the concentrates has been used in all the prerelution experiments.

All the reduction experiments have been carried out at constant temperature in the previously mentioned laboratory scale reactor developed by SINTEF and Elkem to simulate reduction of concentrates during pneumatic transport. This reactor has a maximum operating temperature of 850°C, limited by the steel quality it is made of. The reduction experiments in the present work have been carried out at moderate temperatures in the range 700-850°C. Experiments have been carried out for 12-60 seconds in batches and each batch has been chemically analyzed. Because of material loss during the experiments a practical limit of 60 seconds have been set for the length of each experiment.

Reducing gas mixtures, initially consisting of CO, CO₂, and H₂ were used. A Ni-catalyst was installed to provide equilibrium for the water-gas shift reaction (WGSR);



The water-gas shift reaction does not change the %RO (the oxidizing potential of the reduction gas), but merely shifts the

oxygen atom between the two reducing gases, H₂ and CO.

The %RO was defined in section 2.2 according to formula 2.3. This quantity is indeed useful because %RO and %CO₂ in the initial gas mixture are identical, as shown in equation 5.1a. A hydrogen balance gives equation 5.1b.

$$\%RO = \frac{P_{H_2O} + P_{CO_2}}{P_{H_2O} + P_{CO_2} + P_{H_2} + P_{CO}} \cdot 100\% \quad (2.3)$$

$$\%RO = \%H_2O + \%CO_2 = \%CO_2^o \quad (5.1a)$$

$$\%H_2^o = \%H_2 + \%H_2O \quad (5.1b)$$

$\%CO_2^o$ = initial CO₂ content prior WGSR equilibrium

$\%H_2^o$ = initial H₂ content

The degree of oxidation is a measure of the oxygen content of the sample compared to pure hematite and it is defined according to formula 5.2. Reduction proceeds from hematite (OX%=100%), to magnetite (OX%=89%), to wüstite (OX%=67-72%), to iron (OX%=0%).

$$OX(\%) = \frac{1.5 \cdot Fe^{3+}(\%) + Fe^{2+}(\%)}{1.5 \cdot Fe^{tot}(\%)} \cdot 100\% \quad (5.2)$$

The results of the chemical analyses are included in sections 5.4-5.6 and in appendix A.3. Optical microscope observations are included in the discussion in sections 5.8 and 5.9. **For a quick understanding of tables and figures it is important to notice the degree of oxidation (OX) and the %RO.** A plan for the hematite reduction was shown in table 1.1. The same table, together with the calculated gas composition for a WGSR in equilibrium at the different temperatures, is presented in table 5.1. Equilibrium constants for the WGSR in table 2.3 were used in the calculations. The gas composition is defined when %RO and the initial H₂ content are given. Most of the experiments have been carried out at 20, 35, or 50%RO with 35%H₂ in the inlet gas. The H₂ content was also varied (0-45%), but the gas composition was kept constant during each experiment.

Table 5.1 Experimental plan for the prereduction of hematite.

Temperature (°C)					RO (%)			H ₂ in inlet gas (%)					Reduction time (s)						Equilibrium ¹ composition (%)				
700	730	760	800	850	20	35	50	0	15	25	35	45	12	20	30	35	40	50	60	H ₂	H ₂ O	CO	CO ₂
		x			x						x		x	x		x	x	x	28.1	6.9	51.9	13.1	
		x				x					x		x	x		x		x	23.1	11.9	41.9	23.1	
		x					x				x		x	x		x		x	18.2	16.8	31.8	33.2	
		x			x			x					x						0	0	80.0	20.0	
		x			x				x				x						12.0	3.0	68.0	17.0	
		x			x					x			x						20.1	4.9	59.9	15.1	
		x			x						x		x						36.2	8.8	43.8	11.2	
		x					x	x					x						0	0	50.0	50.0	
		x					x		x				x						7.6	7.4	42.2	42.6	
		x					x			x			x						12.9	12.1	37.1	37.9	
		x					x				x		x						23.7	21.3	26.3	28.7	
			x		x						x		x						28.0	7.0	52.0	13.0	
				x	x						x		x						"	"	"	"	
x							x				x		x						19.1	15.9	30.9	34.1	
	x						x				x		x						18.6	16.4	31.4	33.6	
			x				x				x		x						17.7	17.3	32.3	32.7	
				x			x				x		x						17.2	17.8	32.8	32.2	

1 Equilibrium gas composition according to the WGSR at the actual temperature

Iron is the equilibrium product in the experiments carried out at 20%RO, while wüstite is the equilibrium product at 50%RO, referring to the phase diagrams in section 2.2 and figure 5.1. The phase diagram in the figure 5.1 shows the experimental conditions during the prereduction experiments (temperature and gas composition). The reduction gas at 760°C and 35%RO is in equilibrium with Fe_{1-y}O and close to equilibrium with iron.

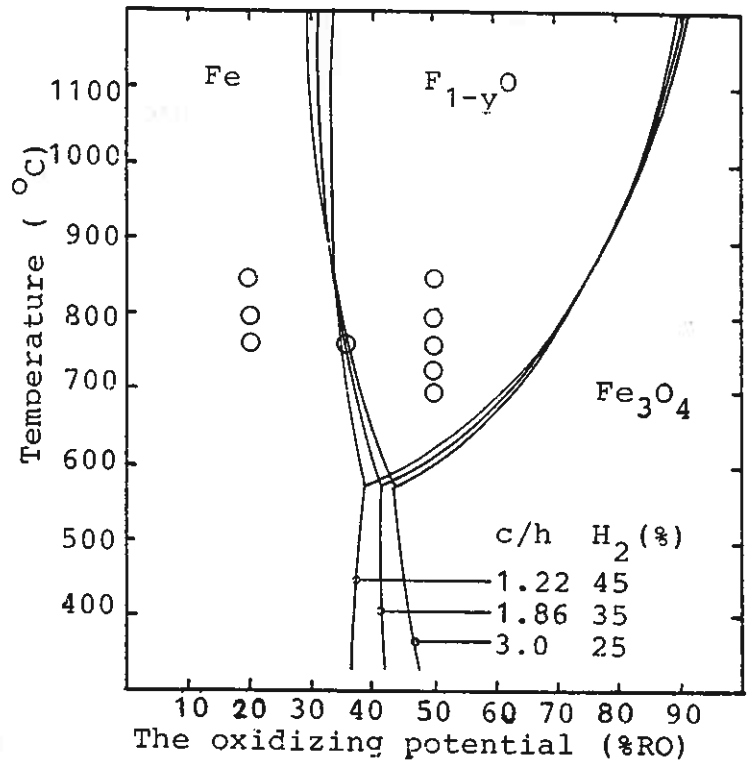


Fig. 5.1 Baur-Glaessner diagram.
o Experimental conditions during reduction.

5.2 Reduction kinetics

5.2.1 Physical models

Reduction of hematite with H_2 or CO proceeds as a sequence of reactions, to magnetite, wüstite, and iron as previously pointed out in section 2.3.1. The rate processes involved are rather complex because of the porous nature of the reduction products and the change of pore structure with reduction temperature. Wüstite is not formed below $570^\circ C$, but at ordinary prereduction temperatures it will be an intermediate product.

Two rather simple idealized models, a topochemical reduction model and a uniform internal reduction model, are often referred to in the literature. These are based on physical observations. The topochemical reduction model is also often called the shrinking core model and the uniform internal reduction model is also called the continuous reaction model. Depending on temperature, particle size, porosity, pore size, and gas composition, one of these models dominates, or an intermediate of the two models is observed.

The topochemical reduction model is shown in figure 5.2, which illustrates the cross section of a large pellet. The indicated phases may be present at the same time during the reduction of large pellets and lumps, although they are not all at chemical equilibrium. During the reduction of concentrates, all these phases are not expected to be found simultaneously. However, each of the reduction reactions may proceed

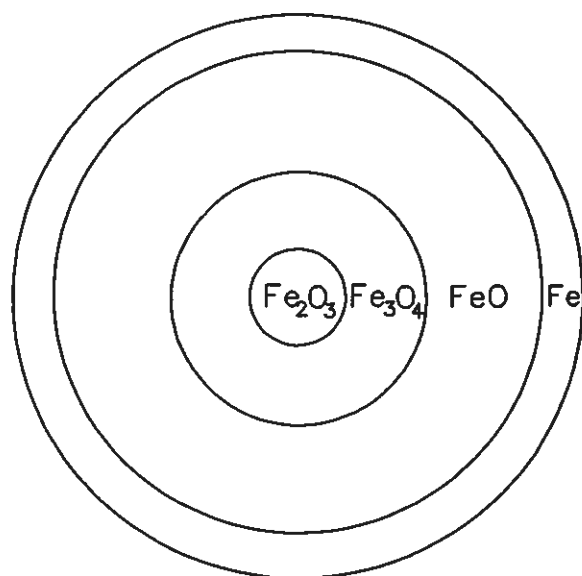


Fig. 5.2 Topochemical reduction of hematite.

topochemically. Two or three, of the respective layers will in this case be found in the grain cross sections. The topochemical model is most commonly observed in all non-catalytic fluid-solid reactions according to Levenspiel (1967). The front may not always be sharply defined as shown in the model.

The uniform internal reduction model is shown in figure 5.3. The figure may for example illustrate reduction of porous wüstite in which droplets of metallic iron have been uniformly formed. This model may dominate in small and porous granules at low temperature according to Turkdogan and Vinters (1971). They found that the chemical reaction on the pore walls

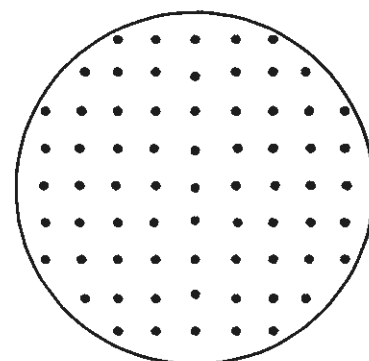


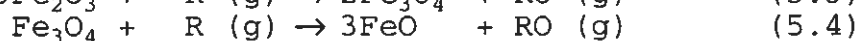
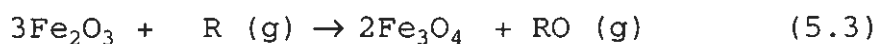
Fig. 5.3 Uniform internal reduction

between the gas and the oxide was rate controlling. The size of the pores must be so large that gas diffusion in the pores offers little hindrance compared to the chemical reaction. The reduction rate is independent of granule size.

Porous pellets, reduced at low temperatures, may show an uniform internal reduction pattern on a macroscopic scale. However, each of the grains, which the pellets are composed of, may be topochemically reduced. The topochemical reduction model has been chosen in section 5.2.2, concerning rate equations for the reduction of concentrates.

5.2.2 Rate equations

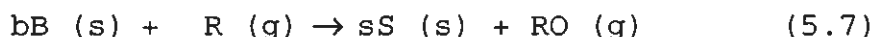
The sequence of reactions occurring during reduction of hematite to iron, can be written as shown in equations 5.3-5.5. R denotes the reducing species in the gas phase, which are H₂ or CO.



Total reaction:



Equation 5.7 is a general term for each of the reactions 5.3-5.6.



During reduction, three steps are considered to offer resistances in series. Whenever one of the steps offer the major resistance, that step alone is considered to be the rate controlling step.

- 1) Diffusion of gaseous reactant R through the gas film surrounding the particle to the particle surface.
- 2) Diffusion of R (g) through the pores of the solid reduction product to the surface of the unreacted core.
- 3) Chemical reaction of R (g) with the iron oxide.

If one of the product layers is not porous, the mass transfer through this layer will not be by pore diffusion according to step 2, but by solid state diffusion. Compact iron and wüstite layers, during the reduction of dense magnetite, have been reported by Wiberg (1941), Edström (1953), Ulvensöen et al. (1991) and others. During reduction of hematite, however, porous magnetite, wüstite, and iron are usually formed (Bogdandy, 1971, page 135). On the other hand, under special conditions, the formation of dense wüstite and iron do occur during hematite reduction (reduction by H₂ at elevated temperatures, observed by Ulvensöen and coworkers (1991)).

The diffusion of gaseous products (RO) from the particle interior to the bulk gas, may also offer resistances to the reactions, but are ignored in the following treatment.

A graphical representation of the above mentioned 3 steps, is presented in figure 5.4 for a spherical particle of unchanged size with radius R. The radius of the shrinking core is called r_c. The figure shows schematically the concentration gradient for gaseous reactant R when all the 3 steps contribute to the

overall resistance. The concentration of R (C_R) decreases towards the centre of the particle. The subscripts g, s, and c, denote gas, solid, and core, respectively, and eq denotes chemical equilibrium between the actual solids and the gaseous reactant R. The driving force in each of these steps is the concentration gradient, as emphasized below:

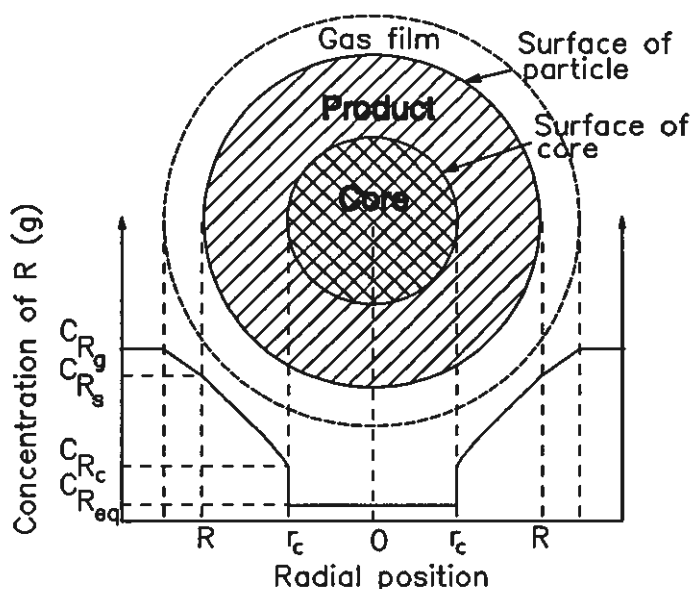


Fig. 5.4 Concentration of gaseous reactant (R) for a spherical particle when all the 3 steps contribute to overall resistance (Levenspiel, 1967)

- 1) Diffusion in the gas film: $(C_{R_g} - C_{R_s}) / (R_g - R)$
- 2) Diffusion in the porous product layer: $(C_{R_s} - C_{R_c}) / (R - r_c)$
- 3) Chemical reaction at the core surface: $(C_{R_c} - C_{R_{eq}})$

The relative importance of the resistances in the gas film and in the solid product layers, to the chemical reactions 5.3-5.5, will vary as conversion progresses. The gas film resistances will remain unchanged during the reduction for each of the reactions. The concentration of R in the bulk gas (C_{R_g}) can be considered to be constant in all the reduction experiments in the present work. Diffusion resistances in the product layers are nonexistent at the start, but become progressively more important as the solid product layers build up.

The mass transfer coefficients k_g , D_p , and k_s , are general measures for resistances (actually conductivities) in gas films, product layers, and of chemical reactions, respectively. The lower the coefficient the higher the resistance. A closer look at the several factors which influence on these coefficients is taken in the next section. Superscripts on D_p and k_s are used to

indicate specific product layers and chemical reactions, respectively.

In the following, each of the steps is considered to offer the major resistance and hence be rate controlling. The review is based on the work by Levenspiel (1967) with the assumptions of spherical particles and constant particle volume during the reactions. It differs in that he treats irreversible reactions, instead of reversible reactions as in the present work. A comparison will first be given between the common variable applied by Levenspiel (r_c/R), the loss in weight frequently used in the gravimetric methods, and the variable OX% used in the presentation of the reduction results in the present work.

Comparison of variables

The percentage degree of oxidation ($OX\% = OX \cdot 100\%$) is a measure for the oxygen content of a sample compared to the maximum amount of oxygen the sample can contain after complete conversion to hematite. It is defined according to equation 5.8.

$$OX\% = \frac{1.5 \cdot Fe^{3+}(\%) + Fe^{2+}(\%)}{1.5 \cdot Fe^{tot}(\%)} \cdot 100\% = OX \cdot 100\% \quad (5.8)$$

The fractional loss in weight at any stage during reduction of a sample is defined by equation 5.9. ΔW_i is the actual weight loss and ΔW_{max} is the maximum weight loss on complete reduction.

$$y = \frac{\Delta W_i}{\Delta W_{max}} \quad (5.9)$$

The loss in weight on complete reduction to iron will equal the maximum amount of oxygen a sample can contain if:

- 1) No other iron phases than hematite is contained in the sample before reduction take place.
- 2) The weight loss is only caused by loss of oxygen initially contained in hematite

On these two assumptions, the fractional loss in weight is expressed by formula 5.10, or simply as $y=1-OX$ in formula 5.11.

$$y = \frac{n_{Fe} \cdot 1.5 \cdot A_O - n_{Fe} \left(\frac{1.5 \cdot Fe_i^{3+}(\%)}{Fe_i^{tot}(\%)} + \frac{Fe_i^{2+}(\%)}{Fe_i^{tot}(\%)} \right) \cdot A_O}{n_{Fe} \cdot 1.5 \cdot A_O} \quad (5.10)$$

$$y = 1 - \frac{1.5 \cdot Fe_i^{3+}(\%) + Fe_i^{2+}(\%)}{1.5 \cdot Fe_i^{tot}(\%)} = 1 - OX \quad (5.11)$$

n_{Fe} = The constant number of iron atoms in a sample.
 A_O = Atomic weight of oxygen

A relation between r_c/R , y , and OX is derived on the assumptions that the total reduction from hematite to iron proceeds topochemically for a constant particle volume (V^o), referring to figure 5.5 and formulas 5.12 and 5.13.

The volumes of the iron, wüstite, and magnetite layers are called V^{Fe} , $V^{wü}$, and V^{mt} , respectively, while V^{hm} denotes the volume of the hematite core. The number of iron atoms in the particle (n_{Fe}) is constant during reduction and is assumed to be homogeneously distributed in the particle. For each iron atom there are 3/2, 4/3, or 1, oxygen atoms in the hematite, magnetite, or wüstite phase, respectively. The vacancy concentration in wüstite ($Fe_{1-y}O$) is set to zero ($y=0$).

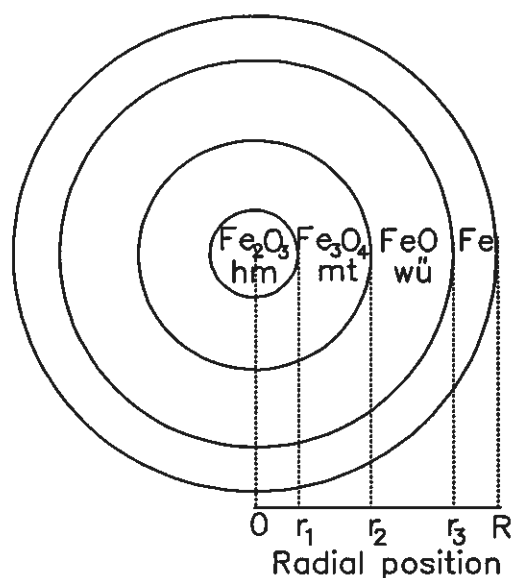


Fig. 5.5 Topochemical reduction of hematite

$$y = \frac{\Delta W_i}{\Delta W_{max}} = \frac{n_{Fe} \cdot 1.5 \cdot A_O - n_{Fe} \left(\frac{V^{hm}}{V^o} \cdot 1.5 + \frac{V^{mt}}{V^o} \cdot \frac{4}{3} + \frac{V^{wü}}{V^o} \cdot 1 \right) A_O}{n_{Fe} \cdot 1.5 \cdot A_O}$$

$$y = 1 - \left(\frac{V^{hm}}{V^o} + \frac{8}{9} \cdot \frac{V^{mt}}{V^o} + \frac{2}{3} \cdot \frac{V^{wü}}{V^o} \right) = 1 - \left(\frac{r_1^3}{R^3} + \frac{8}{9} \cdot \frac{(r_2^3 - r_1^3)}{R^3} + \frac{2}{3} \cdot \frac{(r_3^3 - r_2^3)}{R^3} \right)$$

$$y = 1 - \left(\frac{1}{9} \left(\frac{r_1}{R} \right)^3 + \frac{2}{9} \left(\frac{r_2}{R} \right)^3 + \frac{2}{3} \left(\frac{r_3}{R} \right)^3 \right) \quad (5.12)$$

$$OX = \frac{1}{9} \left(\frac{r_1}{R} \right)^3 + \frac{2}{9} \left(\frac{r_2}{R} \right)^3 + \frac{2}{3} \left(\frac{r_3}{R} \right)^3 \quad (5.13)$$

Formula 5.14 is derived for $r_1=r_2=r_3$. By this is understood an iron layer around a hematite core, a hypothetical situation.

$$OX = \left(\frac{r_1}{R} \right)^3 = 1 - y \quad (5.14)$$

In the following a few special cases are derived for subsequent reactions. However, parallel reactions are expected to occur during reduction, especially when the reduction gas is strong. Formula 5.15 and 5.16 are derived for $r_2=r_3=R$. This is the situation during the early stage of the reduction when a growing magnetite layer covers a decreasing hematite core.

$$OX = \frac{1}{9} \left(\frac{r_1}{R} \right)^3 + \frac{8}{9} \quad (5.15)$$

$$d(OX) = \frac{1}{3R^3} \cdot r_1^2 \cdot dr_1 \quad (5.16)$$

Formula 5.17 and 5.18 are derived for $r_3=R$ and $r_1=0$. At this stage of the reduction the hematite has disappeared. The wüstite layer is growing around a decreasing magnetite core.

$$OX = \frac{2}{9} \left(\frac{r_2}{R} \right)^3 + \frac{2}{3} \quad (5.17)$$

$$d(OX) = \frac{2}{3R^3} \cdot r_2^2 \cdot dr_2 \quad (5.18)$$

Equation 5.19 and 5.20 are derived for $r_1=r_2=0$. The hematite and the magnetite have disappeared. There is a growing iron layer around a decreasing wüstite core.

$$OX = \frac{2}{3} \left(\frac{r_3}{R} \right)^3 \quad (5.19)$$

$$d(OX) = \frac{2}{R^3} \cdot r_3^2 \cdot dr_3 \quad (5.20)$$

Diffusion in the gas film controls

The concentration gradient of the gaseous reactant R around and through a spherical particle, when the resistance in the gas film controls the rate of the reaction, is shown in figure 5.6.

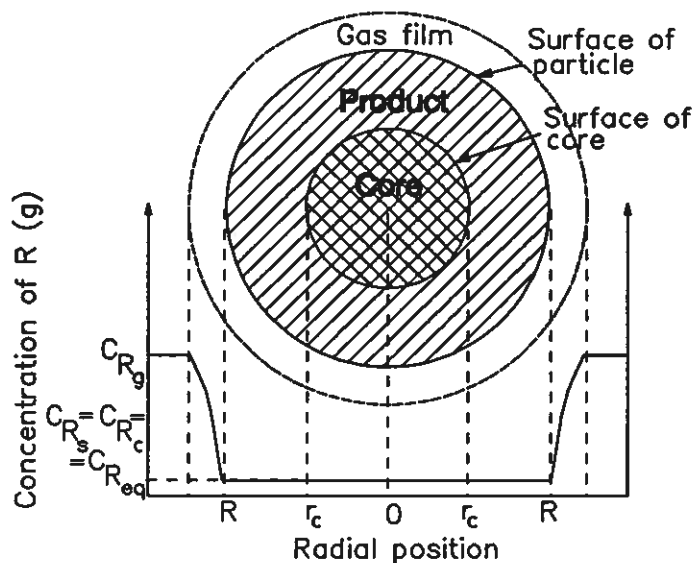
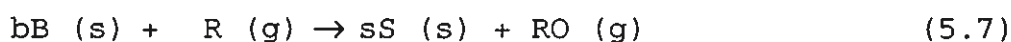


Fig. 5.6 Concentration gradient for a spherical particle when diffusion through the gas film controls (Levenspiel, 1967)

The number of moles of B (n_B) in the particle is defined by formula 5.21. M_B , ρ_B , and ϵ_B , denote the molecular weight, the density, and the porosity of the solid material B, respectively. The subscript B substitutes both hematite (hm), magnetite (mt), and wüstite (wü), because equation 5.7 expresses the reduction of each of these solids, as earlier pointed out.

$$n_B = \frac{\rho_B}{M_B} \cdot V^o (1 - \epsilon_B) \quad (5.21)$$



The porosity is defined by the ratio of the pore volume to the particle volume. The porosity of each material is assumed to be constant during the reaction, unaffected by the influence of temperature. On the assumption of a constant particle volume, the porosity of magnetite and wüstite can be calculated as a function of the hematite porosity, referring to appendix A.2. For $\epsilon_{hm}=0$, the porosity of magnetite and wüstite are calculated to 2.2 and 17.3%, respectively. The decrease in n_B with time can be expressed by equation 5.22.

$$-\frac{dn_B}{dt} = -\frac{\rho_B (1 - \epsilon_B) dV}{M_B \cdot dt} = -\frac{4\pi\rho_B (1 - \epsilon_B) d(r_c^3)}{3M_B \cdot dt} = -\frac{4\pi\rho_B (1 - \epsilon_B) r_c^2}{M_B} \cdot \frac{dr_c}{dt} \quad (5.22)$$

The rate of reaction of gaseous reactant R at the surface of the particle is expressed by equation 5.23, where n_R denotes the number of moles R. The exterior surface area (S_{ex}) is assumed to remain unchanged during the reaction.

$$-\frac{dn_R}{dt} = k_g \cdot S_{ex} (C_{R_g} - C_{R_s}) \quad (5.23)$$

When the diffusion in the gas film is rate controlling, the concentration of gaseous reactant R at the surface of the particle is in equilibrium with the solids B and S. Realizing that $dn_B = b \cdot dn_R$, from stoichiometrical considerations of equation 5.7, we obtain formula 5.24 from the equations 5.22 and 5.23 by inserting $S_{ex} = 4\pi R^2$ for a spherical particle.

$$-\frac{dn_B}{dt} = b \cdot k_g \cdot S_{ex} (C_{R_g} - C_{R_{eq}}) = -\frac{4\pi \rho_B (1 - \epsilon_B)}{M_B} \cdot r_c^2 \cdot \frac{dr_c}{dt}$$

$$-r_c^2 \cdot dr_c = \frac{b \cdot k_g \cdot M_B \cdot R^2}{\rho_B (1 - \epsilon_B)} \cdot (C_{R_g} - C_{R_{eq}}) dt \quad (5.24)$$

Integration of formula 5.24 gives equation 5.25 for a particle of unchanged size.

$$\left(\frac{r_c}{R}\right)^3 = 1 - \frac{3 \cdot b \cdot k_g \cdot M_B}{R \cdot \rho_B (1 - \epsilon_B)} \cdot (C_{R_g} - C_{R_{eq}}) \cdot t \quad (5.25)$$

For topochemical reduction of hematite to magnetite, equations 5.26 and 5.27 apply prior wüstite formation. During the reaction, $0.889 \leq OX \leq 1$ for $0 \leq t \leq t_1$. Formula 5.26 is derived from the equations 5.16 and 5.24 for $r_c = r_1$ by inserting $b=3$ and $(r_c)^2 \cdot dr_c = (r_1)^2 \cdot dr_1$. Integration of equation 5.26 and subsequent rearranging gives formula 5.27.

$$-\int_1^{OX} d(OX) = \frac{k_g \cdot M_{hm}}{R \cdot \rho_{hm} (1 - \epsilon_{hm})} \cdot (C_{R_g} - C_{R_{eq}}^{hm/mt}) \cdot \int_0^t dt \quad (5.26)$$

$$OX = 1 - \frac{k_g \cdot M_{hm}}{R \cdot \rho_{hm} (1 - \epsilon_{hm})} \cdot (C_{R_g} - C_{R_{eq}}^{hm/mt}) \cdot t \quad (5.27)$$

If magnetite is assumed to be topochemically reduced to wüstite after the complete conversion of hematite, equations 5.28 and 5.29 apply. During this reaction, $0.667 \leq OX \leq 0.889$ for $t_1 \leq t \leq t_2$. The formulas are derived from the equations 5.18 and 5.24 ($b=1$ and $r_c=r_2$), referring also to appendix A.2. However, reactions are not subsequent, but parallel, during reduction with strong reduction gases.

$$-\int_{\frac{8}{9}}^{OX} d(OX) = \frac{2 \cdot k_g \cdot M_{mt}}{3 \cdot R \cdot \rho_{mt} (1 - \epsilon_{mt})} \cdot (C_{R_g} - C_{R_{eq}}^{mt/wu}) \cdot \int_{t_1}^t dt \quad (5.28)$$

$$OX = \frac{8}{9} - \frac{2 \cdot k_g \cdot M_{mt}}{3 \cdot R \cdot \rho_{mt} (1 - \epsilon_{mt})} \cdot (C_{R_g} - C_{R_{eq}}^{mt/wu}) \cdot (t - t_1) \quad (5.29a)$$

$$OX = \frac{8}{9} - \frac{k_g \cdot M_{hm}}{R \cdot \rho_{hm} (1 - \epsilon_{hm})} \cdot (C_{R_g} - C_{R_{eq}}^{mt/wu}) \cdot (t - t_1) \quad (5.29b)$$

If wüstite is assumed to be topochemically reduced to iron after the complete conversion of both hematite and magnetite, the equations 5.30 and 5.31 apply. During this reaction, $OX \leq 0.667$ for $t \geq t_2$. The formulas are derived from the equations 5.20 and 5.24 ($b=1$ and $r_c=r_3$).

$$-\int_{\frac{2}{3}}^{OX} d(OX) = \frac{2 \cdot k_g \cdot M_{wu}}{R \cdot \rho_{wu} (1 - \epsilon_{wu})} \cdot (C_{R_g} - C_{R_{eq}}^{wu/Fe}) \cdot \int_{t_2}^t dt \quad (5.30)$$

$$OX = \frac{2}{3} - \frac{2 \cdot k_g \cdot M_{wu}}{R \cdot \rho_{wu} (1 - \epsilon_{wu})} \cdot (C_{R_g} - C_{R_{eq}}^{wu/Fe}) \cdot (t - t_2) \quad (5.31a)$$

$$OX = \frac{2}{3} - \frac{k_g \cdot M_{hm}}{R \cdot \rho_{hm} (1 - \epsilon_{hm})} \cdot (C_{R_g} - C_{R_{eq}}^{wu/Fe}) \cdot (t - t_2) \quad (5.31b)$$

With the resistance of the gas film controlling, there is a linear relationship between OX and the time, OX decreases with time. The time needed to complete each of the reactions is proportional with the radius of the spherical particle (R).

Pore diffusion controls

The concentration gradient, when the resistance to diffusion through the porous product layer is rate controlling, is shown in figure 5.7. The concentration of the gaseous reactant R (C_R) in the bulk gas and at the surface of the particle is of the same size. C_R at the core surface equals C_R at chemical equilibrium.

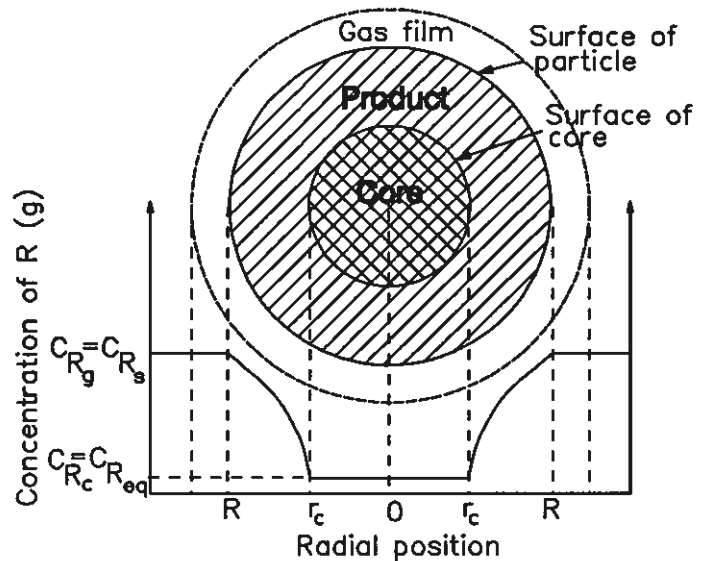


Fig. 5.7 Concentration gradient for a spherical particle when pore diffusion through the product layer controls (Levenspiel, 1967)

A two step analysis is used to develop an expression between time and the radius and in turn, the degree of oxidation (OX). Quasi steady state conditions for the diffusing reactant R is assumed. The rate of reaction of reactant R is at any instant expressed by its rate of diffusion through a shell with radius r in the product layer, as presented in equations 5.32 and 5.33 (Levenspiel, 1967).

$$-\frac{dn_R}{dt} = 4\pi r^2 \cdot D_p \cdot \frac{dC_R}{dr} = \text{constant} \quad (5.32)$$

$$-\frac{dn_R}{dt} \cdot \int_R^{r_c} \frac{dr}{r^2} = 4\pi D_p \cdot \int_{C_{Rg}}^{C_{Req}} dC_R \quad (5.33)$$

Integration of equation 5.33 is conducted by considering dn_R/dt to be constant.

$$-\frac{dn_R}{dt} \cdot \left(\frac{1}{r_c} - \frac{1}{R} \right) = 4\pi D_p (C_{Rg} - C_{Req}) \quad (5.34)$$

Equation 5.35 is derived by substituting dn_R in formula 5.34 with dn_B/b and inserting dn_B/dt as expressed by formula 5.22. On

integration, equation 5.36 is derived for a particle with unchanged size.

$$-\int_R^{r_c} r_c^2 \left(\frac{1}{r_c} - \frac{1}{R} \right) \cdot dr_c = \frac{b D_p M_B}{\rho_B (1 - \epsilon_B)} \cdot (C_{R_g} - C_{R_{eq}}) \cdot \int_{t'}^t dt \quad (5.35)$$

$$1 - 3 \left(\frac{r_c}{R} \right)^2 + 2 \left(\frac{r_c}{R} \right)^3 = \frac{6 \cdot b \cdot D_p \cdot M_B}{R^2 \cdot \rho_B (1 - \epsilon_B)} \cdot (C_{R_g} - C_{R_{eq}}) \cdot (t - t') \quad (5.36)$$

For the first reaction from hematite to magnetite, we have $t' = 0$, $r_c = r_1$, and $b = 3$. Equation 5.37 is derived from formula 5.36 by inserting r_1/R expressed by equation 5.15. Formula 5.37 applies in the range where $0.889 \leq OX \leq 1$ and $0 \leq t \leq t_1$, prior wüstite formation.

$$OX - \frac{1}{6} (9 \cdot OX - 8)^{\frac{2}{3}} - \frac{5}{6} = \frac{D_p^{mt} \cdot M_{hm}}{R^2 \cdot \rho_{hm} (1 - \epsilon_{hm})} \cdot (C_{R_g} - C_{R_{eq}}^{hm/mt}) \cdot t \quad (5.37)$$

For the subsequent second reaction from magnetite to wüstite, after the complete conversion of the hematite, we have $t' = t_1$, $r_c = r_2$, and $b = 1$. Equation 5.38 is derived from formula 5.36 by inserting r_2/R expressed by equation 5.17, referring also to appendix A.2 for the transformation of equation 5.38a to 5.38b. Formula 5.38 applies in the range: $0.667 \leq OX \leq 0.889$ and $t_1 \leq t \leq t_2$, provided subsequent reactions. However, parallel reactions will take place during reduction with strong reduction gases.

$$OX - \frac{1}{3} \left(\frac{9}{2} \cdot OX - 3 \right)^{\frac{2}{3}} - \frac{5}{9} = \frac{2 \cdot D_p^{wu} \cdot M_{mt}}{3 R^2 \cdot \rho_{mt} (1 - \epsilon_{mt})} \cdot (C_{R_g} - C_{R_{eq}}^{mt/wu}) \cdot (t - t_1) \quad (5.38a)$$

$$OX - \frac{1}{3} \left(\frac{9}{2} \cdot OX - 3 \right)^{\frac{2}{3}} - \frac{5}{9} = \frac{D_p^{wu} \cdot M_{hm}}{R^2 \cdot \rho_{hm} (1 - \epsilon_{hm})} \cdot (C_{R_g} - C_{R_{eq}}^{mt/wu}) \cdot (t - t_1) \quad (5.38b)$$

If the third reaction from wüstite to iron takes off after the complete conversion of magnetite to wüstite, we have: $t' = t_2$, $r_c = r_3$, and $b = 1$. Equation 5.39 is derived from formula 5.36 by inserting r_3/R expressed by equation 5.19, referring also to appendix A.2 for the transformation of equation 5.39a to 5.39b. Formula 5.39 applies for $OX \leq 0.667$ and $t \geq t_2$.

$$OX - \left(\frac{3}{2} \cdot OX\right)^{\frac{2}{3}} + \frac{1}{3} = \frac{2 \cdot D_p^{Fe} \cdot M_{wu}}{R^2 \cdot \rho_{wu} (1 - \epsilon_{wu})} \cdot (C_{R_g} - C_{R_{eq}}^{wu/Fe}) \cdot (t - t_2) \quad (5.39a)$$

$$OX - \left(\frac{3}{2} \cdot OX\right)^{\frac{2}{3}} + \frac{1}{3} = \frac{D_p^{Fe} \cdot M_{hm}}{R^2 \cdot \rho_{hm} (1 - \epsilon_{hm})} \cdot (C_{R_g} - C_{R_{eq}}^{wu/Fe}) \cdot (t - t_2) \quad (5.39b)$$

The time needed to complete each of the reactions, or to achieve a certain degree of oxidation (OX), increases proportionally with the square of the particle radius (R).

Chemical reaction controls

The concentration gradient, when the resistance to the chemical reaction is rate controlling, is shown in figure 5.8. The concentration of the gaseous reactant R (C_R) in the bulk gas and at the surface of the particle and of the core are of the same size.

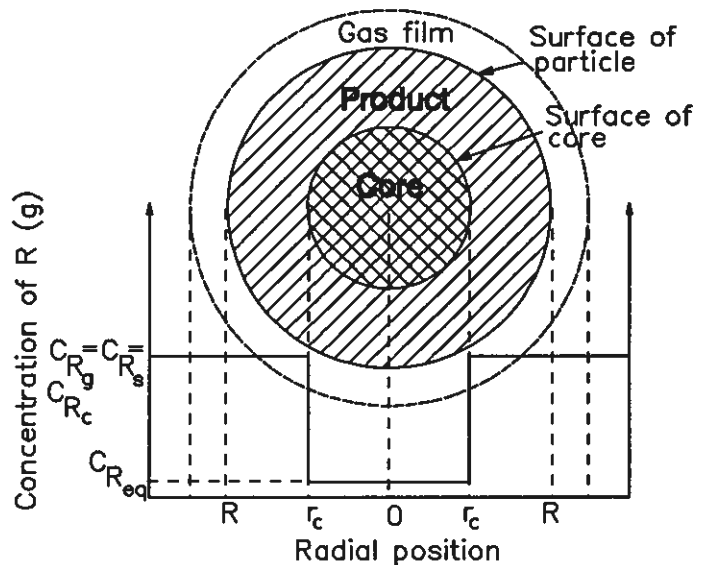


Fig. 5.8 Concentration gradient for a spherical particle when chemical reaction controls (Levenspiel, 1967)

The reaction rate is independent of the depth

of the porous product layer, because gas diffusion in the pores is now assumed to be very rapid. The rate of the chemical reaction is proportional to the available interior surface area. In the topochemical reduction model, the available surface area is the decreasing surface area of the core (S_i).

$$-\frac{dn_R}{dt} = S_i \cdot k_s \cdot (C_{R_c} - C_{R_{eq}}) = 4\pi r_c^2 \cdot k_s \cdot (C_{R_g} - C_{R_{eq}}) \quad (5.40)$$

The rate of reaction may be expressed by equation 5.41, recalling that $dn_R = dn_B/b$, and inserting dn_B/dt expressed by equation 5.22 into formula 5.40.

$$-\frac{dn_B}{dt} = 4\pi \cdot r_c^2 \cdot b \cdot k_s (C_{R_g} - C_{R_{eq}}) = -\frac{4\pi \cdot \rho_B (1 - \epsilon_B)}{M_B} \cdot r_c^2 \cdot \frac{dr_c}{dt} \quad (5.41)$$

Equation 5.42 is derived on rearranging and integration of formula 5.41.

$$-\int_R^{r_c} dr_c = \frac{b \cdot k_s \cdot M_B}{\rho_B (1 - \epsilon_B)} \cdot (C_{R_g} - C_{R_{eq}}) \cdot \int_{t'}^t dt \quad (5.42)$$

For a spherical particle of unchanged size, we have:

$$\frac{r_c}{R} = 1 - \frac{b \cdot k_s \cdot M_B}{R \cdot \rho_B (1 - \epsilon_B)} \cdot (C_{R_g} - C_{R_{eq}}) \cdot (t - t') \quad (5.43)$$

For the first reaction from hematite to magnetite, we have $t' = 0$, $r_c = r_1$, and $b = 3$. Equation 5.44 is derived from formula 5.43 by inserting r_1/R expressed by equation 5.15. Formula 5.44 applies in the range: $0.889 \leq OX \leq 1$ and $0 \leq t \leq t_1$, prior wüstite formation.

$$OX = \frac{8}{9} + \frac{1}{9} \left(1 - \frac{3 \cdot k'_s \cdot M_{hm}}{R \cdot \rho_{hm} (1 - \epsilon_{hm})} \cdot (C_{R_g} - C_{R_{eq}}^{hm/mt}) \cdot t \right)^3 \quad (5.44)$$

If the subsequent second reaction from magnetite to wüstite takes place after the complete conversion of the hematite, we have $t' = t_1$, $r_c = r_2$, and $b = 1$. Equation 5.45 is derived from formula 5.43 by inserting r_2/R expressed by equation 5.17, referring also to

appendix A.2 for the transformation of equation 5.45a to 5.45b. Formula 5.45 applies in the range: $0.667 \leq OX \leq 0.889$ and $t_1 \leq t \leq t_2$, provided subsequent reactions. However, parallel reactions probably take place during reduction with strong reduction gases.

$$OX = \frac{2}{3} + \frac{2}{9} \cdot \left(1 - \frac{k_s'' \cdot M_{mt}}{R \cdot \rho_{mt} (1 - \epsilon_{mt})} \cdot (C_{R_g} - C_{R_{eq}}^{mt/wu}) \cdot (t - t_1)\right)^3 \quad (5.45a)$$

$$OX = \frac{2}{3} + \frac{2}{9} \cdot \left(1 - \frac{3k_s'' \cdot M_{hm}}{2R \cdot \rho_{hm} (1 - \epsilon_{hm})} \cdot (C_{R_g} - C_{R_{eq}}^{mt/wu}) \cdot (t - t_1)\right)^3 \quad (5.45b)$$

If the third reaction from wüstite to iron takes off after the complete conversion of magnetite to wüstite, we have $t' = t_2$, $r_c = r_3$, and $b = 1$. In this case, formula 5.46 applies for $OX \leq 0.667$ and $t \geq t_2$. Equation 5.46 is derived from formula 5.43 by inserting r_3/R expressed by equation 5.19, referring also to appendix A.2 for the transformation of equation 5.46a to 5.46b.

$$OX = \frac{2}{3} \cdot \left(1 - \frac{k_s''' \cdot M_{wu}}{R \cdot \rho_{wu} (1 - \epsilon_{wu})} \cdot (C_{R_g} - C_{R_{eq}}^{wu/Fe}) \cdot (t - t_2)\right)^3 \quad (5.46a)$$

$$OX = \frac{2}{3} \cdot \left(1 - \frac{k_s''' \cdot M_{hm}}{2R \cdot \rho_{hm} (1 - \epsilon_{hm})} \cdot (C_{R_g} - C_{R_{eq}}^{wu/Fe}) \cdot (t - t_2)\right)^3 \quad (5.46b)$$

The time needed to complete the reactions, or to obtain a certain degree of oxidation, increases proportionally with the particle radius.

The overall reaction rate

The overall reaction rate for each of the reactions can be expressed by the resistances to the diffusion in the gas film and in the porous reaction product, and to the chemical reaction, by neglecting the solid state diffusion resistance. Solid state diffusion is not to be expected to contribute to the overall

reaction in the initial period of 60 seconds, because of the porous nature of the reaction products in the actual temperature range in the present work. Pore diffusion and solid state diffusion are parallel steps, but pore diffusion will always be far quicker than solid state diffusion. Rate equations for the solid state diffusion of iron during the reduction of dense wüstite, are given in a review by Bogdandy and Engell (1971, page 132-136).

When the resistances to diffusion in the gas film and in the porous reaction product, and to the chemical reaction, all contribute to the overall rate, the rate of each reaction can be expressed by the equations 5.47, 5.48, and 5.49, respectively. These equations are analog to the equations 5.23, 5.34, and 5.40, when each step was considered to be rate controlling.

$$-\frac{dn_R}{dt} = k_g \cdot 4\pi R^2 (C_{R_g} - C_{R_s}) \quad (5.47)$$

$$-\frac{dn_R}{dt} = \frac{4\pi D_p (C_{R_s} - C_{R_c})}{\frac{1}{r_c} - \frac{1}{R}} \quad (5.48)$$

$$-\frac{dn_R}{dt} = 4\pi r_c^2 \cdot k_s \cdot (C_{R_c} - C_{R_{eq}}) \quad (5.49)$$

Equation 5.50 is derived by elimination of C_{R_s} and C_{R_c} (C_{R_s} and C_{R_c} are expressed by equations 5.47 and 5.49, respectively, which are inserted in formula 5.48).

$$-\frac{dn_R}{dt} = \frac{4\pi (C_{R_g} - C_{R_{eq}})}{\frac{1}{R^2 \cdot k_g} + \frac{\frac{1}{r_c} - \frac{1}{R}}{D_p} + \frac{1}{r_c^2 \cdot k_s}} \quad (5.50)$$

Introduction of $dn_R=dn_B/b$ and dn_B/dt expressed by equation 5.22 into formula 5.50, gives equation 5.51 on rearranging.

$$-\int_R^{r_c} \left(\frac{1}{R^2 \cdot k_g} + \frac{\frac{1}{r_c} - \frac{1}{R}}{D_p} + \frac{1}{r_c^2 \cdot k_s} \right) r_c^2 \cdot dr_c = \frac{M_B \cdot b (C_{R_g} - C_{R_{eq}})}{\rho_B (1 - \epsilon_B)} \int_{t'}^t dt \quad (5.51)$$

Equation 5.52 is derived from 5.51 by integration, for a spherical particle with unchanged size during the reduction.

$$\frac{1}{k_g} \left(1 - \left(\frac{r_c}{R} \right)^3 \right) + \frac{R}{2D_p} \left(1 - 3 \left(\frac{r_c}{R} \right)^2 + 2 \left(\frac{r_c}{R} \right)^3 \right) + \frac{3}{k_s} \left(1 - \frac{r_c}{R} \right) = \frac{3bM_B (C_{R_g} - C_{R_{eq}}) (t - t')}{R \cdot \rho_B (1 - \epsilon_B)} \quad (5.52)$$

The time needed to reach a certain reduction stage is the sum of the times needed for each of the individual steps (gas diffusion in the gas film and the product layer and the chemical reaction) when it is rate controlling. This is easily seen by comparing equations 5.27, 5.36, and 5.43 with 5.52. Equations with the variable OX instead of r_c/R may be derived by assuming a complete conversion in each of the reactions before the subsequent reaction proceeds. This has already been done for each of the steps when it is rate controlling. The procedure will be quite analog and will not be repeated here.

Gas film resistance can on several occasions be neglected. It may contribute to the overall resistance at an early stage of the reaction. As the product layer builds up, the resistance to diffusion in the pores grows more important. Diffusion in the pores will always contribute to a higher resistance than diffusion in the gas film. The gas film resistance decreases for an increasing relative gas velocity between gas and solid. By conducting experiments at a relative high gas velocity, gas film resistance may be neglected.

5.2.3 The mass transfer coefficients

The mass transfer coefficients k_g , D_p , and k_s , are used as general measures for the resistances to diffusion in gas films, product layers, and to the chemical reactions, respectively. The lower the coefficient, the higher the resistance, and the lower the reaction rate. Superscripts on D_p and k_s , in section 5.2.2, are used to indicate specific product layers and chemical reactions. A closer look at the several factors which influence on these coefficients, is taken in this section. Special attention is paid to the temperature dependence of the mass transfer coefficients, and to the influence of temperature on the rate of reaction when the corresponding resistances are rate controlling.

Gas film diffusion

Film resistance at the surface of a particle, is dependant on several factors such as particle size, the relative velocity between particle and gas (u), the gas viscosity (μ), and the gas density (ρ). These have been correlated by semiempirical dimensionless equations. The mass transfer coefficient for diffusion through the boundary layer around a particle (k_g), is expressed by the Sherwood number (Sh). For free-falling spheres of a diameter d_p , under conditions of forced convection, Sherwood's number is correlated to Reynold's number (Re) and Schmidt's number (Sc), by formula 5.53 (Levenspiel, 1967).

$$Sh = 2.0 + 0.60 \cdot (Sc)^{\frac{1}{3}} (Re)^{\frac{1}{2}} \quad (5.53)$$

$$\frac{k_g \cdot d_p \cdot y}{D} = 2.0 + 0.60 \cdot \left(\frac{\mu}{\rho \cdot D} \right)^{\frac{1}{3}} \left(\frac{d_p \cdot u \cdot \rho}{\mu} \right)^{\frac{1}{2}}$$

D is the diffusion coefficient for diffusion in free space (treated under pore diffusion) and y is the mole fraction of the diffusing component (R) in the gas. For particles of other shapes than spherical, d_p in equation 5.53 may be substituted by $\psi \cdot d_d$, where ψ is the shape factor and d_d is the equivalent sphere

diameter (the diameter of a sphere with the same volume as the actual particle).

Similar correlations between these numbers have been obtained for solids in fixed beds and for solids in fluidized beds. An overall plot for fluid-solid mass transfer, taken from Kunii & Levenspiel (1969), is shown in figure 5.9. It appears that:

$$k_{g, sphere} < k_{g, fluidized} < k_{g, fixed} \quad Re_p > 80-100$$

If solids are completely dispersed in flowing gas, the Sherwood number should approach 2, the theoretical minimum for diffusion in a stagnant medium, according to equation 5.53. As the Reynold's number is lowered, referring to figure 5.9, the Sherwood number drops sharply from the expected values for gas fluidized beds.

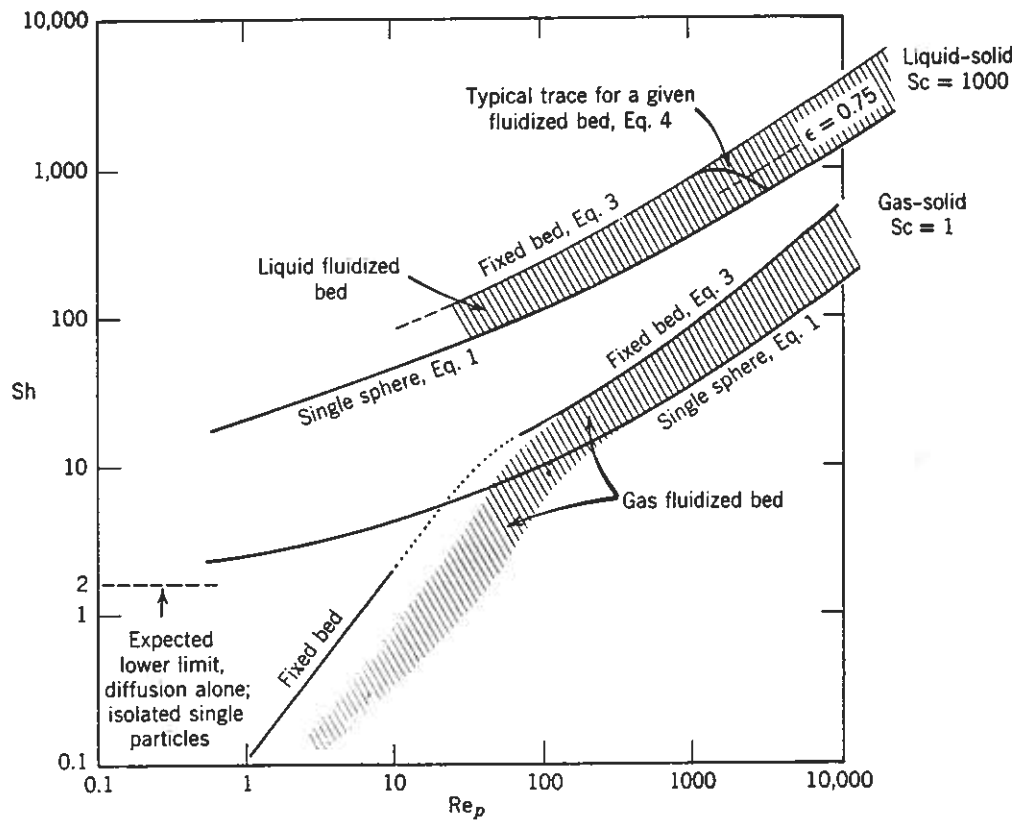


Fig. 5.9 Overall plot for fluid-solid mass transfer for single particles, fluidized beds and fixed beds (Kunii & Levenspiel, 1969).

The Sherwood number is significantly smaller than expected for particles smaller than about 5 mm (Rosenqvist, 1985 b). The deviation is believed caused by the formation of bubbles. A similar drop is observed with gas-solid heat transfer. However, the mass transfer coefficient is still fairly large.

A closer look at the mass transfer coefficient for small particles is taken, because the present work is only dealing with small particles. Figure 5.9 shows that the Sherwood number is approximately proportional to the Reynold number for gas fluidized beds when $Re < 80-100$. An approximate correlation between Sh and Re , for gas fluidized beds consisting of particles smaller than about 5 mm and for Re smaller than about 100, is given in the formulas 5.54a and 5.54b. The equation fits the data in figure 5.9 for gas fluidized bed when the Reynold number is less than about 100.

$$Sh = 0.05 \cdot (Re)^{1.2} \quad \begin{array}{l} Re < 100 \\ d_p < 5mm \end{array} \quad (5.54a)$$

$$\frac{k_g \cdot d_p \cdot Y}{D} = 0.05 \cdot \left(\frac{d_p \cdot u \cdot \rho}{\mu} \right)^{1.2} \quad (5.54b)$$

$$k_g = \frac{0.05}{Y} \cdot \left(\frac{d_p}{D} \right)^{0.2} \cdot \left(\frac{u}{Sc} \right)^{1.2} \quad (5.54c)$$

The mass transfer coefficient k_g is approximately independent or only weakly dependant on the particle size in this range. It increases proportionally to the gas diffusivity (D) and approximately proportionally to the gas density and to the relative velocity (u) between the gas and the particles. Further, k_g decreases for an increasing gas viscosity.

The mass transfer coefficient k_g increases approximately proportionally to the temperature. This is seen by considering equation 5.54c. The Schmidt's number is approximately temperature independent, analogous to the Prandtl's number for heat transfer. The diffusivity increases with T^n for $1.5 < n < 2$ (referring to pore diffusion on the next page), while there is a linear relation between velocity and temperature. When diffusion through the gas film is rate controlling, the rate of reaction will be approximately independent or only weakly dependant on the temperature at a constant pressure. This is seen by inserting $C = P/RT$ in equation 5.23.

Pore diffusion

In the diffusion through pores, the cross-section available for diffusion is limited compared to diffusion in the free space. This is taken into account by correlating the diffusion coefficient for pore diffusion (D_p) to the diffusion coefficient for diffusion in the free space (D) by the porosity of the product layer (ϵ) and a labyrinth factor (ξ), as shown in equation 5.55 (Bogdandy and Engell, 1971). The formula does not apply for very small pores, when the semi-diameter of the pores is less than the mean free path of the gas molecules.

$$D_p = D \cdot \epsilon \cdot \xi \quad 5.55$$

The variables, ϵ and ξ , may vary with temperature and gas composition, but only their dependence on characteristic hematite properties is emphasized here. Their temperature dependence is temporarily disregarded.

The porosity will differ for the different product layers. As previously mentioned, $\epsilon=0.02$ for magnetite and $\epsilon=0.17$ for wüstite, on the assumptions of a constant particle volume and $\epsilon=0$ for hematite, referring to appendix A.2. However, the porosity of the product layers is dependant on the porosity of the hematite. The porosity of the hematite grains will vary from ore to ore. Hence, D_p is dependant of the hematite type.

The labyrinth factor is a measure for the orientation of the pores relative to the diffusion path and also for the branching and cross-linking of the pores. With other words, the labyrinth factor is a measure for the pore structure. The pore structure of chemically identical product layers, may differ from ore to ore, because of different subgrain structures and variable pore structures of the original hematites. Hence, D_p is indeed dependant on characteristic hematite properties.

The temperature dependency of D , as given by Rosenqvist (1985 a) in equation 5.56, is derived on the basis of kinetic gas theory.

$$D_{R-RO} = \frac{K_{R-RO}}{P_R + P_{RO}} \cdot T^{\frac{3}{2}} \quad (5.56)$$

D_{R-RO} is the diffusivity of a pair of counter diffusing gases (R and RO). It is a function of the weight and size of the gas molecules, the total pressure, and the temperature. K_{R-RO} is a constant which is independent of temperature and pressure. Empirically, the relation given in equation 5.57 has been found (Rosenqvist, 1985a) where v_R and v_{RO} are the molar volumes of the gases R and RO in a condensed state. The coefficient 0.0043 applies to K_{R-RO} having the dimension $\text{cm}^2 \cdot \text{atm} \cdot \text{sec}^{-1} (\text{K})^{-3/2}$.

$$K_{R-RO} = \frac{0.0043}{\left(\frac{1}{v_R^{\frac{1}{3}}} + \frac{1}{v_{RO}^{\frac{1}{3}}} \right)^2} \cdot \left(\frac{1}{M_R} + \frac{1}{M_{RO}} \right)^{\frac{1}{2}} \quad (5.57)$$

A stronger temperature dependence for D than equation 5.56 suggests, has been reported for binary gas mixtures and a constant pressure, and is also referred to by Bogdandy and Engell (1971, page 53).

$$D \sim T^n \quad 1.75 < n < 2 \quad (5.58)$$

On the basis of the temperature dependency of D in equation 5.56, and disregarding the influence of temperature on ε and ξ , D_p increases proportionally to $T^{1.5}$. When pore diffusion is rate controlling, the rate of reaction is proportional to the concentration and the pore diffusivity, as previously pointed out in equation 5.34. Hence, the rate of reaction is proportional to the square root of the absolute temperature for a constant pressure (insert $C = P/RT$ in equation 5.34). The temperature influence on the reaction rate is summarized in equation 5.59, by also taking the findings in equation 5.58 into account.

$$-\frac{dn_R}{dt} \sim T^n \quad 0.5 < n < 1 \quad (5.59)$$

The diffusion coefficient for CO₂/H₂-mixtures is largely independent of the mixing ratio (Bogdandy and Engell, 1971). The same authors report the following diffusion coefficients for mixtures and pure gases at normal pressure and temperature:

$$D_{H_2/CO_2} = 0.55 \frac{cm^2}{sec} \quad D_{H_2} = 1.24 \frac{cm^2}{sec} \quad D_{CO_2} = 0.104 \frac{cm^2}{sec}$$

Generally, the diffusion coefficients of binary mixtures with H₂ are about 4 times greater than those of binary mixtures with CO (Bogdandy and Engell, 1971). The higher rate of reaction for reduction with H₂ compared to reduction with CO, may partly be accounted for by the higher diffusion rate for H₂.

On the other hand, for diffusion through tiny pores, the deduced temperature relations are not valid. When the semi-diameter of the pores ($d/2$) is less than the mean free path of the gas molecules, collisions between the pore walls and the gas molecules are more frequent than between gas molecules with one another. For diffusion through such small pores, the Knudsen diffusion coefficient is relevant (Bogdandy and Engell, 1971).

$$D_{K,R} = \frac{d}{6} \left(\frac{8RT}{\pi \cdot M_R} \right)^{\frac{1}{2}} \quad (5.60)$$

The Knudsen diffusivity is proportional to the square root of the absolute temperature, and is independent of the total pressure. For a constant pressure, the temperature dependency of the reaction rate is expressed by equation 5.61 instead of 5.59, when Knudsen diffusion is rate controlling. In this case, the reaction rate decreases for an increasing temperature.

$$-\frac{dn_R}{dt} \sim T^{-0.5} \quad (5.61)$$

The Knudsen diffusion coefficient is also dependant on the pore shapes and their interconnections. Kolbeinsen (1982) have substituted $d/6$ by $4K_0$ in equation 5.60. K_0 is a characteristic parameter for the porous material and has the dimension length.

Chemical reaction

The mass transfer coefficient for a chemical reaction (k_s) is also called the rate constant. The temperature dependence of the rate constant is most usually expressed by equation 5.62, which is called the Arrhenius' equation.

$$k_s = k_o e^{-\frac{E}{RT}} \quad (5.62)$$

E is the activation energy of the actual reaction and k_o is usually called the frequency factor. A slightly different expression has also been proposed. The main difference between the two expressions is the incorporation of a linear temperature term in the latter. Since k_s increases exponentially with increasing temperature, this temperature dependence is much stronger than the linear temperature term, which usually is disregarded. The activation energy is usually determined by the slope in an Arrhenius plot between $\ln(k_s)$ and $1/T$.

$$\ln k_s = \ln k_o - \frac{E}{R} \cdot \frac{1}{T} \quad (5.63)$$

The activation energy varies greatly for different types of reactions, but may be in the order of 50 to 500 kJ for chemical reactions (Rosenqvist, 1985 a). The rate constant has a much stronger temperature dependence than D_p and k_g . The temperature dependency for the diffusion through gas films and pores, may also be set up in Arrhenius plots. In this case much lower values for the activation energy are found. Strictly speaking, the term "activation energy" should only be applied in connection with well defined reaction steps.

When a first order chemical reaction is rate controlling, the rate of reaction is proportional to k_s and the concentration ($C=P/RT$), in accordance with equation 5.40. The temperature dependency of the reaction rate is shown in equation 5.64 for a constant pressure.

$$-\frac{dn_R}{dt} \sim T^{-1} \cdot e^{-\frac{E}{RT}} \quad (5.64)$$

The reaction rate increases exponentially with increasing temperature. The influence of the linear temperature term, being much weaker, may be neglected.

Both k_0 and E are dependant on the reaction mechanism for the actual reaction and the rate controlling step. The rate determining step in the overall reaction from hematite to iron, is thought to be the separation of oxygen from $Fe_{1-y}O$ (Bogdandy and Engell, 1971) in the following sub-reaction:



The rate of reaction of this sub-reaction is dependant on the number of active sites on the surface. Several factors may influence on the number of active sites, such as the presence of inert gas or reaction products occupying active sites, and nucleation and nuclei growth. The reason why one site is active and another not, is not fully understood. The geometrical shape of the sites, such as sharp corners, is thought to play a part. Foreign ions may serve as nuclei. The mobility of iron ions in the neighbourhood of the sites may also be important. The mobility, or the solid diffusion rate, of iron ions is also dependant on the vacancy concentration, foreign ions, and other lattice defects. In this way, the rate constant is specific for each hematite type.

Reported numerical values for k_0 and E varies for the same reaction, but the variation is the greater for k_0 . From the above mentioned factors affecting k_0 and E , this could be expected, but various experimental conditions and mathematical treatment may partly account for the deviations. An indication of the numerical values for E in the reduction by CO, calculated by Trushenski, Li, and Philbrook (1974) by using a non-topochemical mathematical reduction model, is given here. The values lie within the range of reported activation energies.

Hematite → magnetite:	$E^{hm/mt} = 69.0$ kJ/mole
Magnetite → wüstite:	$E^{mt/wü} = 78.2$ "
Wüstite → iron:	$E^{wü/Fe} = 116$ "

Similar numerical values for H₂ reduction have been calculated in a topochemical three-interface mathematical model by Hara et al. (1976). However, Bogdandy and Engell (1971) have pointed out that, when the chemical reactions are rate controlling, a ratio of the reduction rates in H₂ and in CO of about 40 is said to be found.

5.2.4 Physical factors affecting the reduction

The nature of the solid changes during the course of the reduction. The changes should be related to characteristic hematite properties or variables which we are able to control, such as reduction temperature and time, gas flow rate, and gas mixture composition. The actual behaviour of the solid during reduction have been observed by several authors. Physical factors and changes, which are thought to be important for the course of the reduction, are emphasized in the following. For example, the volume, porosity, pore structure, and specific surface area are changing. Cracking may occur, and anisotropy of the reduction rate have been observed during the reduction. Some of these variables are invoked in the rate equations (specific surface and porosity), others are a prerequisite (constant volume), while some will be incorporated in the mass transfer coefficients.

Volume changes

For the reduction of hematite crystals to magnetite by CO at 1000°C, Edström (1953) measured an expansion of 25%. For the reduction to wüstite, a further expansion of 7-13% was measured. Due to metal sintering during the final reduction step, the overall expansion was only 25-27%. The reason for the expansion is thought to be the structural changes taking place during the reduction of hematite to magnetite. The oxygen atoms have to undergo a severe readjustment to convert the hexagonal lattice to a cubic lattice.

The expansion on reduction from hematite to magnetite and wüstite is temperature dependant (Brill-Edwards et al., 1965), as shown in figure 5.10. A minimum of only 16% expansion is observed at 700-800°C for the reduction to magnetite by H₂/H₂O. The minimum is associated with a change in the direction of the magnetite growth and the subsequent cracking. The expansion at 1000°C is 23% for the reduction from hematite to magnetite and about the same, 25%, for the reduction to wüstite. A slightly higher expansion was measured by Edström after reduction by CO at the same temperature.

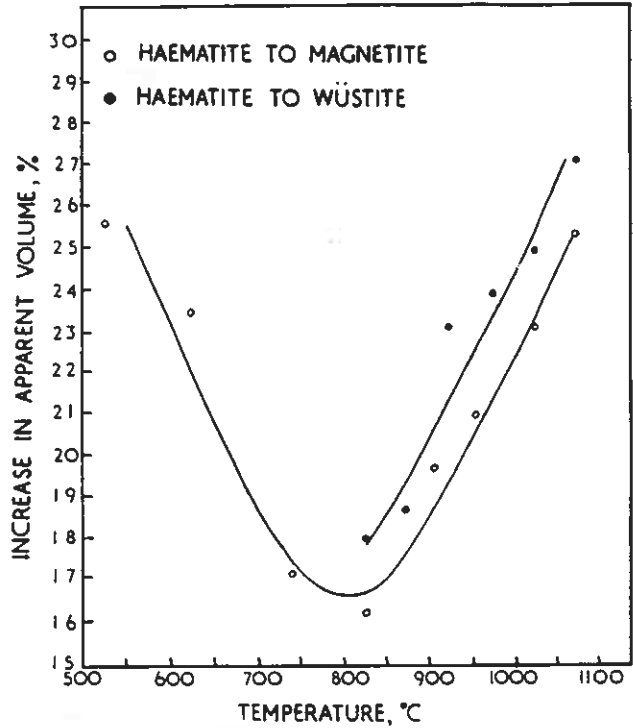


Fig. 5.10 Effect of reduction temperature on the expansion of dense polycrystalline hematite specimens ($\epsilon=0.12$) in H₂/H₂O (Brill-Edwards et al., 1965).

Slack (1979) measured the volume change of dense pellets ($\epsilon=0.10$) during the reduction in gas mixtures of H₂, CO, and CO₂, and found it to be independent of the gas mixture at 925°C, as shown in figure 5.11. However, the reducing potential is high for all the gas mixtures, since maximum content of CO₂ is 30%. Maximum expansion was 20-30%, usually within the first 40% of the reduction. Due to sintering, the pellets shrink so that

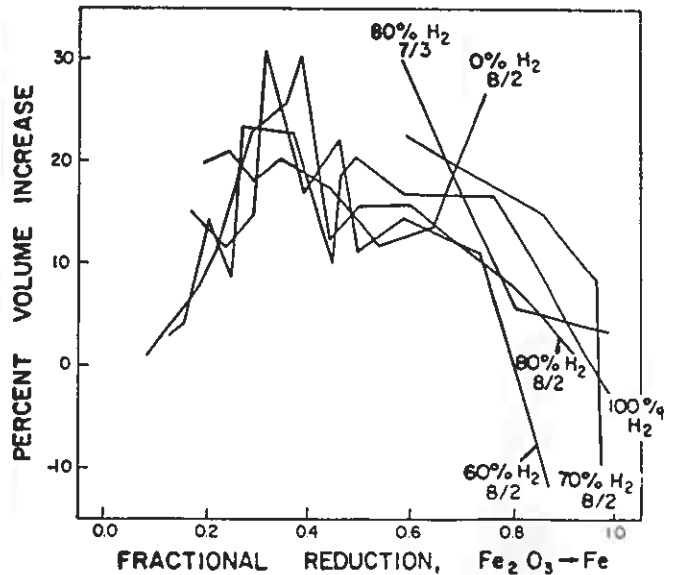


Fig. 5.11 Swelling of pellets reduced at 925°C in mixtures of H₂, CO, and CO₂ (CO/CO₂=7/3, 8/2), (Slack, 1979).

they are within a few per cent, or even less, of their initial size during the last 20% of the reduction. At lower temperatures, 725°C and 825°C, maximum expansion for all the samples was below 50% and 25%, respectively, except for the ones reduced in CO/CO₂ without hydrogen addition, which experienced abnormal swelling.

Other reduction tests with CO/CO₂=40/60 at approximately the same temperatures, 750, 850, and 950°C, have revealed a maximum expansion of only 10% for the reduction of hematite to wüstite at 950°C (Ekanem and Walker, 1989). Since the porosity of these pellets was about 12%, the same as those reduced by Slack and Brill-Edwards, the low expansion is probably due to a lower reducing potential and a lower rate of reduction. For the same reasons, an expansion of only 5% was found at 950°C for the reduction to magnetite with CO/CO₂=10/90. Using the same low reducing potential (CO/CO₂=10/90), Rupp et al. (1982) were able to measure an anisotropic volume change during the reduction of single hematite crystals to magnetite at 650°C. Parallel and vertical to the c-axis, a volume change of +4% and -1% was found, respectively. Among possible reasons for this anisotropic volume change is an anisotropic reduction rate (page 159).

Only little volume change is observed during the reduction to wüstite of highly porous specimens ($\epsilon=0.53$) made of reagent-grade hematite powder of small grain sizes (about 10 μm) (Pepper et al., 1976), although the reduction was carried out with CO/CO₂=60/40 in the temperature range 725-925°C. Stresses due to structural changes are dissipated in the porous specimens. Due to the small grain size some thermal sintering may occur. However, during a final reduction to iron, using higher CO contents, an expansion of about 40% did occur at the same time as whisker growth from the individual grains was observed.

Abnormal swelling

Swelling of 2-4 times of original size has been reported several times. Swelling causes operation difficulties in the blast

furnace and is often referred to as "catastrophic swelling". In the absence of hydrogen ($\text{CO}/\text{CO}_2 = 7/3$) in the previously mentioned experiments by Slack (1979), abnormal swelling of 200% took place at 50% degree of reduction at 725°C. The swelling was less pronounced at higher temperatures, and only normal expansion was observed at 925°C.

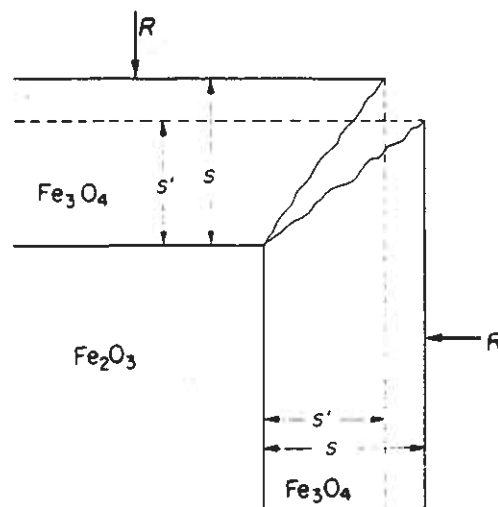
Abnormal swelling is often said to be caused by the growth of the iron phase as fibrous whiskers in CO (Watanabe and Yoshinaga (1968), Bleifuss (1972), Slack (1979), Gudenau et al. (1985)). The phenomenon is associated with non-topochemical reduction of wüstite (Bleifuss, 1972). Whiskers do not grow in H_2 , according to Slack (1979), Gudenau et al. (1980) and John and Hayes (1982). The influence of temperature and different CO/CO_2 -gas ratios on the precipitation and growth behaviour of metallic iron on wüstite, have been studied in situ during the reduction in a specially developed SEM by Gudenau et al. (1983 and 1985). Whiskers developed in the temperature range 700-1000°C for $60\% < \text{CO} < 80\%$, while porous iron developed for higher contents of CO above 800°C, and dense iron formed below 800°C for $\text{CO} > 90\%$.

A survey of the experimental factors controlling the tendency for whisker formation has been given by Nicolle and Rist (1979). The abnormal swelling of ores and pellets is fundamentally related to their original microstructure (Watanabe and Yoshinaga, 1968). Hematite "intergrowth" (texture appearing when magnetite is oxidized at low temperatures) and microtwins are thought to serve as weak planes along which rapid reduction from hematite to magnetite and rapid growth of whiskers occur.

Cracking

Grain fracture due to expansion during the reduction from hematite to magnetite, has been schematically illustrated by Meyer et al. (1967) and later by Ball et al. (1973), as shown in figure 5.12. It is assumed that reduction proceeds topochemically and that the volume increases perpendicular to the

hematite cube face. The thickness, S , of the magnetite layer is assumed to be $1.11S'$, where S' is the thickness of the original hematite layer. This volume increase causes the cube to split along the boundary faces. Cracking contributes to a more rapid reduction.



During the reduction of polycrystalline hematite in H_2/H_2O , both transgranular and intergranular cracks have been observed in the magnetite formed below $700^\circ C$ by Brill-Edwards et al. (1965). Above this temperature fractures occur in the hematite.

Degradation of sinters during reduction at about $500-600^\circ C$, is caused by the transgranular cracks which develop in the reduction stage of hematite to magnetite (Watanabe and Yoshinaga, 1968). The cracks are more vigorously developed in CO than in H_2 atmosphere and accompanied by carbon deposition.

Decrepitation, on the other hand, may occur during heating of hematite to about $300-500^\circ C$ for two reasons (Watanabe and Yoshinaga, 1968). When compact hematite ores contain small amounts of limonite/goethite, the compact structure make expulsion of combined water difficult, resulting in decrepitation. Hematite ores, composed of parallel arrangement of schistose specular hematite which is elongated parallel to the basal plane (0001), may be exfoliated along the lineation during heating by the thermal expansion (example: a brazilian ore).

Anisotropy of the reduction velocity

Hematite is preferentially reduced in a direction vertical to the c -axis (Meyer et al., 1967). The phenomenon is called anisotropy of the reduction velocity and is visualized in figure 5.13 as

presented by Ball et al. (1973). Two adjacent hematite crystals with c-axes perpendicular to one another are shown in the figure. As a result of preferential reduction perpendicular to the c-axis, reduction proceeds further into crystal b than into crystal a. When hematite is reduced to magnetite, the hexagonal oxygen lattice of the

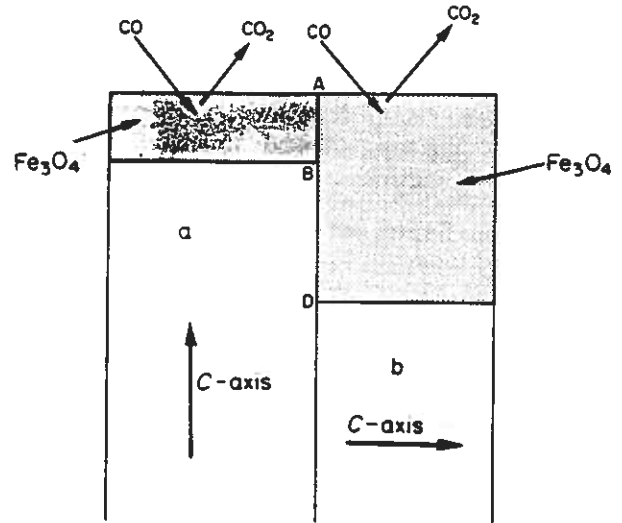


Fig. 5.13 Anisotropy of the reduction velocity in adjacent hematite grains (Ball et al. 1973)

hematite structure has to be

transformed to a cubic oxygen lattice of the magnetite structure. Perpendicular to the c-axis of the hematite crystal, this transformation is carried out by a minimum degree of oxygen migration, at the highest rate. The preferred growth direction is conjectured to be in the (0001) plane of the hematite and the (111) plane of the magnetite above 700°C, according to Brill-Edwards et al. (1965) and Swann and Tighe (1977). Elongated hematite grains, with parallel orientated crystals and the c-axis parallel to the direction of elongation, can be expected to be reduced to magnetite at a higher rate than similar grains with the c-axis vertical to the elongation direction.

Anisotropy of the reduction velocity is considered to contribute to pellet weakness during the course of reduction (Meyer et al., 1967 and Ball et al., 1973). Due to the greater volume increase in the magnetite formed in crystal b in figure 5.13, disruptive forces are set up along the crystal boundary BD, which lead to tearing. The tendency for tearing to occur will depend on the disparity of the c-axis in adjacent hematite crystals.

Pore structure changes

On the assumption of a constant volume, the intermediate and final products in the reduction of nonporous hematite obtain a

porosity of 2% for magnetite, 17% for wüstite, and 53% for iron, referring to appendix A.2. The actual pore structure formed is dependant on both the degree of reduction, reduction temperature, time, and gas mixture, besides the initial hematite pore structure.

Since magnetite is an intermediate product in the reduction of hematite, the microstructure of the magnetite may have a significant effect on the kinetics of the hematite reduction and the subsequent magnetite reduction. Brill-Edwards et al. (1965) reduced polycrystalline dense hematite specimens ($\epsilon=0.12$) to magnetite, using hydrogen. They found that the pores formed between 400°C and 700°C are spherical and randomly distributed, while those formed between 700°C and 900°C are elongated and directional. Brill-Edwards and coworkers did further observe that the amount of porosity decreased at temperatures above 900°C, being completely absent at 1000°C. Pores were, however, formed at 1000°C if the reduction was carried out rapidly.

Srinivasan and Sheasby (1981) reduced hematite particles (105-140 μm) to magnetite with H_2 in a fluidized bed at 700°C. They observed that the magnetite adjacent to the hematite cores appeared pore free. The solid band of magnetite moved in with the shrinking core, developing pores in the outer circumference. The mean pore diameter was 0.043 μm after 12 seconds reduction, measured by SEM. The mean pore diameter increased with time to 0.109 μm after 120 seconds. By raising the temperature from 700 to 800°C, the mean pore size approximately doubled.

According to Ünal and Bradshaw (1983), porous magnetite is formed at 600°C and dense magnetite is formed at 1000°C if the reduction of hematite is carried out in CO/CO_2 , analog to H_2 reduction. At 600°C the magnetite formed topochemically, but at 1000°C the magnetite appeared as parallel lamellas in each grain. The lamellas thickened sideways as the reaction progressed. At 600°C, about 8.8% microporosity was formed with the pores ranging in radius from 0.025 to 0.35 μm . The pore structure became finer

for an increasing CO pressure (at faster rates). No further pore coalescence occurred once the pore structure had formed.

The pores (called tunnels) developed in magnetite are about two times smaller for H_2 - H_2O reduction than for CO - CO_2 reduction of hematite single crystals (observations in SEM by Porter and Swann, 1977). Increasing the temperature from 400 to 700°C, caused the "tunnel" diameter to increase by a factor of about 10, from 8 to 80 nm.

The formation of two distinct morphological types of magnetite is dependant on the oxygen potential in the reduction gas, both when the reduction is carried out with H_2/H_2O (Baguley et al., 1983) and with CO/CO_2 (Hayes and Grieveson, 1981). Porous magnetite is formed at relatively low oxygen potentials and lath magnetite at high oxygen potentials, as shown in figure 5.14 for the H_2 - H_2O system (Baguley et al., 1983). Lath magnetite is dense, and grows directionally as lamellas in the hematite. The conditions for the formation of porous or lath (plate) magnetite, predicted by Hayes and Grieveson (1981), are indicated by the dotted line in the figure. The predictions are based on the transition to take place at a constant free energy difference between the hematite and the reducing gas mixture. The predicted dotted line coincides with a transition zone where both lath and

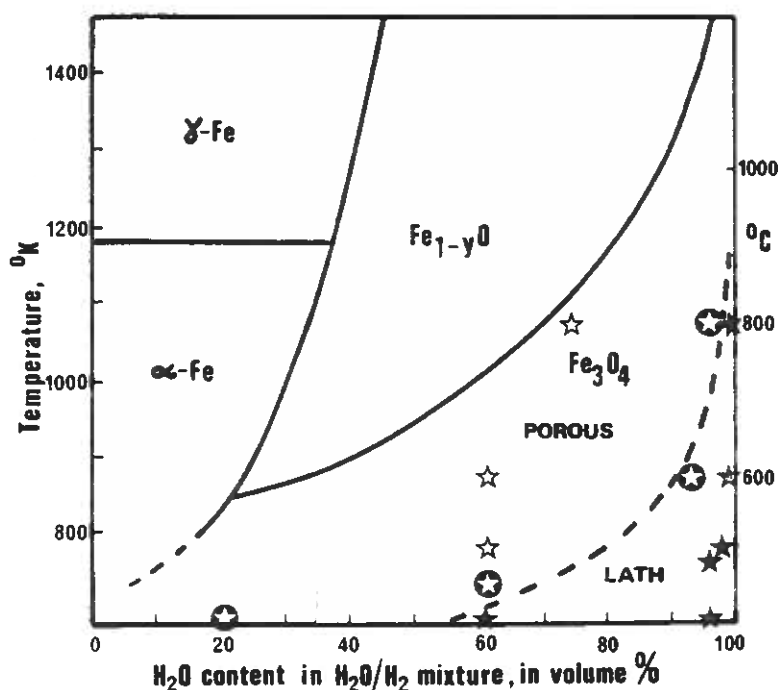


Fig. 5.14 Product morphology observed during reduction in H_2 - H_2O gas mixtures (Baguley et al., 1983). Open stars: porous, closed stars: lath magnetite, closed circles with open stars: both porous and lath magnetite

porous magnetite is found (open stars in closed circles). There is obviously some disagreement concerning the morphological types formed at high temperatures ($>900^{\circ}\text{C}$), since figure 5.14 indicates formation of porous magnetite, while other authors, Brill-Edwards and coworkers (1965) and Porter and Swann (1977), also find dense magnetite at this temperature.

The nature of the wüstite formed is affected by the initial reduction step from hematite to magnetite, the reduction gas mixture, temperature and time. Bleifuss (1972) finds that after reduction for one hour in $\text{CO}/\text{CO}_2=50/50$ at 900°C the wüstite formed is very fine-grained open and porous, but at 1100°C a much denser wüstite is formed with fewer, but larger pores. Holding the wüstite at 1100°C for an additional hour allows time for recrystallization and development of coarse particles. Pellets reduced to wüstite at 840°C are more quickly reduced to iron than pellets initially reduced to wüstite at 1020°C (Walker and Carpenter, 1970). The higher reduction rate is attributed to the higher porosity of the wüstite formed at the lower temperature.

The mean pore size of the iron obtained, increases with increasing reduction temperature, as shown in figure 5.15 by Turkdogan and coworkers (1971a). Above 900°C the increase is rapid. Below 900°C the pore structure becomes finer for a decreasing

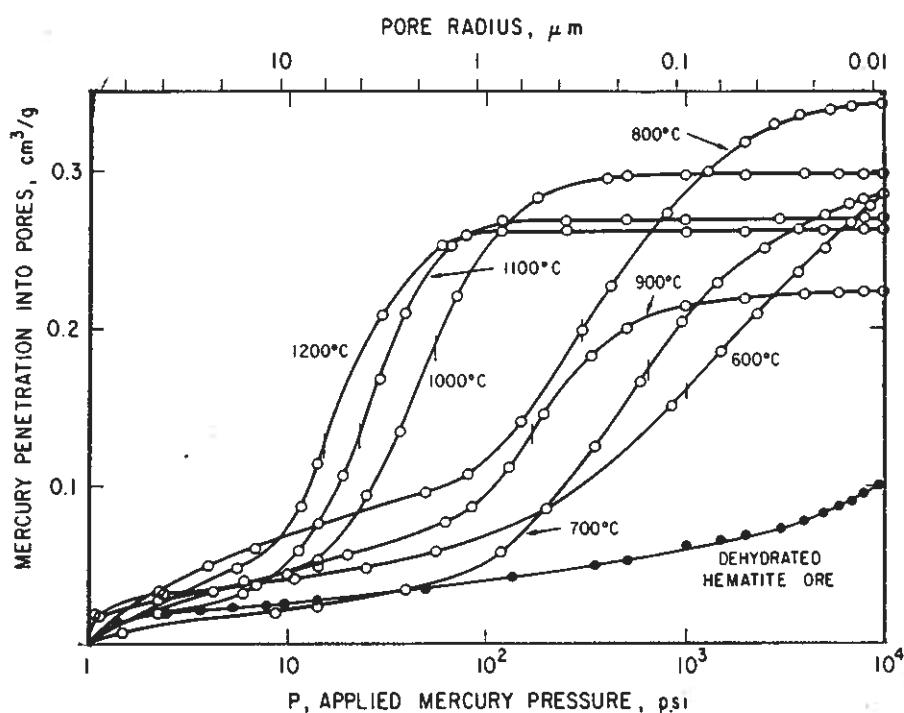


Fig. 5.15 Effect of temperature on pore size distribution in iron formed during H_2 reduction of hematite granules (Turkdogan et al 1971 b).

temperature. This is accompanied by a rapid increase in the specific surface area. The reduction was accomplished on high-grade hematite granules (diameter about 1mm) in hydrogen. Bleifuss (1972) could not observe any further structural change on holding the iron at temperature once reduction was complete.

Microscopic observations by Edström (1953) have shown that reduction of hematite crystals by H_2 yields a more finely porous wüstite and iron than reduction by CO. Turkdogan and Vinters (1972) observed that a more finely porous iron does also develop during H_2 reduction of dense wüstite. The pore size distributions in cylindrical porous pellets after reduction by H_2 , CO and $H_2/CO=40/60$, are shown in figure 5.16 by Szekely and El-Tawil (1976). It is shown that the higher the CO content of the reduction gas the larger the resultant pore diameter. The time required to attain a given extent of reduction is markedly dependant on the gas composition, as previously pointed out. Szekely and El-Tawil (1976) find that the composition dependence on the reaction time is nonlinear. For example, 4 minutes was enough to reach a 40% degree of reduction by H_2 , 6 minutes by $H_2/CO=50/50$, but 10 minutes was required by CO.

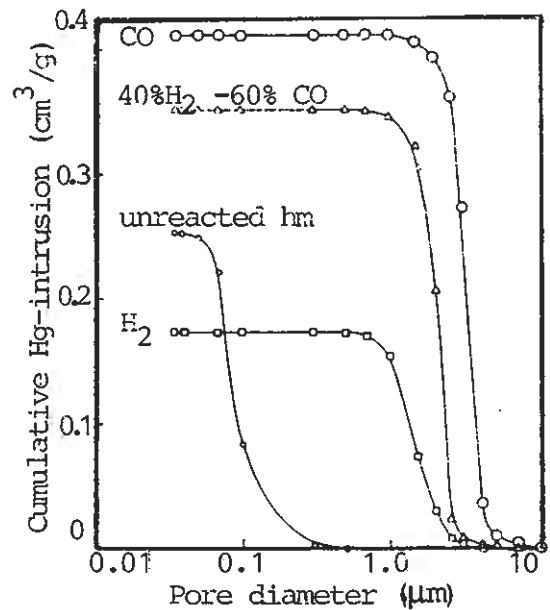


Fig. 5.16 Pore size distribution of unreacted hematite and after reduction (Szekely and El-Tawil, 1976)

Specific surface area changes

Specific surface area is a convenient measure for concentrates which have not been formed into pellets or briquettes. The change in surface area during the reduction is closely connected with the previously mentioned physical factors, especially to the porosity. The specific surface area is dependant on variables such as temperature, time and gas mixture, but also on initial

surface area.

Doherty et al. (1985) reduced Brazilian hematite concentrate (MBR pellet feed fines) of grain sizes in the range 180-250 μm in a fluidized bed. Particles obtained by sieving the ore as received, had a specific surface area of 3 m^2/g after degassing at 180 $^\circ\text{C}$, while particles of the same size, obtained by crushing larger lumps, had a surface area of 1 m^2/g . During heating in inert atmosphere, the surface areas of both samples initially increased and then rapidly decreased, as shown in figure 5.17 a. The main difference between the two samples is in the proportion of small particles (2-5 μm) separated and subsequently sintered in the preheating period. Scanning electron micrographs showed that the increase in surface area is mainly due to the opening of cracks, about 1 μm across.

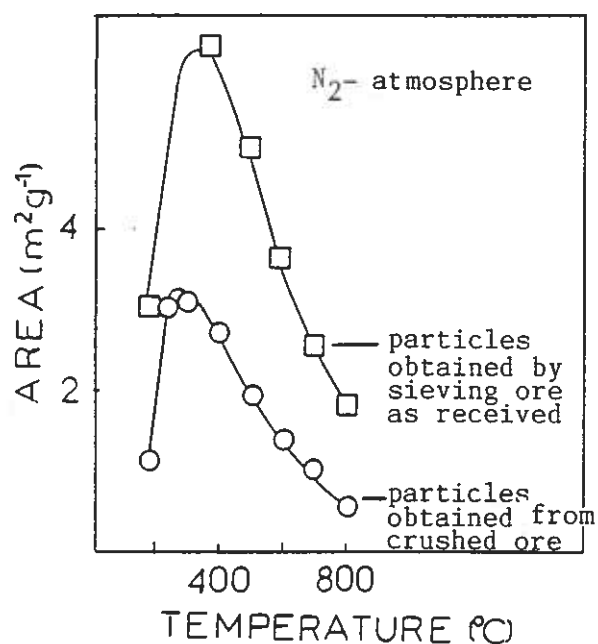


Fig. 5.17a Effect of heating in N_2 for 15 min. on surface area (Doherty et al., 1985).

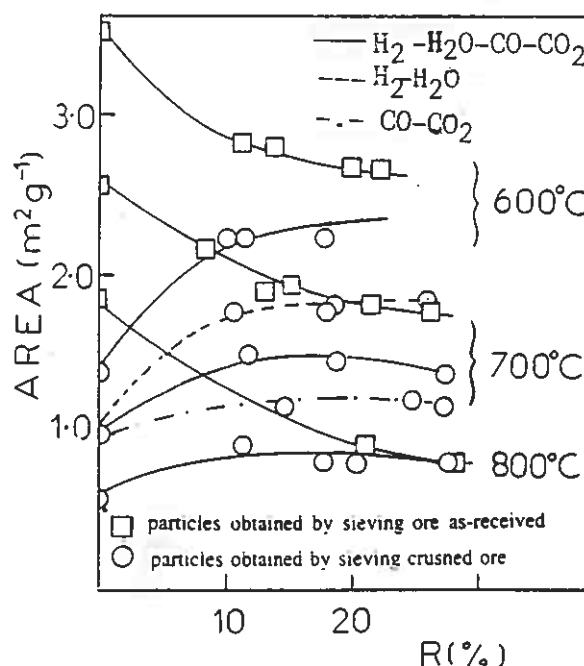


Fig. 5.17b Changes in surface area during the reduction to wüstite, (Doherty et al., 1985).

The changes in specific surface areas during the subsequent reduction to wüstite ($R=30\%$) are shown in figure 5.17b. Most of the reduction experiments were carried out in gas mixtures of H_2 , H_2O , CO , and CO_2 (unbroken lines in the figure). While there is an initial increase in the surface area for the sample with an

area of $1 \text{ m}^2/\text{g}$ prior preheating, there is an initial decrease for the sample with a surface area of $3 \text{ m}^2/\text{g}$. The surface areas after the reduction do not differ much for the two different samples. The surface area decreases considerably for an increasing reduction temperature due to pore coarsening during sintering. The surface area is only slightly altered during the magnetite to wüstite step.

The effect of gas composition on the specific surface area can be observed both in figure 5.17 b and 5.18. Larger surface areas are obtained after reduction with $\text{H}_2\text{-H}_2\text{O}$ than after reduction with CO-CO_2 . Surface areas obtained after reduction with gas mixtures are larger than those obtained using CO-CO_2 and smaller than those obtained using $\text{H}_2\text{-H}_2\text{O}$, referring to figure 5.17b. Similar results were obtained by Hutchings et al. (1987).

When hematite is reduced in CO/CO_2 mixtures the surface areas of both iron and wüstite are about 2/3 of those for $\text{H}_2/\text{H}_2\text{O}$ reduction in the entire temperature range $800\text{-}1200^\circ\text{C}$ as illustrated in figure 5.18 by Turkdogan and Vinters (1972). The curve b is for iron and wüstite formed by $\text{H}_2/\text{H}_2\text{O}$ reduction and the curve c is for CO/CO_2 reduction. Notice that the surface area of the wüstite formed is only slightly smaller than of the iron formed.

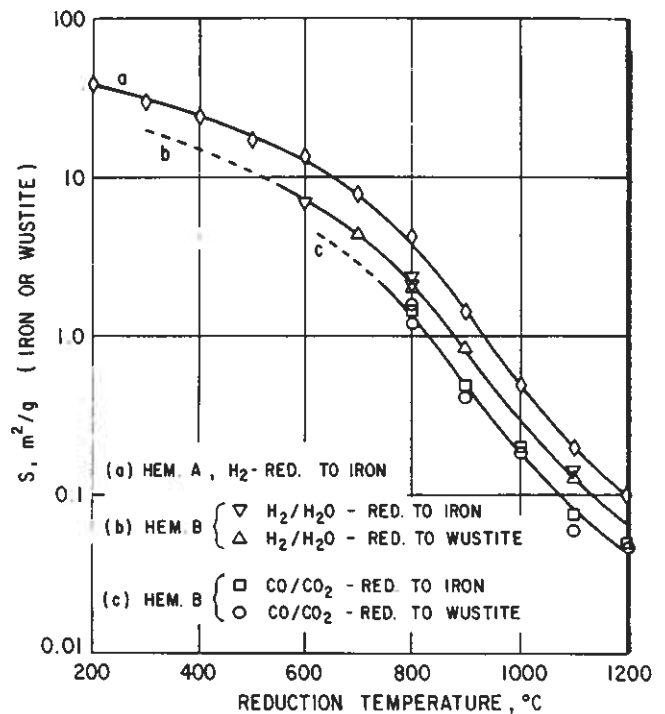


Fig. 5.18 Internal pore surface area of iron and wüstite formed by reduction of hematite ores (Turkdogan and Vinters, 1972).

The changes in surface area during the complete reduction to iron in hydrogen, are shown in figure 5.19 by Sheasby and Gransden

(1975). Three high-grade specular hematites, from S. America¹, Canada², and Australia³, in the size range 109-140 μm , were reduced in a fluidized bed, which defluidized shortly after iron formation. The surface areas of the three hematites increase rapidly during the reduction to magnetite, while the surface areas are only slightly changed during the magnetite to wüstite step.

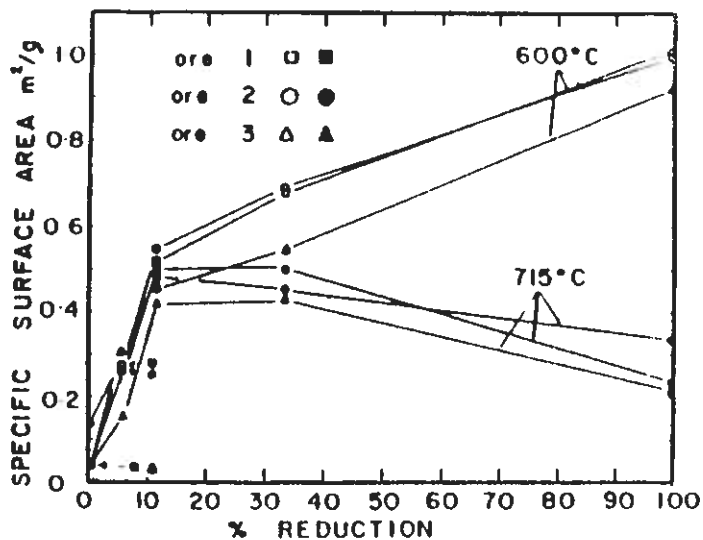


Fig. 5.19 Surface area developed during H_2 reduction for three specular hematites (109-140 μm), Sheasby and Gransden (1975).

The same trend during the initial reduction, was observed in figure 5.17b for the hematite with the smallest surface area. It appears from figure 5.19 that further reduction to iron is accompanied by a small decrease in surface area due to sintering at 715°C, while the surface area continues to increase at 600°C where sintering is not pronounced. (The latter iron spontaneously warm from room temperature on exposure to air, due to reoxidation.) Sheasby and Gransden (1975) found that the surface area developed during reduction is smaller the slower the rate of reduction. Surface areas of partly reduced samples change only slowly at the reduction temperature, or even higher temperatures, in an inert atmosphere.

The decline in surface area which takes place when a hematite ore is held at temperature in a nitrogen atmosphere, is also shown in figure 5.20 (from the experimental work by Koo and Evans, 1978, reviewed by Sohn and Wadsworth, 1979). The decrease in surface area is more severe the higher the temperature. The surface area of iron produced by hydrogen reduction shows the same trend. These experiments were carried out with a Venezuelan ore sample consisting of 59% goethite and 40% hematite. Two other ores containing less goethite (37% and 20%) revealed the

same trend. The structural change occurring during both preheating and reduction is a coalescence of small pores to form larger pores and not a removal of pores.

Bleifuss (1972) stated that sponge iron has a unique texture in that it does not seem to reflect the microtexture of the original ore, but is controlled by the microtexture and grain size of the wüstite formed.

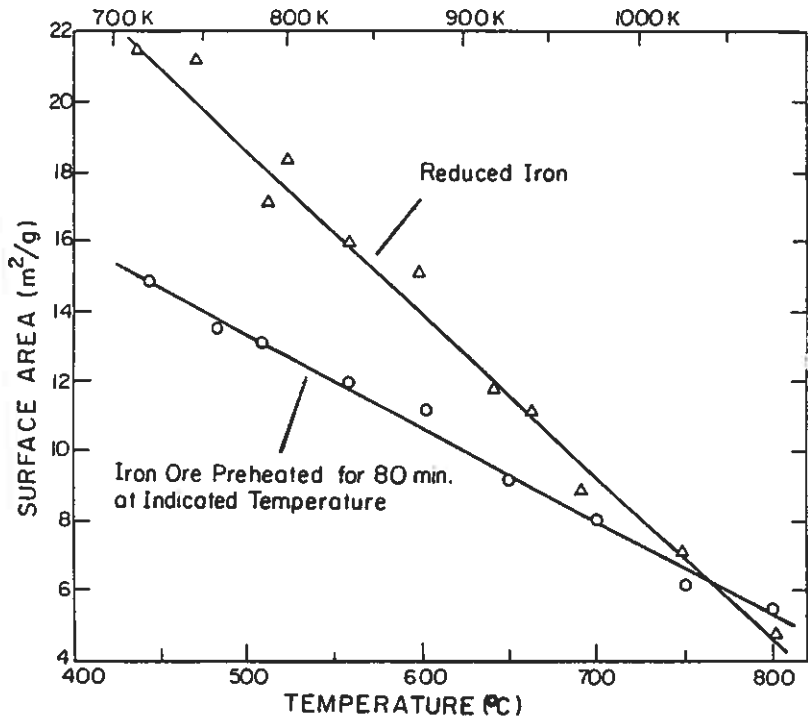
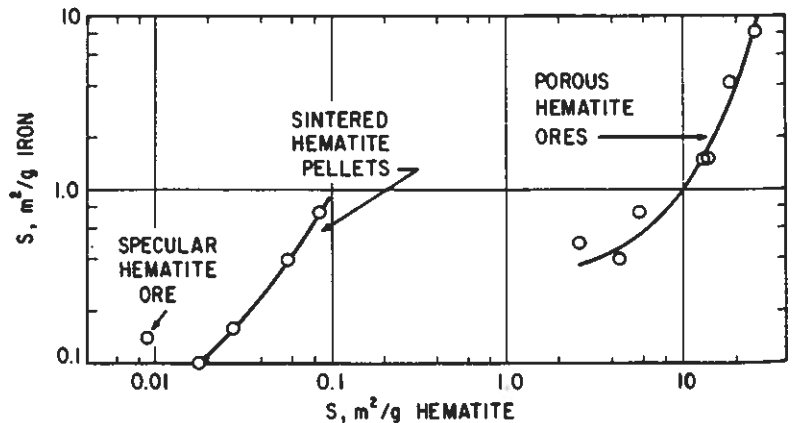


Fig. 5.20 The effect of holding for 80 min. under N₂ at various temperatures on the ore surface compared to the iron surface produced by hydrogen reduction of the hematite (Koo and Evans, 1978).

Turkdogan and Vinters (1972), on the other hand, observed that the larger the pore surface area of the hematite ore, the larger the pore area of the iron formed, referring to figure 5.21.



In accordance with the findings of Turkdogan and Vinter (1972) it may be concluded that the original hematite microstructure may affect the rate of reduction and the microtexture of the iron formed. The nature of the wüstite formed is of course also important.

Fig. 5.21 Relation between the internal pore surface area of H₂-reduced iron at 800°C, and the pore surface area of the corresponding hematite (Turkdogan and Vinters, 1972).

5.2.5 Chemical factors affecting the reduction

Trace elements in the hematite lattice, substituting Fe^{3+} , may enhance, retard, or not affect the reduction rate. The development of intermediate phases may be modified. Bleifuss (1972) states that small amounts of manganese tend to lower both the temperature and the reduction potential required for wüstite formation. Trace elements at the grain surfaces or in the lattice may act as catalysts or nuclei for the formation of intermediate and final products and hence increase the rate of the reduction. The presence of trace elements at the grain surfaces is likely if the hematite has undergone metamorphism. Trace elements crystallized in separate inclusions during the formation of the hematite, or separate phases formed during reduction, may also influence on the rate of the reduction.

Trace elements in the lattice

Theoretically, cations larger than Fe^{3+} tend to open the hematite lattice because of their size. Most of the actual larger cations have a lower charge and tend to open the structure because of their charge deficiency. Hence, diffusion is favoured and the rate of reduction is expected to increase. The opposite effect is expected for cations smaller than Fe^{3+} . The rate enhancing effect is expected to increase for an increasing cation size. Ionic radii (SI, 1974) of cations which possibly may substitute Fe^{3+} (0.64 Å):

<u>Rate enhancing</u>	<u>Rate retarding</u>
K^+ (1.33 Å)	P^{5+} (0.35 Å)
Ca^{2+} (0.99 Å)	Si^{4+} (0.42 Å)
Na^+ (0.97 Å)	Al^{3+} (0.51 Å)
Mn^{2+} (0.80 Å)	Cr^{3+} (0.63 Å)
Zn^{2+} (0.74 Å)	
Ni^{2+} (0.69 Å)	
Ti^{4+} (0.68 Å)	
Mg^{2+} (0.66 Å)	

The ionic radius of Fe^{2+} (0.74 Å) is slightly larger than of Fe^{3+} (0.64 Å). Hence, in the further reduction to wüstite and iron, it would be expected that the effect of Mg^{2+} (0.66 Å) and Ni^{2+} (0.69 Å) substitution changes from rate increasing to rate retarding. Ti^{4+} is reduced to Ti^{2+} (0.94 Å) and the rate retarding

effect may be expected to continue. Zn^{2+} , having the same ionic radius as Fe^{2+} , is not expected to disturb the lattice structure.

Trace elements in the lattice may locally act as catalysts for the water-gas shift reaction inside grain pores. In this way the rate enhancing effect of H_2 is maintained. Known catalysts are among others Cu, Co, Ni and Cr, as previously mentioned in section 2.3.2. The mentioned elements have been traced in the hematites in the present investigation, reported in chapter 4.

Alkalis

The influence of alkalis on the reduction of iron oxides and ores has been dealt with by numerous authors (22 references by Roederer et al., 1987 a). Different treatments (pelletizing, sintering...) have been applied, making it difficult to derive an overall view of the obtained results. However, it is generally admitted that alkalis (especially the heavier) favour the reduction from hematite to iron, when added in small quantities (a few percents), and that the presence of alkalies is detrimental to the mechanical properties.

Alkalis (K^+ and Na^+) promote whisker growth (Nicolle and Rist, 1979), swelling and degradation (Stephenson et al., 1980). Concentrations of K_2O and Na_2O above 0.2% promote pellet swelling, but addition of SiO_2 eliminates excessive swelling as alkali silicates are formed (Ball et al., 1973). Alkalis (0.5-2%) added in the form of carbonates (K_2CO_3 , Na_2CO_3 and $NaKCO_3$) promote catastrophic swelling or disintegration due to fissuring, but added as chlorides (KCl and NaCl) alkalis contribute to normal swelling (Bleifuss, 1972).

The rate of reduction is increased on addition of potassium, at all stages (Nakagawa and Ono, 1985), both during reduction of hematite to magnetite and wüstite (Roederer et al., 1987 a,b,c) and during reduction of wüstite to iron (Gougeon et al., 1986). However, neither of these authors were able to detect potassium dissolved in the lattices of neither the oxides nor the iron. Regardless of the doping techniques applied by Gougeon et al.,

annealing the wüstite single crystals with K_2CO_3 (1%) at 1000/1100°C for 1-24 hours, surface doping at room temperature (dipping in a solution of K_2CO_3), or gas phase doping, no potassium was detected in the wüstite lattice or in the reduced iron. Wüstite doping affects only the surface of the particles, and nucleation and growth of iron are favoured. All these authors find that the reduction products, it be magnetite, wüstite or iron, are more porous as a consequence of potassium doping. Further reduction is partly enhanced because of the better permeability for the gas.

The effect of potassium on the reduction of dense plates of hematite, magnetite and wüstite is seen in the figures 5.22-5.24, respectively (Nakagawa and Ono, 1985). The doping were accomplished by immersing the plates in KCl saturated solutions. The reduction experiments were all carried out at 900°C. The gas composition in each step was:

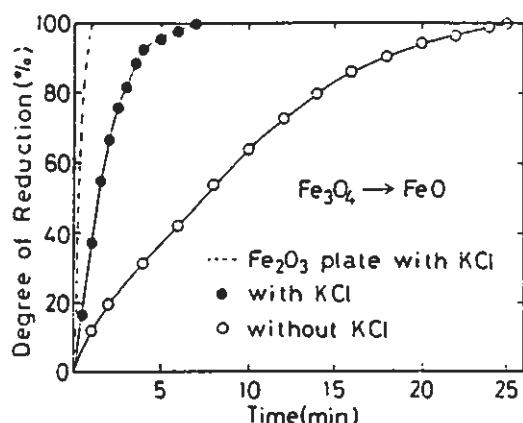
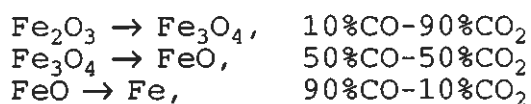


Fig. 5.23 Effect of KCl dip-doping on reduction of dense Fe_3O_4 plate to FeO , Nakagawa and Ono (1985).

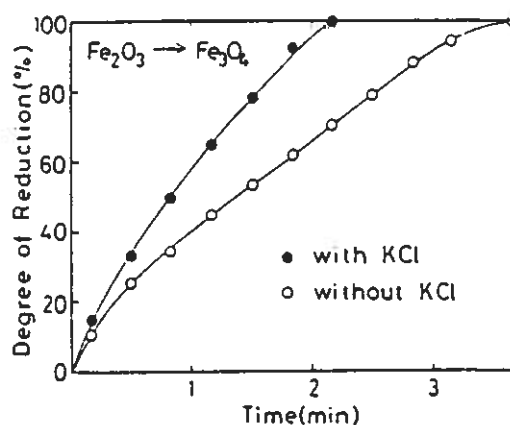


Fig. 5.22 Effect of KCl dip-doping on reduction of dense Fe_2O_3 plate to Fe_3O_4 , Nakagawa and Ono (1985).

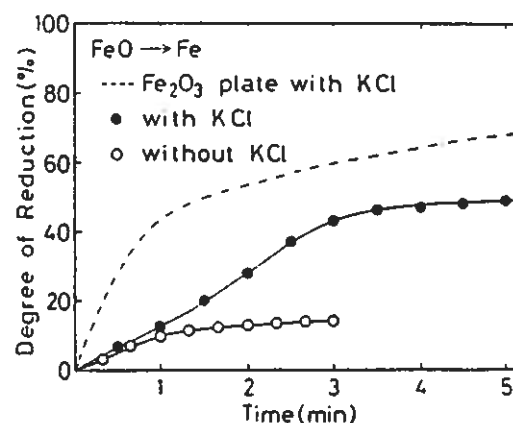


Fig. 5.24 Effect of KCl dip-doping on reduction of dense FeO plate to Fe , Nakagawa and Ono (1985).

From the figures 5.22-5.24 it is obvious that potassium has a rate enhancing effect at all the reduction stages. Hence, the

increased reduction rate of intermediate products, magnetite and wüstite, is not only an effect of the increased porosity.

On CO/CO₂ reduction of hematite single crystals, dip-doped in a solution of K₂CO₃, Roederer et al. (1987 a, c) find that the rate enhancing effect decreases with increasing temperature from 500°C to 940°C and thereafter increases. The potassium favours porous magnetite growth rather than lamellar growth and concentrates in a dense layer of magnetite between the hematite core and the outer porous magnetite. In fact, the potassium is mainly found in the core centre after the complete reduction to magnetite. The proposed interpretation is based on the transient formation of KFe₁₁O₁₇, which acts as a nucleation catalyst and lower the activation energy from 75.2 kJ/mole to 42.6 kJ/mole. According to Roederer et al. (1987 a), diffusion of K⁺ into the oxide lattice is improbable, due to the large size difference between K⁺ and Fe³⁺.

Earth alkalis

The reported effects on reducibility of additions of limestone, dolomite, or lime to pellet feed mixes are quite varied and in some instances not in agreement, possibly because of differences in the concentrates or the balling, drying and induration procedures (Stephenson et al., 1980). MgO in the pellet feed material, however, appears to increase reducibility, decrease low-temperature breakdown and improve strength (Stephenson et al., 1980). There seem to be an optimum MgO content (1.5%) in fluxed pellets at which the reducibility is the best (Friel and Erickson, 1980). Dip-doping of hematite in a solution of Ca(OH)₂ increases the reduction rate (Ettabirou et al., 1986).

The reduction rate, of synthetically prepared sintered hematite tablets with a total impurity content of 1% based on the elements Ca or Mg, is the highest for the tablets containing MgO during the initial hematite reduction and for the CaO tablets during magnetite and wüstite reduction (Bruijn et al., 1990). There was an expansion in the tablets containing CaO and a contraction in the MgO containing tablets at the later stage of the reduction. On adding 0.5% Si to tablets containing 0.5% Ca or 0.5% Mg,

swelling is considerable at the later stage of the reduction (900°C) due to formation of Ca- or Mg- silicates, and the reduction rate is retarded due to some fayalite formation ($2\text{FeO}\cdot\text{SiO}_2$) which cover each grain.

While Ca^{2+} dissolved in the wüstite promotes whisker growth, observed by many, Mg^{2+} does not (Nicolle and Rist, 1979). The reason is thought to be the size difference of these ions. Ca^{2+} , being larger than Fe^{2+} , tends to open the wüstite lattice, making diffusion favoured relative to the chemical reaction. Whisker growth is dependant on a high diffusion rate. Mg^{2+} , being smaller than Fe^{2+} , has an opposite effect on the wüstite lattice. Hence, the chemical reaction is favoured relative to diffusion. If CaO is added to pellets and fired, calcium ferrite crystals develop and no Ca^{2+} dissolves in the wüstite during reduction. This prevents whisker formation (Nicolle and Rist, 1979).

The presence of a small amount of CaO (0.5%) can cause a high degree of swelling in pellets, particularly if the SiO_2 content is low, but further addition of CaO has proved effective in preventing abnormal swelling (Ball et al., 1973 and Stephenson et al., 1980). This behaviour of pellets is understood from what has already been mentioned. The formation of Ca-silicates causes a high degree of swelling while fayalite formation (at high SiO_2 contents) does not. Formation of Ca-ferrite from the added lime, if fired prior to reduction, prevents whisker formation and excessive swelling.

The effect of lime addition to wüstite is to extend considerably the range of gas conditions where porous iron is formed (Nakiboglu et al., 1986). The amount of lime needed to change the iron morphology from dense to porous is dependant on reduction temperature and gas composition. 0.02% CaO is enough at 800°C in a strong reducing gas (90% H_2 /10% H_2O), while 0.10% CaO is necessary in 80% H_2 /20% H_2O . More lime is necessary to change the iron morphology for reduction by CO/CO_2 than by $\text{H}_2/\text{H}_2\text{O}$. Dense iron layers are formed at first, which break down and become porous. No calcium was dissolved in the iron.

Si

There is a general agreement in the literature that Si retards the rate of reduction of hematite (Suzuki et al, 1981, Bruijn et al., 1990, Ettabirou et al., 1986). However, the rate retarding effect is mainly due to the formation of separate phases, especially fayalite ($2\text{FeO}\cdot\text{SiO}_2$), or due to surface effects, and not because of distribution of Si^{4+} in the lattice.

Fayalite is capable of coating surfaces and in this way it effectively retards the rate of reduction. SiO_2 may react with both magnetite and wüstite to form fayalite at moderate reduction temperatures, but not with hematite. Fayalite formation became important at 1000°C during the reduction of a hematite ore (Carol Lake), containing 4.2% SiO_2 , to magnetite (Ünal, 1985). Fayalite formed from wüstite becomes important above 800°C (Ünal, 1985). The formation of fayalite is dependant on grain sizes and gas composition, and may start at lower temperatures.

SiO_2 addition to pellets is known to fight abnormal swelling and decrepitation (Stephenson et al., 1980), but it is not as efficient as CaO (Ball et al., 1973).

The rate of reduction of synthetically prepared sintered hematite tablets containing 1% Si is much lower than those containing 1% Ca or 1% Mg (Bruijn et al., 1990). The rate retarding effect is thought to be due to fayalite formation which also contributes to a contraction in the tablets (no swelling) at the later stage of the reduction. On adding 0.5% Ca or 0.5% Mg to tablets containing 0.5% Si, swelling is considerably at the later stage of the reduction (at 900°C) due to formation of Ca- or Mg-silicates, as previously mentioned.

However, Ettabirou et al. (1986) found that the rate retarding effect of SiO_2 (quartz) in the reduction of Itabira hematite to magnetite and to wüstite was most pronounced at the lower temperatures ($<800\text{--}900^\circ\text{C}$) where fayalite formation is not expected to be important. At 1000°C there was a small rate

retarding effect during reduction to magnetite with $\text{CO}/\text{CO}_2=10/90$, while there was a small rate enhancing effect with $\text{CO}/\text{CO}_2=2/98$. A weak reducing gas implies long reduction times to obtain the same degree of reduction. Hence, fayalite formation will be more complete. However, other reactions with impurities in the ore are also possible (formation of Ca-silicate). The specimens without SiO_2 were made by dissolving the quartz in the ore, using HF. This could lead to false interpretation of the result, since HF treated specimens will be more porous and have a more rough surface. For this reason, the effect of surface doping pure hematite crystals with a SiO_2 powder, was also studied by Ettabirou et al. (1986). The rate of reduction to magnetite by $\text{CO}/\text{CO}_2=10/90$ was retarded, both at 600 and 700°C. Hence, there is a rate retarding effect of Si during reduction of hematite at low to intermediate temperatures, which is not due to fayalite formation.

Al

Addition of Al_2O_3 powder in sintered pure hematite tablets have a markedly rate retarding effect (Suzuki et al., 1981, Bruijn et al., 1990 and Chinje and Jeffes, 1989).

Suzuki et al. (1981) find this rate retarding effect far more pronounced for the addition of 5% $\gamma\text{-Al}_2\text{O}_3$ powder than 5 % amorphous SiO_2 . The tablets were preheated 6 hours at 1100°C prior reduction in hydrogen at a rising temperature (10°C/min). The greater rate retarding effect of Al_2O_3 (1%) is observed once the hematite has disappeared, during the further reduction to wüstite and iron at 800-900°C (Bruijn et al., 1990).

Bruijn et al. (1990) find that the rate retarding effect probably is due to formation of hercynite ($\text{FeO}\cdot\text{Al}_2\text{O}_3$). Only low expansion during the late stage of reduction was experienced.

Additions beyond 1% Al_2O_3 have a small rate retarding effect on reduction of hematite to magnetite and wüstite (Chinje and Jeffes, 1989), referring to figure 5.25. These workers prepared

hematite tablets with (0-5%) Al_2O_3 carefully to obtain solid solution before reduction. The desired amounts were ball milled for 24h, compressed, indurated for 1-5 days at 1200-1300°C in air, crushed, compressed and reindurated for 12h at 1200°C. Lamellar formation of magnetite in Al_2O_3 treated specimens was never observed during reduction at 960°C in CO/CO_2 , unlike the magnetite formation in pure hematite specimens. The reason is probably due to a slower rate of iron ion diffusion caused by a lattice contraction due to the small size of Al^{3+} substituting Fe^{3+} . In the peripheral magnetite growth there is no need for long range diffusion. Chinje and Jeffes (1989) found that 0.5% Al_2O_3 was dissolved in the wüstite lattice. The introduction of Al^{3+} caused strains in the lattice and introduced fractures in the spinel, reducing effective grain size and increasing rate at a late stage during the reduction to wüstite.

Cr

The reduction rate of hematite is increased upon addition of (0-5%) Cr_2O_3 (Chinje and Jeffes, 1989), referring to figure 5.25. These specimens were prepared in the same way as above described for Al_2O_3 containing specimens. The rate enhancing effect increases with increasing concentration of the additive during

the reduction to magnetite by $\text{CO}/\text{CO}_2=18/82$ at 960°C. Since Cr^{3+} and Fe^{3+} are of about the same sizes, Cr^{3+} is not expected to disturb the lattice. The enhanced reduction rate is probably caused by the catalytic effect of Cr_2O_3 on the chemisorption

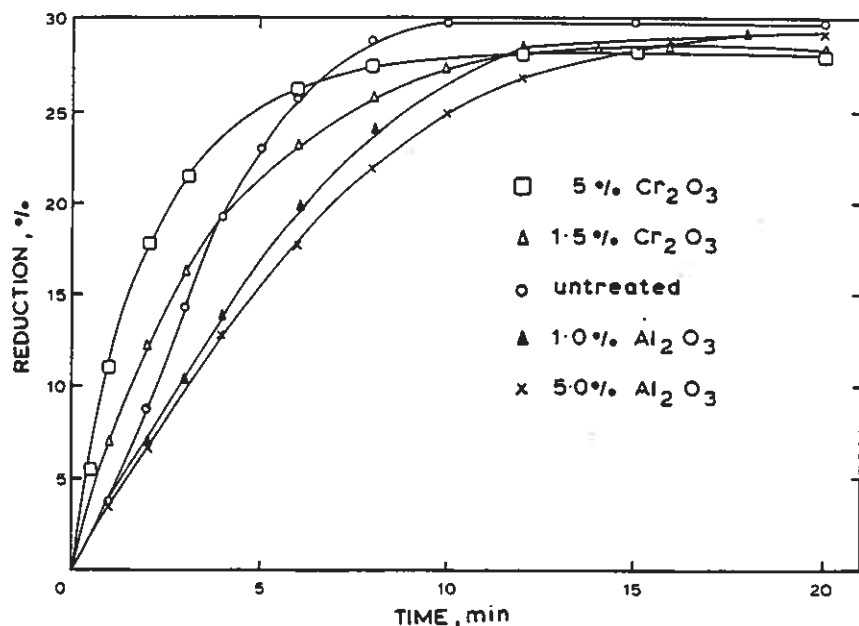


Fig. 5.25 Effect of addition of Cr_2O_3 and Al_2O_3 to hematite on reduction to wüstite at 960°C by 70% CO -30% CO_2 (Chinje and Jeffes, 1989)

of CO (Chinje and Jeffes).

In the reduction of hematite to wüstite, there is an initial rate enhancing effect of the Cr_2O_3 addition, but referring to figure 5.25, the reduction is retarded at a later stage (Chinje and Jeffes, 1989). The retarding effect is expected, as far as ionic sizes are concerned, because Cr^{3+} is smaller than Fe^{2+} . The solubility of Cr_2O_3 in wüstite was found to be 2.65% at this temperature. The lattice parameter of wüstite remained constant after the introduction of 0.55% Cr^{3+} , but the metal deficit decreased by 0.011. Further addition of Cr^{3+} resulted in both a contraction of the lattice and an increase in the metal deficit.

The reducing gas

Sulphur in the gas phase (5-50 ppm) enhances the reduction of magnetite to wüstite, but the reduction rate is retarded once iron precipitates (Haas et al., 1979). The presence of sulphur promotes whisker formation (Haas et al., 1979 and Nicolle and Rist, 1979). Sulphur adsorbs on the wüstite surface and inhibits the chemical reaction (Nicolle and Rist, 1979). Hence, the rate of reduction is retarded. Carburization of the iron is also retarded because sulphur is chemisorbed on the iron surface (Haas et al., 1979). Diffusion is enhanced relatively to the chemical reaction and whisker growth is favoured. Nicolle and Rist found that catastrophic swelling of Carol Lake pellets was promoted using a feed gas of 99%CO and 0.2% SO_2 . Sulphur in the reducing gas is also detrimental for the nickel catalyst used to catalyse the water-gas shift reaction in the present work.

As previously discussed in section 2.2, experimental conditions are chosen to avoid carbon deposition by the Boudouard reaction. However, carbon may be solved in the iron precipitated. If a dense iron layer is formed topochemically around each grain, further supply of reductant proceeds by solved carbon, and the reduction proceeds at the wüstite-iron border (Edström, 1956). In this way a pressure of 40 atm may build up at 1000°C for a carbon activity of 0.6 in the iron. The iron layer is disrupted where the gas bursts out, and the rate of reduction is increased.

5.3 Experimental

5.3.1 Raw materials

Raw materials were preoxidized magnetite from Sydvaranger and natural hematite concentrates, described in sections 3.4-3.5 and in chapter 4, respectively. The fraction 63-90 μ m of the concentrates was reduced. Reduction gases were mixtures of CO, H₂ and CO₂. Cooling and sample transport gases were Ar and N₂.

CO 20 Typical content: CO \geq 99%
 O₂+Ar $<$ 0.5%
 N₂ $<$ 0.2%
 H₂ $<$ 0.2%
 Hydrocarbons $<$ 0.2%

H₂ 30 Guaranteed content: H₂ \geq 99.9%
 O₂ \leq 10 ppm
 H₂O \leq 21 ppm
 N₂ \leq 300 ppm

H₂ 27 Guaranteed content: H₂ \geq 99.7%
 O₂ \leq 5 ppm
 H₂O \leq 10 ppm
 N₂ \leq 0.3%

CO₂ 30 Guaranteed content: CO₂ \geq 99.9%

N₂ 40 Guaranteed content: N₂ \geq 99.99%
 O₂ \leq 40 ppm
 H₂O \leq 21 ppm
 Ar \leq 30 ppm

Ar 40 Guaranteed content: Ar \geq 99.99%
 O₂ \leq 20 ppm
 H₂O \leq 10 ppm
 N₂ \leq 60 ppm

5.3.2 Equipment

The reactor was developed by Elkem and SINTEF in cooperation and

especially designed to study gas/solid-reactions on a laboratory scale. The laboratory equipment has been thoroughly described in earlier SINTEF reports by Grøntvedt et al. (1986) and Monsen et al. (1988), in M. Sc.-theses by Steinmo (1986), Baumann (1985), and Storemyr (1986 b), and in publications by Kolbeinsen et al. (1988 and 1989).

The reactor was placed inside a chamber furnace together with heating coils for reducing and inert gas, and a catalyst container, as shown in figure 5.26. Reactor, heating coils, and catalyst container were made of stainless steel.

The catalyst container was holding approximately 2 kilos of NiO. The surface of the NiO rottrings was reduced to Ni before use because Ni is a better catalyst for the water-gas shift reaction. The reduction to Ni was accomplished at 350°C during 6 hours in a H₂ atmosphere.

The gas mixing unit was equipped with 4 identical FTC channels (Flow Transmitter & Controller) which were used at 5 bars back pressure. Calibration of each FTC channel was dependant on the gas. The gases were mixed after they had passed the FTC channels.

The furnace was a ceramic chamber furnace, N150, fabricated by Naber. The equipment placed inside the furnace was made of stainless steel. This limited the recommended maximum operating temperature to 850°C.

Preheating of the reduction gas was carried out in heating coils with a total length of 5 m. Tube diameter was 10 mm.

Temperature regulation was conducted by a Naber Temperature Processor TP10 and regulation temperature was measured with a Pt/Pt10%Rh-thermocouple which was placed inside the furnace lining. The temperature was also measured with a Chromel Alumel thermocouple which was placed in a drilled hole in the massive

steel reactor.

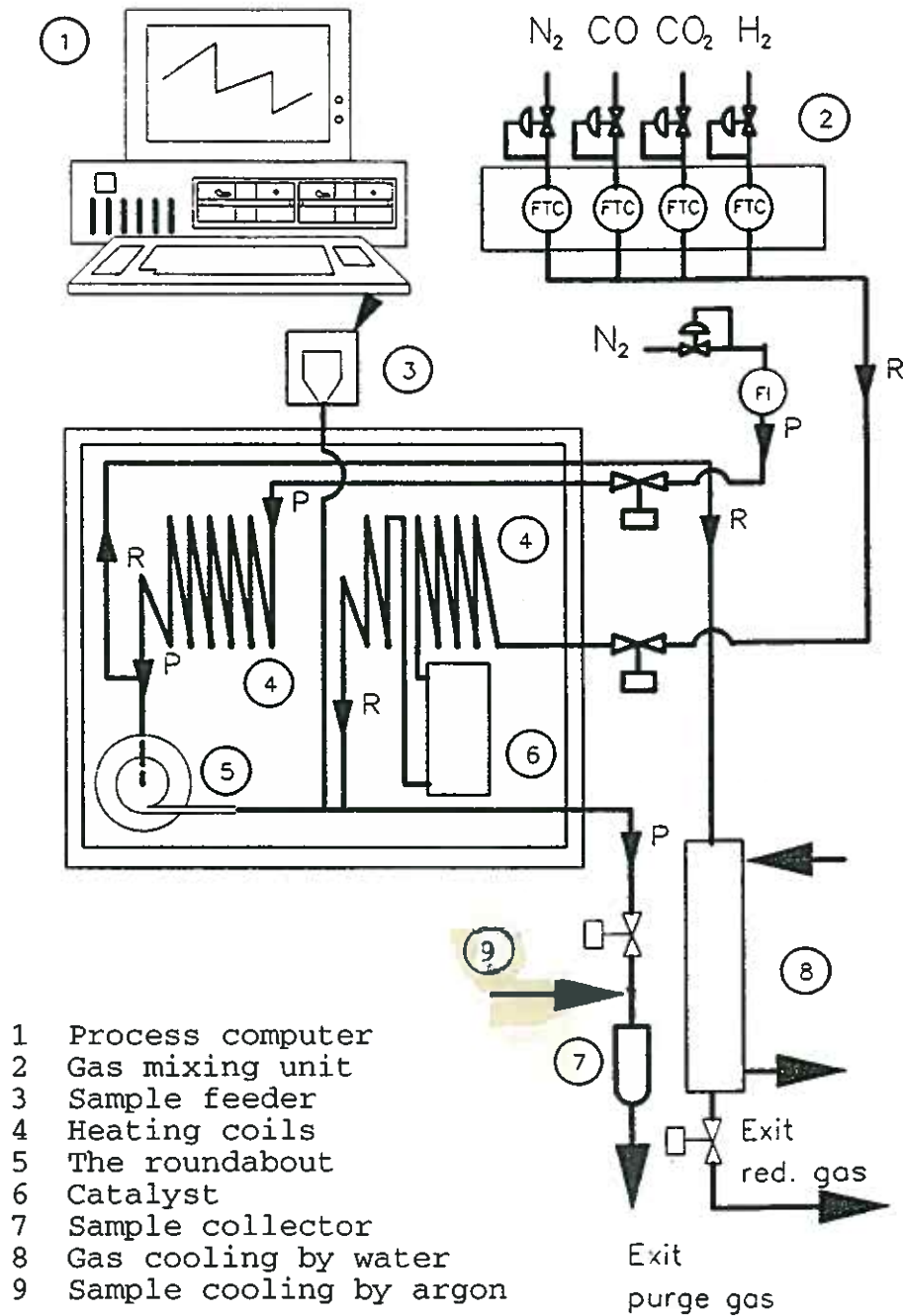


Fig. 5.26 Prereduction unit including reactor (the roundabout), heating coils, and catalyst inside the furnace and accessory equipment outside.

The reactor (the roundabout) is shown in detail in figure 5.27 where two characteristic features are indicated: The reactor walls are rounded and the inside radius of the reaction chamber decreases from the point where the gas enters (R_1) and the full circle around to (R_2).

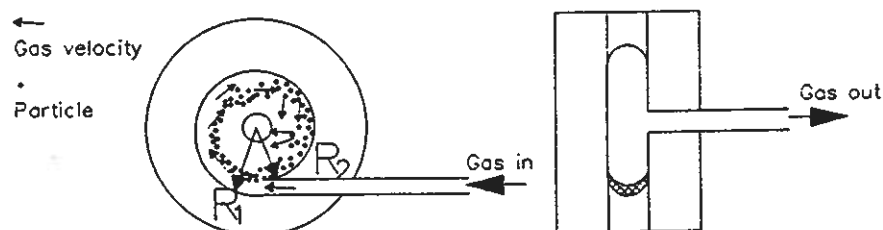


Fig. 5.27 Reactor (the roundabout) with inside radius varying from 25 mm (R_1) to 22 mm (R_2) and parallel wall distance of 12 mm.

In cold plexiglas models, Kolbeinsen et al. (1989) have observed that the particles seem to ride on the top of (or rather at the inside of, referring to figure 5.27) the gas stream 3/4 of the rotation if the gas velocity at the inlet is within a certain range. For most gas mixtures these authors found that the optimal velocity, of minimum material loss, was about 100 m/s.

The sample feeder was a plexiglas container with a stopper at the bottom. The sample was placed in the container with the stopper in a closed position. Argon gas at 5 bars pressure was applied to flush the sample into a stream of reducing gas at the same time as the stopper was opened manually.

The sample collector was a cellulose filter filled with Pyrex wool to trap the sample as the exit gas passed after the period of reduction. When the filter contained a reduced sample, it was automatically flushed with Ar to provide cooling and to avoid oxidation.

The process computer was a real time multi-tasking computer, MACSYM 350, delivered by Analog Device. The computer program was developed at SINTEF by Kolbeinsen et al. (1989) and provided all

the necessary functions by means of a menu based user interface.

Operation of the prereduction unit

Operation of the prereduction unit was provided for by the process computer. Valve operations and time periods for reduction and flushing/purging were controlled by the computer. Hence, identical experiments can be done. Constant gas composition during each experiment was selected. The desired and the actual gas compositions were displayed in graphs for inspection before and after each experiment.

Before an experiment was started the reduction time was set and the command "Hold initial gas values" was selected from the menu. The computer caused the gas mixing unit to maintain a constant gas composition corresponding to the desired constant composition. The gas passed from the gas mixing unit to the heating coils, through the catalyst, into the reactor and out through the gas cooler, following the arrows marked R in figure 5.26. The mean residence time of the gas in the reactor was approximately 0.002 seconds.

The sample was placed in the feeder. When constant gas composition was achieved, the experiment was started by opening the feeder stopper and flushing the sample with argon into the reducing gas flow. Simultaneously the command "Start experiment" was selected. The sample was transported by the reducing gas to the reactor where the centrifugal forces acting on the particles kept the main part of the sample in the reactor while the reducing gas flew through the reactor and out as described ahead.

The computer timer was automatically reset to zero on the command "Start experiment". When the prereduction time had come to an end, the computer automatically terminated the experiment. The reduction gas was stopped and the corresponding valve was closed. The N₂ back purging valve was opened and the sample was flushed in N₂ out to the sample collector, following the arrows marked P in figure 5.26. This sample transfer normally took 3 seconds (Kolbeinsen et al., 1989). The N₂-purge valve and the sample valve were closed and the Ar-purging was started.

5.3.3 Experimental procedure

The operation of the prereduction unit was described in section 5.3.2. The back purging time with N₂ was set to 10 seconds and the sample cooling time in Ar was selected to 20 seconds.

Prereduction experiments were carried out using a total gas flow of 4.5 m³/h. Reduction gas mixtures of CO, CO₂, and H₂ were applied, without addition of inert gas. The H₂ 30 quality was used, except in the first experiments with 35% CO₂ in the inlet gas where the H₂ 27 quality was used.

The temperature and the gas composition were constant during each experiment. The temperature was set to 760°C in most of the experiments, but experiments have also been carried out at 700, 730, 800 and 850°C. The inlet gas composition was also varied: 0-45%H₂ at constant %CO₂, and 20, 35, and 50% CO₂ at constant %H₂. Reduction time was selected in the range 12 - 60 seconds.

Fraction 63-90µm of oxidized magnetite from Sydvaranger and natural hematite iron ore concentrates was used. More than 1 g single samples caused uneven reactor operation (Kolbeinsen et al., 1989). These authors recommended 0.5 g single samples and 0.5 g was for this reason used in the present work. Usually at least five single samples were treated consecutively and collected in the same filter, called one run in figure 5.28. The total weight of prereduced samples in one run should be 1.5-2 g. The weight was recorded. Prereduced samples were sieved through a 212 µm screen to separate Pyrex wool and sample. Each sample was split in two parts, one for wet chemical analyses (minimum 0.5 g, usually 1 g) and one for optical microscopy.

Optical microscopy

Polished surface specimens were made by moulding the powder in a two component epoxy (Epofix) which needed 8-12 hours to harden. The specimens were mechanically polished and cleaned, the last step being on a 1 µm NAP-cloth.

A Leitz Wetzlar optical microscope from Germany and a Reichert MeF3 A optical microscope from Austria, both with devices for photographing, were used to look at and take pictures of polished surfaces in plain reflected and polarized light.

Wet chemical analyses - accuracy

Wet chemical analysis was carried out by MOLAB. The total amount of Fe (Fe^{tot}), Fe^{2+} , and the metallic part of the sample (Fe^{met}) were determined in 3 separate analyses. Three different solutions were made and indicator and an acid solution were added to these cold solutions before they were titrated with $\text{K}_2\text{Cr}_2\text{O}_7$.

Fe^{tot} was determined by making a solution of approx. 0.2 g sample in HCl and reduction by SnCl_2 .

$\text{Fe}^{2+} + \text{Fe}^{\text{met}}$ were determined together in another 0.2 g sample by reduction by NaHCO_3 in HCl without access to air.

Fe^{met} was determined by dissolving about 0.2 g sample in FeCl_3 (200 g/l). Solid particles were filtered from the solution.

Fe^{2+} was calculated by subtracting Fe^{met} from $\text{Fe}^{2+} + \text{Fe}^{\text{met}}$.

Fe^{3+} was also calculated: $\text{Fe}^{3+} = \text{Fe}^{\text{tot}} - \text{Fe}^{2+} - \text{Fe}^{\text{met}}$

The accuracy of the chemical analyses has been tested on parallels from the same run while the accuracy of both the chemical analyses and the experimental conditions have been tested on parallels from different runs. The principle of the parallel samples is illustrated in the figure 5.28. Three parallel runs were carried out on different days for the two concentrates RHP and GUL. In one of the 3 runs, enough material were reduced to split the samples in 4 parts each of 0.5 g or more. 3 parts were analyzed. The results are shown in table 5.2. All the chemical analyses are reported in appendix A.3. Samples from different runs may have been analyzed in different series at the laboratory.

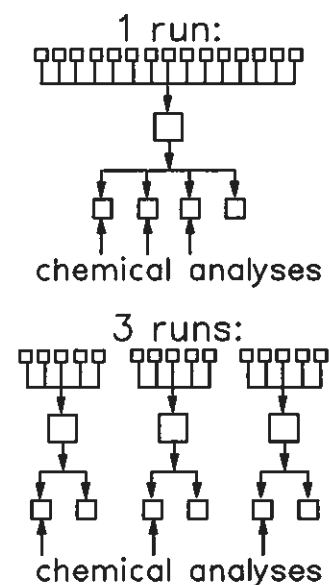


Fig.5.28 Parallels

Table 5.2 Standard deviations (STD¹) of the individual wet chemical analyses and the calculated degree of oxidation (OX).

Samples, reduced at: 760°C, 35%H ₂	Parallels from:	Degree of oxidation (OX)		Mean value of 3 analyses and the standard deviation		
		OX±STD (%)	maxSTD ⁴ %	Fe ^{tot} (%)	Fe ²⁺ (%)	Fe ^{met} (%)
RHP ² : 20s at 50%RO	1 run	88.4±0.1	0.2	69.6±0.1	23.2±0.2	0.3±0.06
	3 runs	88.3±0.4	0.4	69.5±0.4	23.4±0.7	0.3±0.01
GUL ³ : 40s at 20%RO	1 run	70.0±1.4	1.7	75.9±0.3	64.0±3.4	1.5±0.1
	3 runs	70.3±0.6	1.3	76.1±0.3	63.6±1.9	1.4±0.3

- 1) $STD = \{(X_1 - X_m)^2 + (X_2 - X_m)^2 + (X_3 - X_m)^2\}^{1/2}/2$, referring to section 3.5.2
- 2) The analyses are found in the tables A.3.9, A.3.12 and A.3.14
- 3) The analyses are found in the table A.3.11.
- 4) Max. deviation is calculated from STD of the individual analyses.

The accuracy of the chemical analysis of Fe^{tot} is good. The standard deviation is about 0.3%, both for 1 and 3 runs.

The accuracy of the Fe²⁺-analysis, is good when the content of metallic iron is negligible (for RHP). The standard deviations of parallels from the same and different runs are 0.2% and 0.7%, respectively. The analysis of Fe²⁺ is rather uncertain in the presence of metal (for GUL). The standard deviation is 3.4% in the same run, while it is only 1.9% in the different runs. This indicate that the accuracy of the experimental conditions is better than the accuracy of the analysis. For this reason, double and triple analyses of Fe²⁺ from the same run have been carried out for several samples in this investigation. For one sample an even larger deviation than 3.4% is found. Only a few analyses, which were completely out of range, have been excluded.

The detecting level of Fe^{met} is 0.2%. Values below this level are reported as 0.0% in the tables A.3.2-A.3.15. Since the standard deviation for Fe^{met} in different runs is 0.3% (for GUL), the detected amount of 0.3% Fe^{met} is a quite uncertain analysis.

The standard deviation of the degree of oxidation at 88% OX is low, 0.1% and 0.4% for the same and different runs, respectively. In the presence of metal at 70% OX it is rather large, 0.6-1.4%. Maximum deviations, 0.4% at 88% OX and 1.7% at 70% OX, are calculated from the STD of the individual analyses.

5.4 Prereduction results: preoxidized Sydvaranger magnetite

Sydvaranger magnetite was completely oxidized to hematite at eight different temperatures during 3 hours (24h at 799°C) and named S1-S8 for short, corresponding to an increasing temperature from 799°C to 1244°C. The experimental method and a characterization of the subgrain structures are found in sections 3.4-3.5. The subgrain structure changes gradually from S1 to S8. In S1 each grain consists of numerous subgrains (crystals), while grains of S8 have no or only a few subgrains.

The prereduction results are in the following presented in figures. Double and triple points are mostly parallels in the chemical analyses, and are usually not parallel runs. Chemical analyses, the calculated degree of oxidation, and the output of material in percentage of input weight in each experiment, are presented in appendix A.3, in tables A.3.2-A.3.8.

5.4.1 Prereduction at 760°C

Prereduction experiments have been carried out at 50 and 20%RO for 12, 20, 35, and 60 seconds to study the progress of reduction for S1 and S8. The results are shown in the figures 5.29-5.31 after reduction at 760°C with 35%H₂ in the inlet gas.

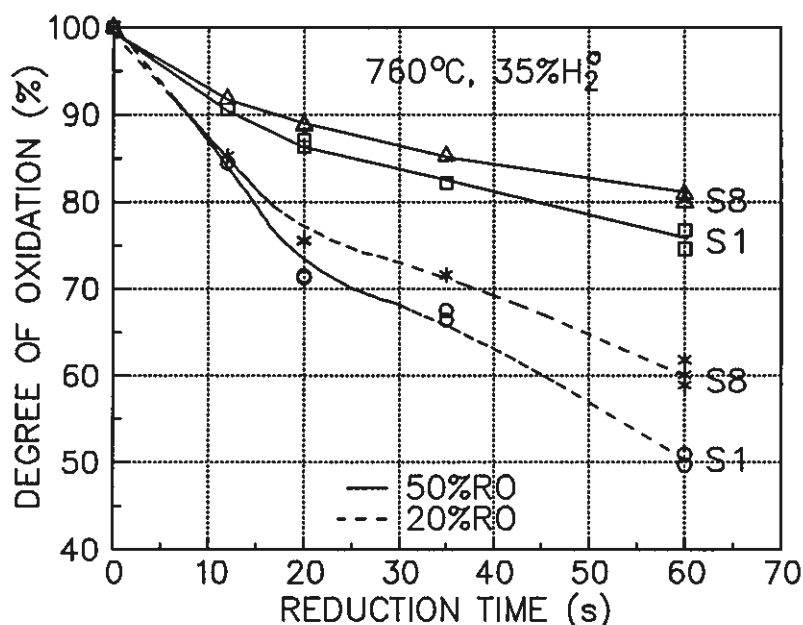


Fig. 5.29 Prereduction at 760°C of preoxidized Sydvaranger magnetite. S1 was preoxidized at 799°C and S8 at 1244°C.

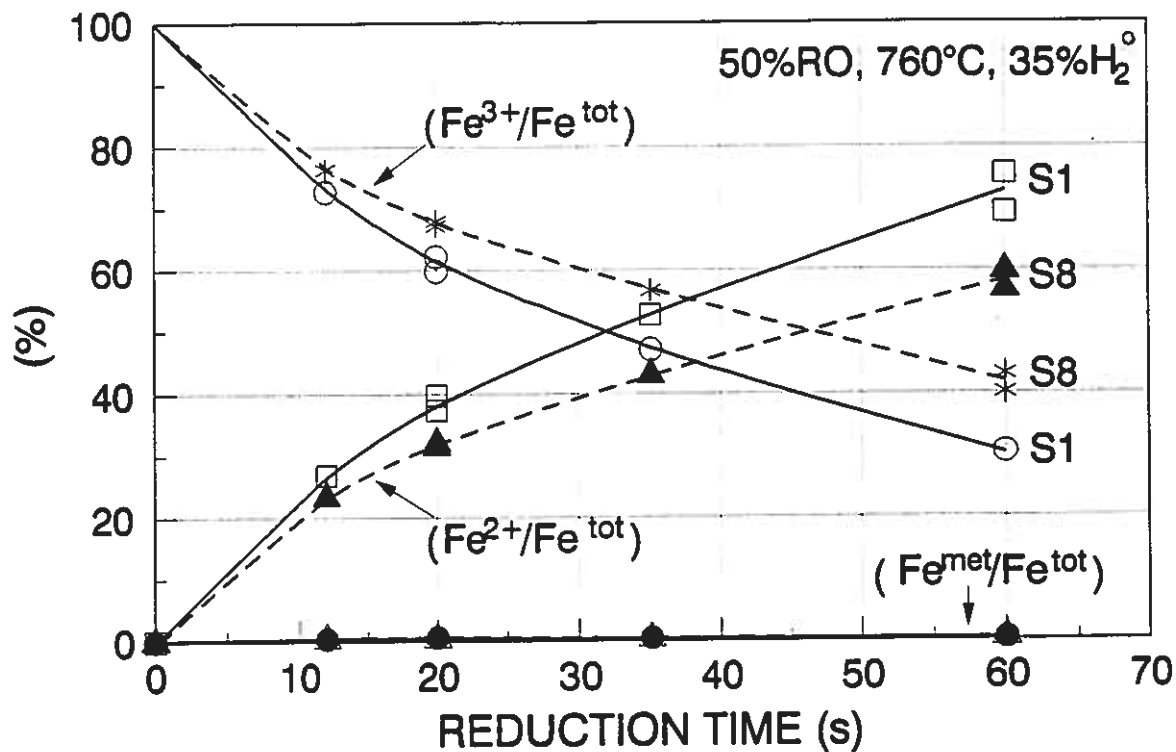


Fig. 5.30 The progress of prereduction at 50%RO with reference to figure 5.29.

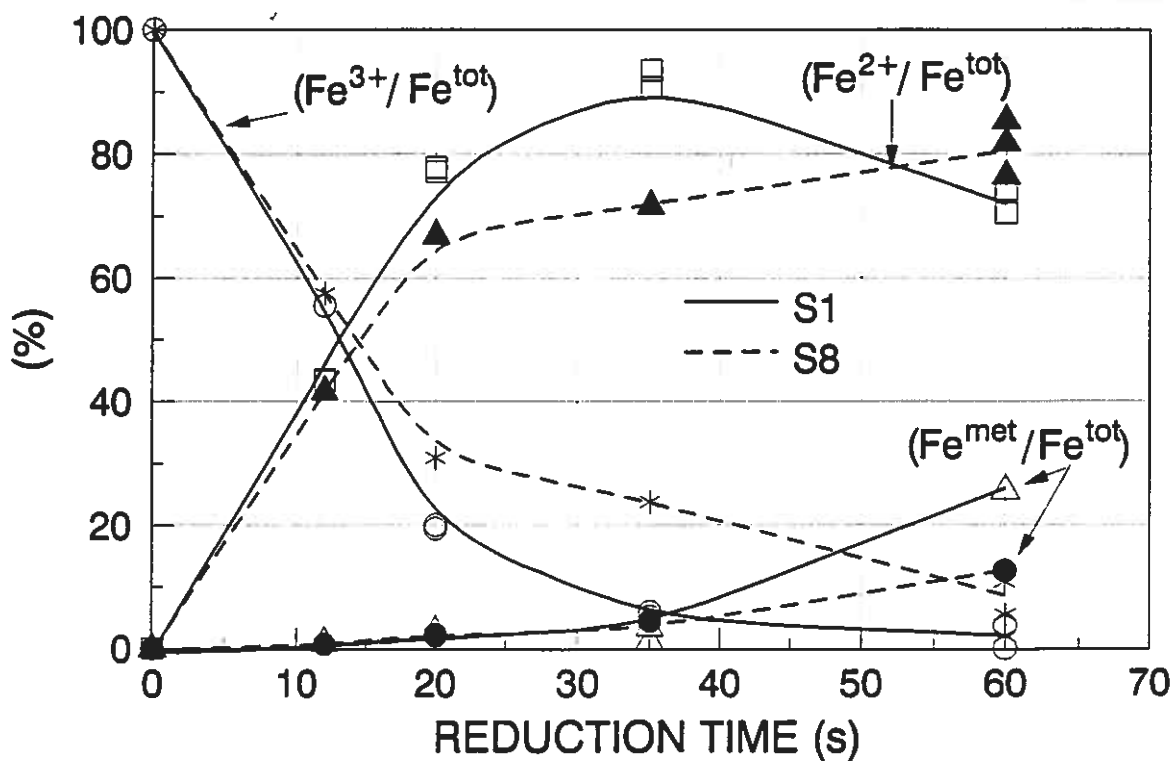


Fig. 5.31 The progress of prereduction at 20%RO with reference to figure 5.29.

Figure 5.29 shows that S1 is reduced at a higher rate than S8, both at 20 and 50%RO. This indicates that the low temperature subgrain structure of S1, with lots of subgrains in each grain, enhances the reduction rate.

Figure 5.30 illustrates the formation of Fe^{2+} at 50%RO on expense of Fe^{3+} relative to the total weight of iron in each sample. As expected, the formation of Fe^{2+} is more rapid in S1 than in S8. This is also the case for the reduction at 20%RO, shown in figure 5.31, but only the first 35 seconds. At this point the maximum amount of Fe^{2+} in S1 is reached while formation of Fe^{2+} still proceeds in S8. After 35 seconds there is only a few percentage Fe^{3+} remaining in S1 and the formation of metallic iron starts on expense of Fe^{2+} . Formation of Fe^{met} and consumption of Fe^{3+} is slower in S8 than in S1.

5.4.2 Effect of reduction temperature

The effect of reduction temperature on preoxidized Sydvaranger magnetite is shown in figure 5.32. The experiments were carried out for 20 seconds at 20 and 50%RO, with 35% H_2 in the inlet gas.

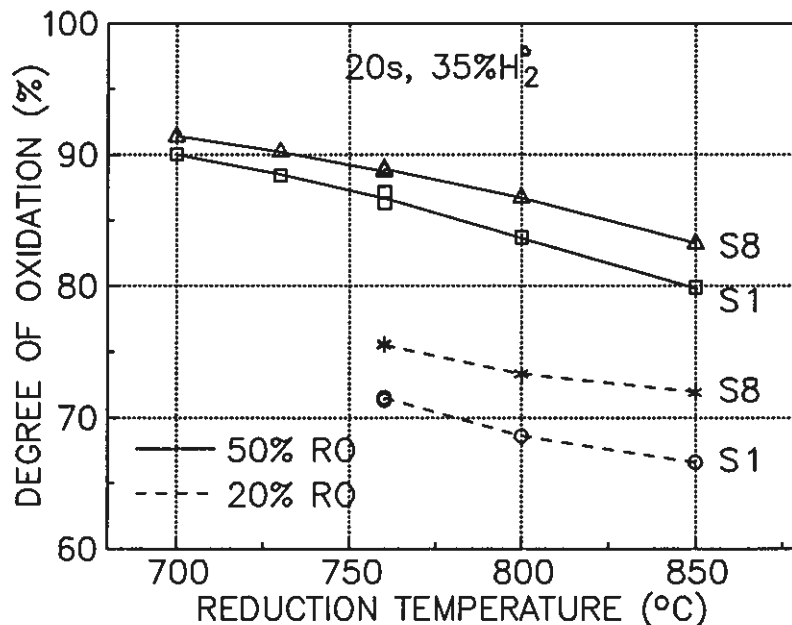


Fig. 5.32 Effect of reduction temperature on preoxidized Sydvaranger magnetite. S1 was preoxidized at 799°C and S8 at 1244°C.

It is clearly seen from figure 5.32 that the degree of oxidation is gradually decreasing with increasing reduction temperature, as expected. More interesting is the fact that S1 has been reduced at a higher rate of reduction than S8, both at 20 and 50%RO. The differences in reduction rates are more pronounced at 20%RO than at 50%RO. The results indicate that the low temperature subgrain structure of S1 enhances reduction rates at all reduction temperatures in the range 700 - 850°C.

Referring to appendix A.3, a larger amount of Fe^{2+} is formed (and a corresponding amount of Fe^{3+} is consumed) in S1 than in S8 at all temperatures, both at 50 and 20%RO. The rate of formation and consumption increases with temperature. The amount of Fe^{2+} formed and of Fe^{3+} consumed are a lot larger at 20%RO than at 50%RO. About 2% metallic iron has formed at all temperatures after 20s reduction at 20%RO.

5.4.3 Effect of gas composition

The reduction experiments were carried out with gas mixtures which initially consisted of CO , CO_2 and H_2 . The amount of hydrogen is varied in this series of experiments, by substituting CO by H_2 , while the reduction potential is constant, 50%RO. Preoxidized samples of Sydvaranger magnetite (S1 and S8) were reduced for 20 seconds at 760°C, and the results are presented in figure 5.33.

Figure 5.33 shows that without H_2 in the reducing gas ($\text{CO}/\text{CO}_2=1$) the reduction rate is retarded both for S1 and S8. An addition of 15% H_2 to the gas has a positive effect on the reduction. The effect of increasing the H_2 content from 15 to 35% is negligible, and there is no effect in raising it from 35 to 45%.

The reducibility of S1 is better than of S8 in the entire range investigated (0-45% H_2), as illustrated in figure 5.33. This

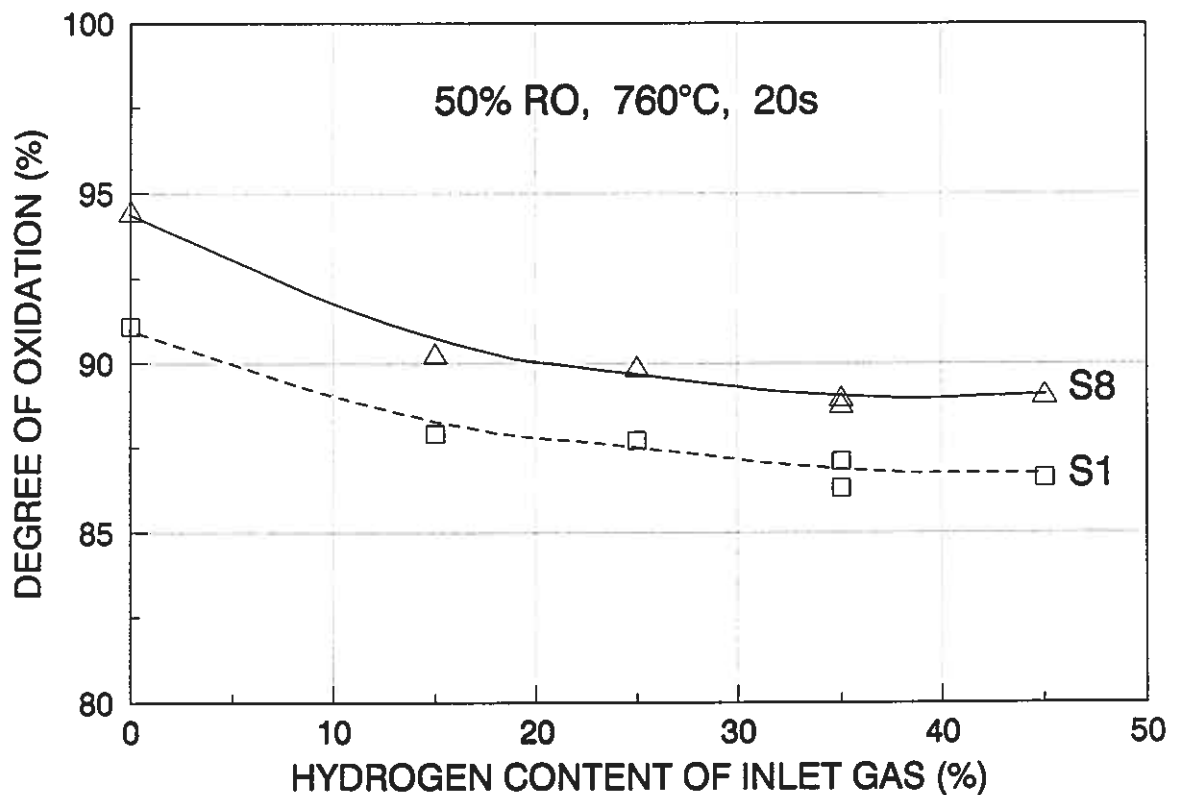


Fig.5.33 Effect of the substitution of CO by H₂ on 20s prereduction at 760°C and 50%RO. The Sydvaranger magnetite was preoxidized at 799°C (S1) and 1244°C (S8).

indicates that the reducibility of the low temperature subgrain structure of S1 is better than the reducibility of the high temperature subgrain structure of S8, independent of gas composition.

5.4.4 Effect of preoxidation temperature

Further prereduction experiments were carried out to investigate the effect of preoxidation temperature on the reduction. The experiments were all carried out at 760°C and with 35%H₂ in the initial gas mixture, and both at 20 and 50%RO and for 20 and 60 seconds. The results are presented in figure 5.34.

The effect of the temperature of preoxidation is most pronounced after 60s reduction and the effect is best demonstrated at 20%RO.

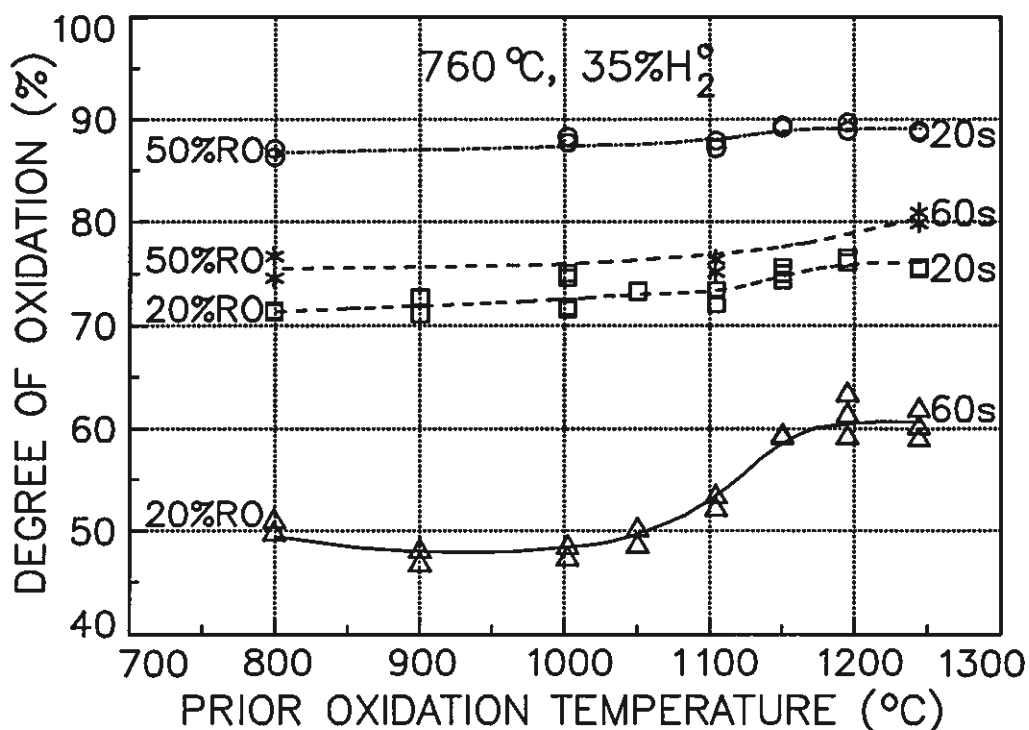


Fig. 5.34 Effect of preoxidation temperature for Sydvaranger magnetite on the reduction at 760°C (35%H₂ in inlet).

The degree of oxidation after 60 seconds reduction at 20%RO is about 48-50% for the samples preoxidized at 799-1050°C, but only 59-61% for the samples preoxidized at 1150-1244°C. This means that the reduction rate is retarded when preoxidation is carried out at temperatures above 1100-1150°C.

The decrease in reducibility mentioned above corresponds to a decrease of about 10% in the metal analyses in appendix A.3. Samples preoxidized at low temperatures contain 20-23% Fe^{met} after reduction while the samples preoxidized at elevated temperature contain 9-10% Fe^{met}. At the same time there is no Fe³⁺ left in the samples oxidized at low temperatures while there remains a few percent in the samples oxidized at elevated temperatures.

5.5 Prereduction results: natural hematites

The six natural hematites included in this investigation have been characterized in chapter 4. Short terms for the concentrates are presented in section 4.2 and are used in the following tables and figures. MBA and MBL are short terms for the Brazilian hematites from the Minas Gerais district, an angular and laminated type, respectively. GUL is from Guinea and LIL is from Liberia, but both are from the Nimba Range district. CCL is from Carol Lake mine in Canada and RHP is from Rana district in Norway.

The reduction results are in the following presented in figures. Double and triple points are generally parallels in one or two of the chemical analyses, and are not parallel runs. Chemical analyses, the calculated degree of oxidation, and the output of material in percentage of input weight in each experiment, are presented in appendix A.3, in the tables A.3.9-A.3.15.

5.5.1 Prereduction at 760°C

Prereduction experiments have been carried out at a constant oxidizing potential in the reduction gas of 50, 35 and 20%RO, to study the progress of reduction of the natural hematite concentrates at 760°C in the initial first 60 seconds. The reduction gas contained 35% H₂ in all these experiments. Figures 5.35-5.36, 5.37-5.38, and 5.39-5.41 shows the results from the experiments at 50, 35, and 20%RO, respectively. These results are in the following commented in the mentioned order.

Referring to figure 5.35, MBL is reduced at the highest rate of the six at 50%RO. MBL has achieved a degree of oxidation (OX) of 75% after 60 seconds reduction, which is 3.5-5.5% lower than for the 5 others. GUL and LIL are the least reduced (OX=80-81%). However, GUL and LIL have initially been reduced at the same high rate as MBL, or a slightly higher rate, while RHP have been reduced at the slowest initial rate, observed after 12 seconds.

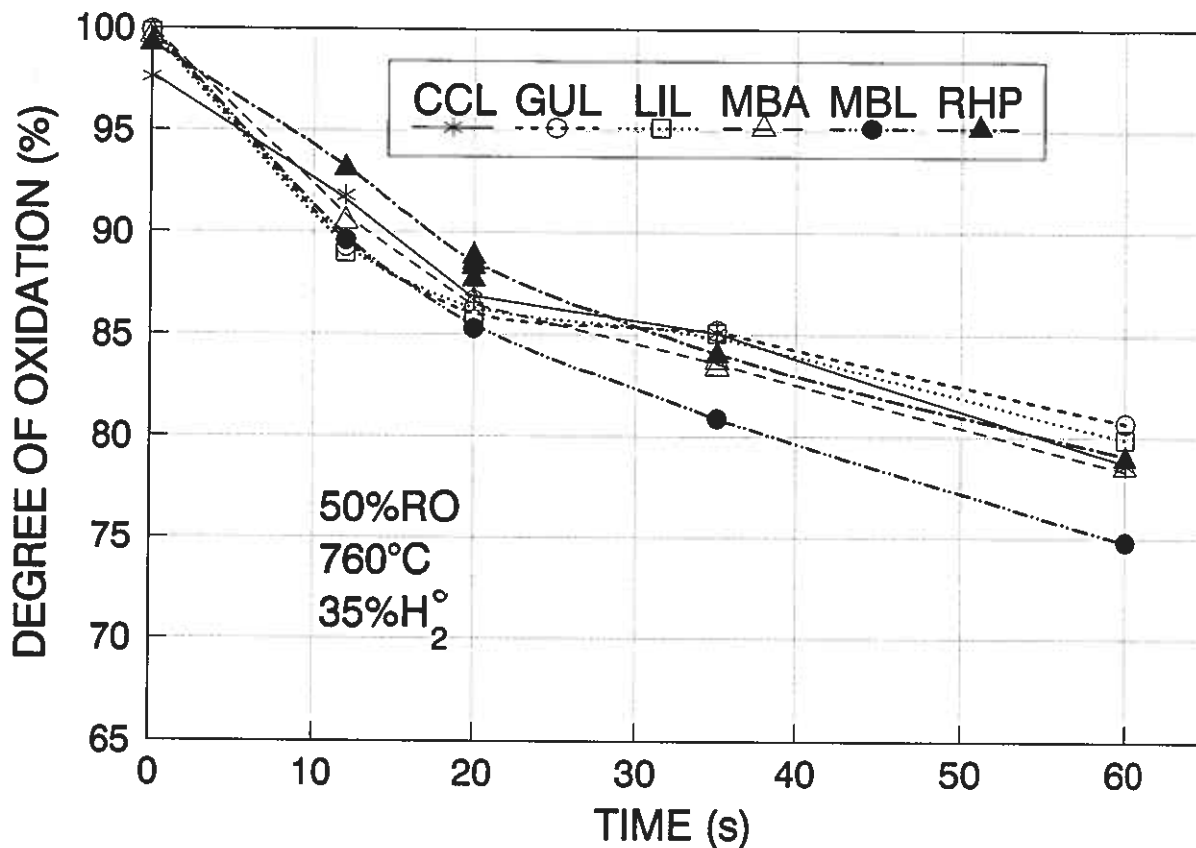


Fig. 5.35 Prereluction of the natural hematites at 760°C. Reduction gas: 50%RO, 35%H₂ in inlet gas.

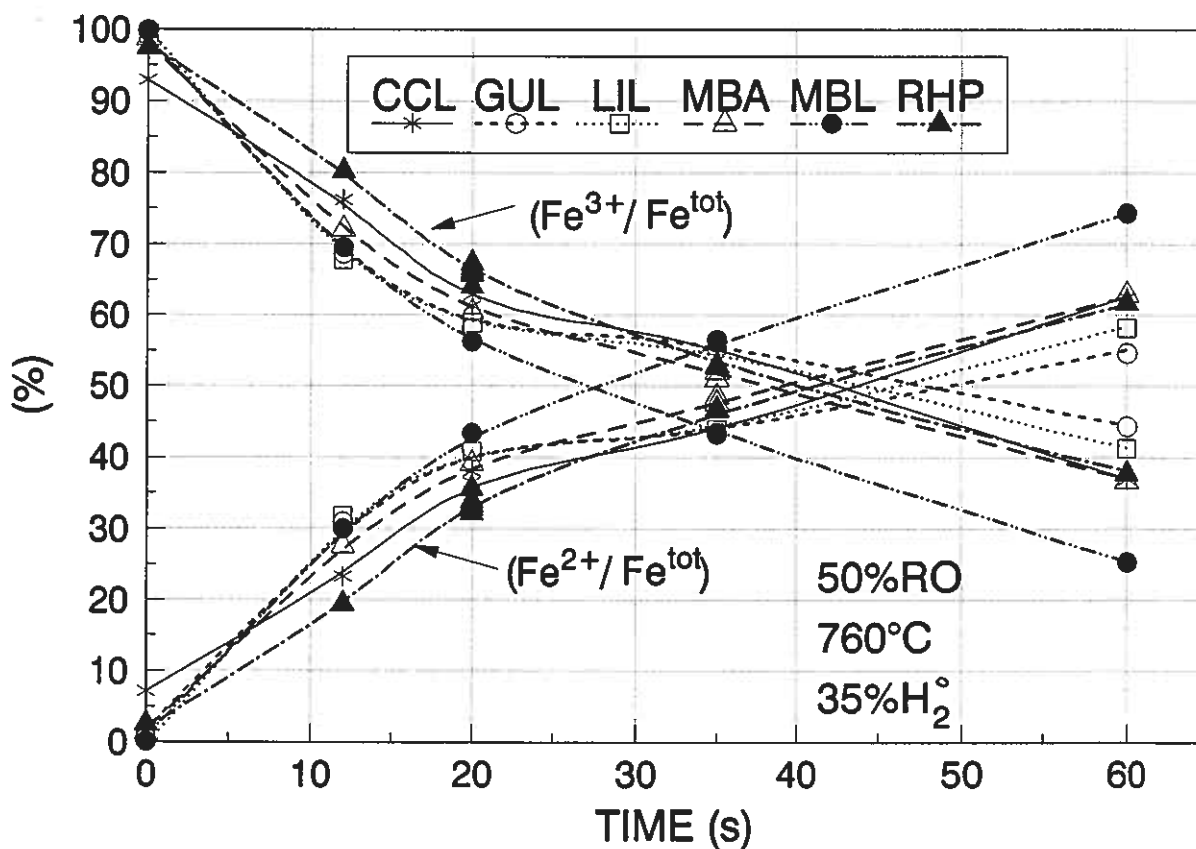


Fig. 5.36 Formation of Fe²⁺ on expense of Fe³⁺ during the prereluction referred to in figure 5.35.

Figure 5.36 shows the formation of Fe^{2+} on the expense of Fe^{3+} relative to the total amount of Fe in each sample, and corresponds to the degree of oxidation in figure 5.35. The formation of Fe^{2+} is very rapid for MBL, but initially equally rapid for GUL and LIL, or even faster. After 60 seconds, 25% of Fe^{3+} (relative to Fe^{tot}) remains in MBL, but as much as 37-44% remains in the other 5 hematites.

The higher reduction rate of MBL is also observed at **35%RO**. The equilibrium product is wüstite both at 35 and 50%RO. The higher reduction rate of MBL is appearing at an earlier stage and is more pronounced at 35% RO than at 50% RO. This could be expected because of the larger driving force. Referring to figure 5.37, after 20 seconds the degree of oxidation of MBL is approximately 77% compared to 84-86% of the others. Again LIL and GUL are reduced at the highest initial rate of reduction (or at the same rate as MBL), but turns out to be the least reduced after 60 seconds, together with CCL.

Referring to figure 5.38, 12% of Fe^{3+} relative to Fe^{tot} remains in MBL after 60 seconds, but as much as 27% remains in LIL and GUL. The metal content is not shown in the figures 5.36 and 5.38, because it is in the range 0.0-0.4% in most of the samples, and less than 0.8% in all the samples, referring to the tables A.3.9 and A.3.10. Metal should not be formed at all at 50 and 35%RO, provided equilibrium of the water-gas shift reaction.

Referring to figure 5.39, MBL has a much higher rate of reduction than the 5 other concentrates at **20%RO**. The degree of oxidation of MBL is 46% after 60 seconds, while it is as high as 65-66% for GUL and LIL which once more are the least reduced ores.

Fe^{met} is the stable phase at chemical equilibrium at 20%RO. The high reduction rate of MBL at 20%RO can to a large extent be attributed to easy metal nucleation and growth.

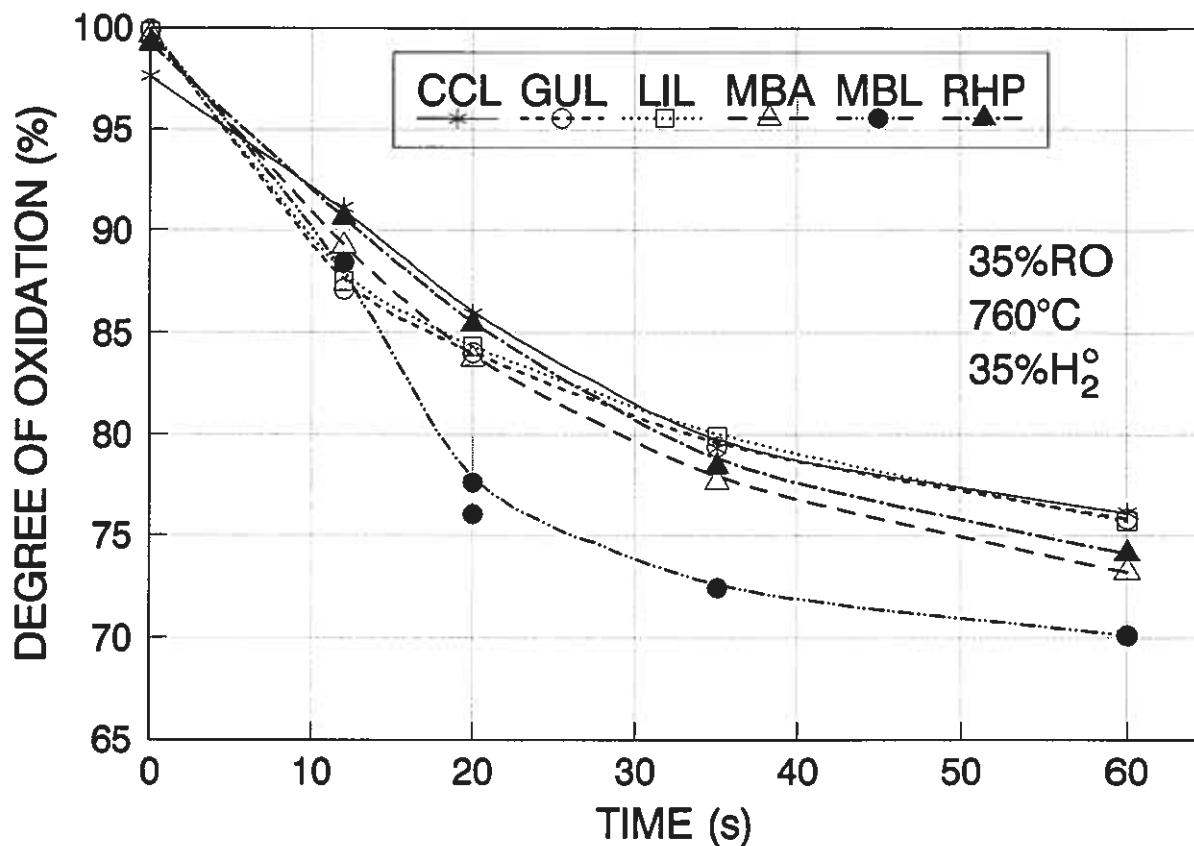


Fig. 5.37 Prereduction of the natural hematites at 760°C. Reduction gas: 35%RO, 35%H₂ in inlet gas.

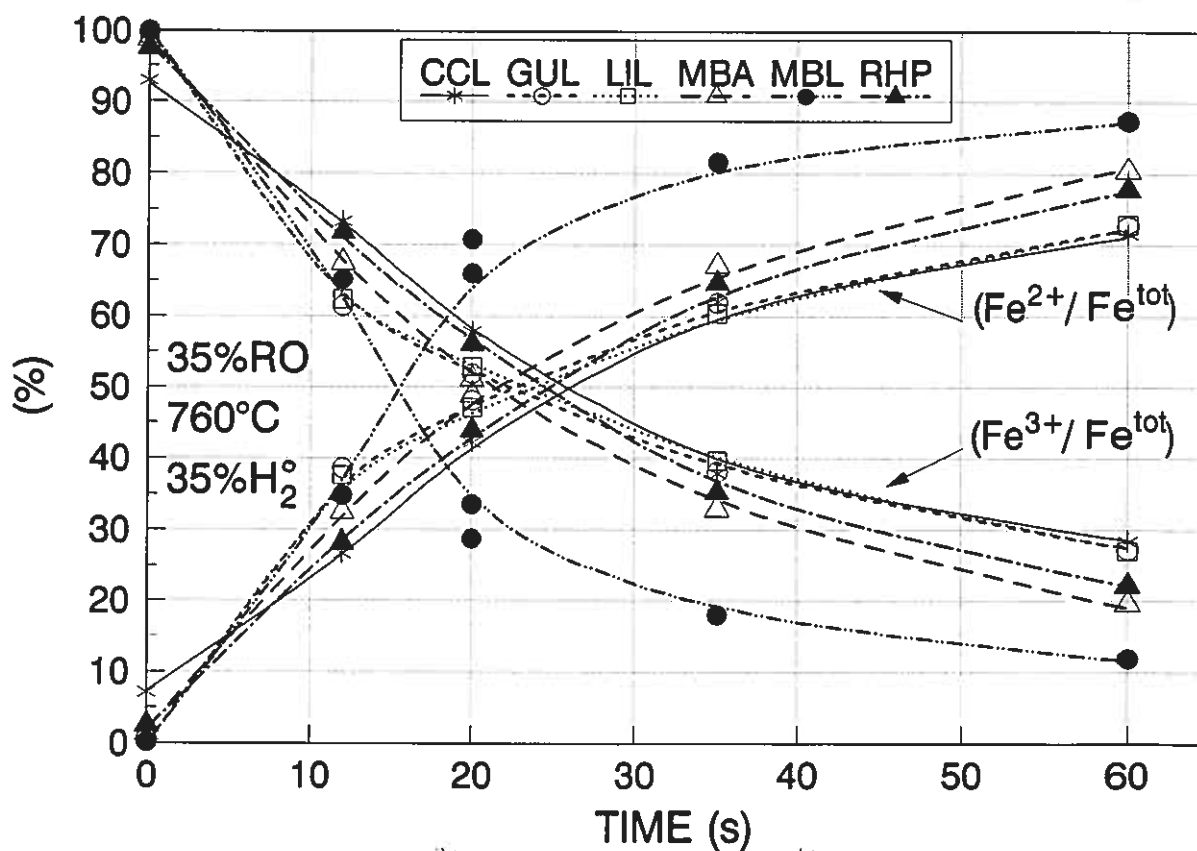


Fig. 5.38 Formation of Fe²⁺ on expense of Fe³⁺ during the prereduction referred to in figure 5.37.

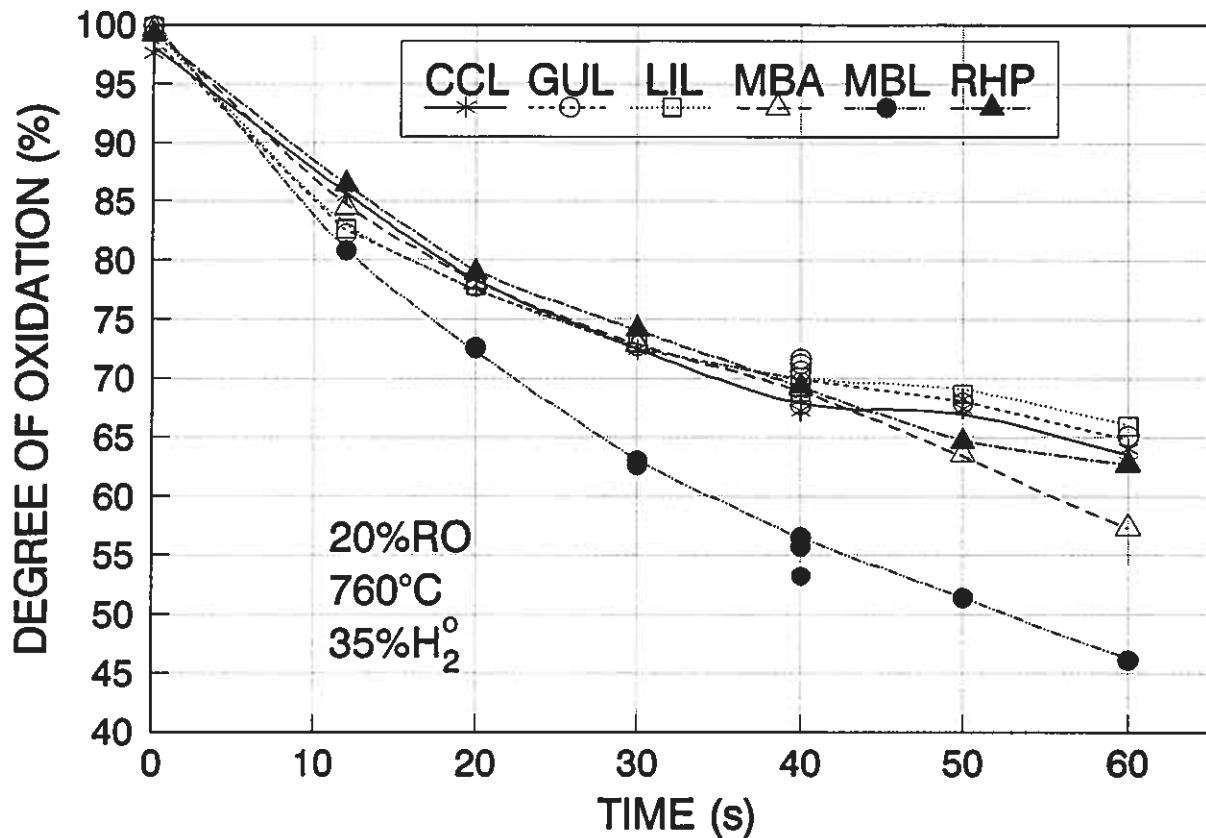


Fig. 5.39 Prereluction of the natural hematites at 760°C.
Reduction gas: 20%RO, 35%H₂ in inlet gas.

Referring to figure 5.41, metallization of MBL is as high as 31% after 60 seconds, while metallization of the other hematites is only 15% or less. Metallization of GUL and LIL is very low, only 7%. For MBL, metallization starts after about 20 seconds and the rate of metallization is approximately linear (0.78% Fe^{met}/s) in the period 20-60 seconds. Referring to figure 5.40, the relative Fe²⁺ content reaches a maximum after 30 seconds, and at this time only 3% of Fe³⁺ relative to Fe^{tot} is left.

Fe³⁺ remains in all the concentrates when metallization starts, indicating that metallization starts prior the complete conversion of magnetite to wüstite. In CCL, the relative Fe²⁺ content reaches a maximum after about 35 seconds, but during the decrease, the relative Fe³⁺ content is constant around 20%. The high content of Fe³⁺ can be attributed to the high initial content of magnetite in CCL, which is very slowly reduced.

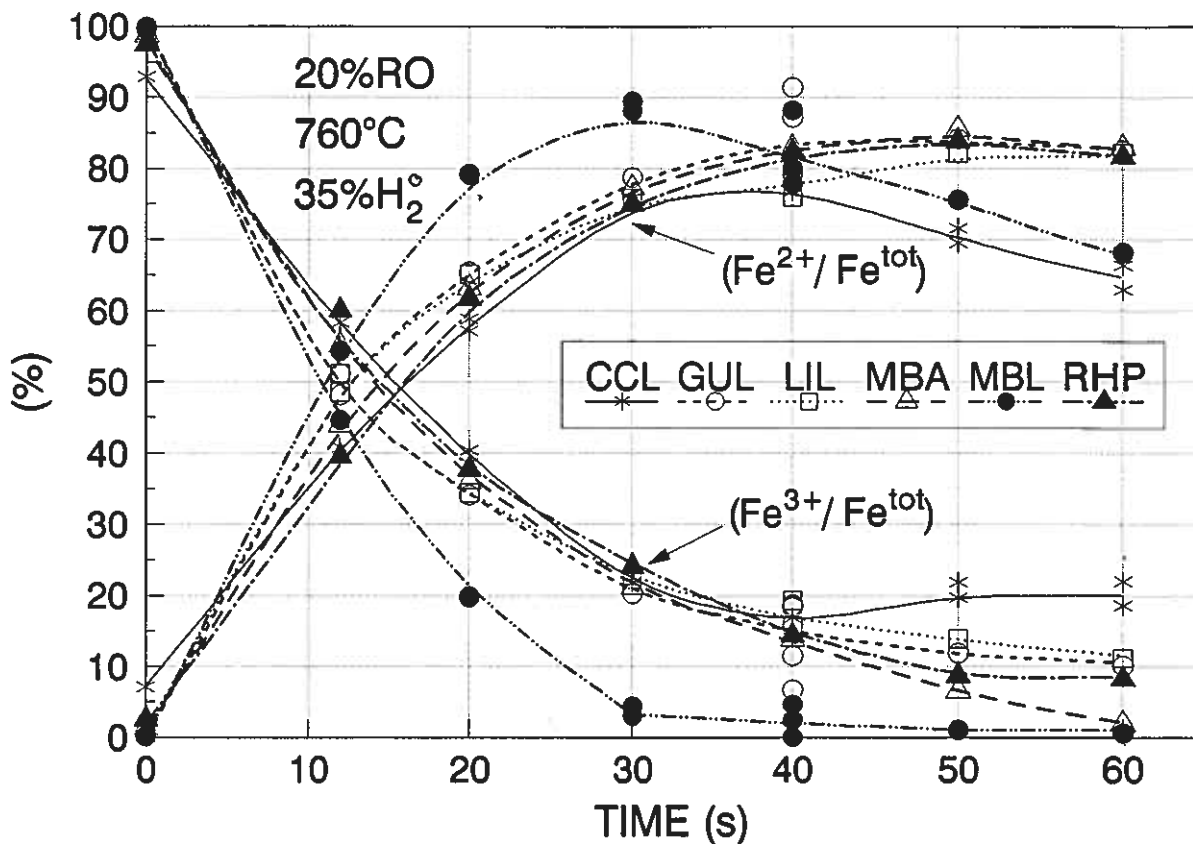


Fig. 5.40 Formation of Fe^{2+} and consumption of Fe^{3+} during the prereduction referred to in figure 5.39.

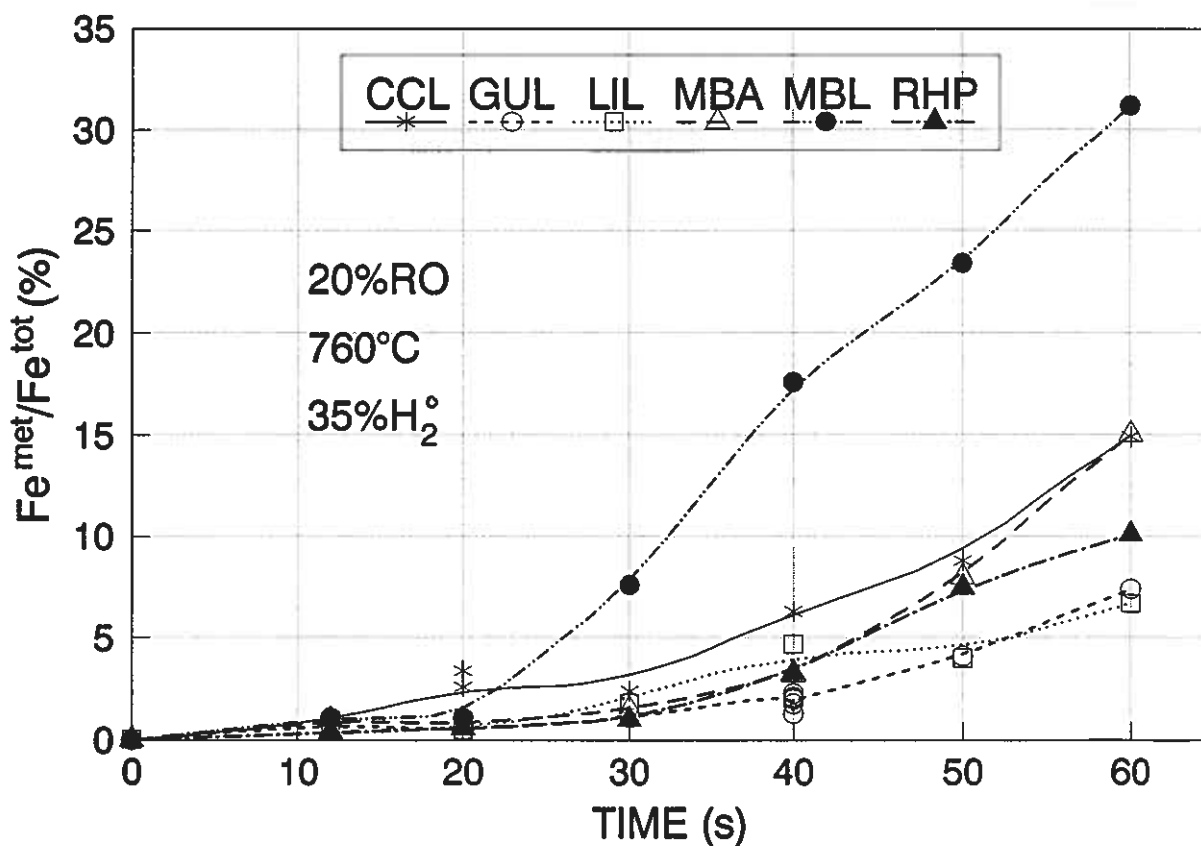


Fig. 5.41 Metallization during the prereduction referred to in figure 5.39.

Referring to figure 5.41, metallization increased 12% for MBA in the period 40-60 seconds. Figure 5.40 shows that the relative Fe^{3+} content decreased accordingly, while the relative content of Fe^{2+} is constant in the same period. The rate of formation and consumption of Fe^{2+} are probably equal.

5.5.2 Effect of reduction temperature

The effect of temperature on the reduction rate is illustrated in figure 5.42 at 50%RO and figure 5.43 at 20%RO. The samples were reduced for 20 seconds with 35% H_2 in the inlet gas. Both figures show that the reducibility of MBL is best, but MBL is only slightly more reduced than the others at 50%RO, while it is markedly more reduced at 20%RO.

The significantly better reducibility of MBL at 800-850°C (20%RO) can mainly be attributed to a higher level of metallization. Metallization has commenced, although the samples were reduced for only 20 seconds. Referring to the table A.3.13 in appendix A.3, 5.9% of Fe^{met} has formed in MBL at 850°C, but only 1.6% or less in the others. Chemical analyses in table A.3.12 confirm that no metal is produced at 50%RO.

Referring to figure 5.42, the degree of oxidation decreases from 89-91% at 700°C to 82-84% at 850°C for all the hematites. The differences between the hematites after reduction at 50%RO, are rather small. After reduction at 20%RO, the differences between the hematites, apart from MBL, are also rather small.

However, the effect of reduction temperature on each hematite is not similar. While LIL and GUL have been reduced at the same high rate as MBL at 700°C and 50%RO, they are the least reduced at 850°C. After reduction at 20%RO, GUL, LIL, and CCL are slightly more reduced than RHP and MBA at 760°C, but the same 3 hematites are the least reduced at 850°C. On the contrary, RHP is the least reduced at the lower temperature, while it is the second most reduced at higher temperatures, both at 50 and 20%RO.

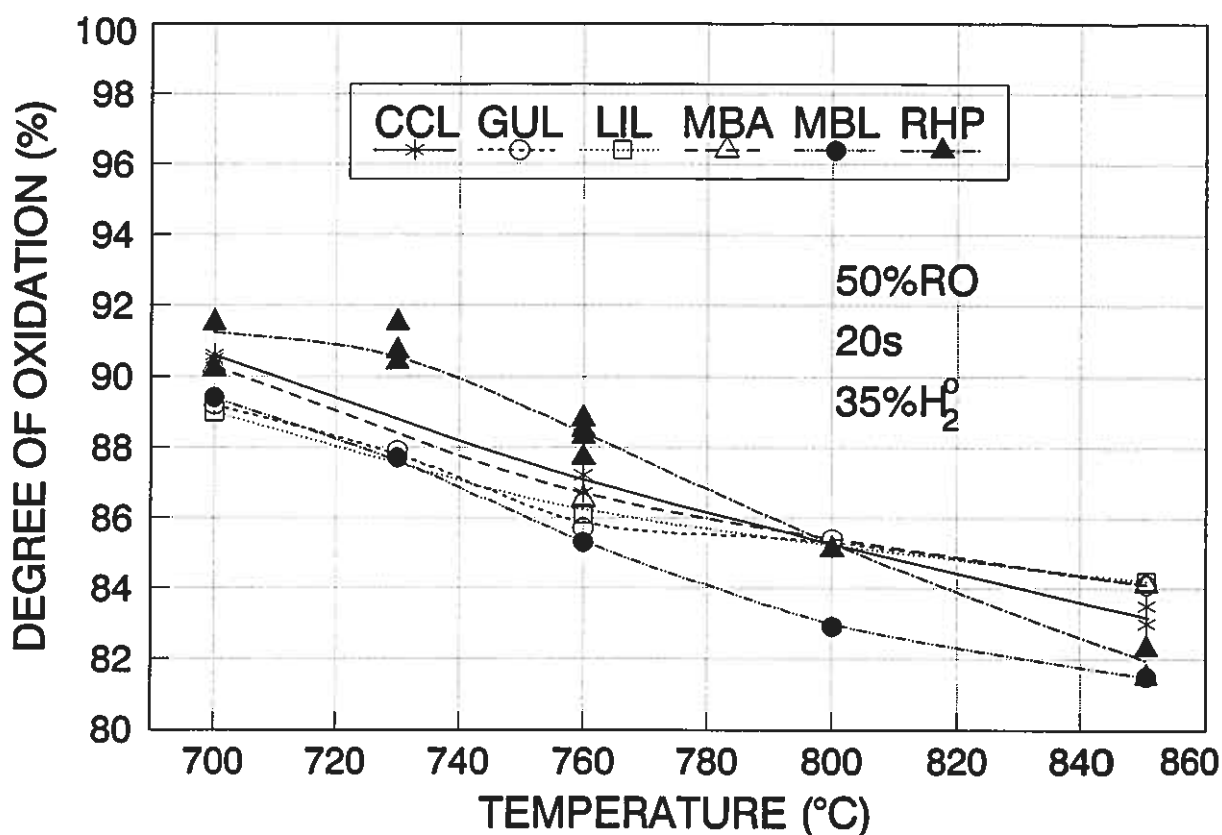


Fig. 5.42 Effect of reduction temperature on the natural hematites after 20s at 50%RO (35% H_2 in inlet gas).

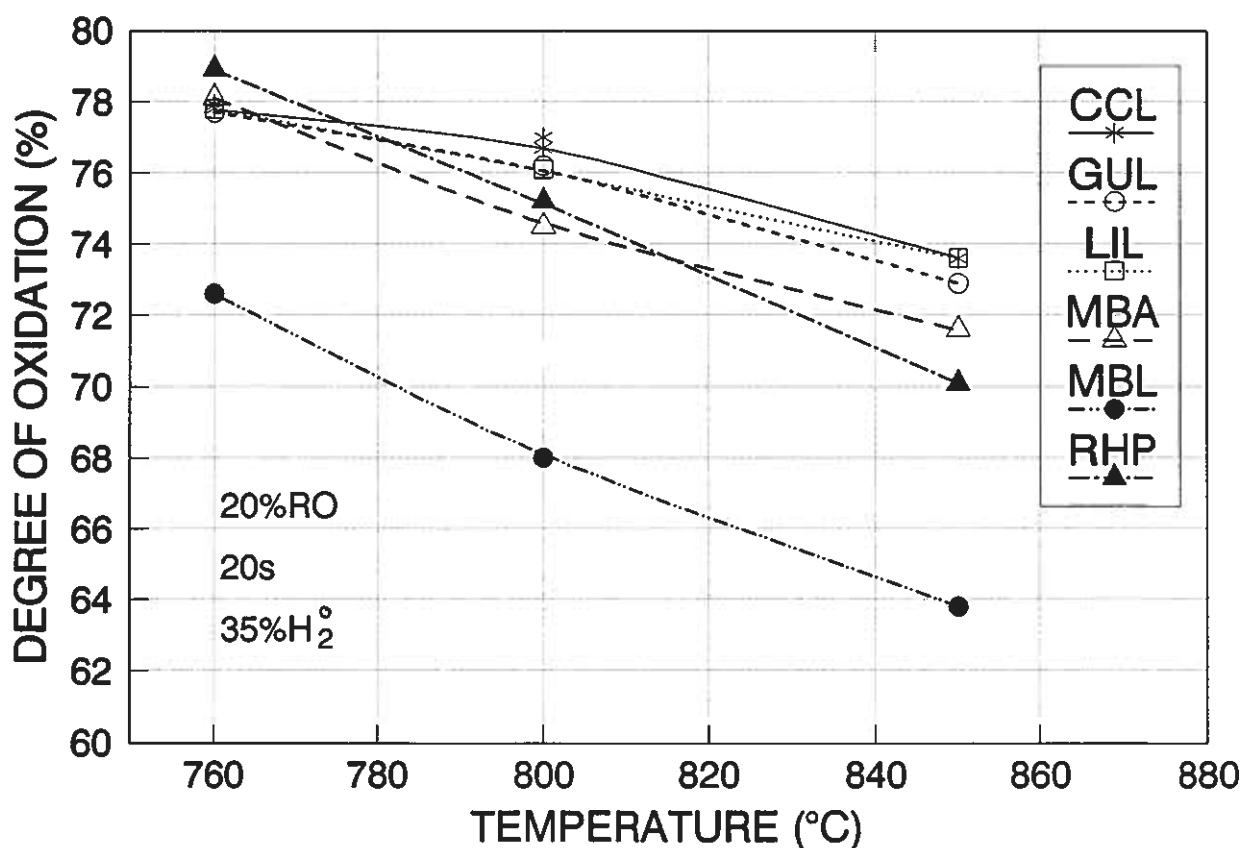


Fig. 5.43 Effect of reduction temperature on the natural hematites after 20s at 20%RO (35% H_2 in inlet gas).

5.5.3 Effect of gas composition

The amount of hydrogen in the reduction gas is the variable in this series of reduction experiments, while the reduction potential is constant at either 50 or 20%RO. Starting without hydrogen with CO/CO₂=1 (50%RO) or CO/CO₂=4 (20%RO) in the inlet gas in the first experiments, CO is successively substituted by H₂ in the other experiments. The natural hematites were reduced for 20 seconds at 760°C and the results are presented in figure 5.44 at 50%RO and figure 5.45 at 20%RO.

Figure 5.44 shows that without H₂ in the reduction gas at 50%RO, the reduction rate is retarded both for RHP and MBL, but not for GUL. The effect of raising the H₂ content from 15 to 35% is rather small and there is no effect in raising it from 35 to 45%. GUL is the most reduced at low H₂ contents, while MBL is insignificantly more reduced at higher H₂ contents. RHP is the least reduced of these 3 hematites independent of H₂ content.

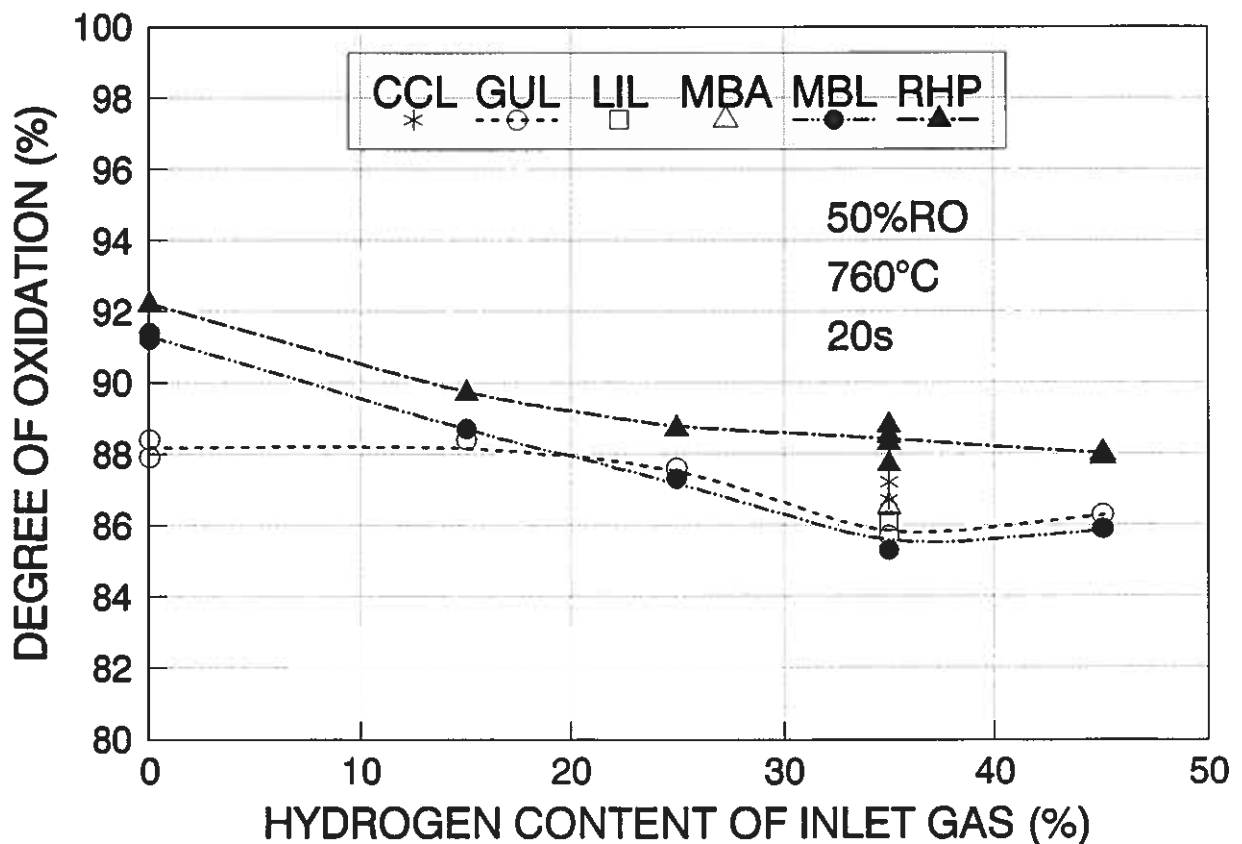


Fig. 5.44 Effect of the substitution of CO by H₂ at 760°C and 50%RO, on 20s prereluction of the natural hematites.

The effect of an increased H_2 content is considerably more pronounced at 20%RO than at 50%RO. Again there is no effect of raising the content of H_2 from 35 to 45% as shown in figure 5.45. However, there is a significant rate enhancing effect on substitution of up to 35% CO by H_2 .

GUL and LIL are the most reduced samples when H_2 is not added to the reduction gas at 20%RO. The degree of oxidation of MBL, MBA, RHP and CCL is found in the interval 87-89%, differences being small. At higher H_2 contents, MBL is considerably more reduced than the others, while RHP again is the least reduced.

Referring to the chemical analyses in the tables A.3.14 and A.3.15 in appendix A.3, no metal has been formed at 50%RO, and less than 1% at 20%RO.

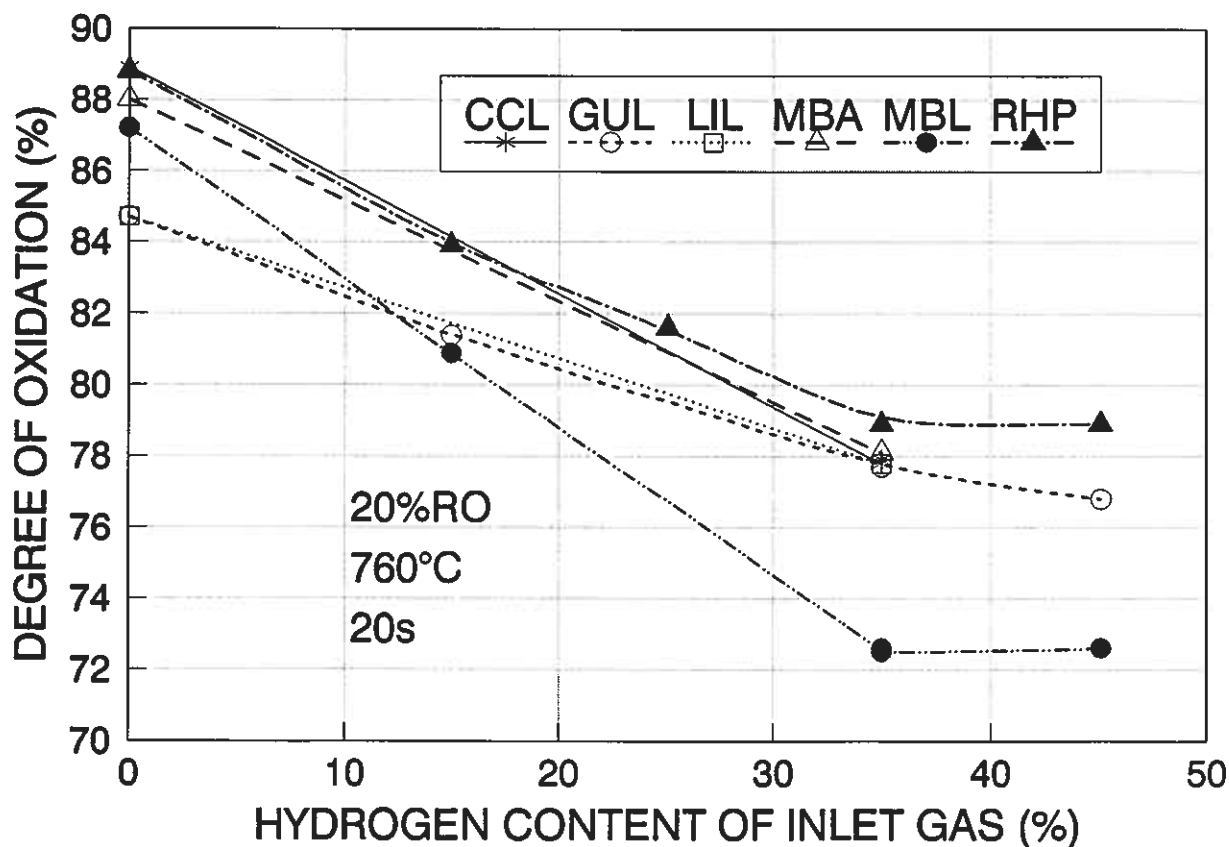


Fig. 5.45 Effect of the substitution of CO by H_2 at 760°C and 20%RO, on 20s prereluction of the natural hematites.

5.6 Tables of main prereduction results

The main prereduction results for the natural hematites and preoxidized Sydvaranger magnetite are gathered in the tables 5.3 and 5.4, respectively. Mean degree of oxidation have been calculated from mean values of parallel chemical analyses. The individual analyses are found in appendix A.3.

Table 5.3 Main prereduction results for the natural hematite concentrates. Short terms are given in section 5.5.

Temp. (°C)	RO (%)	H ₂ ^o (%)	Time (s)	Degree of oxidation, OX (%)					
				CCL	GUL	LIL	MBA	MBL	RHP
760	20	35	0	97.6	99.9	99.8	99.6	100.0	99.2
			12	85.5	82.2	82.6	84.4	80.8	86.4
			20	77.7	77.7	77.8	78.1	72.6	78.9
			30	72.4	72.7	72.9	72.8	62.8	74.1
			40	67.6	70.1	69.4	69.1	55.1	69.3
			50	67.8	67.9	68.6	63.5	51.4	64.6
			60	63.5	65.1	65.9	57.3	46.1	62.7
760	35	35	12	91.1	87.1	87.5	89.2	88.4	90.6
			20	85.9	84.0	84.3	83.7	76.8	85.4
			35	79.3	79.4	79.9	77.6	72.4	78.4
			60	76.1	75.8	75.7	73.2	70.1	74.1
760	50	35	12	91.8	89.3	89.0	90.5	89.6	93.1
			20	87.0	85.7	86.1	86.5	85.3	88.4
			35	85.1	85.2	85.1	83.6	80.9	84.0
			60	78.6	80.7	79.9	78.5	74.8	78.9
760	20	0	20	88.9	84.7	84.7	88.0	87.2	88.8
		15	-	81.4	-	-	80.9	83.9	
		25	-	-	-	-	-	81.6	
		35	77.7	77.7	77.8	78.1	72.6	78.9	
		45	-	76.8	-	-	72.6	78.9	
760	50	0	20	-	88.2	-	-	91.3	92.2
		15	-	88.4	-	-	88.7	89.7	
		25	-	87.6	-	-	87.3	88.7	
		35	87.0	85.7	86.1	86.5	85.3	88.4	
		45	-	86.3	-	-	85.9	88.0	
760	20	35	20	77.7	77.7	77.8	78.1	72.6	78.9
800			76.8	76.2	76.1	74.5	68.0	75.2	
850			73.6	72.9	73.6	71.6	63.8	70.1	
700	50	35	20	90.6	89.2	89.0	90.3	89.4	90.8
780			-	87.9	-	-	87.7	90.8	
760			87.0	85.7	86.1	86.5	85.3	88.4	
800			-	85.4	-	-	82.9	85.1	
850			83.3	84.1	84.2	84.1	81.5	81.9	

Table 5.4 Degree of oxidation after prereduction of preoxidized Sydvaranger magnetite.

TIME ⇒

Preox. temp sample (°C)		12s		20s		35s		60s	
		% RO		% RO		% RO		% RO	
		20	50	20	50	20	50	20	50
S1 →	799	84.5	90.6	71.4	86.7	67.0	82.2	50.3	75.7
S2 →	900	-	-	71.9	-	-	-	47.4	-
S3 →	1002	-	-	73.3	88.0	-	-	47.9	-
S4 →	1050	-	-	73.3	-	-	-	49.3	-
S5 →	1104	-	-	72.9	87.6	-	-	52.7	75.8
S6 →	1150	-	-	75.0	89.3	-	-	59.2	-
S7 →	1195	-	-	76.3	89.3	-	-	61.2	-
S8 →	1244	85.3	91.8	75.6	88.8	71.6	85.3	60.3	80.4

REDUCTION CONDITIONS: 760°C, 35% H_2 IN INLET GAS

TEMPERATURE ⇒

Preox. sample	700°C		730°C		760°C		800°C		850°C	
	% RO		% RO		% RO		% RO		% RO	
	20	50	20	50	20	50	20	50	20	50
S1 →	-	90.0	-	88.4	71.4	86.7	68.6	83.7	66.7	79.9
S8 →	-	91.4	-	90.2	75.6	88.8	73.3	86.7	71.9	83.2

REDUCTION CONDITIONS: 20s, 35% H_2 IN INLET GAS

H_2 CONTENT IN INLET GAS ⇒

Preox. sample	0%		15%		25%		35%		45%	
	% RO		% RO		% RO		% RO		% RO	
	20	50	20	50	20	50	20	50	20	50
S1 →	-	91.1	-	87.9	-	87.7	71.4	86.7	-	86.6
S8 →	-	94.4	-	90.2	-	89.8	75.6	88.8	-	89.0

REDUCTION CONDITIONS: 760°C, 20s

5.7 Discussion of method

5.7.1 Introduction

The reactor and its accessory equipment provides an excellent means of bringing small particles in thorough contact with the gas. Each particle will always experience fresh gas because of the relatively high gas velocity and spent gas is removed at the same time. Hence, gas concentration is known (and in the present work also constant) at any instant during each experiment. Diffusion through the gas film around each particle can safely be excluded as rate controlling mechanism during reduction.

The method is not continuous as the gravimetric method. Samples are reduced in batches and each batch is chemically analyzed. Many experiments and subsequent chemical analyses are required. At the same time an opportunity is given to investigate grain cross sections in microscope and in this way also to study the progress of the reduction. A better understanding of what is physically taking place during the reduction may be achieved.

Factors affecting the accuracy of this experimental method are; accuracy of wet chemical analyses and gas mixing unit, changing grain sizes and material loss during experiments, which will be treated in the following. Reduction of the different materials was carried out using equal grain sizes, but size cut was not efficient and grain sizes decrease during reduction. A large material loss is sometimes observed, which contributes to diminish the accuracy of the method.

The set %RO of the reduction gas is systematically a little too high, but this does not affect differences in reduction rates. The accuracy of the gas mixing unit was controlled by analyzing the mixed gas by chromatography (Grøntvedt et al., 1986). The analyses of CO₂ were generally too high, +4.6% at 50%CO₂. The analyses of CO were both too high and too low (max. deviation: +1.6% at 20%CO and -5.2% at 50%CO). The one analysis of H₂ was 4.4% too low at 60%H₂. The uncertainty of each analysis was ±2%.

5.7.2 Accuracy of wet chemical analyses

The accuracy of the chemical analyses and the calculated degree of oxidation and metallization is acceptable, although the amount of sample, of which Fe^{tot} , Fe^{2+} and Fe^{met} were analyzed, was rather small (0.5-1.0 g). The accuracy was tested on parallels both from 1 and from 3 different runs, as described in section 5.3.3. The accuracy of the chemical analysis of Fe^{tot} is good. The standard deviation is about 0.3% both for 1 and 3 runs.

The accuracy of the analysis of Fe^{2+} is good when the content of metallic iron is negligible. The standard deviations for 1 and 3 runs are 0.2 and 0.7%, respectively. However, the analysis of Fe^{2+} is rather uncertain in the presence of metal. The standard deviation is 3.4% in the same run while it is only 1.9% in the different runs, indicating that the accuracy of the experimental conditions is better than the accuracy of the chemical analysis. Hence, parallel analyses of Fe^{2+} have been accomplished in several runs, referring to appendix A.3, tables A.3.2-A.3.15. The parallels were mainly carried out because the first ones were believed to be a little out of range.

The standard deviation of Fe^{met} is 0.3% in different runs at low metal levels (1.5%). Maximum deviation of the metallization ($100\% \cdot \text{Fe}^{\text{met}}/\text{Fe}^{\text{tot}}$), calculated from the standard deviations of the individual analyses, is 0.4%. The detecting level of Fe^{met} is 0.2%. No metal should be formed at 50%RO with the water-gas shift reaction in equilibrium, but 0.2-0.4% is sometimes found. Being of comparable size with the standard deviation, it is possible that metal is not present in some of these samples. However, metallic particles, sticking to the reactor walls from previous experiments, can have loosened and followed the sample out. Metallized particles have been verified in microscope. The reaction, $4 \cdot \text{Fe}_{1-y}\text{O} \rightarrow \text{Fe}_3\text{O}_4 + \text{Fe}$, can also take place below 570°C, during cooling.

Maximum deviation of the degree of oxidation prior metallization is low, 0.4%. Maximum deviation when metallization has commenced (at OX=70%) is rather large, 1.7%.

5.7.3 Changing grain sizes

The same narrow fraction of each concentrate has been reduced so that differences in grain size should not mask the effect of other characteristics on the reduction rate. However, size cut was not efficient and the grain sizes of all the concentrates decrease during the reduction experiments, referring to figures 5.46 a-h. Hence, the effects of different grain sizes on the reduction rates have to be considered. The decrease in grain size contributes to an increased reduction rate.

The decrease in grain size can partly be attributed to the rough treatment in the laboratory equipment (rapid heating and milling effects), but differences in grain diminishing effect can be attributed to properties characteristic of the concentrates.

There is a small grain diminishing effect of milling in the reactor. The small decrease in grain size during the reduction of CCL, RHP and S1 can largely be attributed to milling. The large decrease in grain size, observed for MBA, MBL, GUL, LIL and S8, can also be attributed to decrepitation upon heating or degradation during initial reduction. Anisotropy of the reduction velocity causes cracking along subgrain boundaries and subsequent degradation because of unequal volume expansion in adjacent hematite crystals (ref. section 5.2.4). GUL, LIL, MBL and MBA, having lots of subgrains in each grain, experience large decreases in grain size. Degradation of CCL and RHP is insignificant because their grains contain no subgrains, referring to figures 4.6-4.7.

The samples, of which the grain size were controlled, were reduced for either 20s at 20%RO or 35s at 50%RO, at 760°C and with 35% H₂ in the inlet reduction gas. In addition, the grain size of GUL was controlled after reduction at 35%RO. The grain size distribution after reduction for 20s at 20%RO roughly equals the grain size distribution of the same material after reduction for 35s at 50%RO for most of the material types. RHP is the finest and GUL the coarsest of the raw materials, while MBA is the finest and CCL the coarsest of the reduced samples.

There is no obvious connection between the degree of oxidation after reduction and the changes in grain size for different materials. The degree of oxidation is about 78% for CCL, GUL, LIL, MBA, and RHP after 20s reduction at 20%RO, but the grain size of MBA, GUL, and LIL has become much finer while the grain size of RHP and CCL have not changed much.

Referring to figure 5.46a, the change in grain size for GUL is by far most pronounced during the initial reduction of hematite to magnetite within the first 12 seconds of reduction at 35%RO. The degree of oxidation (OX) after 12s is 87.1%, while OX=88.9% for magnetite. The further decrease in grain size from 12, to 20, 35 and 60 seconds is much less pronounced. Hence, the main grain diminishing effect is probably caused by degradation during initial reduction, although decrepitation due to thermal shocks on heating can not be excluded. The grain diminishing effect during the further reduction is probably caused by milling.

The higher rate of reduction at 20%RO than at 50%RO probably causes an increased degradation of MBL at 20%RO, referring to figure 5.46c. MBL is the only sample for which the grain sizes of the most reduced sample after 20s (20%RO) are significantly finer than the least reduced sample after 35s (50%RO). Exfoliation upon heating along the lineation between subgrains may cause decrepitation, since MBL is a schistose hematite, but this fact can not account for the increased degradation at 20%RO.

The grain diminishing effect is particularly large for MBA, referring to figure 5.46d, which can partly be attributed to decrepitation upon heating. MBA contains small inclusions of goethite, according to descriptions in chapter 4. The combined water does not have any chance to escape through the compact grains without disrupting the grains (along subgrain boundaries).

The grain size of CCL in figure 5.46f is slightly coarser after reduction at 20%RO for 20s (OX=77.9) than after reduction at 50%RO for 35s (OX=85.1). Only milling can account for the small grain diminishing effect, since the sample with the longer retention time has become the finer, although it is least reduced.

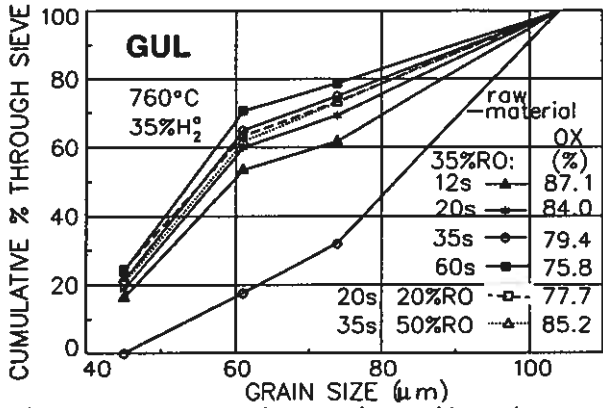


Fig. 5.46a Size distribution of GUL before and after reduction.

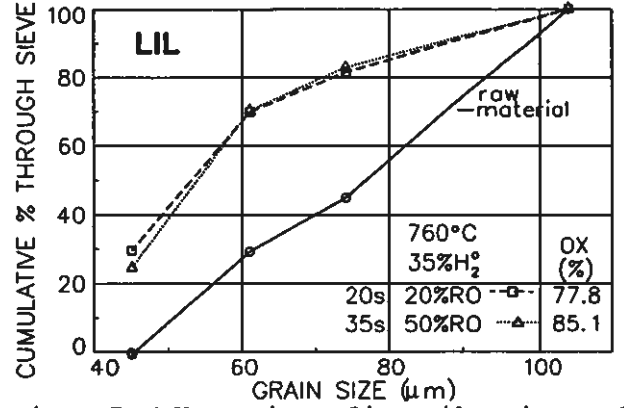


Fig. 5.46b Size distribution of LIL before and after reduction.

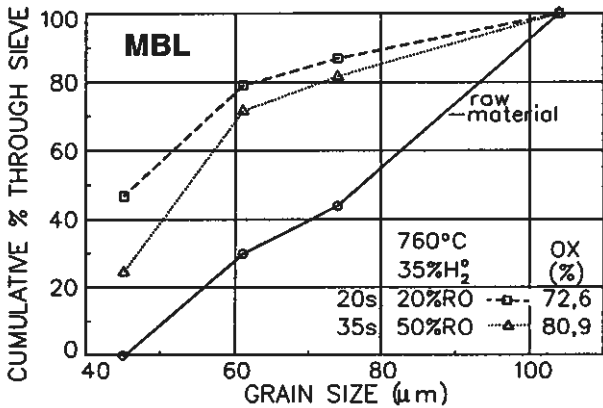


Fig. 5.46c Size distribution of MBL before and after reduction.

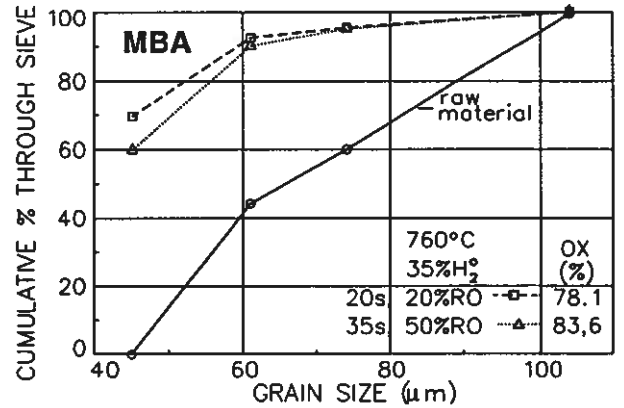


Fig. 5.46d Size distribution of MBA before and after reduction.

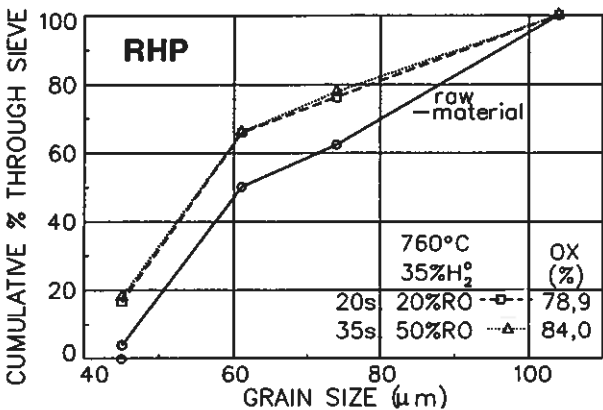


Fig. 5.46e Size distribution of RHP before and after reduction.

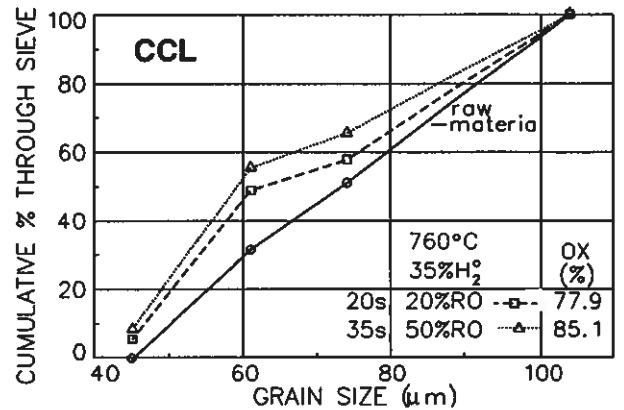


Fig. 5.46f Size distribution of CCL before and after reduction.

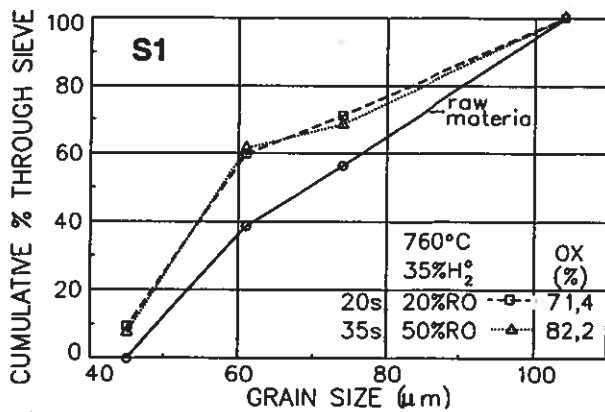


Fig. 5.46g Size distribution of S1 before and after reduction.

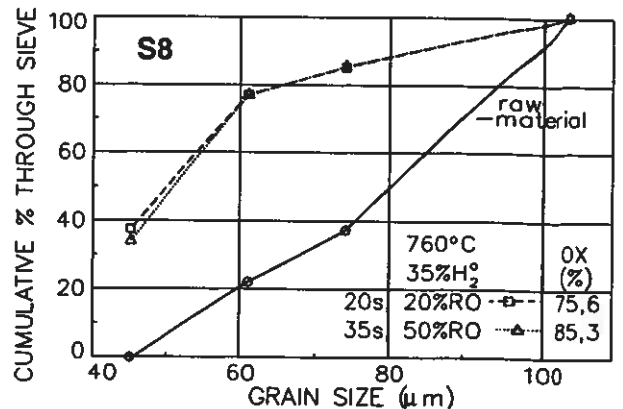


Fig. 5.46h Size distribution of S8 before and after reduction.

Referring to the figures 5.46 g-h, the small size decrease of S1 compared to S8 is difficult to account for. While the grains of S8 contains a few if any subgrains, the grains of S1 are comprised of numerous subgrains (ref. figures 3.18-3.19). Hence, S1 should be more inclined to degradation than S8. Probably is stress along subgrain boundaries in S1 accommodated for by the huge amount of subgrains randomly distributed in the grains.

Several possible reasons for the grain size to change during reduction experiments, are listed below. The moments 1-5 have been thoroughly discussed in section 5.2.4.

- 1) **Decrepitation** on heating due to thermal shock, caused by:
 - 1a) expulsion of combined water in compact hematite grains
 - 1b) exfoliation along the lination in schistose hematite
- 2) **Volume expansion** caused by the lattice transformation during the reduction from hematite to magnetite and wüstite
- 3) **Degradation** during the reduction to magnetite, caused by:
 - 3a) development of transgranular cracks
 - 3b) tearing along subgrain boundaries due to an anisotropic reduction rate which causes unequal volume expansion in adjacent hematite crystals
- 4) **Swelling** due to growth of iron whiskers
- 5) **Contraction** due to iron sintering
- 6) **Selective material loss** to the flue gas, examples are:
 - 6a) the finest fraction of a material is lost
 - 6b) grains with special shapes (sheetlike) are lost
- 7) **Milling** effects in the reactor may cause the grain size to decrease, while the "dust" may be lost in the flue gas.
- 8) **Decrepitation** due to thermal shock on cooling

A coarsening of the grain size was not observed in the present reduction experiments. Iron was not precipitated in the samples referred to. Hence, contraction due to iron sintering is not the reason for the decrease in grain size. Decrepitation due to thermal shock on cooling implies broken grains. Such broken grains have only rarely been observed in microscope.

5.7.4 Material loss

A large material loss is sometimes obtained due to sticking and elutriation of particles in the flue gas, which contributes to diminish the accuracy of the method. Loss of material during the reduction will affect the reduction results if the removal of particles is selective, otherwise not. The material loss increases with reduction time, and is strongly dependant on material type. The material loss is accelerated during metallization, because metallized particles tend to stick to the reactor walls. The material which is not lost, is called the output from the reactor. The outputs are reported in appendix A.3. The relative output (B) is the ratio of the actual yield and a theoretical yield calculated from the chemical analyses prior to and after the reduction. The relative output is in this way corrected for the weight loss caused by the reduction, being 100% if no material is lost. The output is a rough measure, but the trends in the figures 5.47-5.50 are quite clear.

The material loss of MBL is the largest, both at 50 and 20%RO, referring to the figures 5.47-5.48. The relative outputs decrease most at start due to elutriation. 40% MBL material is lost after 12 seconds reduction at 760°C, while 20-30% of the MBA, GUL and LIL materials are lost. The rather large initial material loss of these 4 concentrates can be connected to their large decrease in grain size due to decrepitation upon heating and degradation during initial reduction, previously linked to their subgrain structure. However, the material loss is the largest for MBL, but the grain size of reduced MBA is the finest.

The material loss is accelerated after about 40 seconds at 20%RO when metallic iron has precipitated, especially for RHP, CCL and S1, as shown in figure 5.48. Metallization has reached 8% or more after 50 seconds reduction, referring to the figures 5.41 and 5.31. The outputs of S1 and CCL after 60 seconds are 10-20%, only. Sticking of particles to the reactor walls is the reason. By opening the reactor it has been confirmed that particles stick to the walls. The location is in the latter 1/4 part of the rotation where the inside radius is smallest.

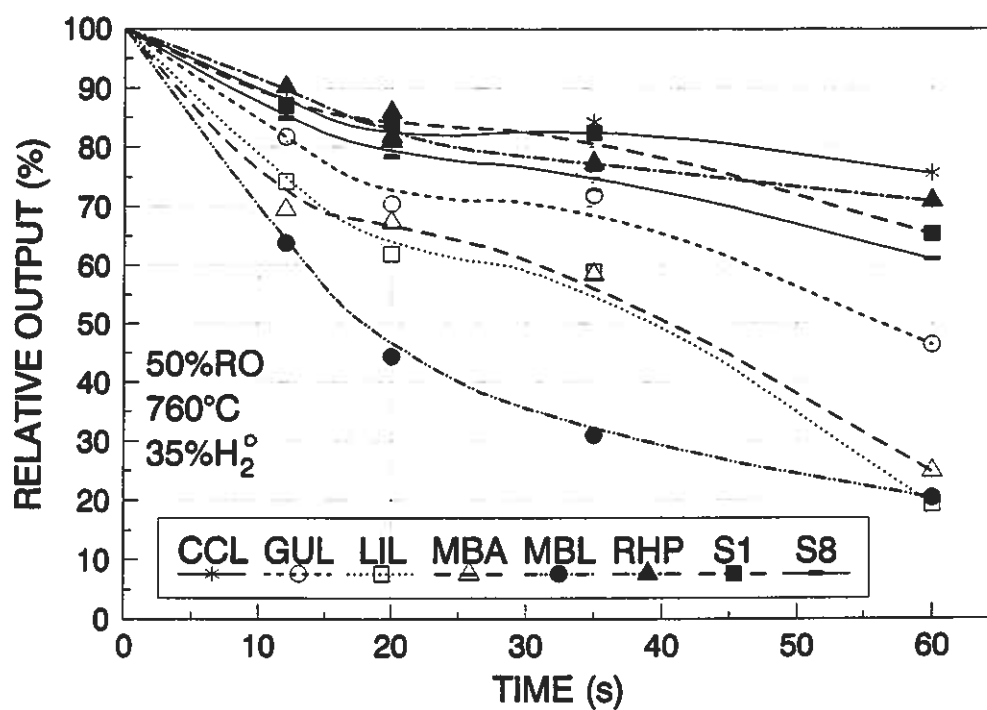


Fig. 5.47 Relative output of the reactor after reduction at 760°C and 50%RO and with 35%H₂ in the inlet gas.

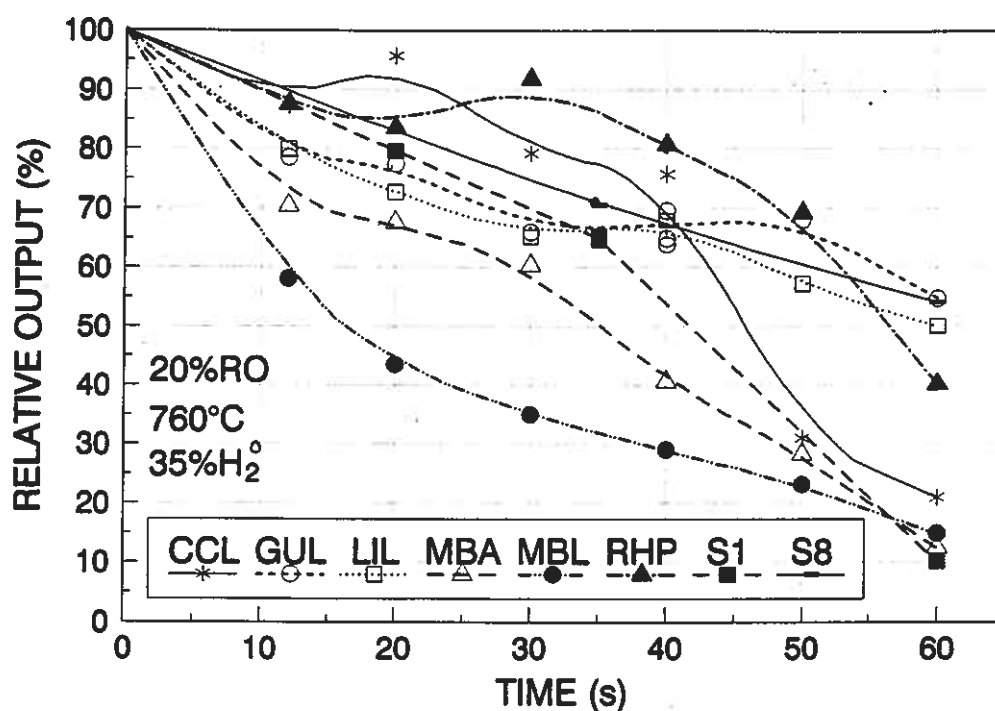


Fig. 5.48 Relative output of the reactor after reduction at 760°C and 20%RO and with 35%H₂ in the inlet gas.

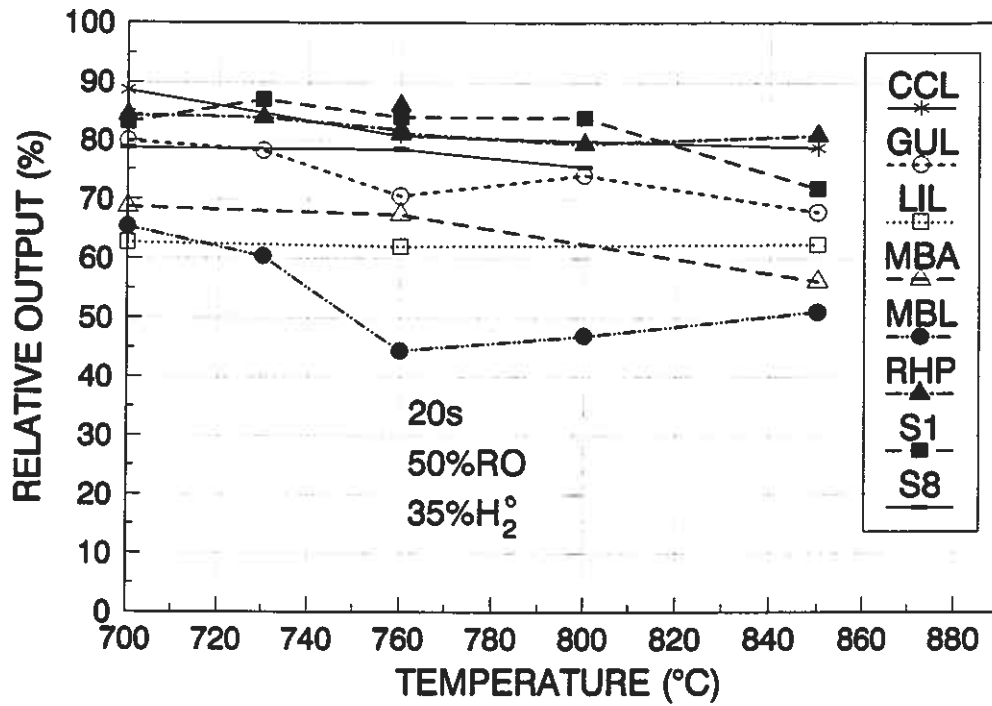


Fig. 5.49 Effect of the reduction temperature on the relative output from the reactor after reduction at 50%RO for 20s and with 35%H₂ in the inlet gas.

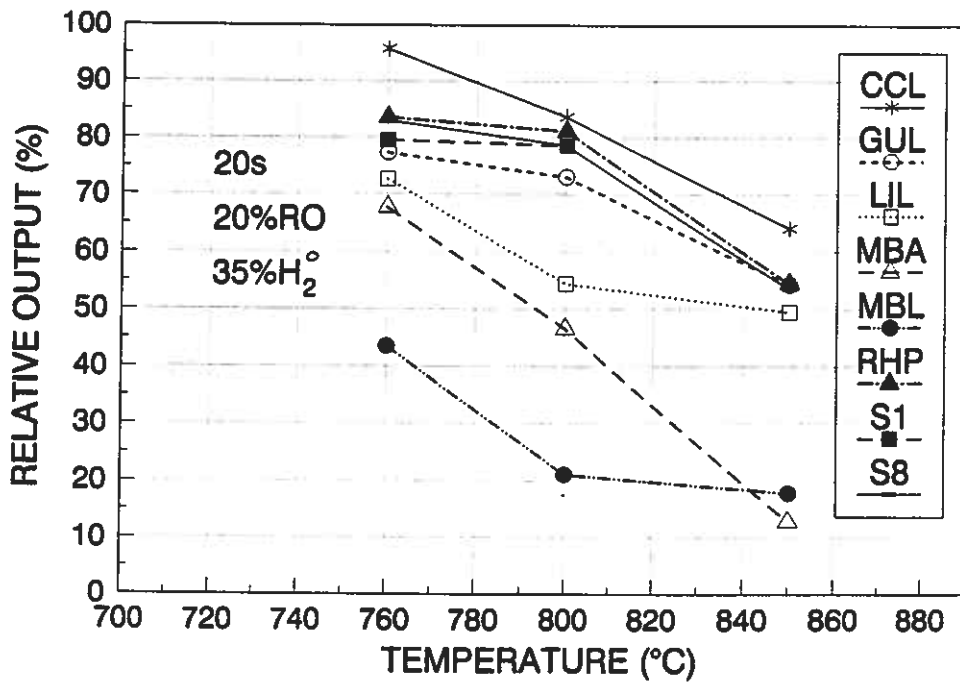


Fig. 5.50 Effect of the reduction temperature on the relative output from the reactor after reduction at 20%RO for 20s, with 35%H₂ in the inlet gas.

The highest relative outputs, 80-90%, are obtained for CCL, RHP and S1 within the first 30 seconds after reduction at 50%RO in the temperature range 700-850°C (ref. figures 5.47 and 5.49). These materials are less inclined to changes in grain size than the others. For the natural hematites CCL and RHP, this has been connected to the lack of subgrains in their grains. Since the decrease in grain sizes during the reduction of CCL, RHP and S1 was largely attributed to milling, it is possible that the lost material is "dust" from the milling. However, the grain size of the lost material may have been evenly distributed.

The relative outputs decrease only slightly by an increase in temperature at 50%RO when metal is not produced, referring to figure 5.49. However, the material loss is markedly accelerated for an increasing temperature at 20%RO, as illustrated in figure 5.50, mainly due to sticking. Metallization increases with temperature, especially for MBL, MBA, and RHP, but not very much (referring to table A.3.13). Variations in the content of H₂ in the inlet gas (0-45%) do not affect the outputs, referring to appendix A.3 (tables A.3.6, A.3.14 and A.3.15).

Magnetite grains do not stick during prereluction, since magnetite is reduced at a very slow rate compared to hematite, and metallization in magnetite grains starts at a later stage. CCL has the far highest content of magnetite grains. Hence, reduced CCL samples may have a too high content of these magnetite grains, but this is not very likely.

Apart from elutriation and sticking, leakages caused material loss in the experiments at 35%RO (except for MBL). Otherwise no leakage was observed. Leakages, in the transport tubes or in the reactor, are considered not to cause selective material loss. Material loss caused by elutriation or sticking, may be selective. Causes of selective material loss are listed below.

- 1) Elutriation of:
 - 1 a) the fine fraction of a sample (reduces at a higher rate)
 - 1 b) "dust" from milling (the most reduced part of the particles)
 - 1 c) schistose particles (reduces at a higher, anisotropic rate)
- 2) uneven metallization causes selective sticking (the most metallized grains are restrained)

The mentioned causes of selective material loss imply that the calculated degree of oxidation is too high, since the remaining particles are less reduced than those lost.

The reduction results have shown that MBL is reduced at the highest rate. Since the outputs are the lowest, the uncertainty naturally is higher than for the other materials. However, if the material loss has been selective, the most reduced particles or parts of particles probably have been lost. Hence, the calculated degree of oxidation has been too high and not too low.

5.7.5 Concluding remarks

The accuracy of the chemical analyses and the calculated degree of oxidation and metallization is acceptable.

A large material loss is sometimes obtained due to sticking and elutriation of particles in the flue gas. This contributes to diminish the accuracy of the method, but only if the removal of particles is selective. If the material loss has been selective, the most reduced particles or parts of particles probably have been lost. Hence, the calculated degree of oxidation is too high.

Differences in grain sizes may mask effects of other characteristics and should be taken into account, since size cut was not efficient and grain sizes decrease during the reduction. The decrease in grain size can partly be attributed to the rough treatment in the laboratory equipment (rapid heating and milling effects). The effect of milling is small compared to the large decrease in grain size due to decrepitation upon heating and degradation during initial reduction.

Differences between the concentrates in grain diminishing effects and material losses can be attributed to characteristics of the concentrates. A large initial material loss and decrease in grain size can be linked to the subgrain structure of the natural hematites. Decrepitation upon heating and degradation during initial reduction cause cracking along subgrain boundaries.

5.8 Discussion of prereduction results: preoxidized magnetite

5.8.1 Introduction

The progress of reduction is first described on the basis of observations in optical microscope for the samples preoxidized at low (800-1000°C) and elevated (1150-1250°C) temperatures. The significance of the differences in reduction rates, based on chemical analyses, is further discussed. Possible reasons for the slower rate of reduction for samples preoxidized at elevated temperatures are finally discussed.

5.8.2 The progress of reduction by optical microscope

50%RO

The reduction from hematite to magnetite proceeds topochemically, as shown in figure 5.51. The grains in the figure have been reduced for 12 seconds at 760°C and 50%RO (35% H_2 in the inlet gas). The degree of oxidation of the samples has nearly reached that of magnetite, 88.9%, but large hematite cores are still present. Some wüstite has been formed on the pore walls of the magnetite at the same time as the hematite was topochemically reduced, both in grains preoxidized at low and elevated temperatures. Hematite (hm) has a white appearance in plain reflected light in optical microscope, as shown in the photos 5.51a, c, and d. An outer layer of magnetite (mt) and wüstite (wü) covers the hematite cores, but magnetite and wüstite have both a grey appearance and etching is necessary to differentiate between them. The grains in figure 5.51c and d have been etched. The grains reduced at 50%RO were not affected by etching with 1% HCl in alcohol. Etching in 5% aqueous hydrofluoric acid, however, enabled to resolve magnetite (mt) and wüstite (wü) in accordance with the work of Brill-Edwards et al. (1965) and Walker and Carpenter (1970). Wüstite turns dark grey on etching while magnetite remains unchanged. By comparing grains of the sample S112 before and after etching (figure 5.51a and c), it is seen that the outer layer consists mainly of magnetite.

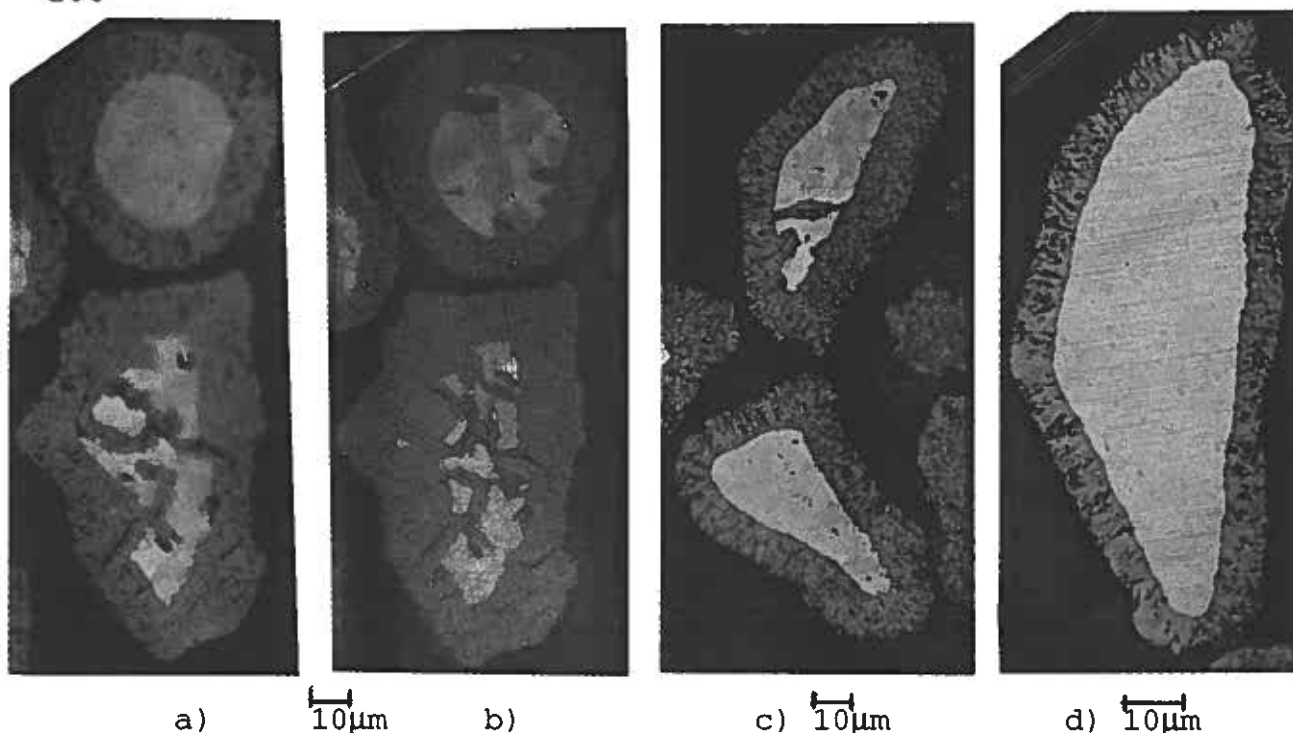


Fig. 5.51 Samples reduced at 760°C and 50%RO (35% H_2) for 12s.
 white:hm, grey:mt/wü, dark:pores or also wü if etched
 a) S112 OX=90.6%, reflected light, preoxidized at 799°C (24h)
 b) " " polarized light (hm in grey colours) "
 c) " " etched by 5%HF for 60s "
 d) S812 OX=91.8%, " preoxidized at 1244°C (3h)

On some occasions the conversion from hematite to magnetite and thereafter to wüstite also proceeds ahead of the topochemical front, as shown in the lower grain in figure 5.51a. The subgrain structure of the same hematite grain, which was obtained by oxidizing at a low temperature, is seen in polarized light in figure 5.51b. By comparing the two photos it can be seen that the reduction sometimes proceeds along subgrain planes.

During the further reduction the hematite core shrinks. Hematite is still present after 20 seconds reduction in most grains, but after 60 seconds there is no hematite left. The layer of magnetite grows while wüstite on the pore walls builds up. The reduction of magnetite to wüstite proceeds close to the uniform internal reduction model and this conversion is also nearly complete after 60 seconds reduction. Wüstite is in equilibrium with the reducing gas at 50%RO (ref. figure 5.1). Hence, the reduction does not proceed further to iron metal. In the etched grains in figure 5.52b and d, small relics (droplets) of uniformly distributed magnetite (grey) in a matrix of wüstite

(dark grey) are seen. The reduced grains which were preoxidized at an elevated temperature (Fig. 5.52d) contain more magnetite than grains preoxidized at a low temperature (Fig. 5.52b).

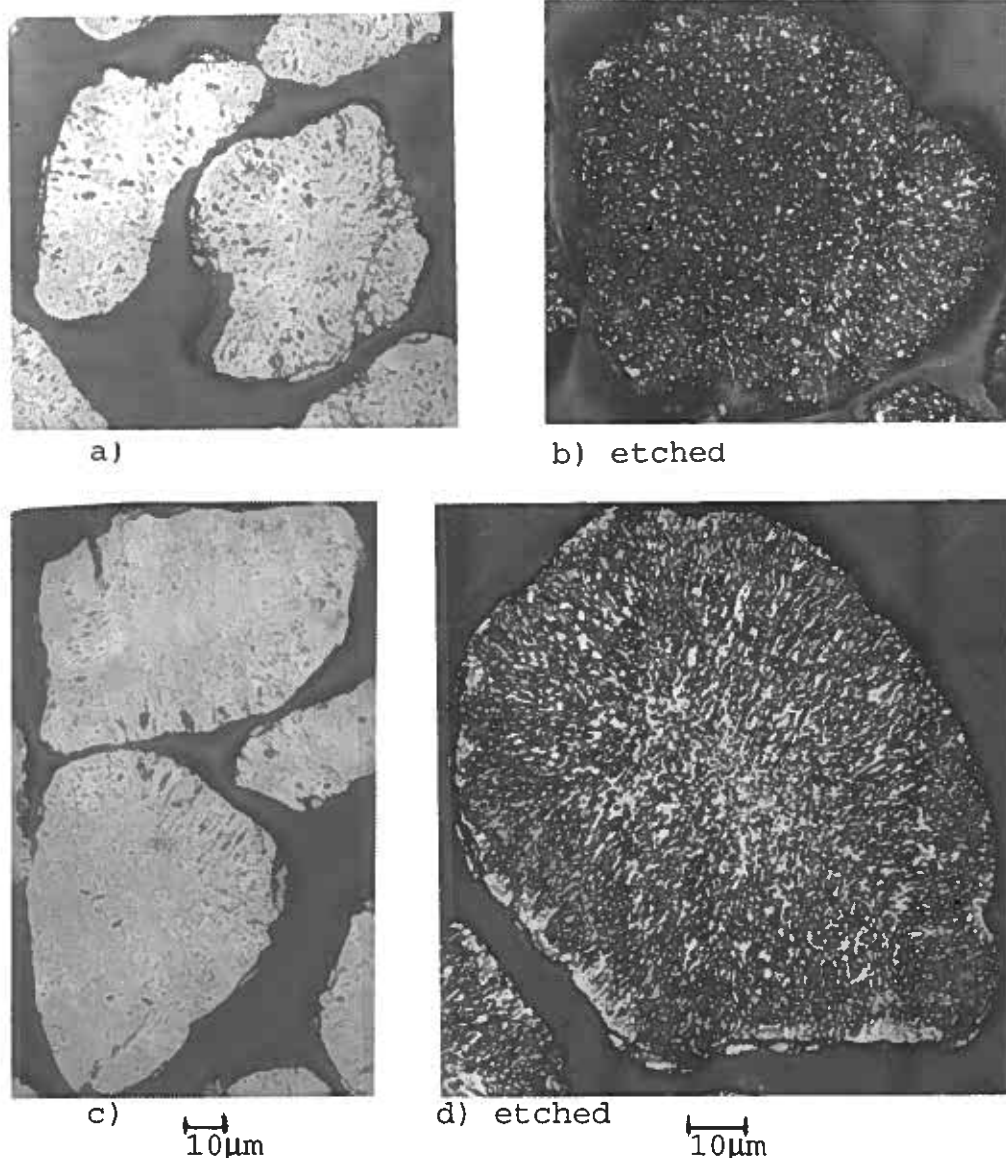


Fig.5.52 Grains reduced for 60s at 760°C and 50%RO
a,b) S14 (OX=74.6), preoxidized at 799°C
c,d) S84 (OX=79.9) " 1244°C

Since pores and wüstite after etching both have a dark grey appearance, the pore structure is better observed before etching. The pores in the grains preoxidized at the lower temperature seem to be the coarser, as illustrated by figure 5.52a compared to 5.52c. This sample was also reduced at a higher reduction rate.

An outer relatively dense layer (grey) is seen in some of the grains which were preoxidized at an elevated temperature, as shown in figure 5.52d. This may be relatively dense magnetite.

20%RO

At an early stage of the reduction at 760°C and 20%RO, hematite is topochemically reduced in the same way as observed at 50%RO, but at a higher rate. While most grains have hematite cores after reduction for 20 seconds at 50%RO, only a few of the grains preoxidized at low temperatures, and less than half of the grains preoxidized at elevated temperatures, have hematite cores after reduction for 20 seconds at 20%RO. After 35 seconds reduction, a core of hematite is still present in a few grains preoxidized at elevated temperature, shown in the upper grain in Fig. 5.53c.

Magnetite is quasi topochemically reduced to wüstite. The border between magnetite and wüstite is not very sharp and magnetite relics are left behind the topochemical front, as illustrated in figure 5.53. Magnetite and wüstite were successfully differentiated by etching with 1% HCl in alcohol after reduction with the "strong" reducing gas at 20%RO. Wüstite did turn dark grey on etching in accordance with the experience of Edström (1953). The hematite core and the magnetite and the wüstite layers are all seen in the upper grains in figure 5.53a and c, while the two latter phases are seen in the lower grains. The degree of oxidation is approximately 71.5% for both samples, but the grains in figure 5.53a have been reduced for 20 seconds after preoxidation at low temperature while the grains in figure 5.53c have been reduced for 35 seconds after preoxidation at an elevated temperature. The reduction pattern is mainly the same, but the rate of reduction is higher for the sample preoxidized at the lower temperature. Uniformly distributed remnants of magnetite in a matrix of wüstite is typical after 35s reduction in grains preoxidized at low temperature, shown in figure 5.53b.

The reduction proceeds to iron at 20%RO, but metallization is insignificant during the first 35 seconds. After 60 seconds reduction, the metal content is 23.3% in the sample S32 which was preoxidized at a low temperature (1002°C). Referring to figure 5.54a, metallization proceeds according to the uniform internal reaction model. Contrary, the metal content in the sample S62,

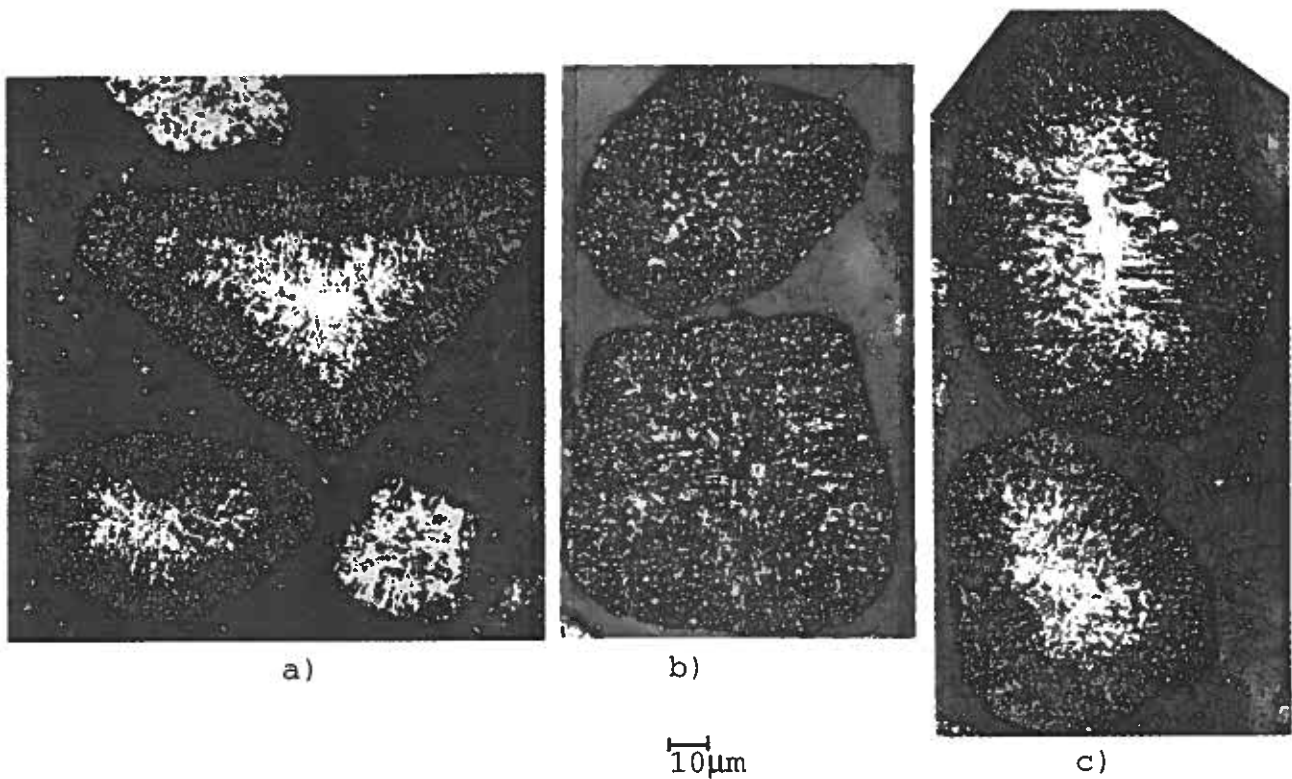


Fig. 5.53 Grain sections, reduced at 760°C and 20%RO (35% H_2).
Etched for 1 minute in 1% HCl in alcohol.
White phase: hematite, grey: magnetite, dark: wüstite

a) S11:	reduced for 20s, OX=71.3%,	preoxidized at 799°C (24h)
b) S116:	reduced for 35s, OX=66.4%,	" " "
c) S816:	reduced for 35s, OX=71.6%	" " 1244°C (3h)

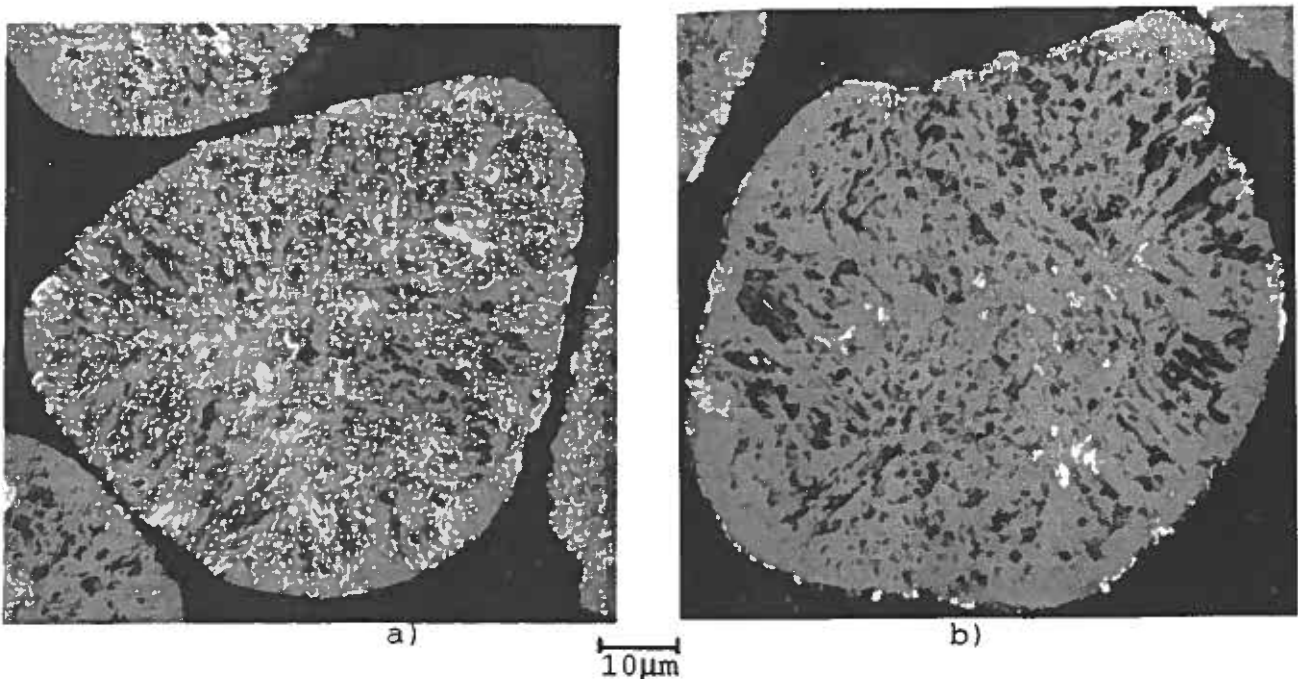


Fig. 5.54 Samples reduced for 60s at 760°C and 20%RO (35% H_2).
Reflected light, white: iron, grey: wüstite

a) S32:	OX=47.9%, $Fe^{met}=23.3\%$,	preoxidized at 1002°C (3h)
b) S62:	OX=59.2%, $Fe^{met}=8.9\%$,	" " 1150°C "

which was preoxidized at an elevated temperature (1150°C), has only reached a level of 8.9%. The formation of metal does also have a more topochemical nature, as shown in figure 5.54b, but iron precipitates are also found in the interior.

5.8.3 Significance of differences in reduction rates

An increase in the temperature of preoxidation from 800°C to 1250°C is accompanied by a decrease in the subsequent reduction rate, according to the results in the figures 5.29, 5.32 and 5.33. A rate retarding effect of elevated oxidation temperatures is always found, although reduction conditions have been varied.

This rate retarding effect is most pronounced for an increase in oxidation temperature from about 1050°C to 1150°C, as repeatedly indicated here in figure 5.34. The samples preoxidized at the elevated temperatures are markedly less reduced. The effect is best seen in the lower curve in figure 5.34 after

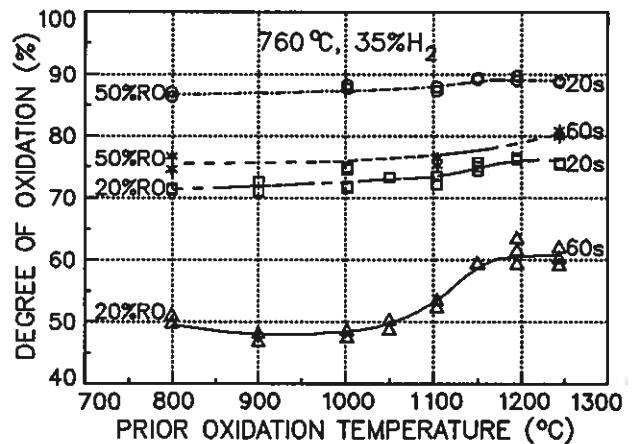


Fig. 5.34 Effect of temperature of oxidation on the reduction rate.

reduction for 60 seconds at 760°C and 20%RO (35%H₂ in the inlet reducing gas). The metal content is well above 20% in the samples preoxidized at 800-1050°C, while it is below 10% in the samples preoxidized at 1150-1250°C. About 5% Fe³⁺ remains in samples preoxidized at 1200-1250°C, which is contained in magnetite according to observations in microscope. No Fe³⁺ is left in samples preoxidized at 900-1050°C, referring to table A.3.8. Hence, the only reaction taking place at this stage is the reduction of wüstite to iron. The differences in degree of oxidation between the samples preoxidized at low and elevated temperatures is 13.4% after reduction for 60 seconds at 20%RO.

This difference is highly significant, since maximum deviation calculated from STD of the individual analyses is 1.7%, referring to section 5.7.2.

Raising the preoxidation temperature from 800°C to 900°C is not thought to affect the rate of reduction during wüstite and metal formation, provided oxidation is complete. According to table 5.4, the degree of oxidation after 60 seconds reduction at 20%RO is higher for the sample preoxidized at 799°C (OX=50.3%) than for the one preoxidized at 900°C (OX=47.4%). By comparing the two lower curves in figure 5.34, it is seen that the reduction of the magnetite preoxidized at 900°C has proceeded at the higher rate between 20 and 60 seconds. A higher rate of reduction is not observed in the initial period of 20 seconds, during which the reduction of hematite and magnetite dominates (ref. figure 5.53a). Microscopic observations in section 3.4.3 have shown that the sample preoxidized at 799°C did have remnants of magnetite in 1 of 100 grain cores. These dense magnetite relics may have retarded the formation of wüstite and metal. However, the actual difference in degree of oxidation is only 2.9%, which is less than the double maximum deviation in this range.

The rate retarding effect is also present during the early stages of the reduction prior to metallization, as shown in the 3 upper curves in figure 5.34. The upper curve in figure 5.34 shows the obtained degree of oxidation after the first 20 seconds of the reduction at 50%RO. It is $(86.7 \pm 0.4)\%$ for the sample S1 which was preoxidized at the lower temperature (799°C) compared to $(88.8 \pm 0.4)\%$ for the sample S8 which was preoxidized at an elevated temperature (1244°C). During this period the reduction of hematite to magnetite dominates, referring to figure 5.51. The double maximum deviation in this range is 0.8% (ref. section 5.7.2), significantly less than the difference in degree of oxidation (2.1%). Hence, a rate retarding effect of elevated oxidation temperatures on the rate of reduction from hematite to magnetite is observed, although not very pronounced. The upper curve in figure 5.34 does also indicate that the rate retarding

effect during the reduction of hematite is increasing gradually for an increasing preoxidation temperature.

The rate retarding effect of elevated preoxidation temperatures on the subsequent rate of reduction is maintained during the magnetite to wüstite step. The difference in degree of oxidation has increased from 2.1% after 20 seconds reduction to 4.7% after 60 seconds reduction at 50%RO. Referring to figure 5.52a and c, this may be attributed to lower porosity in the magnetite, which may have been caused by the slower initial reduction.

The curve obtained after 20 seconds reduction at 20% RO in figure 5.34, confirms the gradual increase in the rate retarding effect for an increasing preoxidation temperature during the initial reduction. The slope of the curve is steeper between a preoxidation temperature of 1100 and 1200°C, while a further increase in preoxidation temperature has no effect. The difference in degree of oxidation after reduction between samples preoxidized at low and elevated temperatures is 4.2% (OX=71.4% and 75.6% for samples preoxidized at 799 and 1244°C, respectively). This difference is of the same size as the difference after reduction for 60 seconds at 50%RO, and the reactions taking place are the same. Again, maximum deviation prior metallization (0.4%) is considerably less than this difference in degree of oxidation.

5.8.4 Possible reasons for the rate retarding effect

The rate retarding effect of elevated preoxidation temperatures on the rate of prereduction, will in the following be related to one or several of the properties characteristic of the preoxidized grains. Characteristics, which may have been differently affected by the different preoxidation temperatures are; grain size and shape, surface area and subgrain structure.

Grain size. Differences in grain sizes are not thought to contribute to the observed differences in reduction rates.

Reduction was carried out, using the fraction 63-90 μm . However, figure 5.55 shows that size cut was not efficient and that grains within this fraction are coarser after preoxidation at elevated temperatures (S8) than at low temperatures (S1). In accordance with the obtained reduction results, a higher reduction rate of S1 than of S8 can be predicted

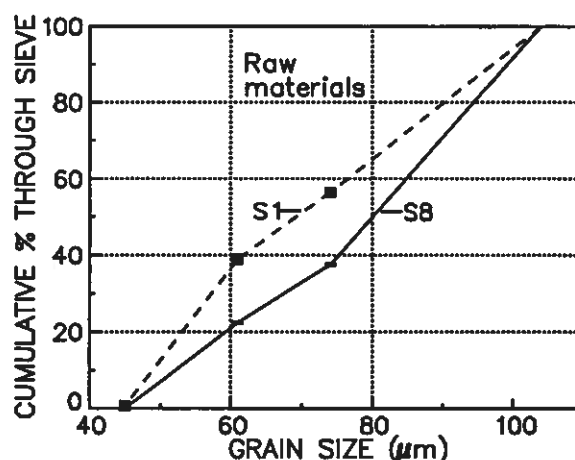


Fig. 5.55 Size distribution after preoxidation at 799°C (S1) and 1244°C (S8).

from the differences in initial grain sizes. However, the rate retarding effect is most pronounced during metallization. At this stage of the reduction, the grains are highly porous and are mainly uniformly reduced. Grain size is not important for the reduction rate when grains are uniformly reduced.

Grain sizes change differently during the reduction. Hence, predictions of reduction rates from the original grain sizes are difficult. In fact, the grains of S8 are considerably finer than the grains of S1 after the reduction, referring to the figures 5.46 g and h. The grain size changes have no effect on reduction rates if the changes in grain sizes have occurred on cooling (occasionally observed after reduction of S8). On the other hand, if this grain diminishing effect mainly has been caused by decrepitation during heating or degradation during the reduction, it may influence on the reduction rate. Since the grains of S8 are finer than the grains of S1 after 20 seconds reduction, a higher rate of reduction for S8 than for S1 could be predicted if grain size is important. Contrary, S1 is reduced at the higher rate of the two samples. Hence, differences in grain sizes are not expected to be the major cause of the rate retarding effect of elevated preoxidation temperatures.

Grain shape. The rate retarding effect of elevated preoxidation temperatures, is not caused by differences in particle shape.

Referring to section 3.5.3, the shape factor is 0.66 ± 0.03 independent of preoxidation temperature in the range 800-1250°C.

The shape of the particles was characterized by a planar shape factor (ψ), as defined by formula 3.31 in section 3.5.2.

$$\psi = \frac{4 \cdot \pi \cdot A}{L^2} \quad (3.31)$$

$A = \text{particle cross section}$
 $L = \text{particle perimeter}$

Both highly rugged surfaces and elongated particles imply relatively long perimeters (L) and low values of the shape factor. The reduction rate is expected to increase for a decreasing shape factor in both cases.

Due to sintering at elevated oxidation temperatures, the shape of the particles is expected to grow more spherical and surface ruggedness is expected to decrease. As a consequence, the shape factor is expected to increase and the reduction rate is expected to decrease. The reduction rate does decrease for an increasing oxidation temperature, in accordance with these predictions, but not due to an increasing shape factor. The original shape of the grains is perhaps more or less restored through gentle crushing after preoxidation at elevated temperatures. The impression of shape and surface ruggedness from the photos of grain sections in figures 3.18-3.19, does also indicate that particle shape is independent of preoxidation temperature in the actual range.

The specific surface area of the preoxidized samples has not been measured. However, differences in surface areas of the preoxidized samples in the present work are probably small and are not thought to be the main cause of the observed rate retarding effect. A slightly decreasing specific surface area with increasing preoxidation temperature can be expected, since the grains are a little coarser after preoxidation at elevated temperatures than at low temperatures, while the shape of the particles are independent of oxidation temperature.

The sample with the largest surface area is supposed to be

reduced at the highest initial rate, provided that other variables are identical. In accordance with these predictions, the initial reduction rates are the highest for the samples preoxidized at low temperature.

However, the rate retarding effect is not most pronounced during the initial reduction, but during metallization. Referring to section 5.2.4, surface areas are changing during the reduction. Initial specific surface areas are not considered to be important during metallization in the present work, because the surface areas of all the preoxidized samples must have been considerably enlarged since the grains are highly porous at this stage of the reduction. Variations in initial surface areas are only causing small differences in the surface areas of partly reduced samples according to Doherty et al. (1985) and Sheasby and Gransden (1975), but there is a relation between initial and final surface areas upon reduction according to Turkdogan and Vinters (1972).

The subgrain structure alters as preoxidation temperature increases, repeatedly shown by the SBA curve (length of subgrain boundaries/area) in figure 3.21. This change is considered to be the reason for the rate retarding effect of elevated preoxidation temperatures. The initial reduction rate and the SBA curve both decrease gradually with increasing preoxidation temperature. The rate of metallization is markedly retarded if the preoxidation temperature is raised from 1050 to 1150°C. This temperature range coincides with the steepest part of the SBA curve (1050-1200°C).

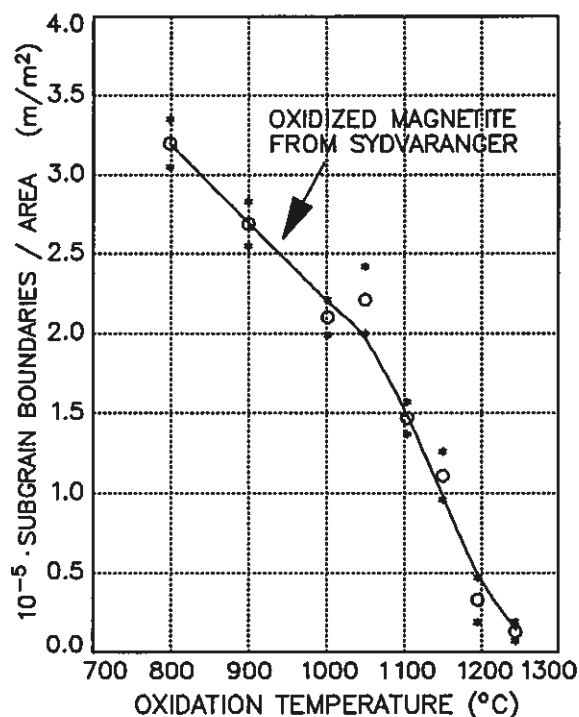


Fig. 3.21 Subgrain structure after preoxidation for 3h (24h at 799°C).

Subgrain boundaries can serve as preferential reduction paths, referring to figure 5.51a,b. Hematite is mainly topochemically reduced to magnetite, but on some occasions the conversion also proceeds ahead of the topochemical front along subgrain boundaries. The tendency for reduction along crystal boundaries to occur, depends on several factors: vacancies, defects, foreign ions, or a tearing tendency along subgrain boundaries. Gas diffusion and solid state diffusion along subgrain interfaces are facilitated. Tearing and vacancies along subgrain boundaries are perhaps the most probable causes.

Tearing along subgrain interfaces can occur due to expansion during topochemical reduction. Rupp et al. (1982) measured an anisotropic volume change of +4% parallel and -1% vertical to the c-axis on reduction to magnetite. Disruptive forces are set up along crystal boundaries due to an anisotropic reduction velocity (Meyer et al., 1967 and Ball et al., 1973). The tendency for tearing to occur, depends on the disparity of the c-axis in adjacent hematite grains. Referring to figure 5.51, tearing may occur, but crack radius and pore radius are of comparable sizes.

A beneficial effect of anisotropy on the initial reduction rate for grains preoxidized at the lower temperatures is possible, but not very probable. Referring to section 5.2.4, below the heading "anisotropy of the reduction velocity", the **orientation** of the subgrains (hematite crystals) is important for the rate of reduction. Hematite is preferentially reduced in a direction vertical to the c-axis (Meyer et al., 1967). However, studying the photos in figure 3.18 (page 65), the huge number of crystals comprising the grains preoxidized at low temperature seem to be rather randomly orientated. Some of the randomly orientated crystals may have been reduced at a higher rate than others, but the overall rate is probably unaffected by crystal orientation.

The beneficial effect of low preoxidation temperatures on the reduction rate is maintained during the magnetite to wüstite reduction step. This can be attributed to a higher porosity in

the magnetite, caused by a more rapid initial reduction, or to opening of tiny cracks along the initial subgrain boundaries.

The rate retarding effect of elevated preoxidation temperatures is most pronounced during metallization, or during reduction of magnetite relics. The steepest part of the SBA curve in figure 3.21, which is in the temperature range 1050 to 1200°C, coincides with the temperature range during which the reduction rate is markedly retarded during metallization. Iron nucleation is here essentially. Nucleation may have been enhanced by numerous active sites, for example where hematite subgrain planes initially intercepted or by defects, vacancies, foreign ions or tiny cracks along the subgrain boundaries. Iron does probably not nucleate before nearby magnetite remnants have been reduced to wüstite, since iron and magnetite do not coexist at these temperatures. Iron is uniformly precipitated in the grains preoxidized at the lower temperature while the metal is more concentrated on the grain surfaces in grains preoxidized at elevated temperatures, as shown in figure 5.54a and b.

Watanabe and Yoshinaga (1968) regarded defects along weak lines or cracks as nuclei for the observed rapid whisker growth. Weak lines or cracks developed along hematite "intergrowth" and microtwins at the reduction stage of hematite to magnetite, causing rapid initial reduction. Whiskers have not been observed in the present work, as could be expected, because whiskers do not grow in the presence of hydrogen (ref. section 5.2.4). Whiskers growing outwards from the grains are expected to be milled off during the reduction in the "Roundabout". However, the mechanism of iron nucleation may be identical, although the mechanism of further growth differs.

Foreign ions may have migrated to subgrain interfaces and grain surfaces during preoxidation at low and elevated temperatures, respectively. The level of trace elements is of course independent of preoxidation temperature. The beneficial effect of low preoxidation temperatures during metallization can have

been caused by extensive iron nucleation throughout the grains due to a more uniform distribution of manganese. The magnetite contains 0.11% manganese and 0.11% silicon (referring to section 3.4.2). Manganese is most probably distributed in the lattice, while silicon more likely is contained in quartz inclusions. This is supported by SIMS analyses by Storemyr (1989). The detected amount of manganese, silicon and aluminium in a few grains of Sydvaranger magnetite was 1600, 385, and 300 mole ppm, respectively. The detected amount of other elements was ≤ 35 mole ppm. Referring to section 5.2.5, manganese is an actual rate promoting trace element while silicon (and aluminium) have a retarding effect. Silicon contained in separate quartz grains or inclusions is not considered to be rate retarding.

5.8.5 Concluding remarks

Prereduction of Sydvaranger magnetite proceeds at a higher rate after preoxidation at low temperatures than after preoxidation at elevated temperatures. This is attributed to the subgrain structure. Grains preoxidized at low temperature contain lots of subgrains, while grains preoxidized at elevated temperatures contain few if any subgrains. Prereduction rate is markedly retarded during metallization when the preoxidation temperature is raised from about 1050°C to 1150°C. The subgrain structure is markedly changed in the same temperature range. Preoxidation temperature should not exceed 1050°C to obtain the highest reduction rates.

Both the initial reduction rate and the SBA values (length of subgrain boundaries/area) decrease gradually with increasing preoxidation temperature. In accordance with observations in optical microscope, subgrain boundaries serve as preferential reduction paths. Hematite is mainly topochemically reduced to magnetite, but on some occasions the conversion also proceeds ahead of the topochemical front along subgrain boundaries. This

may be attributed to vacancies, defects, foreign ions or a tearing tendency along the interfaces. However, the rate retarding effect of elevated preoxidation temperatures is not very pronounced during initial reduction. The difference in degree of oxidation after 20 seconds reduction at 760°C and 50%RO is only $2.1 \pm 0.4\%$ for the samples preoxidized at 799°C and 1244°C.

The beneficial effect of low preoxidation temperatures on the reduction rate is maintained during the magnetite to wüstite reduction step. This can be attributed to a higher porosity in the magnetite, caused by a more rapid initial reduction, or to opening of tiny cracks along the initial subgrain boundaries. The reduction of magnetite to wüstite begins before the complete conversion of hematite. Magnetite is quasi topochemically reduced at 20%RO, but uniformly reduced throughout the volume if reduction is slow (at 50%RO).

The pronounced rate promoting effect of low preoxidation temperatures during metallization can be ascribed to easy iron nucleation. Nucleation may have been enhanced by numerous active sites where subgrain planes initially intercepted or by defects, vacancies, tiny cracks or foreign ions along the subgrain boundaries. Manganese is an actual rate promoting element in the lattice of Sydvaranger magnetite, which may have migrated to subgrain boundaries and grain surfaces during preoxidation. Metallization proceeds uniformly in grains preoxidized at low temperature, but more topochemically in samples preoxidized at elevated temperatures. The metal content after 60 seconds at 760°C and 20%RO, is well above 20% in samples preoxidized at 800-1050°C, and below 10% in samples preoxidized at 1150-1250°C. The difference in degree of oxidation is highly significant, $(13.4 \pm 1.7)\%$.

5.9 Discussion of prereduction results: natural hematites

5.9.1 Introduction

Prereduction of the 6 natural hematite concentrates is described in the following based on observations in optical microscope. The significance of the differing reduction rates is further treated with a stress on the role of magnetite grains and inclusions in the hematite concentrates. Reduction rates are finally discussed with reference to the other properties characteristic of the concentrates in chapter 4.

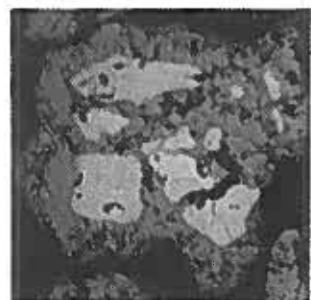
5.9.2 The progress of reduction by optical microscope

50%RO

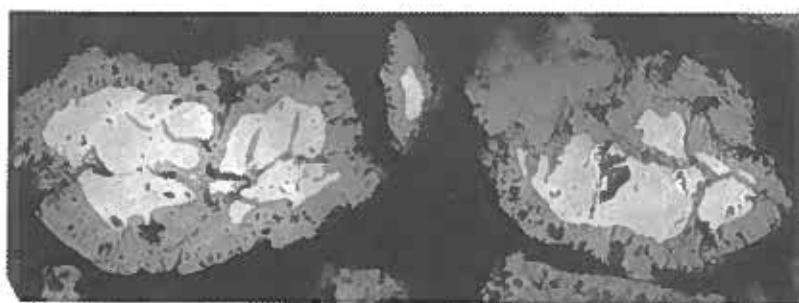
Wüstite is the equilibrium product at 760°C and 50%RO. The reduction of the natural hematite concentrates proceeds mainly in the same manner as in the reduction of oxidized magnetite.

Initially, hematite is topochemically reduced to magnetite. Branches of magnetite-wüstite ahead of the topochemical front are seen along subgrain boundaries, referring to grains reduced for 12 seconds in the photos in figure 5.56, which were taken in optical microscope in plain reflected light (r) and in polarized light (pol). In this way the subgrain planes of MBL, MBA, GUL and LIL (ref. section 4.9) also serve as preferential reduction paths. The branches are porous with tiny cracks, especially in MBL. Twin planes of RHP occasionally serve as preferential reduction paths. Branches of magnetite/wüstite ahead of the topochemical front are frequently found in the reduced grains of LIL, MBA, MBL and GUL (in about 90% of the grains with hematite cores), but only in about 10% of the RHP grains. CCL grains do not have subgrains or twin planes, and branches ahead of the topochemical front are rarely seen.

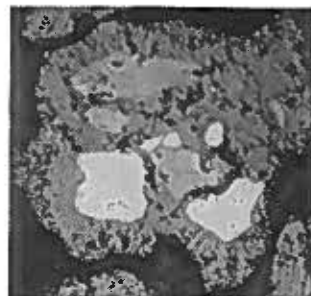
After 12 seconds reduction, hematite cores are found in most of the grains (85-90%) of CCL, RHP, MBA and MBL, and in 50-65% of the grains of LIL and GUL. The degree of oxidation in LIL, GUL and MBL is 89.0, 89.3 and 89.6%, respectively, while it is a



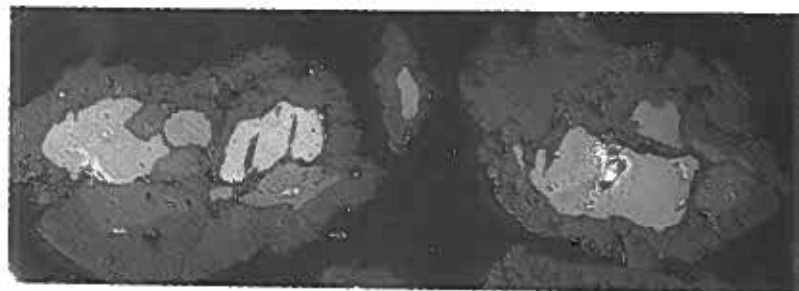
MBL (r) OX=89.6



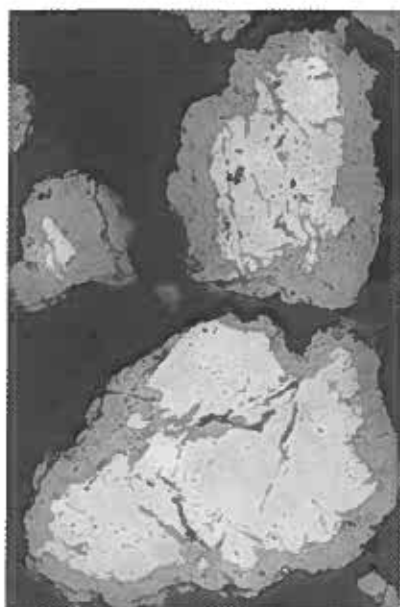
MBA (r) OX=90.5



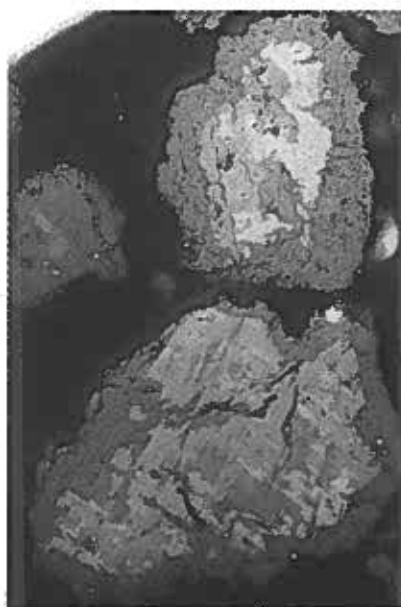
MBL (pol)



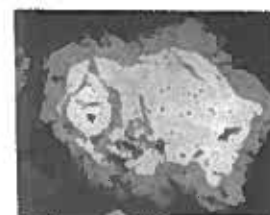
MBA (pol)



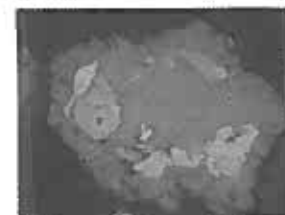
GUL (r) OX=89.3



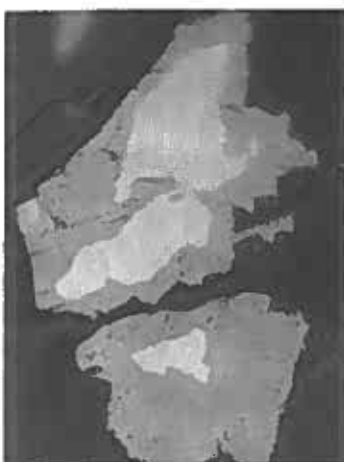
GUL (pol)



LIL (r) OX=89.0



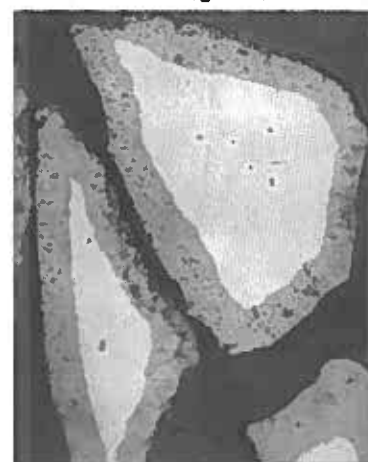
LIL (pol)



RHP (r) OX=93.1



RHP (pol)



CCL (r) OX=91.8

10 μ m

Fig. 5.56 Grain sections reduced for 12s at 50%RO (760°C, 35%H₂).
 (pol) polarized light in optical microscope
 (r) reflected light, white: hematite, grey: magnetite/wüstite

little higher in MBA, CCL and RHP (90.5, 91.8 and 93.1%). The conversion of hematite to magnetite is not complete, but the degree of oxidation is close to that of magnetite (88.9%). Some magnetite has probably converted to wüstite, especially in MBL.

Etching in 5% aqueous hydrofluoric acid enabled to differentiate between magnetite and wüstite, while etching in 1% HCl had no effect on grains reduced at 50 and 35%RO. Wüstite has formed on the pore walls of magnetite while hematite is converted to magnetite in the core. The conversion of magnetite to wüstite proceeds quasi topochemically (relics of magnetite remains behind the topochemical front) in the grains of MBL and CCL and in some grains of MBA, but the front is more diffuse in RHP. The quasi topochemical front can also be seen after the complete conversion of hematite, in MBL, CCL, and MBA, but not in RHP. A few of the grains in these four concentrates consist mainly of wüstite in which magnetite relics are uniformly distributed, but with a magnetite ring inside. The distribution of wüstite in the magnetite is far more uniform in the grains of LIL and GUL than in the other concentrates, both in grains with and without hematite cores. A few grains consist of wüstite with droplets of magnetite concentrated towards the core, or at the surface.

The conversion of hematite is nearly complete after 60 seconds reduction. Remnants of hematite are found in 1 of 10 grain sections in RHP, but rarely in the other concentrates. Hematite remnants are shown as white cores in one grain of RHP and MBL in figure 5.57 and in one grain of GUL and RHP in figure 5.58. The conversion of hematite to magnetite seems to be the slowest in RHP and the fastest in LIL and GUL.

An impression of the porosity of the reduced grains can be obtained by looking at figure 5.57, although the grain porosity varies from grain to grain. The pores in the magnetite/wüstite of RHP, LIL and GUL seem to be rather circular and small. The pores of MBL are far larger and elongated, in some grains radial and in other parallel, the latter having the appearance of tiny cracks. The pores of CCL and MBA seem to be radial elongated and rather large, especially towards the grain surface.

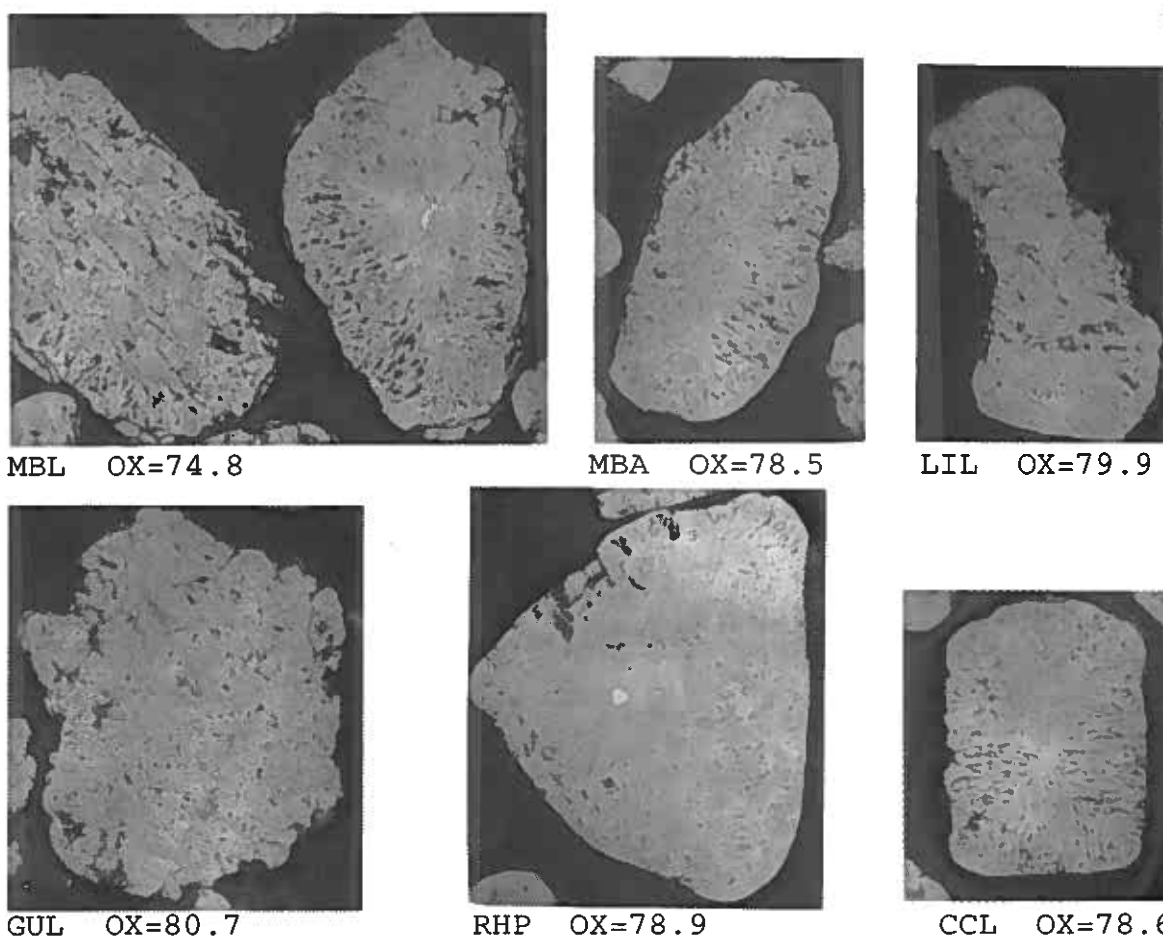


Fig. 5.57 Grain sections reduced for 60s at 50%RO (760°C, 35%H₂).
Reflected light in optical microscope.
Grey: wüstite/magnetite, white: hematite.

10µm

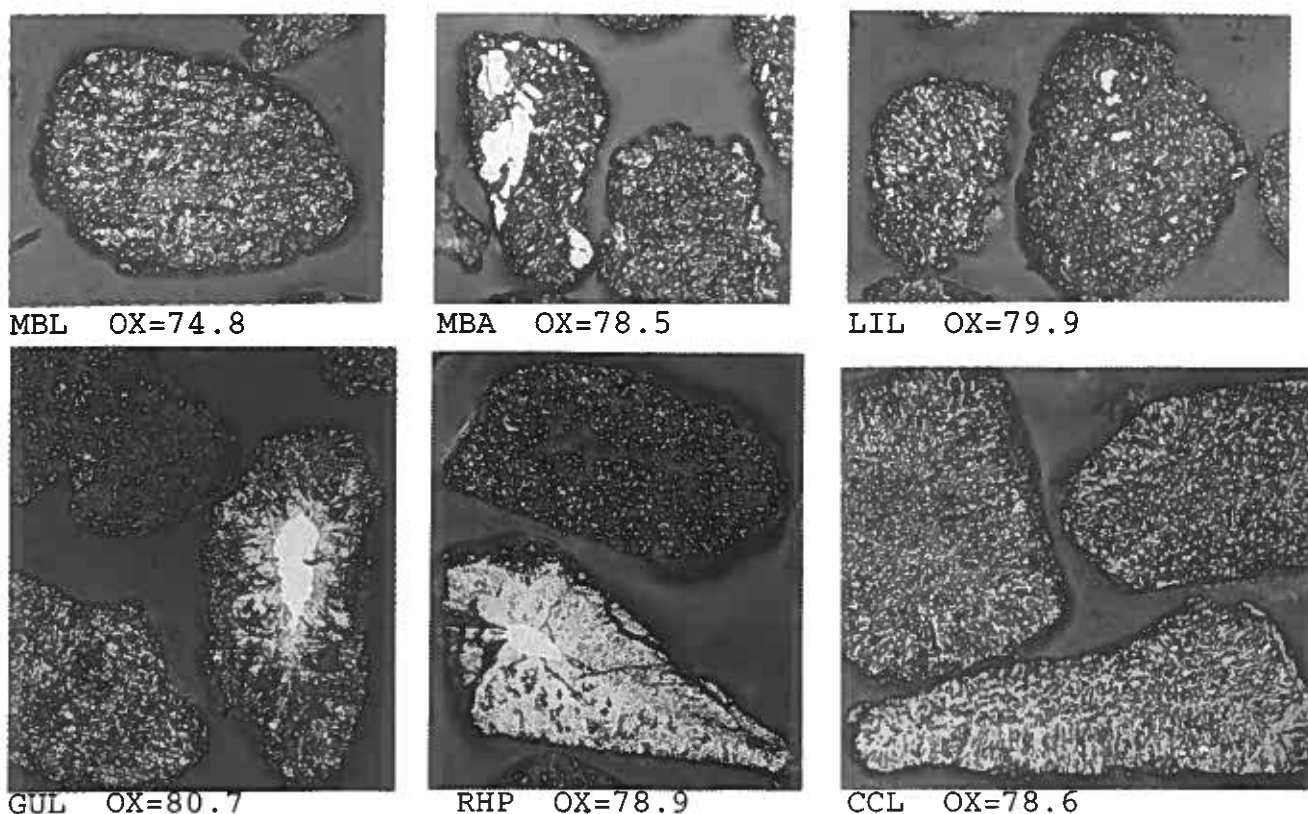


Fig. 5.58 Grain sections etched for 30s in 5%HF.
Same reducing conditions as above (Fig. 5.57).
Dark: wüstite, grey: magnetite, white: hematite.

10µm

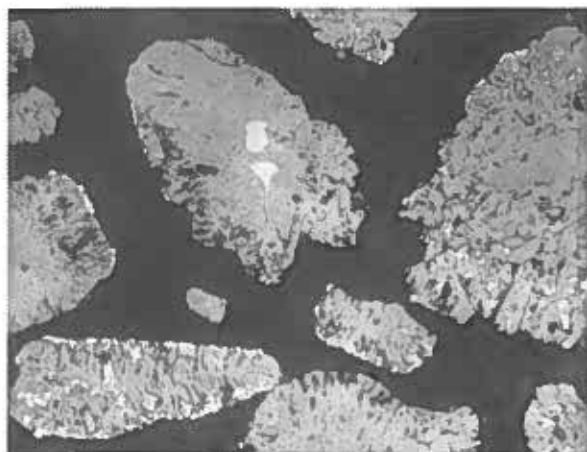
The etched grains in figure 5.58 differentiate between magnetite and wüstite. In the grains of MBA large "islands" (grey) of dense magnetite is seen, and smaller ones in LIL. These spots of dense magnetite are original magnetite, and such magnetite relics are not visibly affected by the reduction. Such magnetite inclusions are also found in the grains of GUL (not shown in the figure), while the grains of RHP and CCL have no magnetite inclusions, but magnetite grains. These magnetite grains are not affected by etching, being dense magnetite also after 60s reduction. Otherwise, magnetite and wüstite are uniformly distributed in all the grains.

20%RO

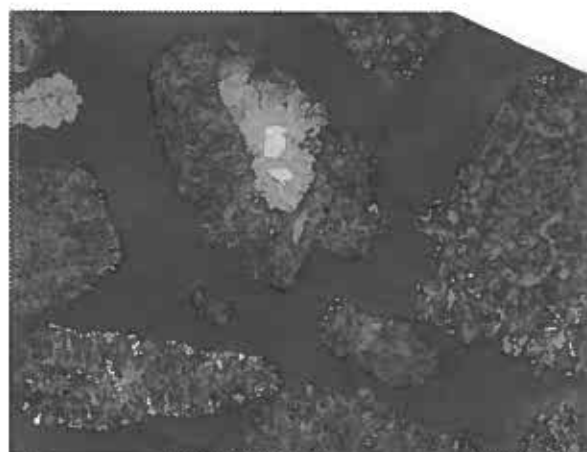
Initially the progress of reduction at 20%RO and 50%RO are analog, but the rate of reduction is the higher at 20%RO. Hematite is topochemically reduced, while magnetite is both quasi topochemically and more uniformly reduced. After 30 seconds reduction there are several hematite cores in RHP while the other concentrates have only a few. Hematite cores are shown in figure 5.59 in MBL and GUL. Magnetite and wüstite are differentiated in the same etched grains in the figure. The quasi topochemical front is far more distinct after the rapid reduction of MBL than after the slow reduction of GUL, and not much magnetite is left behind this front in MBL. The front is also more distinct after rapid reduction at 20%RO than after slow reduction at 50%RO.

Figure 5.59 does also show a part of one of the many magnetite grains in CCL (to the right), which seems unattached by etching after 30 seconds reduction at 20%RO. The same picture shows that the amount of wüstite formed varies from grain to grain. The largest grain in the same picture is finely porous in the centre while the outer pores are coarse and radially elongated towards the surface. This results in an unusual effect, a black core of wüstite with only small relics of magnetite uniformly distributed, while the outer rim still has much magnetite.

Metallization starts after 20 seconds at 20%RO in MBL, and several spots of iron both at the grain surface and in the



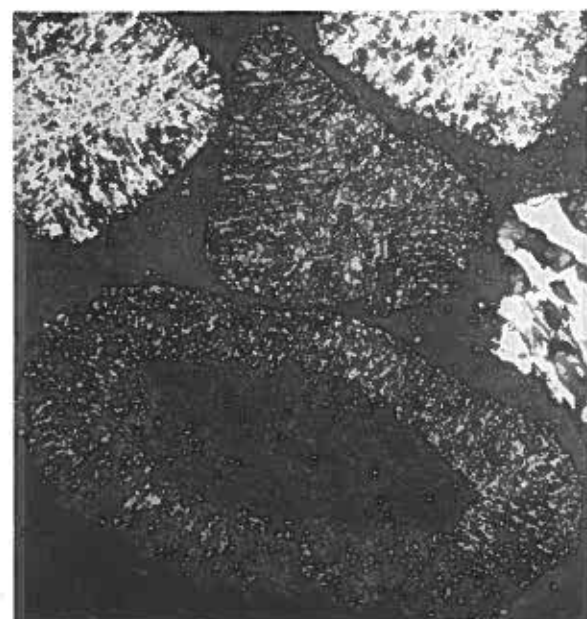
MBL OX=63.0



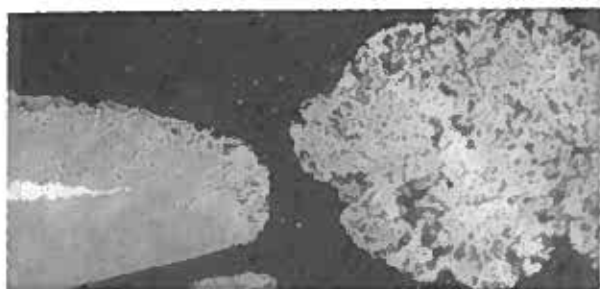
MBL, etched for 20s



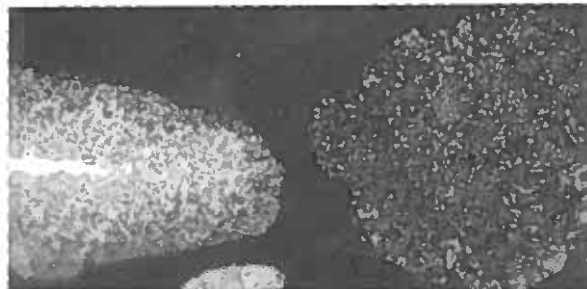
CCL OX=72.4



CCL, etched for 20s



GUL OX=72.7



GUL, etched for 60s

10 μ m

Fig. 5.59 Grain sections reduced for 30s at 20%RO (760°C, 35%H₂).
 Left: not etched, wü/mt: grey, hm/iron: white
 Right: etched in 1%HCl, wü: dark, mt: grey, "

interior are observed after 30 seconds reduction in figure 5.59.

The MBL grain with the hematite core does also have a few iron nuclei at the surface. The metallization in MBL has reached a level of 7.6% at this stage, while it is about 1-2% in the other

concentrates. A few iron nuclei are also observed in CCL, uniformly distributed in the large grain in figure 5.59, while iron nuclei seldom are observed in LIL and GUL.

After 50 seconds, the metallization has reached a level of 23.4% in MBL, 7-9% in RHP, MBA and CCL, but only 4% in LIL and GUL. The situation is illustrated by figure 5.60. The grains

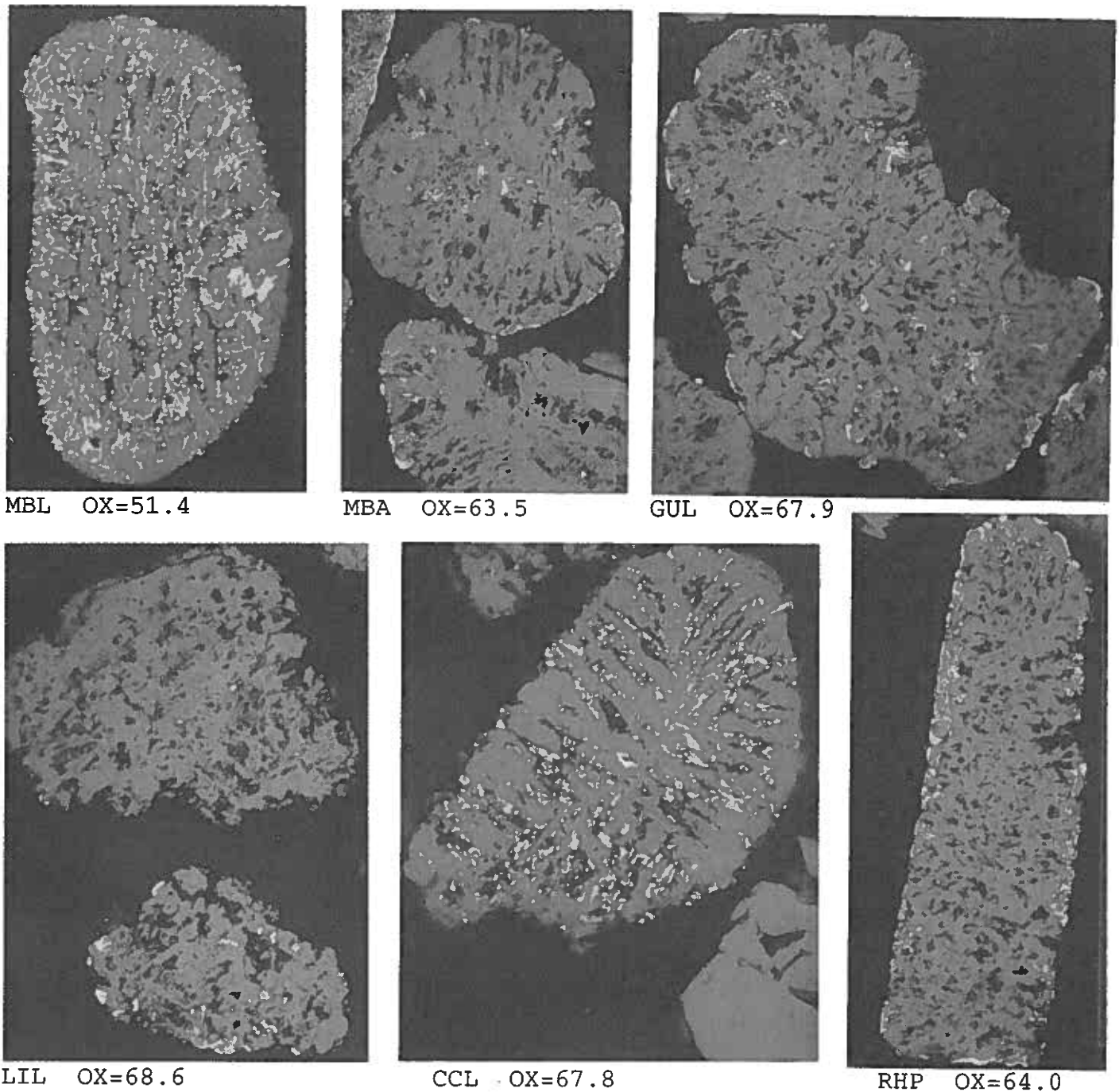


Fig. 5.60 Grain sections reduced for 50s at 20%RO (760°C, 35%H₂).

10µm

Reflected light in optical microscope.

White: iron, grey: wüstite/magnetite, black:pores/matrix.

are highly porous at this stage. However, the parallel and radially elongated pores and cracks in MBL are filled with iron. The iron constitutes a network in the grain shown in figure 5.60. Radially elongated pores in CCL are also filled with iron. Such grains may also be observed in the MBA concentrate in which the extent of metallization varies from grain to grain. The grains of MBA shown in figure 5.60 have some iron nuclei rather uniformly distributed in the grains, perhaps a few more at the surface, and very similar to the iron nuclei in GUL and LIL. The iron at the surface of GUL has nucleated on noses. Iron formation in RHP has a more topochemical nature. The iron is mainly located in an outer rim and only a few iron nuclei are found in the interior of the RHP grains.

Magnetite grains appear to be unaffected after 50 seconds reduction at 20%RO, referring to the lower CCL grain in figure 5.60.

5.9.3 Reduction rates - significance and magnetite corrections

The degree of oxidation after reduction is an important measure characteristic of each concentrate, but it is a combined measure for the reduction of both the hematite and the magnetite in the concentrates. As already emphasized, reduction of magnetite is very slow compared to reduction of hematite. It has just been verified by optical microscopy that magnetite grains and magnetite inclusions are not affected by the mild reducing conditions in the present investigation. Slow reduction is to be expected for concentrates with a high content of magnetite. In other words, a high magnetite content masks the influence of other properties characteristic of the concentrates.

The different concentrates contain various amounts of magnetite, as shown in figure 5.61. The content of magnetite is the highest in CCL (19.1%) and RHP (7.1%) and the lowest in MBL (0.4%). Magnetite is present as separate grains in CCL and RHP, and as inclusions in the hematite grains of MBA, LIL, GUL, and MBL. The calculated amount of magnetite is based on the assumption that

the Fe^{2+} content in the concentrates is contained in magnetite, but minor amounts of Fe^{2+} may be present as iron silicates, ferrodolomite-ankerite-siderite, pyrite, ilmenite, etc.

Corrections for magnetite contents have been done according to the formulas

5.65-5.67. The degree of oxidation after reduction for the hematite in each concentrate (OX_i) has been calculated for each sample i according to formula 5.65 by considering magnetite as inert. The percentage Fe^{2+} (or Fe^{3+}) in each reduced sample which initially was contained in magnetite, is expressed by X_i (or $2X_i$) in formula 5.66. The index o in formula 5.66 indicates analyses before reduction. Corrections for magnetite contents have been done by subtracting X_i from the measured Fe^{2+} content, $2X_i$ from the calculated Fe^{3+} content and $3X_i$ from the total iron content. Metallization in each reduced sample may be corrected accordingly as shown in formula 5.67.

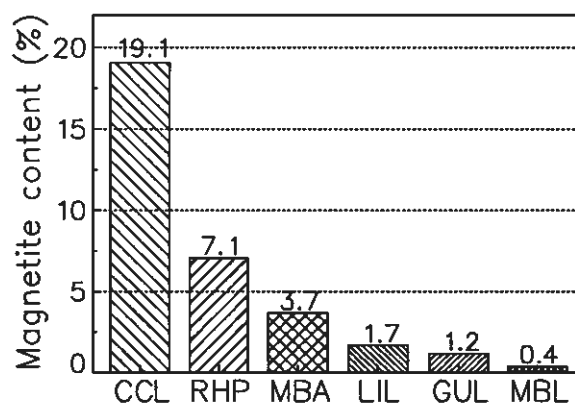


FIG. 5.61 Magnetite contents in natural hematite concentrates.

$$OX_i (\%) = \frac{1.5 \cdot (Fe_i^{3+} - 2X_i) (\%) + (Fe_i^{2+} - X_i) (\%)}{1.5 \cdot (Fe_i^{tot} - 3X_i) (\%)} \cdot 100\% \quad (5.65)$$

$$X_i = \frac{Fe_o^{2+} (\%)}{Fe_o^{tot} (\%)} \cdot Fe_i^{tot} (\%) \quad (5.66)$$

$$Metallization_{mt-inert} (\%) = \frac{Fe_i^{met} (\%)}{(Fe_i^{tot} - 3X_i) (\%)} \cdot 100\% \quad (5.67)$$

The reduction results are in the following presented in figures 5.62-5.69, without corrections to the left (a) and corrected for magnetite contents to the right (b). The mean degree of oxidation is also found in table 5.3 (section 5.6) without corrections, and in appendix A.4 with magnetite corrections.

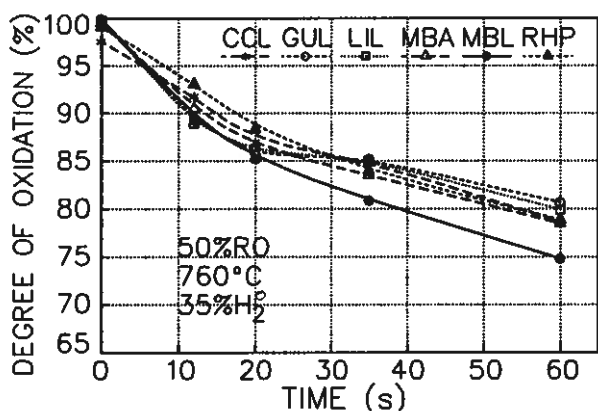


Fig. 5.62a Progress of reduction of the hematite concentrates at 50%RO. (No corrections)

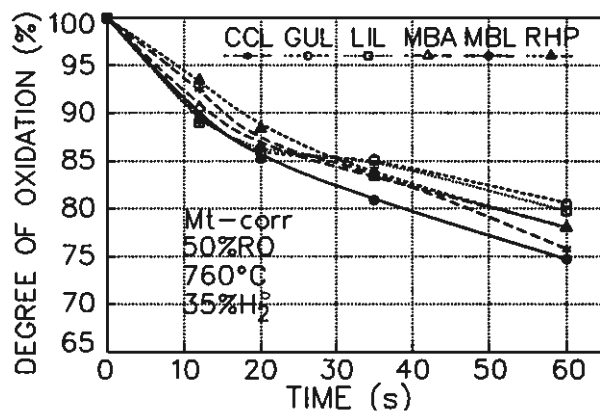


Fig. 5.62b Progress of hematite reduction at 50%RO. Magnetite contents are considered as inert.

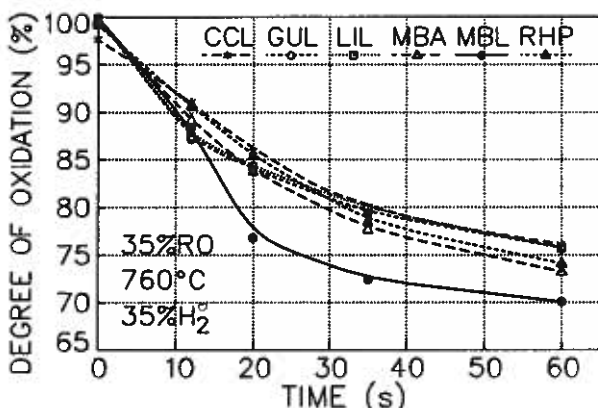


Fig. 5.63a Progress of reduction of the hematite concentrates at 35%RO. (No corrections)

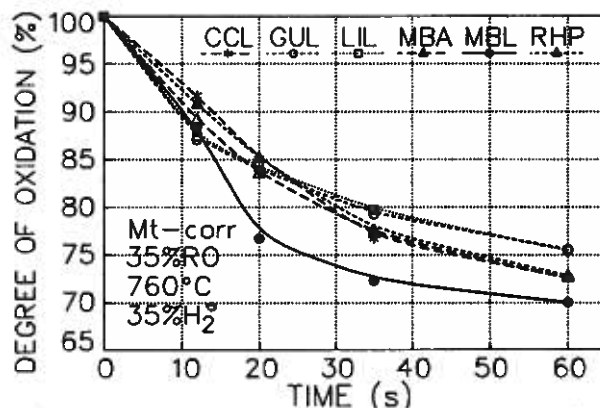


Fig. 5.63b Progress of hematite reduction at 35%RO. Magnetite contents are considered as inert.

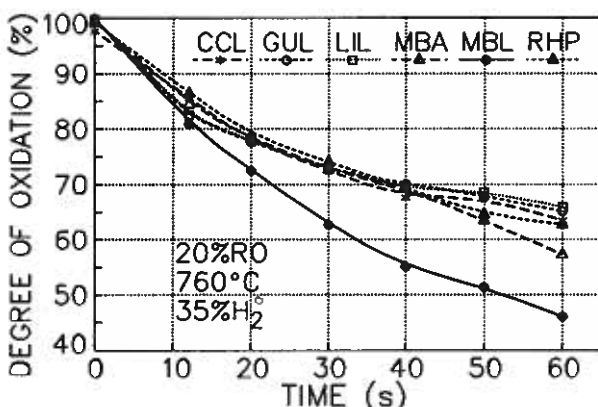


Fig. 5.64a Progress of reduction of the hematite concentrates at 20%RO. (No corrections)

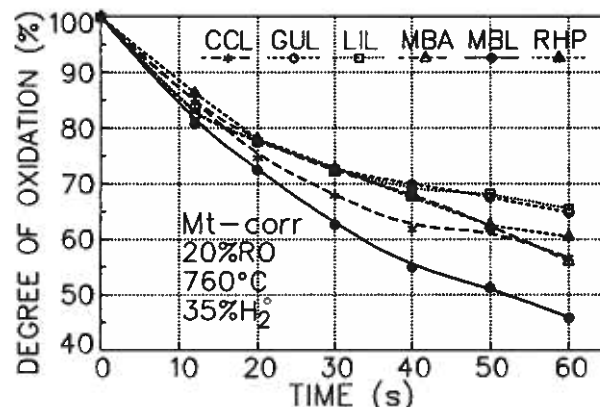


Fig. 5.64b Progress of hematite reduction at 20%RO. Magnetite contents are considered as inert.

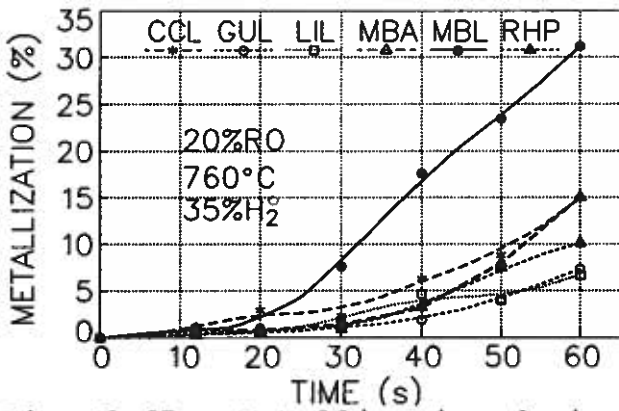


Fig. 5.65a Metallization during reduction of hematite ores at 20%RO. (No corrections)

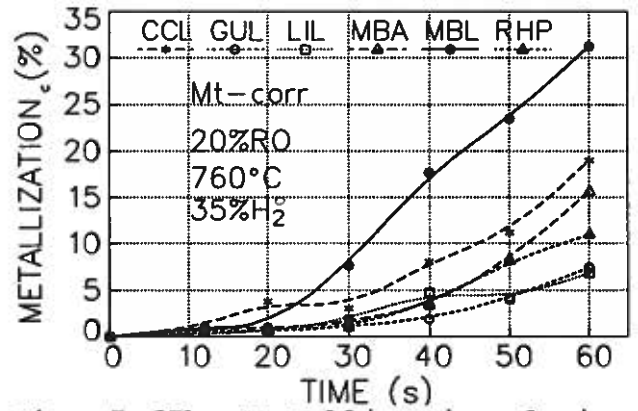


Fig. 5.65b Metallization during the reduction at 20%RO. Magnetite contents are considered as inert.

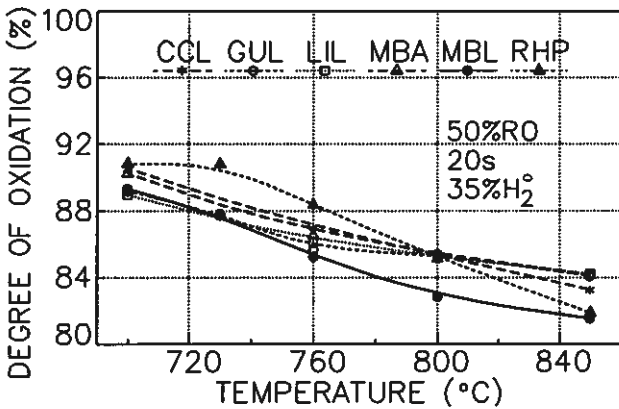


Fig. 5.66a Effect of temperature on the reduction at 50%RO. (No corrections for magnetite)

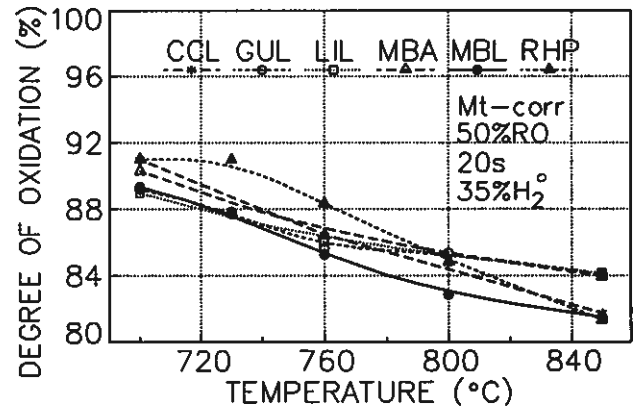


Fig. 5.66b Effect of temperature on reduction at 50%RO. Magnetite contents are considered as inert.

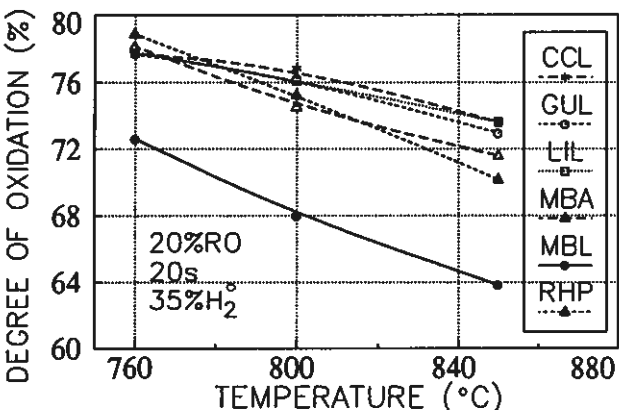


Fig. 5.67a Effect of temperature on the reduction at 20%RO. (No corrections for magnetite)

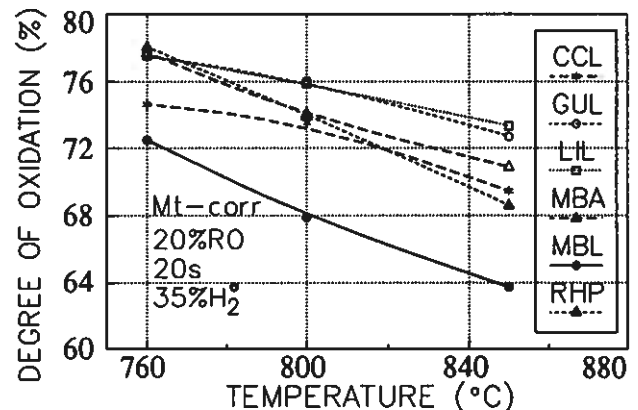


Fig. 5.67b Effect of temperature on reduction at 20%RO. Magnetite contents are considered as inert.

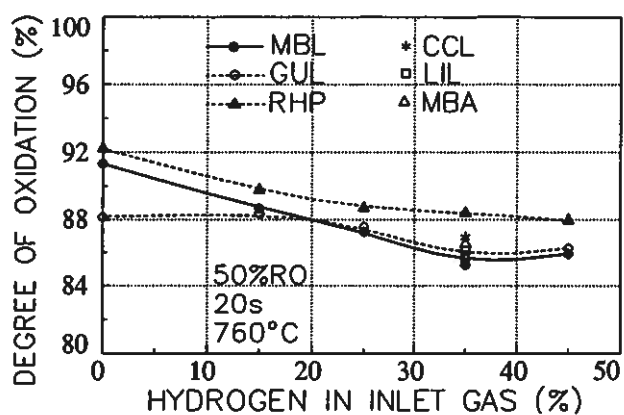


Fig. 5.68a Effect of hydrogen at 50%RO on the reduction rate. (No corrections for magnetite)

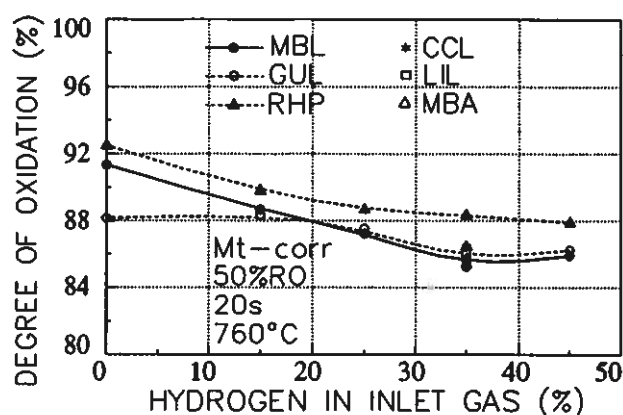


Fig. 5.68b Effect of hydrogen at 50%RO on reduction rate. Magnetite contents are considered as inert

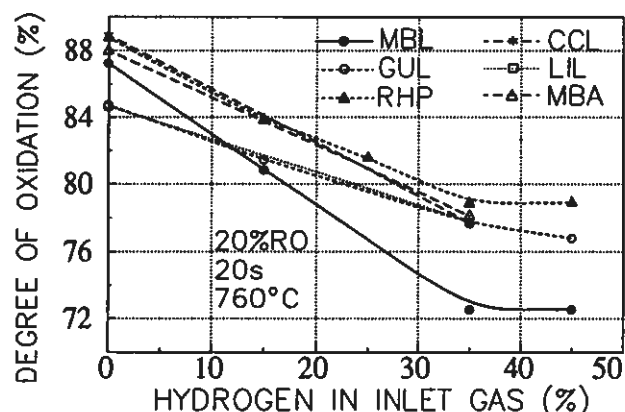


Fig. 5.69a Effect of hydrogen at 20%RO on the reduction rate. (No corrections for magnetite)

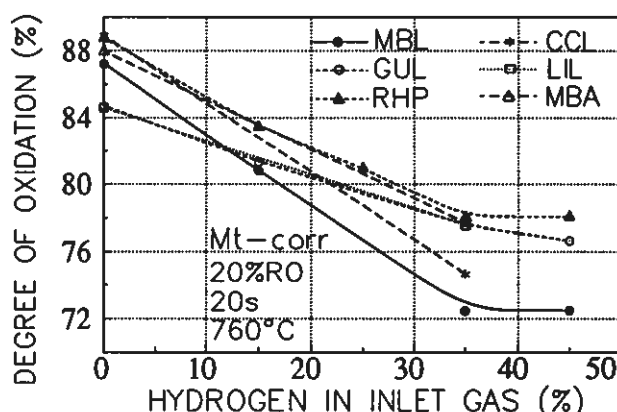


Fig. 5.69b Effect of hydrogen at 20%RO on reduction rate. Magnetite contents are considered as inert

The correction lead to a higher degree of oxidation (OX) in the interval 88.9-100%, but a lower degree of oxidation for $OX < 88.9\%$. Referring to the results after 20 seconds reduction at 50%RO in figures 5.66 and 5.68, there is no significant effect of magnetite corrections in the vicinity of $OX = 89\%$. The influence of the magnetite correction increases as the reduction proceeds. Maximum correction in the present investigation is reached at 20%RO after 60 seconds reduction. Referring to figure 5.64 a and b, the maximum magnetite correction is small for MBL, GUL and LIL, contributing to a decrease of 0.2-0.4% in the degree of oxidation (without correction: $OX = 46.1, 65.1$ and 65.9% , respectively, and with correction: $OX = 45.9, 64.8$ and 65.5%). Maximum correction is greatest for CCL, for which the degree of

oxidation decreases from 63.5% to 56.6%, a difference of 6.9%. Accordingly, $OX=62.7 \rightarrow 60.4\%$ (-2.3%) for RHP and $OX=57.3 \rightarrow 56.0\%$ (-1.3%) for MBA.

The correction is probably too high for CCL and RHP since about 0.6% Fe^{2+} may be present in ferrodolomite-siderite, pyrite, ilmenite, or iron silicates, and not in the magnetite, as referred to in section 4.6. If so, the maximum decrease in the degree of oxidation is -5.7% instead of -6.9% for CCL and -1.4% instead of -2.3% for RHP.

By comparing a and b in the figures 5.62-5.64, it is seen that MBL is reduced at the highest overall rate, both with and without magnetite corrections. LIL and GUL have the highest initial rate during hematite reduction, but the slowest rate during the conversion of magnetite and wüstite. RHP has the slowest initial reduction rate, closely followed by CCL. The concentrate CCL (a) is reduced at a slow further rate, while the hematite in the concentrate (b) is reduced at a moderate rate.

Referring to figures 5.66 and 5.67, after 20 seconds reduction, MBL is markedly more reduced than the others in the entire temperature range (760-850°C) at 20%RO, but only slightly more reduced than the others at 50%RO in the temperature range 700-850°C. The reason is the moderate high reduction rate of MBL hematite to magnetite, which dominates at 50%RO, and a particularly high rate during the next reduction step to wüstite, which contributes significantly at 20%RO.

GUL and LIL are the most reduced samples after 20 seconds reduction when the reduction gas does not contain hydrogen, while MBL reduces at the highest rate at higher hydrogen contents, referring to the figures 5.68 and 5.69. This change can be attributed to the high reduction rate of GUL and LIL from hematite to magnetite and the slow further reduction to wüstite, while MBL is reduced at a very high rate from magnetite to wüstite.

For simplicity, the concentrates may be grouped in 3 according to the reduction rates of the hematite in the concentrates;

<u>Group</u>		<u>initial rate</u>	<u>further rate</u>
1	GUL and LIL.	high	slow
2	MBL	moderate-high	high
3	RHP, CCL and MBA	slow-moderate	moderate

An impression of the initial rate of reduction, for the reduction of hematite to magnetite, can be obtained after 12 seconds reduction at 50 and 35%RO, see figures 5.62b and 5.63b. (The conversion of magnetite to wüstite has reached too far after 12s at 20%RO.) The corrected degree of oxidation after 12s is:

<u>Group</u>	<u>50%RO</u>	<u>35%RO</u>
1	89.2±0.2	87.3±0.2
2	89.6	88.4
3	90.6-93.5	89.2-91.7

Group 1, GUL and LIL, have been reduced at the highest initial rates both at 35 and 50%RO. The differences between group 1 and 2 are small, 0.4% at 50%RO and 1.1% at 35%RO, compared to maximum deviation based on chemical analyses, which is ±0.4% in this range, referring to section 5.7.2. The scatter within group 3 is large since the initial reduction rate of MBA is moderate while it is slow for RHP and CCL. The differences between group 1 and MBA in group 3 are significant, 1.4% at 50%RO and 1.9% at 35%RO. Appreciably larger are the differences between group 1 and RHP/CCL, nearly 4% both at 35 and 50%RO (10· max. deviation).

The extent of reduction has reached the same level (OX=85%) in CCL, RHP and MBA after 20 seconds reduction at 35%RO or after 30 seconds at 50%RO. The further rate of reduction is about the same for the hematite in these 3 concentrates (see figures 5.62b and 5.63b). The corrected degree of oxidation after 60 seconds reduction at 35%RO is in the range 72.6-72.8% for CCL, RHP and MBA, a value in the middle of that for GUL-LIL (75.5-75.7%) and that for MBL (70.0%). At this point of the reduction the differences in the degree of oxidation between the groups are highly significant. The difference between group 2 (MBL) and

1 (GUL and LIL) is about 5.6%, that is considerably more than the maximum standard deviation in this range, $\pm 0.4\%$. The differences between these two groups are approximately of the same size (5%) after 60 seconds reduction at 50%RO, both with and without magnetite corrections.

The corrected degree of oxidation for CCL after 60 seconds reduction at 50%RO is probably too low, lower than that for MBA and RHP. The CCL curve is not as smooth as the others, probably because the initial magnetite content in CCL is not evenly distributed in each sample, also contributing to wrong corrections. The correction will be too high and the degree of oxidation will be too low if one CCL sample initially contains less magnetite than other CCL samples.

Referring to the accuracy of the wet chemical analyses in section 5.7.2, maximum deviation in the degree of oxidation is $\pm 1.7\%$ when metal has formed at 20%RO. This maximum deviation is much greater than the maximum deviation between the corrected and not corrected degree of oxidation for MBL, GUL, and LIL, but they are of comparable sizes for MBA and RHP. For CCL, however, the maximum decrease in degree of oxidation when magnetite is considered inert is $-(5.7-6.9)\%$, which is considerably greater than the maximum deviation of $\pm 1.7\%$.

The corrected degree of oxidation after 60 seconds reduction at 20%RO is $65.2 \pm 0.4\%$ for group 1 (GUL, LIL), 45.9% for group 2 (MBL) and $58 \pm 2\%$ for group 3 (MBA, RHP, CCL). The difference between the groups 1 and 2 is highly significant, 19.3%, compared to the maximum deviation calculated from the STD of the individual analyses. The differences between the groups 1-3 and 2-3 are also significant, 7 and 12%, respectively. Hence, no faults are committed by stating that MBL has been reduced at a superior high rate of reduction.

Metallization in concentrates with a low content of magnetite, is only slightly affected by magnetite corrections, referring to

figure 5.65a and b. The difference between uncorrected and corrected values is only 0.1% for MBL, GUL and LIL after 60 seconds reduction at 20%RO. This is less than the standard deviation in the analysis of metallic iron which is $\pm 0.3\%$ at rather low concentrations. Without corrections, metallization is 31.2% in MBL, 7.4% in GUL and 6.7% in LIL, while the corrected values are 31.3, 7.5 and 6.8%, respectively. On the other hand, metallization in CCL is significantly affected by the magnetite corrections, increasing from 14.9% to 19.0%. The effect is moderate for RHP (10.1% \rightarrow 11.0%) and MBA (15.0% \rightarrow 15.7%). Anyhow, the extent of metallization is appreciably higher in MBL than in the other concentrates, and the lowest in LIL and GUL, both with and without magnetite corrections.

Magnetite might have been slightly reduced, although not visible in optical microscope. Compared to other sources of failure, the failure committed by considering the initial magnetite contents as inert during the reduction, is insignificant. However, magnetite inclusions may perhaps retard the reduction velocity of the nearby hematite in the same grain. Not initially, but the formation of metal may be retarded since iron and magnetite are not in chemical equilibrium at these temperatures. This may partly explain a low extent of metallization in some grains of MBA, GUL and LIL. The presence of magnetite grains are not thought to retard iron formation in nearby grains.

Referring to in section 5.7, loss of material and grain size degradation during the experiments, will also influence on the accuracy of the reduction results. Both the material loss and the changing grain sizes are dependant on material type.

A large material loss has no influence on the reduction results if the sizes of the lost grains and their degree of oxidation are representative for the samples. The most reduced particles or parts of the particles have more likely been lost due to sticking to the reactor walls or due to elutriation of "dust" in the flue gas. Sticking is a problem during metallization. The material

loss is the greatest for MBL for which the overall reduction rates are the highest (the degree of oxidation is the lowest). If the material loss is selective, the most reduced parts being lost, the calculated degree of oxidation will be too high, and not too low, referring to section 5.7.4. Consequently, the superior high overall rate of reduction of MBL can not be ascribed to the low output. The high initial rates of reduction of GUL and LIL are also accompanied by a relatively low output (75-80%). If the most reduced parts are lost, the degree of oxidation of the remaining samples is not too low. The slow initial rates of reduction (the high degree of oxidation) for RHP and CCL are also trustworthy because these reduced samples are rather representative since the output is high (90%).

Referring to section 5.7.3, the grain size of all the concentrates decreases during the reduction. Since size degradation differs for the different concentrates, the effects of characteristic properties can be masked. The decrease in grain size can partly be ascribed to the rough treatment during the experiments, especially the rapid heating and milling in the reactor. CCL and RHP are least inclined to changes in grain size while the grain sizes of the other four concentrates decrease a lot mainly due to decrepitation upon heating and degradation during rapid reduction. In a pilot plant, the heating is probably accomplished at a slower rate in a separate unit, and the milling effect is probably smaller. Although the decrease in grain size partly can be attributed to a rough treatment in the laboratory equipment, the differences in size degradation may be attributed to properties characteristic of the concentrates. Both decrepitation upon heating and degradation during the reduction are dependant on material properties.

5.9.4 Effects of characteristic hematite properties

Specific surface area

Provided chemical rate control during the topochemical reduction of hematite to magnetite, the reduction rates are initially proportional to the exterior specific surface area, and later to the interior surface area of the shrinking core (formula 5.40). Chemical control can safely be assumed until a relatively thick product layer has built up. The interior surface area of the shrinking core is assumed to depend on the exterior surface area.

The initial reduction rates, during the topochemical reduction of hematite to magnetite, are assumed to be proportional to the specific surface areas, repeatedly shown here in figure 4.5. Hence, other parameters equal, GUL should be reduced at an initial rate, twice that of LIL and 12 times that of RHP.

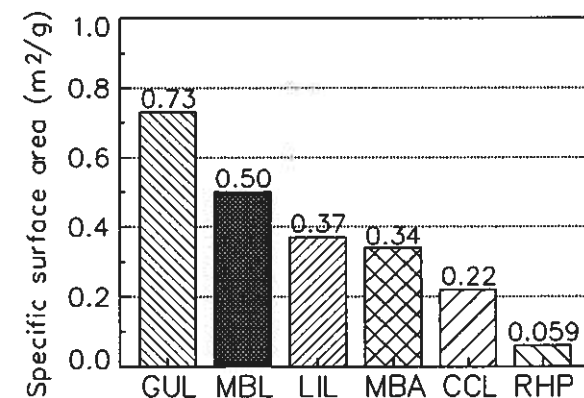


Fig. 4.5 Specific surface areas of natural hematite concentrates

This is not the case, but the specific surface area is an important parameter since its magnitude is roughly reflected in the initial reduction rates. The concentrates GUL, MBL, and LIL have the largest specific surface areas and the highest initial rates of reduction (group 1+2). CCL, and especially RHP, have the smallest specific surface areas and the slowest initial reduction rates (group 3).

The initial specific surface area is assumed to have only minor influence on the further reduction of magnetite and wüstite. The products are rather porous, implying that specific surface areas are highly enlarged. The entire specific surface areas participate during the reduction of both magnetite and wüstite, since these reactions proceed mainly uniformly throughout the volume (or quasi topochemically).

Subgrain structure

During reduction of hematite, branches of magnetite-wüstite ahead of the topochemical front have frequently been observed in MBL, MBA, GUL and LIL. Since the subgrain interfaces serve as preferential reduction paths, an enhanced rate of reduction during the conversion of hematite to magnetite can be

explained. As shown in figure 5.70, GUL has the highest SBA value (subgrain boundaries/area) while MBL and LIL have the next highest scores. Since these 3 concentrates also have the largest specific surface areas, the observed high initial reduction rates (group 1+2) might have been predicted.

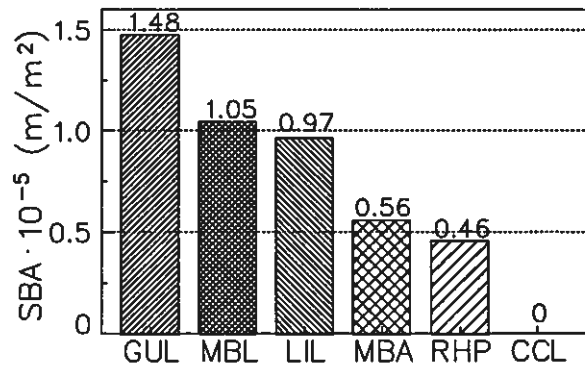


Fig. 5.70 Subgrain structure of natural hematite concentrates

The SBA measure for RHP in figure 5.70 is a measure of boundaries between twin planes, but the twin planes have only rarely served as preferential reduction paths during hematite reduction. Consequently, the observed slow initial rate of reduction for RHP and CCL (group 3) can be explained both from their lack of subgrains and their small specific surface areas.

The rates of further reduction from magnetite to wüstite and from wüstite to iron are slow for GUL and LIL (group 1), moderate for CCL, RHP and MBA (group 3), but high for MBL (group 2). The high rates of reduction for MBL, and the slow rates for GUL and LIL, are believed to originate from their subgrain structures, although this is not reflected by SBA values, decreasing from GUL to MBL to LIL. The subgrain shapes and the subgrain orientation within each grain are instead believed to be two important parameters. There seem to be a tendency of tearing along subgrain boundaries, which this author believe depends on subgrain shape and subgrain orientation.

MBL, CCL, and RHP have been classified in section 4.2 as specular hematites, having smooth reflecting surfaces. While the grains of CCL and RHP contain no subgrains, each grain of MBL is laminated (foliated), containing several subgrains. Exfoliation along the lineations in MBL grains, upon heating and rapid initial reduction, is thought to create tiny cracks along the subgrain boundaries. The specific surface area of MBL is highly enlarged, and as a consequence the rate of reduction to wüstite is high. Tiny parallel cracks and elongated pores constitute a network in many reduced MBL grains (Fig. 5.57) where metal seems to nucleate easily (Fig. 5.60). These cracks are thought to be the cause of the superior reduction rate of MBL during metallization. This is in accordance with the view of Watanabe and Yoshinaga (1968) who regarded defects along weak lines or cracks as nuclei for rapid whisker growth. In addition to cracks, defects and foreign ions on subgrain interfaces, may also serve as iron nuclei.

Most of the grains of GUL and LIL, on the other hand, consist of subgrains with an anhedral structure, having a lack of crystal shape, as described in sections 4.2 and 4.9. A typical anhedral grain is shown in the upper half of figure 4.7d. The irregularity of subgrain boundaries between anhedral subgrains is thought to link the subgrains together like two cog-wheels. Anhedral subgrains can for this reason be less inclined to tear during rapid heating and initial reduction. The anhedral substructure is believed to be the main reason for the slow further reduction rate for GUL and LIL. Some grains of GUL and LIL have a martitic structure, illustrated by the grain to the right in the same figure (4.7d), showing the typical extinction pattern of crosshatched dark and light stripes. This structure is more similar to Sydvaranger magnetite preoxidized at low temperature. Hence, a high reduction rate should be expected for these grains.

Referring to section 5.2.4, tearing upon initial reduction can occur due to expansion, an anisotropic volume change and/or an anisotropic reduction rate in adjacent subgrains. According to

Ball et al. (1973), the tendency for tearing to occur is dependant on the disparity of the c-axis in adjacent hematite subgrains. The present investigation indicates that there is an increased tendency for tearing to occur along the subgrain boundaries in specular laminated structures (along the lineation). The tearing is believed to occur mainly during the initial reduction and to a lower extent during the heating. If the tiny cracks had opened the structure during heating, MBL should be reduced at a higher initial rate than GUL and LIL, but this is not so. Watanabe and Yoshinaga (1968), on the other hand, believe that parallel arrangement in schistose specular hematite, which is elongated parallel to the basal plane (0001), may be exfoliated along the lineation due to thermal expansion during heating.

Grain size

The main differences in reduction rates can neither be attributed to the small variations in initial grain size nor the larger variations in final grain size.

The grain size was expected to be an important parameter for the reduction rate towards the end of the topochemical reaction from hematite to magnetite, whereas the specific surface area should be important initially. The time to reach a certain stage of reduction is proportional to grain diameter, provided chemical rate control. If diffusion through the growing magnetite layer is rate controlling, the time to reach a certain degree of reduction is proportional to the squared diameter. A high dependence on grain size have not been observed, suggesting chemical rate control throughout the reaction, and/or a predominant importance of other properties characteristic of the concentrates. The grain size is expected to be less important during uniform and quasi topochemical reduction because the entire grain volume participates.

The lack of importance of small variations in initial grain size

is easily seen since the coarsest concentrate, GUL, is reduced at a high rate to magnetite (group 1) while RHP, being the finer, is reduced at a slow rate (group 3).

Referring to figure 5.71, the mean grain size (d_{50}) of the concentrates decreases from $82\mu\text{m}$ for GUL to $61\mu\text{m}$ for RHP. The mean grain size is the grain size for which 50 weight% of the material is coarser. The grain size distributions, within the fraction used, are shown in chapter 4, in figure 4.1.

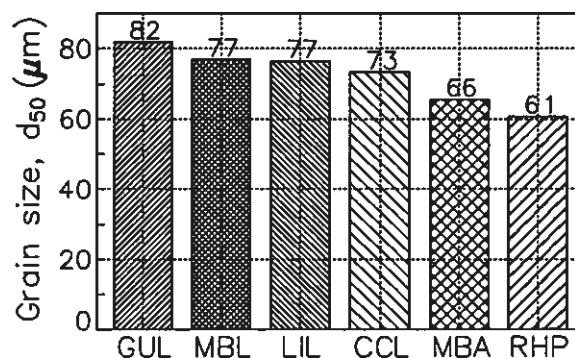


Fig. 5.71 Mean grain size (d_{50}) of natural hematite concentrates

Provided that the initial mean grain size is the only important parameter, the time for the finest, RHP, to reach the same degree of reduction as the coarsest, GUL, can be calculated. Since GUL needs approximately 12s at 50%RO to reach OX=89.3%, RHP should use 7 or 9s, depending on whether diffusion or the chemical reaction is rate controlling. However, RHP needs 18s.

Different grain size degradation has to be taken into account when the reduction rates are compared. As previously pointed out in section 5.7.3, the grain size of all the samples has decreased during the reduction experiments. The decrease in grain size is small for CCL and RHP and large for MBL, MBA, GUL, and LIL. The grain size of MBA is the smallest after reduction. The grain size distributions after reduction for 35s at 50%RO and 20s at 20%RO are compared in the figures 5.72 and 5.73, respectively. The degree of oxidation (OX), without magnetite corrections, is incorporated in the figures.

Differences in the rates of further reduction from magnetite to wüstite and iron can neither be attributed to initial grain size nor to the changes in grain size. MBL is reduced at the highest rate, even though the grains of MBA are finer, both before and after reduction. Hence, the tendency for tearing along the lination is more important for the reduction rates than differences in grain size.

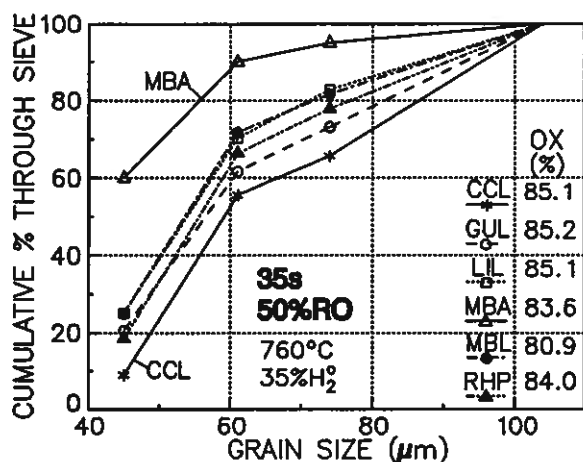


Fig. 5.72 Size distribution after 35s reduction at 50%RO.

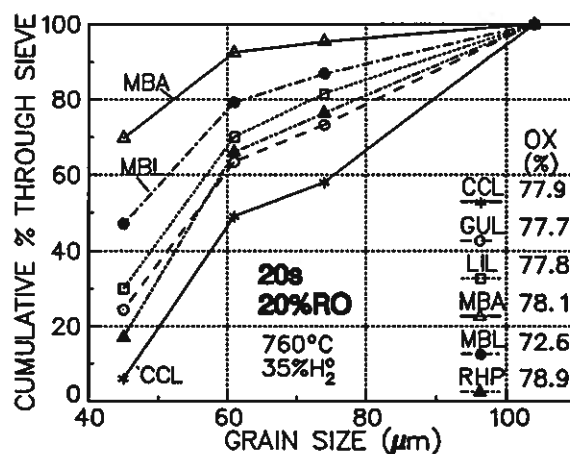


Fig. 5.73 Size distribution after 20s reduction at 20%RO.

Referring to the figures 5.71 and 5.72, MBL and LIL have equal initial mean grain size and identical grain size distribution after 35s reduction at 50%RO, but MBL is much more reduced than LIL (MBL:OX=80.9%, LIL:OX=85.1%). Their initial reduction rates are close, having approximately equal specific surface areas. Referring to figure 5.70, their SBA values are also very close. The superior rate of reduction for MBL can not be attributed to grain size, but to the shape and orientation of subgrains.

Differences in grain size degradation are probably linked to the subgrain structures. CCL and RHP have no subgrains, so the small decrease in their grain size is largely attributed to milling in the reactor. The large decrease in grain size for MBA, MBL, GUL and LIL, is apart from milling, attributed to decrepitation upon heating and degradation during initial reduction. Grains do mainly crack along the subgrain boundaries. Size degradation is most pronounced for MBA, probably because of small goethite inclusions, causing decrepitation along subgrain interfaces upon rapid heating. The second largest grain diminishing effect is observed for MBL during rapid initial reduction at 20%RO, probably because of its tendency of tearing along the lineation between parallel orientated subgrains.

Grain shape

The influence of grain shape on the reduction rate is masked by other more important properties characteristic of the natural hematite concentrates. The grain shapes were characterized by a planar shape factor and an elongation factor in section 4.10, repeatedly presented here in figures 4.9 and 4.10. These two factors are not independent variables. A schematic relation between grain shapes, mean elongation and shape factors is shown in figure 4.11. The concentrates have lower shape factors than what is expected from their elongation factor, because their rugged grain surfaces also results in low shape factors.

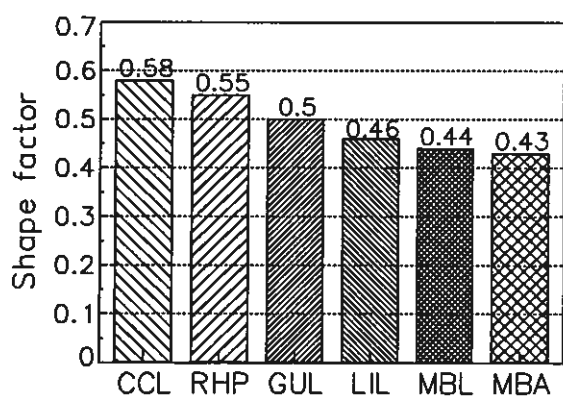


Fig. 4.9 Mean shape factor of natural hematite concentrates

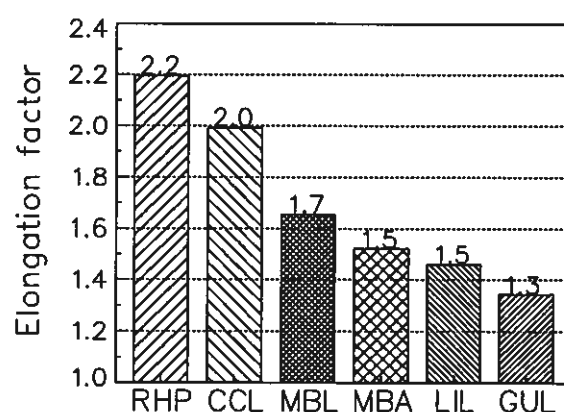


Fig.4.10 Mean elongation factor of the hematite concentrates.

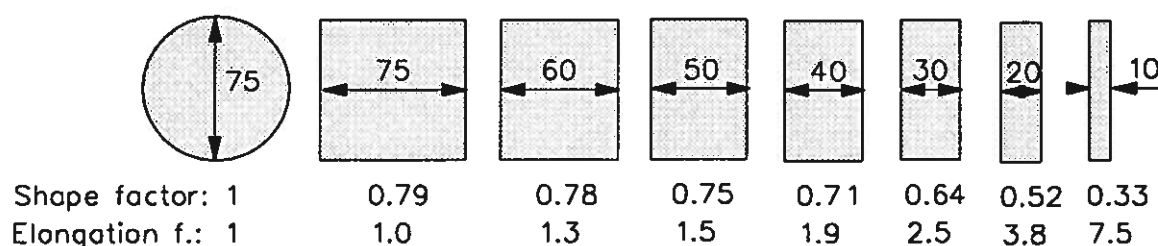


Fig. 4.11 Schematic relation between grain shape and factors.

Elongated grains are expected to have relatively high reduction rates, especially towards the end of topochemical reactions, because of small minor axes. Grain shape is considered unimportant during uniform reactions. Provided that other properties characteristic of the concentrates are equal, high reduction rates are expected for RHP, CCL and MBL because of their high elongation factors, but high reduction rates are also

expected for MBA, MBL, LIL and GUL because of their relatively low shape factors.

However, the shape factor ($4\pi A/L^2$) is a combined measure for both the actual grain shape and the surface ruggedness. Elongated grains have low shape factors, as shown in figure 4.11. Grains with highly rugged surfaces have also relatively long perimeters (L) compared to the area in section (A), resulting in low shape factors. The very low shape factors of MBA, MBL, LIL and GUL (0.43-0.50) can mainly be attributed to their large specific surface areas. The shape factors of RHP and CCL (0.55-0.58) are in fact also rather low, which is largely attributed to their elongated grains. Small differences among the mean shape factors in the range of the standard deviations, ± 0.03 - 0.05 , can be disregarded. The concentrates with very low shape factors have high to moderate initial reduction rates, partly because of their large surface areas. The concentrates with the higher shape factors have slow initial reduction rates, partly because of their smooth grain surfaces. The specific surface areas have already been discussed in this section.

The elongation factor (a/b), being the ratio of major to minor axis, is a true measure of shape. However, the high mean elongation factors of CCL and RHP (2.0-2.2) have not resulted in high reduction rates towards the end of the topochemical reaction of hematite to magnetite. On the contrary, these two have slow initial reduction rates, showing that other properties characteristic of the concentrates are far more important than grain shapes. The particle shapes of CCL and RHP have a wide distribution, shown by the large standard deviations, ± 0.9 - 1.0 . Elongation factors of GUL, LIL, and MBA (1.3-1.5), grains being more spherical, have low standard deviations, ± 0.2 - 0.4 .

Porosity

The higher content of closed pores in the grains of LIL and GUL (having about 2% porosity) than in the grains of the other concentrates (1% or less) may perhaps contribute to the high

initial reduction rate of these two ores. The higher porosity can be the reason for the high initial reduction rate in reduction gases without hydrogen, facilitating access of CO and removal of CO₂. The initial closed porosity of the grains in all these concentrates is rather low compared with the highly porous reduction products, and is for this reason not considered to be important for the further reduction rate.

The closed porosity of the grains was **estimated** in chapter 4 from the measurements of density.

However, reduction via closed pores have not been observed in microscope, but reduction along subgrain boundaries ahead of the topochemical front has frequently been observed.

Trace elements

Trace elements, detected by SIMS (see section 4.7), are in the following grouped in 3 tables according to their rate enhancing and retarding effects. A review of the effects of foreign elements in the lattice, surface effects, and the formation of separate phases from these elements, were given in section 5.2.5 on the basis of previous work. The absolute level of trace elements detected by SIMS are rather uncertain, but can be used for comparisons between the concentrates. If the elements are unevenly distributed in the hematite lattice, there is a chance of false interpretations of the SIMS results, the element concentrations being an average for only 3-6 grains.

The comparatively higher contents of the following elements detected by SIMS, supports the observed reduction rates:

- 1) Si in LIL (and MBA), Al in GUL - slow metallization
- 2) Cr in LIL, Mg in GUL - initially high, followed by slow rate
- 3) Mn in MBL - high overall reduction rate

The rate retarding elements are gathered in table 5.5. The contents of Al_2O_3 , SiO_2 and P_2O_3 , detected by chemical analyses, are included in the table. Phosphorous was not analyzed by SIMS. Contained in the hematite lattice, the respective ions, Al^{3+} , Si^{4+} and P^{5+} , being smaller than Fe^{3+} and the two latter also having a higher charge, tend to contract the lattice and hence retard reduction. Apart from lattice effects, the rate retarding effect of aluminium is probably also due to formation of hercynite ($\text{FeO}\cdot\text{Al}_2\text{O}_3$). The rate retarding effect of silicon is mainly due to formation of fayalite ($2\text{FeO}\cdot\text{SiO}_2$) or due to surface effects.

Table 5.5 Rate retarding foreign elements in the concentrates.

Rate retarding constituents		Hematite concentrate					
		MBL	MBA	LIL	GUL	RHP	CCL
Element content by SIMS (mole ppm)	Si	760	5100	2900	125	25 ¹	20
	Al	1350	3300	1800	5000	2800 ¹	1250
Chemical analyses (wt%)	SiO_2	0.01	0.51	0.44	0.63	1.83	5.4
	Al_2O_3	0.43	0.05	0.03	0.09	0.73	<0.1
	P_2O_3	0.027	0.110	0.057	0.043	0.032	n.a.

1) Analysis of RANA (from the same ore as RHP, see section 4.7)

Aluminium is present in comparatively high concentration levels in all the concentrates, according to the SIMS analyses. The high content of aluminium in GUL, but also in MBA and RHP (5000, 3300 and 2800 mole ppm, respectively), may retard the reduction, if aluminium is distributed in the hematite lattice. Referring to chapter 4, aluminium is present in gibbsite in GUL and MBL and probably in silicates in RHP. Tiny inclusions of gibbsite and silicates are not considered to disturb the reduction.

The high level of silicon detected by SIMS in MBA and LIL (5100 and 2900 mole ppm, respectively) may retard the reduction if it is distributed in the lattice or at the grain surfaces and not in inclusions. Equal order of magnitude of SiO_2 is detected in MBA (0.5-0.4 wt%) and LIL (0.4-0.2 wt%) by chemical analyses and by SIMS. The high content of SiO_2 in CCL, RHP and GUL will not

affect the reduction, because SiO_2 is mainly contained in separate quartz grains and not in the hematite lattice. Very low contents of silicon are detected by SIMS in these hematite grains (only 20, 25 and 125 mole ppm, respectively).

The medium high content of P_2O_3 in GUL and LIL (0.043-0.057%), may retard the reduction if P^{5+} is distributed in the lattice. Since these two concentrates are reduced at a high initial reduction rate, the concentration is probably too low to have any significant effect. The content of P_2O_3 is the highest in MBA (0.11%) and the lowest in MBL and RHP. According to the literature referred to in chapter 4, apatite is present in the mineral assemblage of both MBA, MBL and RHP. The reduction of these ores will probably not be retarded if phosphorous is mainly contained in apatite.

Referring to section 5.2.5, the elements gathered in table 5.6 have a rate enhancing effect on the reduction of hematite to magnetite, but a retarding effect on the further reduction. The effects are mainly caused by an initial expansion and later contraction of the iron oxide lattice, the ionic sizes, Ni^{2+} (0.69Å), Mg^{2+} (0.66Å), Cr^{3+} (0.63Å), being greater than Fe^{3+} (0.64Å) (or of equal size) and smaller than Fe^{2+} (0.74Å).

Table 5.6 Rate promoting and retarding trace elements in the hematite concentrates.

Rate promoting and retarding trace elements		Hematite concentrate					
		MBL	MBA	LIL	GUL	RANA ¹	CCL
Element content by SIMS (mole ppm)	Ni	7	15	20	35	5	35
	Mg	15	85	90	190	11	12
	Cr	150	16	240	23	95	10

1) Analysis of RANA (from the same ore as RHP, referring to section 4.7)

The initial high, and later slow, reduction rate of LIL and GUL may partly be attributed to their comparatively higher contents of the elements chromium and magnesium, respectively. All the concentrations are rather low, however, and effects are not

expected to be large. Nickel and chromium are also catalysts for the water-gas shift reaction (Thomas, 1970 and Grenoble et al., 1981), and may locally act as catalysts inside grain pores. Catalytic effects of nickel and chromium are not the reason for the high reduction rate of MBL, since MBL has the second lowest content of nickel and only second highest content of chromium.

MgO was also detected by chemical analyses of RHP and CCL, in much higher concentrations than by SIMS. Magnesium is probably contained in separate grains or inclusions of dolomite-ferrodolomite, apatite or silicates, which will not interfere with the reduction of other grains.

The elements in table 5.7 have a rate promoting effect both initially and during the further reduction, referring to section 5.2.5. Exception is Zn^{2+} substituting Fe^{2+} . Since these ions are of equal size, there will be no effects on the late reduction.

Table 5.7 Rate promoting trace elements in the concentrates.

Rate promoting trace elements		Hematite concentrate					
		MBL	MBA	LIL	GUL	RANA ¹	CCL
Element content by SIMS (mole ppm)	K	6	15	10	75	<0.02	<0.05
	Ca	6	80	70	11	<0.45	<0.25
	Na	6	20	40	35	0.1	40
	Mn	430	215	245	265	65	100
	Zn	50	25	<6	<8	<300	25
	Ti	270	120	110	30	2850	85

1) Analysis of RANA (from the same ore as RHP, referring to section 4.7)

The high content of manganese in MBL (430 mole ppm) may partly explain its high overall rate of reduction, if it is contained in the hematite lattice or on the subgrain boundaries. Located on subgrain boundaries, iron nucleation may be facilitated. The Mn-content in MBL is about twice as high as that of MBA, LIL and GUL and 4-6 times as high as that of CCL and RHP. However, much more manganese was detected by chemical analyses of RHP and CCL.

Manganese is probably contained in separate grains or inclusions of dolomite-ankerite in these two concentrates, which is not considered to have any effect on the reduction.

MBA/LIL and GUL have the highest contents of the elements calcium and potassium, respectively, detected by SIMS. Rate promoting effects are insignificant, since these concentrates are reduced at a slow to moderate reduction rate at a late stage of the reduction. The concentrations of calcium, potassium and sodium are rather low (<80 mole ppm) in all the concentrates, hence rate promoting effects must be small. Especially low is the concentration of potassium and calcium in RANA and CCL (<0.5 mole ppm). Calcium is probably mainly contained in separate grains or inclusions of carbonates in RHP and CCL, since calcium was detected by chemical analyses in comparatively large amounts.

There seem to be no rate promoting effect of the 10 times higher concentration of titanium in RANA (2850 mole ppm) (RHP) than in any of the other concentrates, since RHP is reduced at a slow initial rate and moderate further rate. The content of TiO_2 detected is even 2.5 times higher by chemical analyses than by SIMS. TiO_2 is probably mainly contained in rutile/ilmenite lamellas. Ion micrographs of 2 grains by Storemyr (1989) show that the amount of titanium differ widely from grain to grain, and that titanium also is distributed in the hematite lattice.

Scandium, cobalt and copper were also detected by SIMS, but in so small amounts (<6 mole ppm in all, but <40 mole ppm Cu in RHP) that possible effects on the reduction rates are not noticeable.

Vanadium was also detected by SIMS in rather low concentrations, <50 mole ppm apart from in RHP and MBL (200 and 100 mole ppm, respectively). If Fe^{2+} is substituted by V^{2+} , the latter being the larger, the reduction of RHP and MBL may be enhanced at a late stage. The effect of vanadium is difficult to predict, however, having all the valences +5, +4, +3 and +2 and ionic radius increasing from 0,59Å (V^{5+}) to 0.88Å (V^{2+}) (SI, 1974).

5.9.5 Concluding remarks

The SBA measures of the natural hematites can not be used directly to predict reduction rates. Additional information about subgrain shape and orientation is necessary. A laminated subgrain structure is reduced at the highest overall rate while anhedral substructures are slowly reduced to wüstite and metal. Grains consisting of subgrains are reduced at a higher initial rate than those without subgrains, because of rapid reduction along subgrain boundaries. The specific surface area is also an important parameter for the initial reduction rate.

Original magnetite contents in the hematite concentrates should be low, because magnetite reduces so slowly that magnetite can be considered to be inert during prereduction. To compare the reduction rates of the hematite in the concentrates, magnetite corrections have been made.

During the topochemical reduction of hematite to magnetite, branches of magnetite/wüstite ahead of the topochemical front have frequently been observed in the grains of MBL, MBA, GUL and LIL (in about 90% of the grains with hematite cores). The faster initial reduction of these 4 concentrates compared with CCL and RHP may be attributed to preferential reduction along subgrain boundaries and to the larger specific surface areas. The grains of the 4 concentrates have several subgrains, while the grains of CCL and RHP have no subgrains. The grains of RHP have twin planes, but twin planes rarely serve as preferential reduction paths. The very slow initial reduction of RHP can partly be attributed to its particularly small specific surface area.

During further reduction, MBL is reduced at the highest rate. The subgrain orientation is considered to be the reason for this. MBL is a specular, schistose (laminated) hematite and exfoliation along the lineation in MBL grains upon rapid initial reduction is thought to create tiny cracks along the subgrain boundaries. Consequently the rate of reduction from magnetite to wüstite is

high. Tiny elongated pores and cracks constitute a network in many reduced MBL grains in which iron seem to nucleate easily. Nucleation may have been enhanced by manganese on the subgrain boundaries, the content of Mn (by SIMS) being the highest in MBL.

The anhedral subgrain structures (lack of crystal shapes) of GUL and LIL are considered to be the main reason for the slow rates during further reduction. The rapid initial reduction does not lead to cracking between anhedral subgrains because the subgrains act as cog-weals. Iron nucleation may also have been retarded by aluminium and magnesium in the lattice of GUL and silicon and chromium in the lattice of LIL. Initially, it is possible that chromium and magnesium have a rate promoting effect. The initial rate may also have been enhanced by the high content of closed pores (2%).

Wüstite starts forming in the magnetite pores before the conversion of the hematite core is completed. Magnetite is mainly quasi topochemically reduced (relics of magnetite remains behind the topochemical front). The front is most distinct during rapid reduction, being most distinct for MBL, and being more distinct after reduction at 20%RO than at 50%RO. The slow reduction of GUL and LIL proceeds rather uniformly at 50%RO. Metallization proceeds uniformly in all the natural hematites, except perhaps in RHP.

RHP, CCL and MBA are further reduced at a moderate rate. The high magnetite contents in CCL and RHP (19 and 7%, respectively) do not retard the reduction of the hematite grains because magnetite is contained in separate grains. The rate of reduction for MBA is higher than for GUL/LIL, but lower than for MBL. This can be predicted from subgrain shape and orientation. The crystal shape of the MBA subgrains is well developed, but being angular, and not laminated, the tendency of cracking along subgrain boundaries is less pronounced. A high content of silicon (by SIMS) may also have retarded the reduction.

5.10 Comparisons of reduction rates of natural hematites and preoxidized magnetite

Prereduction of Sydvaranger magnetite proceeds at a higher rate after preoxidation at low temperatures (800-1050°C) than after preoxidation at elevated temperatures (1150-1250°C). The beneficial effect of low preoxidation temperatures is attributed to the subgrain structure, which is illustrated by the SBA curve (length of subgrain boundaries per area in section) in figure 4.8. The initial reduction rate and the SBA curve both decrease gradually for an increasing preoxidation temperature. Metallization is markedly retarded if the preoxidation temperature is raised from 1050 to 1150°C. This temperature range coincides with the steepest part of the SBA curve (1050-1200°C).

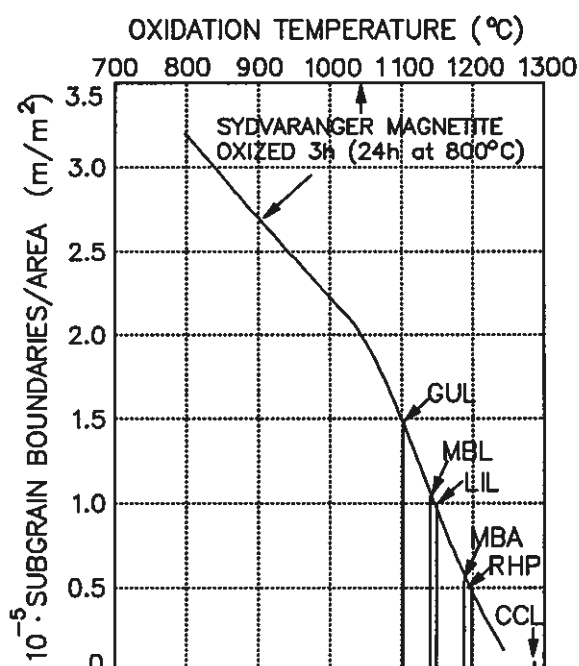


Fig. 4.8 Subgrain structure

In accordance with observations, the subgrain planes serve as preferential reduction paths during the reduction of hematite to magnetite. Tearing and vacancies along subgrain planes are the most probable causes for rapid initial reduction of Sydvaranger magnetite preoxidized at low temperatures. Metallization proceeds uniformly after preoxidation at low temperatures, but more topochemically after preoxidation at elevated temperatures. During metallization, iron nucleation may have been enhanced by numerous active sites where subgrain interfaces intercepted, or by vacancies, tiny cracks, defects, and foreign ions along the boundaries. Manganese is a rate promoting element in the lattice of Sydvaranger magnetite which may have migrated to subgrain boundaries and grain surfaces during preoxidation.

The close correlation between the SBA curve for preoxidized Sydvaranger magnetite and reduction rates can not be used directly to predict reduction rates of natural hematites from their SBA values. Referring to figure 4.8, all the natural hematites have rather low SBA values, corresponding to the SBA values of magnetite preoxidized at elevated temperatures ($\geq 1140^{\circ}\text{C}$), except GUL. Using the SBA curve for preoxidized magnetite as a reference for the reduction rate, these natural hematites should have been reduced at a slow rate. However, figures 5.74-5.76 show that 4 of the natural hematites are reduced at a higher rate than S8 (magnetite preoxidized at 1244°C). Figures to the left (a) are not corrected for magnetite contents. Magnetite is considered to be inert in the figures to the right (b) and corrections have been made according to formulas 5.65-5.67 in section 5.9.3.

During the topochemical reduction of hematite to magnetite, branches of magnetite/wüstite ahead of the topochemical front have been observed far more frequently in the grains of MBL, MBA, GUL and LIL (in about 90% of the grains with hematite cores) than in the grains of preoxidized magnetite. The main reason for the faster initial reduction of these 4 natural hematites is probably that reduction along subgrain boundaries is faster in natural hematites than in preoxidized magnetite with a comparable SBA value. Besides, the faster initial reduction can partly be attributed to larger specific surface areas of the same 4 natural hematites. Specific surface area of preoxidized magnetite has not been measured, but the high shape factor (0.65 ± 0.03) compared to the shape factors of these 4 hematites (0.43-0.50), indicates that the grain surface of preoxidized magnetite is relative smooth.

RHP and CCL, on the other hand, are initially reduced at an equally slow or even slower reduction rate than magnetite preoxidized at elevated temperatures. Since these two natural hematites have no subgrains (the SBA value for RHP refers to twin planes), a slow initial reduction could be predicted. Twin

planes rarely serve as preferential reduction paths. The very slow initial reduction of RHP can partly be attributed to its particularly small specific surface area. Reduction rates of RHP, CCL, and S8 are approximately equal during the further reduction.

During further reduction, MBL is reduced equally fast as, or even faster than S1 (magnetite preoxidized at low temperature, 799°C), although a rather slow reduction rate is predicted from its SBA value ($1.1 \cdot 10^5 \text{ m/m}^2$). The subgrain orientation is considered to be the reason for this. MBL is a specular, schistose (laminated) hematite and exfoliation along the lineation in MBL grains upon rapid initial reduction is thought to create tiny cracks along the subgrain boundaries. Hence, the rate of reduction from magnetite to wüstite is high. Tiny elongated pores and cracks constitute a network in many reduced MBL grains in which iron seems to nucleate easily. Nucleation has probably partly been enhanced by manganese on the subgrain boundaries in both MBL and S1, the content of Mn being twice as high in S1 as in MBL. Referring to figures 5.75 and 5.76, reduction of S1 is a little retarded in the period 20-35 seconds compared to MBL, due to slow initial metallization. Small remnants of magnetite, which was detected in optical microscope, but not by chemical analyses, have perhaps retarded iron nucleation in S1. This is supported by a 3% higher level of metallization in two other samples preoxidized at low temperatures, S2 (900°C) and S3 (1002°C).

GUL and LIL are further reduced at the same slow rate as S8 at 50%RO and at an even slower rate at 20%RO. The anhedral subgrain structures (lack of crystal shapes) of the two natural hematites are considered to be the reason for the slow rates. The rapid initial reduction does not lead to cracking between subgrains because the subgrains act as cog-weals. Iron nucleation may also have been retarded by magnetite inclusions, by aluminium and magnesium in the lattice of GUL, and silicon and chromium in the lattice of LIL. On the other hand, iron nucleation is probably enhanced by manganese on the grain surfaces of S8.

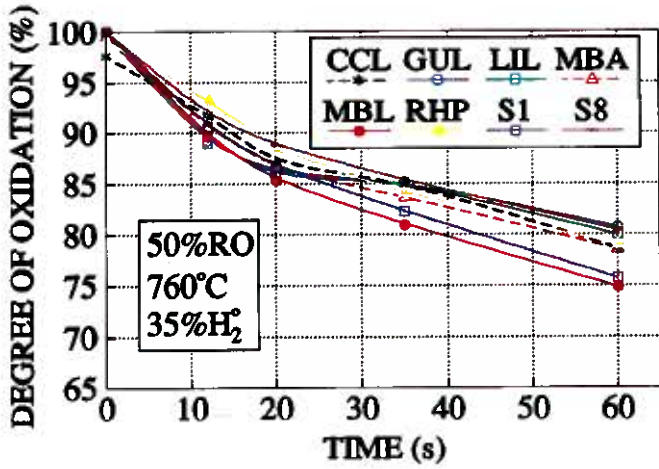


Fig. 5.74a Prereduction at 760°C and 50%RO. No corrections.

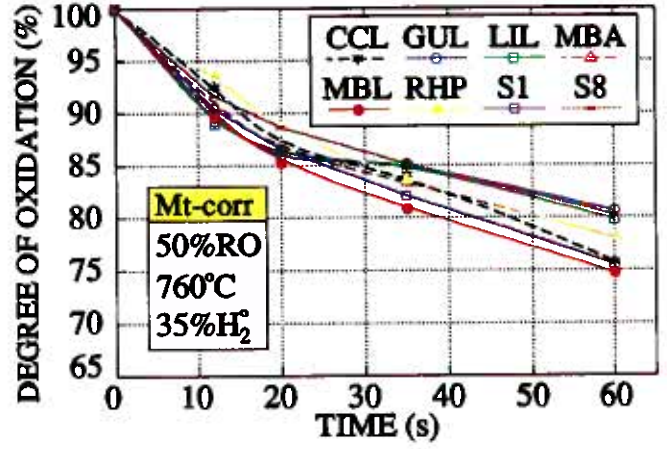


Fig. 5.74b Prereduction at 760°C and 50%RO. Magnetite corrections.

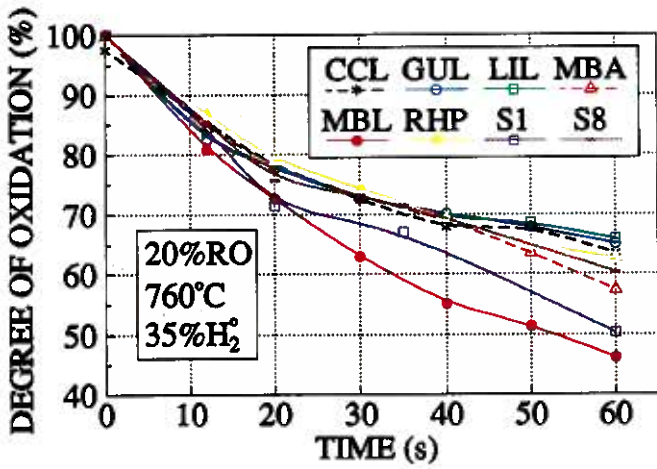


Fig. 5.75a Prereduction at 760°C and 20%RO. No corrections.

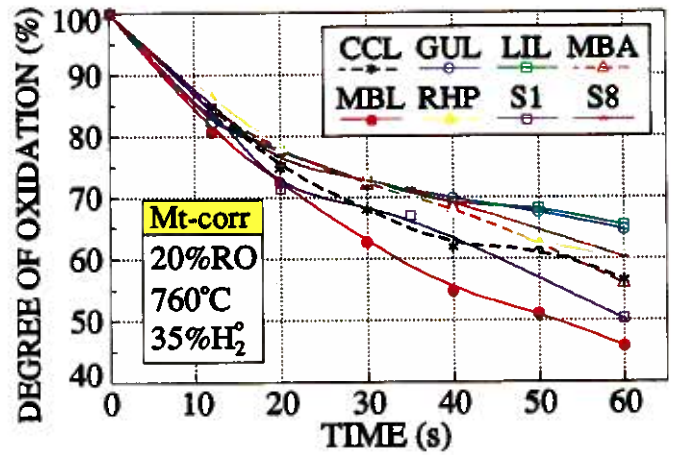


Fig. 5.75b Prereduction at 760°C and 20%RO. Magnetite corrections.

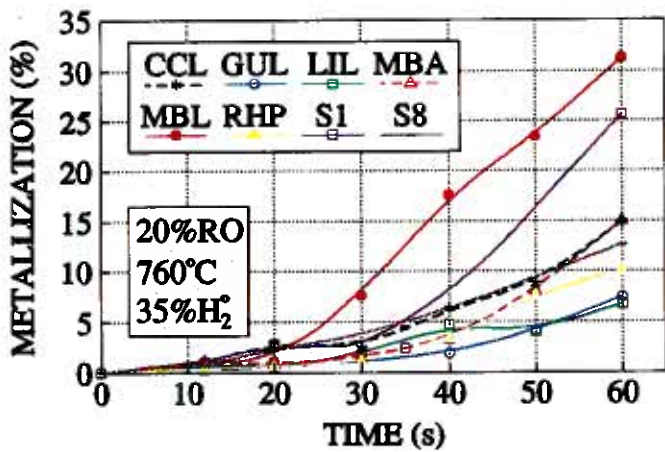


Fig. 5.76a Metallization during prereduction at 760°C and 20%RO. No magnetite corrections.

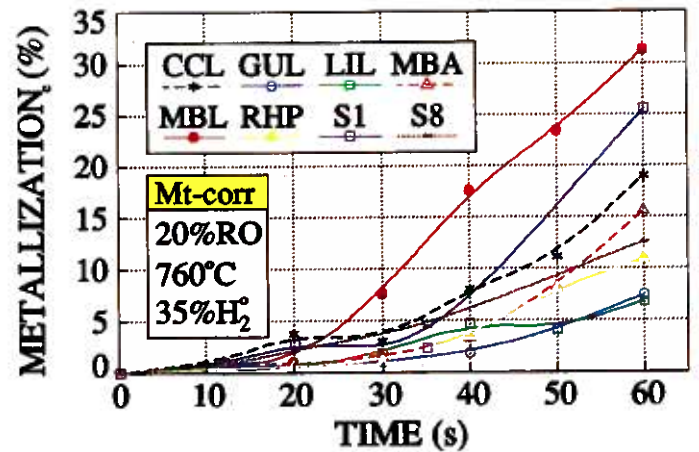


Fig. 5.76b Metallization during prereduction at 760°C and 20%RO. Magnetite is considered as inert.

5.11 Conclusions

Prereduction of Sydvaranger magnetite proceeds at a higher rate after preoxidation at low temperatures (800-1050°C) than after preoxidation at elevated temperatures (1150-1250°C). The beneficial effect of low preoxidation temperatures may be attributed to the subgrain structure. The subgrain structure of the preoxidized magnetite is well characterized by the SBA curve. The initial reduction rate and the SBA curve both decrease gradually for an increasing preoxidation temperature. The rate promoting effect of low temperature subgrain structures is not very pronounced during initial reduction. The rate of metallization is markedly retarded if the preoxidation temperature is raised from 1050 to 1150°C. This temperature range coincides with the steepest part of the SBA curve.

Natural hematite concentrates which contain grains made up of subgrains, are reduced at a higher initial rate than those without subgrains. However, the SBA curve for preoxidized magnetite can not be used directly to predict reduction rates of the natural hematites from their SBA values. Additional information about subgrain shape and orientation is necessary. The specific surface area is also an important parameter for the initial reduction rate. Other characteristics, such as the small variations in mean grain sizes and grain shapes, are of less importance. Differences in grain size degradation and material loss during reduction are considered to have only minor effects on the results, and do not alter the conclusions.

Magnetite contents in the natural hematite concentrates should be low, because magnetite is reduced so slowly that magnetite can be considered to be inert during prereduction. Magnetite corrections were used for comparing reduction rates of the hematite grains.

The subgrain interfaces serve as preferential reduction paths. Branches of magnetite/wüstite have been observed in optical microscope along subgrain boundaries ahead of the topochemical

front during reduction of hematite to magnetite, but far more frequently along the subgrain boundaries of natural hematites than of preoxidized magnetite. Diffusion along subgrain boundaries is probably easier in natural hematites than in preoxidized magnetite with comparable SBA values.

Wüstite starts forming in the magnetite pores before the conversion of the hematite core is completed. Magnetite is reduced either uniformly or quasi topochemically to wüstite. The front is most distinct during rapid conversion. Metallization proceeds uniformly in most of the natural hematites and in Sydvaranger magnetite preoxidized at low temperatures, and more topochemically after preoxidation at elevated temperatures. Iron nucleation may have been enhanced by numerous active sites where subgrain interfaces intercepted, or by vacancies, tiny cracks, defects, and foreign ions along the subgrain boundaries.

Although a rather low reduction rate may be predicted from the SBA value of a specular, schistose (laminated) natural hematite, it is reduced equally as fast, or even faster than magnetite preoxidized at low temperature. Exfoliation along the lineation upon rapid initial reduction is thought to create tiny cracks along the subgrain boundaries. Hence, the rate of reduction from magnetite to wüstite is high. Tiny elongated pores and cracks constitute a network in which iron is easily nucleated. Nucleation may have been enhanced by manganese on the subgrain boundaries of both the laminated hematite and the preoxidized magnetite.

Anhedral subgrain structures of natural hematites are reduced at a high initial rate, which also may have been enhanced by a relatively high content of closed pores. During further reduction they are reduced equally slow, or even slower than magnetite preoxidized at elevated temperatures. The rapid initial reduction does not lead to cracking between subgrains because the subgrains act as cog-weals. Iron nucleation may have been retarded by aluminium, magnesium, silicon or chromium in the lattices.

6 REFERENCES

Ball, D. F., Buttler, F. G. and Ratter, H.: "Some studies of pellet firing. Part II - Oxidation of Magnetite and desulphurization", *Iron Steel*, Vol. 39, pp. 150-152, 1966.

Ball, D. F., Dartnell, J., Davison, J., Grieve, A. and Wild, R.: "Agglomeration of iron ores", Heinemann Educational Books Ltd., London 1973.

Baguley, P., John, D. H. St. and Hayes, P. C.: "The conditions for the formation of lath and porous magnetite on reduction of hematite in H₂/H₂O gas mixtures", *Met. Trans.*, Vol. 14B, pp.513-514, 1983.

Barin, I., Knacke, O. and Kubaschewski, O.: "Thermochemical properties of inorganic substances, supplement", Springer-Verlag, 1977.

Baumann, H. M.: "Reduction of iron ore concentrates with CO and H₂", M. Sc.- thesis NTH, in Norwegian, Norway 1985.

Bentell, L. and Mathisson, G.: "Oxidation and Slag-forming process in Dolomite-fluxed Pellets Based on Magnetite Concentrates", *Scand. J. Metallurgy*, Vol. 7, pp. 230-236, 1978.

Berge, J. W.: "Geology, geochemistry and origin of the Nimba Itabirite and associated rocks, Nimba County, Liberia", *Economic Geology*, 69.1, pp 80-92, 1974.

Berge, J. W., Johansson, K. and Jack, J.: "Geology and origin of the hematite ores of the Nimba Range, Liberia", *Economic Geology* 72.4, pp 582-607, 1977.

Bleifuss, R. L.: "Single particle studies applied to direct reduction and blast furnace operations", Marcel Dekker Inc., 1972.

Bogdandy, L. von and Engell, H. J.: "The reduction of iron ores", Springer Verlag, 1971.

Brekken, H.: "Structure and phase relations in iron ore pellets", Thesis in Norwegian, Institute of Metallurgy, NTH, Trondheim, 1983.

Brill-Edwards, H., Daniell, B. L. and Samuel, R. L.: "Structural changes accompanying the reduction of polycrystalline hematite", J. Iron Steel Inst., Vol. 203, pp.361-368, 1965.

Bruijn, W. de, Heerema, R. H. and Tichelaar, J. P.: "The influence of secondary compounds on the reduction behaviour of blast furnace burdens", Iron & Steel Maker, Vol. 17, no. 7, pp.53-58, 1990.

Bugge, J. A. W.: "Rana Mines - Geological description of the iron ores in Dunderlandsdalen", NGU 171, in Norwegian, Norway 1948.

Bugge, J. A. W.: "Norway", a chapter in the book "Mineral Deposits of north-western Europe", Institution of Mining and Metallurgy, Mineralogical Society, London 1978.

Båsen, T. and Ephithite, R. J.: "The Elkem Polar Process for reduction of ore fines", 7th Process Technology Conference, ISS-AIME, Toronto 1988.

Båsen, T., Ephithite, R. J. and Floa, T.: "Final report Polarstål", restricted report in Norwegian for Elkem and Norsk Jernverk A/S, Norway 1989.

Callender, W.: "Heat hardening of artificial magnetite pellets", in "Agglomeration" ed.: Knepper, W. A., pp. 641-667, New York, 1962.

Caracas, R. W.; Private communication with the MBR (Mineracoes Brasileiras Reunidas) company, Brazil 1987.

Chinje, U. F. and Jeffes, J. H. E.: "Effects of chemical composition of iron oxides on their rates of reduction: Part 1 Effect of trivalent metal oxides on reduction of hematite to lower iron oxides", *Ironmaking and Steelmaking*, Vol. 16, No. 2, pp. 90-95, 1989.

Cooke, H. and Bailey, J.: "Iron Ore Databook", first ed., Metal Bulletin Books, Surrey 1987.

Cooke, S. R. B. and Stowasser, W. F.: "The effect of heat treatment and certain additives on the strength of fired magnetite pellets", *Trans. AIME*, Vol. 193, pp. 1223-1230, 1952.

Cooke, S. R. B. and Ban, T. E.: "Microstructures in Iron Ore Pellets", *Trans. AIME*, Vol. 193, pp. 1053-1058, 1952.

Cubberly, W. H. et al.: "Metals Handbook", American society for metals, 9th ed., Vol. 2, 1979.

Darken, L. S. and Gurry, R. W.: "The system iron-oxygen. II Equilibrium and thermodynamics of liquid oxide and other phases", *J. Am. Chem. Soc.*, Vol. 68, pp. 798-816, 1946.

David, I. and Welch, A. J. E.: "The oxidation of magnetite and related spinels. Constitution of gamma ferric oxide.", *Trans. Faraday Soc.*, Vol. 52, pp. 1642-1650, 1956.

Davies, M. H., Simnad, M. T. and Birchenall, C. E.: "On the mechanism and kinetics of the scaling of iron", *Trans. AIME*, Vol. 191, pp. 889-896, 1951.

DeBoer, F. E. and Selwood, P. W.: "The activation energy for the solid state reaction $\gamma\text{-Fe}_2\text{O}_3 \rightarrow \alpha\text{-Fe}_2\text{O}_3$ ", *J. Amer. Chem. Soc.*, Vol. 76, pp. 3365-3367, 1954.

Doherty, R. D., Hutchings, K. M., Smith, J. D. and Yörük, S.: "The reduction of hematite to wüstite in a laboratory fluidized

bed", *Met. Trans.*, Vol. 16B, pp. 425-432, 1985.

Dorr, J., "Supergene Iron Ores of Minas Gerais, Brazil", *Economic Geology*, 59.7, pp 1203-1240, 1964.

Dorr, J., "Nature and origin of the high-grade hematite ores of Minas Gerais, Brazil", *Economic Geology*, 60.1, pp 1-46, 1965.

Edström, J. O.: "The mechanism of reduction of iron oxides", *J. Iron Steel Inst.*, Vol. 175, pp. 289-304, 1953.

Edström, J. O.: "Reduction structures of iron powder", in Swedish, *Jernkont. Ann.*, Vol. 140, pp. 116-129, 1956.

Edström, J. O.: "Study of the mechanism and kinetics of oxidation of green magnetite pellets", *Jernkont. Ann.*, Vol. 141, pp. 457-478, 1957.

Ekanem, E. B. and Walker, R. D.: "Stepwise reduction of Itakpe iron ore compacts to magnetite, wüstite, and iron", *Ironmaking and Steelmaking*, Vol. 16, No. 5, pp. 320-324, 1989.

Ettabirou, M., Jeannot, F., Dupré, B. and Gleitzer, C.: "Rôle de la silice dans la réduction d'un minerai hématite en magnétite par CO-CO₂", *Memoires et Etudes Scientifiques Revue de Métallurgie*, Vol. 83, no. 4, pp. 181-189, 1986.

Evans, U. R.: "The corrosion and oxidation of metals", Arnold, pp. 833-834, London 1960.

Exner, H. E.: "Stereological characterization of shape", *Metals Handbook, powder metallurgy*, Vol. 7, 9th ed., pp. 237-241, 1984.

Fitton, J. T. and Goldring, D. C.: "Constitution of iron ore pellets in relation to time and temperature of firing", *J. Iron Steel Inst.*, Vol. 204, pp. 452-459, 1966.

Friel, J. J. and Erickson, E. S.: "Chemistry, microstructure, and reduction characteristics of dolomite fluxed magnetite pellets", *Met. Trans.*, Vol. 11 B, pp. 233-243, 1980.

Gilliot, B., Rousset, A. and Dupre, G.: "Influence of Crystallite Size on the Oxidation Kinetics of Magnetite", *Journal of Solid State Chemistry*, Vol. 25, pp. 263-271, 1978.

Gougeon, M., Dupré, B. and Gleitzer, C.: "An investigation of the critical influence of potassium on the reduction of wüstite", *Met. Trans.*, Vol. 17 B, pp. 657-663, 1986.

Grabke, von H.-J.: "Kinetic der Sauerstoffübertragung aus CO_2 an die Oberfläche von Oxyden", *Ber. Bunsenges. Phys. Chem.*, Vol. 69, pp.48-57, 1965.

Grabke, von H.-J.: "Kinetic der Sauerstoffübertragung aus CO_2 an die Oberfläche von Metallen", *Ber. Bunsenges. Phys. Chem.*, Vol. 71, pp.1067-1073, 1967.

Grenoble, D. C., Estadt, M. M. and Ollis, D. F.: "The chemistry and catalysis of the water gas shift reaction. 1. The kinetics over supported metal catalysts", *Journal of catalysis*, Vol. 67, pp. 90-102, 1981.

Grøntvedt, P.O., Kolbeinsen, L. and Lindstad, T.: "Prereduction of iron ore concentrates, laboratory experiments", restricted SINTEF-report STF34 F86080, in Norwegian, Norway 1986.

Gudenau, H. W., Burchard, W.-G. and Rupp, H.: "Direkte Beobachtung von Reduktionsreaktionen an Eisenoxiden mittels Zusatzgerät zum Rasterelektronenmikroskop mit Hochtemperatur- und Gasbehandlungsmöglichkeit", *Arch. Eisenhüttenwes.*, Vol. 51, pp. 329-334, 1980.

Gudenau, H. W., Burchard, W.-G., Schaefer, H. C. and Kobayashi, M.: "Untersuchungen zum Eisenwachstum auf Wüstitoberflächen nach

isothermer CO/CO₂-Reduktion", Fachberichte Hüttenpraxis Metallweiterverarbeitung, Vol. 21, No.10, pp. 698-711, 1983.

Gudenau, H. W., Burchard, W.-G. and Schiller, M.: "Zum Ausscheidungsverhalten von Eisen während der Reduktion", Fachberichte Hüttenpraxis Metallweiterverarbeitung, Vol. 23, No. 10, pp. 812-820, 1985.

Haas, H. de, Grebe, K. and Oeters, F.: "Einfluss der Reduktionsbedingungen auf die Vorgänge bei der Reduktion von Eisenerzen in kohlenmonoxidhaltigen Gasen", Stahl und Eisen, Vol. 99, No. 17, pp. 914-919, 1979.

Hara, Y. et al.: "Mathematical model of the shaft furnace for reduction of iron-ore pellets", Tetsu-to-Hagane, Vol. 62, no. 3, pp. 315-323, 1976.

Hayes, P. C. and Grieveson, P.: "Microstructural changes on the reduction of hematite to magnetite", Met. Trans., Vol. 12B, pp. 579-587, 1981.

Himmel, L., Mehl, R. F. and Birchenall, C. E.: "Self-diffusion of iron in iron oxides and the Wagner theory of oxidation", Trans. AIME, Vol. 197, pp. 827-843, 1953.

Holt, N. J.: "Quality of iron ore pellets. Fine grained/large grained hematite", restricted SINTEF note in norwegian, project no. 341311, 1985.

Hurlbut, C. S. and Klein, H.: "Manual of mineralogy", 19th ed., John Wiley & Sons, 1977.

Hutchings, K. M., Smith, J. D., Yörük, S. and Hawkins, R. J.: "Reduction of hematite in a fluidized bed using H₂, CO, and H₂-CO mixtures", Ironmaking and Steelmaking, Vol. 14, No. 3, pp. 103-109, 1987.

JANAF Thermochemical Tables, 3rd ed., Part I and II, Am. Chem. Soc., Am. Inst. Phys., and Natl. Bur. Std., 1985.

John, D. H. St. and Hayes, P. C.: "Microstructural features produced by the reduction of wüstite in H₂/H₂O gas mixtures", Met. Trans., Vol. 13B, pp. 117-124, 1982.

Karabasov, Y. S. et al.: "Influence of heat treatment temperature of ferric oxide on its reactivity", Steel in the USSR, Vol. 14, no. 7, pp. 311-312, 1984.

Karim, G. A. and Mohindra, D.: "A kinetic investigation of the water gas shift reaction in homogeneous systems", Journal of the institute of fuel, pp. 219-223, 1974.

Klein, C. J.: "Mineralogy and petrology of the metamorphosed Wabush iron formation, southwestern Labrador", Journal of Petrology, Vol. 7, part 2, pp 246-305, 1966.

Kolbeinsen, L.: "Iron Ore reduction. Mathematical model for process control", Dr. ing. thesis (in norwegian) at NTH, Trondheim, Norway 1982.

Kolbeinsen, L., Lindstad, T. and Grøntvedt, P.O.: "Physical Modelling of Gas/Solid Transport Reactors", Conference on Flash Reaction Processes 1988, Utah 1988.

Kolbeinsen, L., Lindstad, T. and Grøntvedt, P.O.: "Physical modelling of gas/solid transport reactors", Fluidization 7, Canada 1989.

Kolesnik, N. F. and Pierre, G. R. St.: "The influence of water vapour on the decomposition of carbon monoxide on reduced iron oxide", Met. Trans. B, Vol. 11B, pp. 285-289, 1980.

Koo, C.-H. and Evans, J. W.: "Structural and reduction characteristics of some venezuelan iron ores", Transactions ISU,

Vol. 19, pp. 95-101, 1978.

Kunii, D. and Levenspiel O.: " Fluidization engineering", John Wiley & Sons, New York 1969.

Levenspiel, O.: "Chemical reaction engineering, an introduction to the design of chemical reactors", 5th. printing, John Wiley & Sons, New York 1967.

Levin, E. M., Robbins, C. R. and McMurdie, H. F.: "Phase diagrams for ceramists", The American Ceramic Society, suppl., 1969.

Lindner, R.: "Diffusion von radiaktiven Eisen in Eisen (3) - oxyd und Zink - Eisen - Spinell", Arkiv för Kemi, Vol. 4, pp. 381-384, 1952.

Mazanek, E., Krupinska, Z. and Kulgawczuk, D.: "On the oxidation reaction of magnetite", Arch. Eisenhüttenwes., Vol. 44, pp. 571-577, 1973.

Meschter, P. J. and Grabke, H. J.: "Kinetics of the water-gas shift reaction on an "FeO" surface", Met. Trans. B, Vol 10B, pp. 323-329, 1979.

Meyer, K. von, Rausch, H. and Ottow, M. von: "Zerfall hocheisenhaltiger Pellets während der Reduktion", Stahl und Eisen, Vol. 87, no. 11, pp. 654-660, 1967.

Monsen, B. et al.: "Partial reduction of iron ore concentrates in gas suspension with stress on prior oxidation", restricted SINTEF-report STF34 F88050, in Norwegian, Norway 1988.

Muan, A.: "Phase equilibrium at high temperatures in iron silicate systems", Am. Ceram. Soc. Bull., Vol. 37, pp. 81-84, 1958.

Nakagawa, H. and Ono, Y.: "Effects of potassium chloride on the

reduction of iron oxides", *Trans. Iron Steel Inst. Jpn.*, Vol. 25, pp. 1021-1024, 1985.

Nakiboglu, F., John, D. H. St. and Hayes, P. C.: "The gaseous reduction of solid calciowüstites in CO/CO₂ and H₂/H₂O gas mixtures", *Met. Trans.*, Vol. 17 B, pp. 375-381, 1986.

Nicolle, R. and Rist, A.: "The mechanism of whisker growth in the reduction of wüstite", *Met. Trans.*, Vol. 10B, pp. 429-438, 1979.

Olsen, S. E. and Malvik, T.: "Mineralogy of iron ore and structure of the pellets", *ICHEME 5th int.conf. on agglomeration*, pp. 299-310, 1989

Olsson, R. G. and Turkdogan, E. T.: "Catalytic effect of iron on decomposition of carbon monoxide: II. Effect of additions of H₂, H₂O, CO₂, SO₂ and H₂S", *Met. Trans.*, Vol. 5, pp. 21-26, 1974.

Papanastassiou, D. and Bitsianes, G.: "Mechanisms and Kinetics Underlying the Oxidation of Magnetite in the Induration of Iron Ore Pellets", *Met. Trans.*, Vol.4, pp. 487-496, 1973.

Pepper, M. W., Li, K. and Philbrook, W. O.: "Solid structural changes during the reduction of iron oxides", *Canadian Metallurgical Quarterly*, Vol. 15, No. 3, pp. 201-209, 1976.

Porter, J. R. and Swann, P. R.: "High-voltage microscopy of reduction of hematite to magnetite", *Ironmaking and Steelmaking*, Vol. 4, pp. 300-307, 1977.

Roederer, J., Dupré, B. and Gleitzer, C.: "Influence and role of potassium in the reduction of hematite with CO/CO₂, Part 1: The hematite-magnetite step", *Steel Research*, Vol. 58, No. 6, pp. 247-251, 1987a.

Roederer, J., Gautier, E., Dupré, B. and Gleitzer, C.: "Etude par analyse d'image de la porosité des oxydes obtenus par réduction

de l'hématite pure ou dopée par le potassium", Mém. Etud. Sci. Rev. Métall., Vol. 84, No. 7-8, pp. 375-385, 1987b.

Roederer, J., Jeannot, F., Dupré, B. and Gleitzer, C.: "Influence and role of potassium in the reduction of hematite with CO/CO₂, Part 2: The hematite-magnetite-wüstite double reaction", Steel Research, Vol. 58, No. 6, pp. 252-256, 1987c.

Rosenqvist, T.: "Principles of extractive metallurgy", 2nd edition, McGraw-Hill, 1985 a.

Rosenqvist, T.: "Kinetics of metallurgical processes", Lecture notes given in conjunction with a graduate course at NTH, Trondheim, Norway 1985 b.

Rupp, H., Gudenau, H.-W. and Burchard, W.-G.: "Ausgewählte Probleme der Strukturveränderungen bei der Reduktion von Eisenoxiden - In-situ-Untersuchungen in Rasterelektronenmikroskop", Stahl und Eisen, Vol. 102, pp. 911-915, 1982.

Ruston, W. R. et al.: "The solid reaction products of the catalytic decomposition of carbon monoxide on iron at 550°C", Carbon, Vol. 7, pp. 47-57, 1969.

Satterfield, C. N.: "Heterogenous Catalysis in Practice", McGraw-Hill, New York 1980.

Schrader, R. von and Büttner, G.: "Eine neue Eisen (III) - oxidphase: ϵ -Fe₂O₃", Z. anorg. allg. chem., Vol. 320, pp. 220-234, 1963.

Sheasby, J. S. and Gransden, J. F.: "The development of porosity during the reduction of iron ore", paper on int. symp.: Met.-Slag-Gas React. Processes, Ontario London, pp. 226-237, 1975.

SI chemical data, 2nd ed., editors: Aylward, G. H. and Findlay, T. J. V., John Wiley & Sons, 1974.

Slack, W. W.: "Interaction among structures and reduction behaviour of natural hematites", Ph. D. at Carnegie Mellon University, 1979.

Smith, R. P.: "Equilibrium of iron-carbon alloys with mixtures of CO-CO₂ and CH₄-H₂", J. Am. Chem. Soc., Vol. 68, pp. 1163-1175, 1946.

Sohn, H. Y. and Wadsworth, M. E.: "Rate Processes of Extractive Metallurgy", pp. 285-302 by Evans, J. W. and Koo, C.-H., Plenum Press 1979.

Srinivasan, M. V. and Sheasby, J. S.: "A study of the reduction of hematite to magnetite using a stabilized zirconia cell", Met. Trans., Vol. 12B, pp. 177-185, 1981.

Steinmo, J. J.: "Mechanism and kinetics in the reduction of Rana and Fosdalen iron ore concentrates", Thesis (in norwegian) at NTH, Trondheim, Norway 1986.

Stephenson, R. L. and Smailer, R. M.: "Direct reduced iron. Technology and economics of production and use", chapter 4 by Hendrickson, L. G. and Sandoval, J. A., The Iron & Steel Society of AIME, USA 1980.

Storemyr, P.: "Reduction of iron ore concentrates - iron ores of the world 1986", open SINTEF-report STF34 A86070 (in norwegian), Trondheim, Norway 1986 a.

Storemyr, P.: "Mineralogical and chemical parameters of importance for the reduction properties of the iron oxides magnetite and hematite", Thesis (in norwegian) at NTH, Trondheim, Norway 1986 b.

Storemyr, P.: "Qualitative and semi-quantitative analyses of trace elements in single grains of iron oxides with secondary ion mass spectrometry (SIMS)", open SINTEF-report STF36 A89026 (in

english), Trondheim, Norway 1989.

Suzuki, Y., Yamamoto, M., Kotanigawa, T. and Nishida, K.: "Some aspects on porous properties of iron oxides containing foreign oxides reduced by hydrogen", Met. Trans., Vol. 12 B, pp. 691-697, 1981.

Swann, P. R. and Tighe, N. J.: "High voltage microscopy of the reduction of hematite to magnetite", Met. Trans., Vol. 8B, pp. 479-487, 1977.

Szekely, J. and El-Tawil, Y.: "The reduction of hematite pellets with carbon monoxide-hydrogen mixtures", Met. Trans., Vol. 7 B, pp. 490-492, 1976.

Sæverud, B.: "Kinetics and mechanism during oxidation of magnetite pellets", Thesis (in norwegian) at NTH, Trondheim, Norway 1984.

Thomas, C. L.: "Catalytic Processes and proven catalysts", Academic Press, New York 1970.

Towhidi, N. and Szekely, J.: "The influence of carbon deposition on the reduction kinetics of commercial grade hematite pellets with CO, H₂, and N₂", Met. Trans., Vol 14B, pp. 359-367, 1983.

Trushenski, S. P., Li, K., and Philbrook, W. O.: "Non-topochemical reduction of iron oxides", Met. Trans., Vol. 5, pp. 1149-1158, 1974.

Turkdogan, E. T., Olsson, R. G. and Vinters, J. V.: "Gaseous reduction of iron oxides: Part II. Pore characteristics of iron reduced from hematite in hydrogen", Met. Trans., Vol. 2, pp. 3189-3196, 1971 a.

Turkdogan, E. T. and Vinters, J. V.: "Gaseous reduction of iron oxides: Part I. Reduction of hematite in hydrogen", Met.

Trans., Vol. 2, pp. 3175-3188, 1971.

Turkdogan, E. T. and Vinters, J. V.: "Gaseous reduction of iron oxides: Part III. Reduction-oxidation of porous and dense iron oxides and iron", Met. Trans., Vol. 3, pp. 1561-1574, 1972.

Turkdogan, E. T. and Vinters, J. V.: "Catalytic effect of iron on decomposition of carbon monoxide: I. Carbon deposition in H₂-CO mixtures", Met. Trans., Vol. 5, pp. 11-19, 1974.

Twenhofel, L. H.: "Changes in the oxidation of iron in magnetite", Econ. Geol., Vol. 22, pp. 180-188, 1927.

Ulvensöen, J. H., Monsen, B., Lindstad, T. and Hoggen, B.: "The production of high quality iron powder for P/M use from Sydvaranger super iron ore", Advances in Powder Metallurgy, Vol. 5, pp. 31-44, 1991.

Ünal, A.: "Fayalite formation in gaseous reduction of Carol Lake material to magnetite", Ironmaking and Steelmaking, Vol. 12, No. 3, pp. 113-117, 1985.

Ünal, A. and Bradshaw, A. V.: "Rate processes and structural changes in gaseous reduction of hematite particles to magnetite", Met. Trans., Vol. 14B, pp. 743-752, 1983.

Walker, R. D. and Carpenter, D. L.: "Influence of reducing gas composition on the structure and reducibility of iron oxides", J. Iron Steel Inst., Vol. 208, pp. 67-74, 1970.

Walker, P. L. jr., Rakszawski, J. F. and Imperial G. R.: "Carbon formation from carbon monoxide-hydrogen mixtures over iron catalysts. II. Rates of carbon formation", J. Phys. Chem., Vol. 63, pp. 140-149, 1959.

Watanabe, S. and Yoshinaga, M.: "The abnormal behaviour of some ore constituents and their effect on the blast furnace

operation", Trans. AIME mining, Vol. 241, pp. 1-15, 1968.

Weast, R. C.: "Handbook of chemistry and physics", 62 ed., CRC Press, 1981-1982.

Zetterstrøm, J. D.: "Oxidation of Magnetite concentrates", US dep. of the Interior Bureau of Mines, Report of Investigation 4728, 1950.

Wiberg, M.: " ", Stahl und Eisen, Vol. 61, pp. 141-143, 1941.

APPENDICES

Appendix A.1

Temperature curves from oxidation experiments in section 3.4

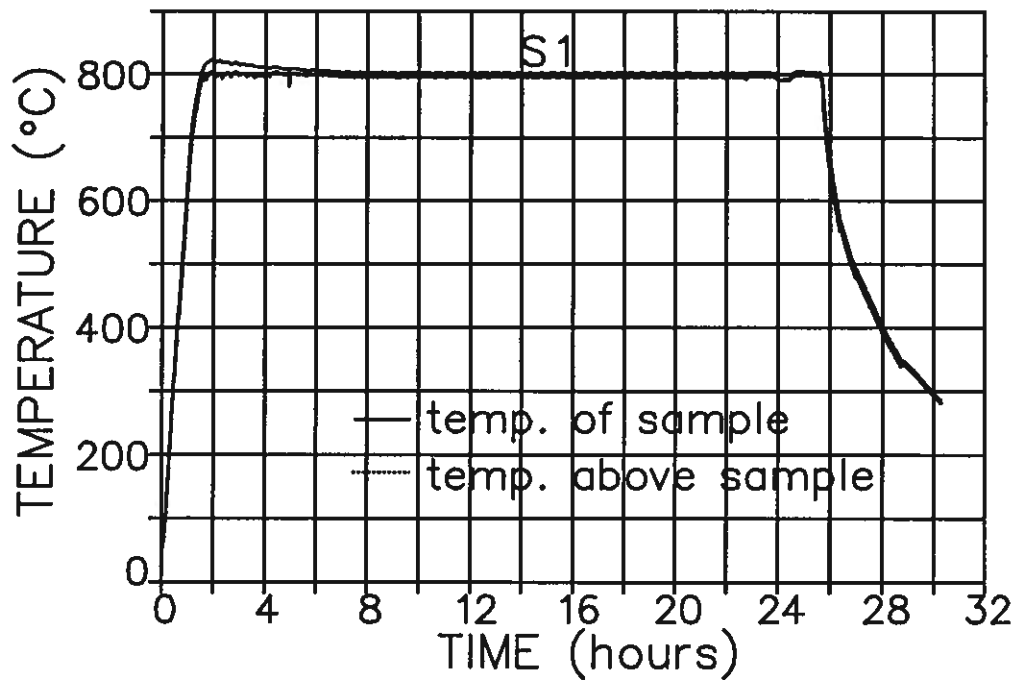


Fig. A.1.1 Oxidation of Sydvaranger magnetite at 800°C in air for 24 hours. Heating and cooling were performed in nitrogen atmosphere.

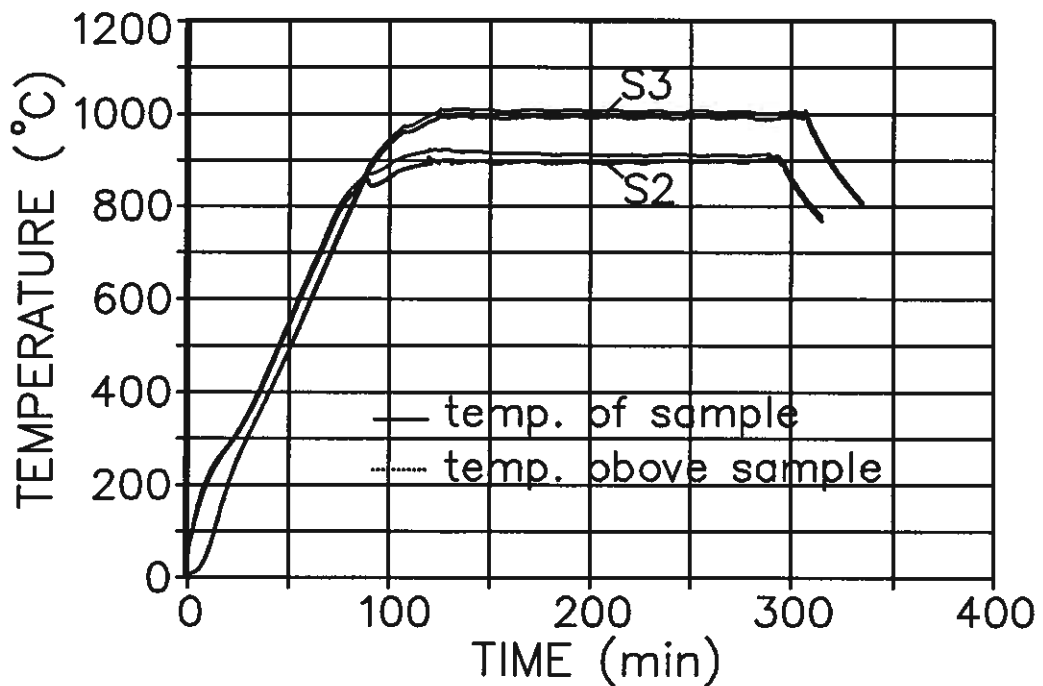


Fig. A.1.2 Oxidation of Sydvaranger magnetite at 900°C (S2) and 1000°C (S3) in air for 3 hours. Heating and cooling were performed in nitrogen atmosphere.

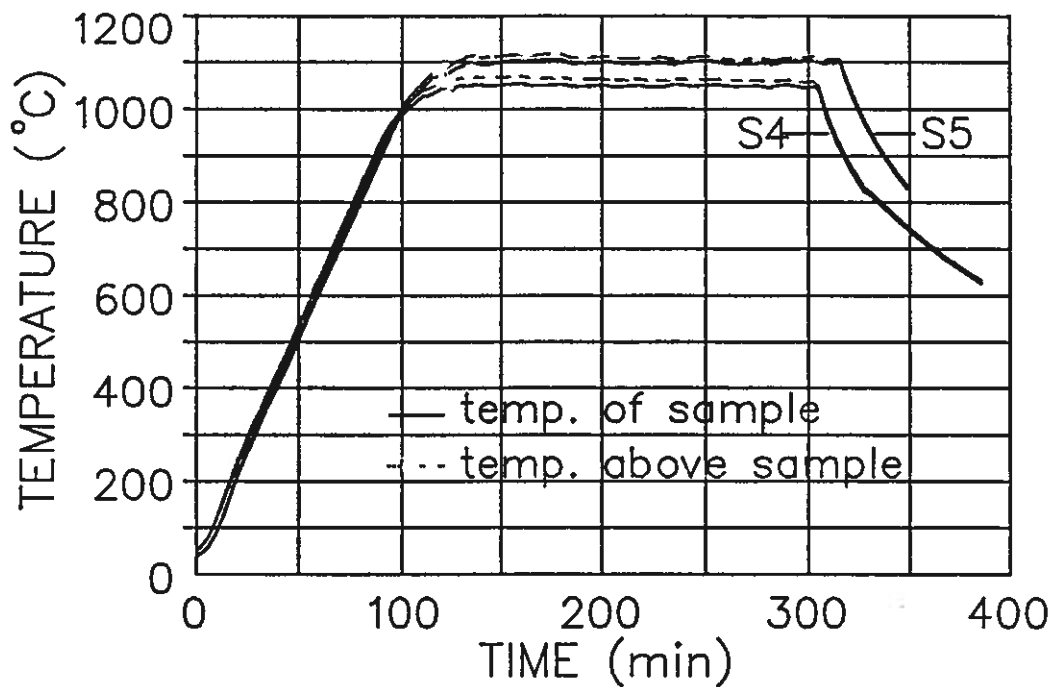


Fig. A.1.3

Oxidation of Sydvaranger magnetite at 1050°C (S4) and 1100°C (S5) in air for 3 hours. Heating and cooling were performed in nitrogen atmosphere.

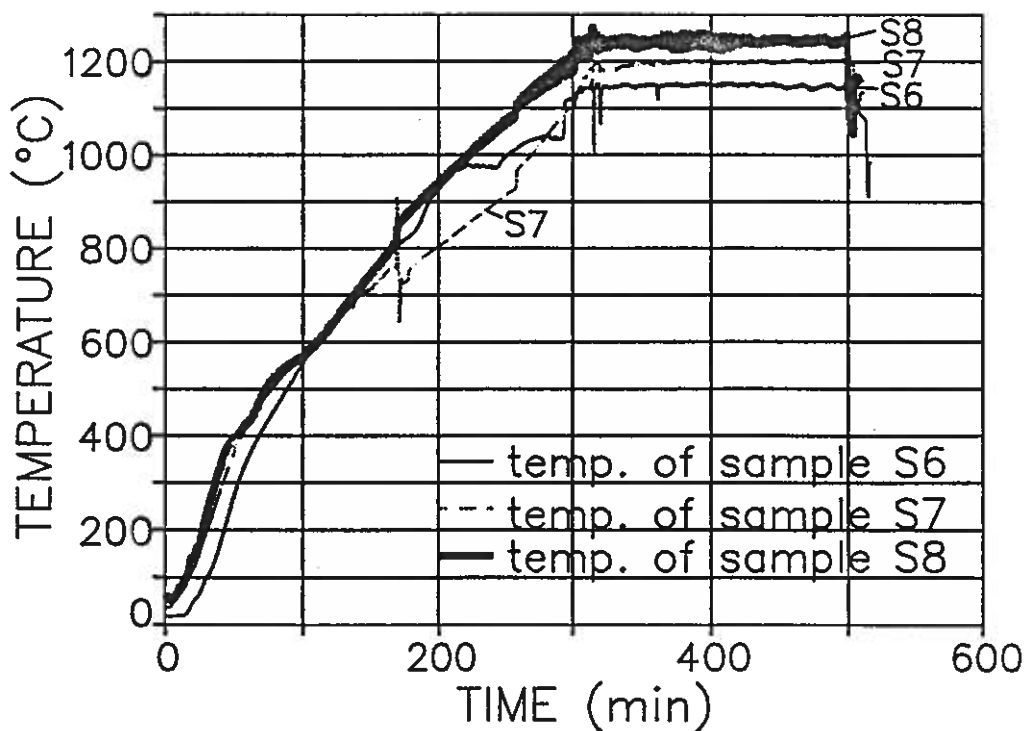


Fig. A.1.4

Oxidation of Sydvaranger magnetite at 1150° (S6), 1200°C (S7), and 1250°C (S8) in air for 3 hours. Heating and cooling were performed in nitrogen atmosphere.

Appendix A.2

Calculated porosity after reduction

The following symbols and abbreviations have been used:

V^o = Volume of particle

n = Number of moles

ϵ = Porosity, defined by the ratio of the pore volume to the particle volume

M = Molecular weight

ρ = Density

hm = Hematite

mt = Magnetite

wu = Wüstite

Fe = Iron

B = Solid B, substitutes both hm, mt and wu

Reactions taking place:



Assumptions:

V^o = constant during reduction

Since n_{Fe} in a hematite particle is constant during the reduction, formula A.2.1 is obtained for the complete conversion to magnetite and wüstite, respectively.

$$n_{\text{Fe}} = 2 \cdot n_{\text{hm}} = 3 \cdot n_{\text{mt}} = n_{\text{wu}} \quad (\text{A.2.1})$$

n_B can be expressed by ρ_B (density of solid without porosity) and the porosity as shown in formula 5.21.

$$n_B = \frac{\rho_B}{M_B} \cdot V^o (1 - \epsilon_B) \quad (5.21)$$

Formula A.2.2 is obtained from formula 5.21 by rearranging.

$$V^o = \frac{n_{\text{hm}} \cdot M_{\text{hm}}}{\rho_{\text{hm}} \cdot (1 - \epsilon_{\text{hm}})} = \frac{n_{\text{mt}} \cdot M_{\text{mt}}}{\rho_{\text{mt}} \cdot (1 - \epsilon_{\text{mt}})} = \frac{n_{\text{wu}} \cdot M_{\text{wu}}}{\rho_{\text{wu}} \cdot (1 - \epsilon_{\text{wu}})} = \frac{n_{\text{Fe}} \cdot M_{\text{Fe}}}{\rho_{\text{Fe}} \cdot (1 - \epsilon_{\text{Fe}})} \quad (\text{A.2.2})$$

By inserting n_{mt} , n_{wu} and n_{Fe} expressed by n_{hm} into formula A.2.2, we get:

$$\frac{M_{hm}}{\rho_{hm} \cdot (1 - \epsilon_{hm})} = \frac{2}{3} \cdot \frac{M_{mt}}{\rho_{mt} (1 - \epsilon_{mt})} = \frac{2 \cdot M_{wu}}{\rho_{wu} (1 - \epsilon_{wu})} = \frac{2 \cdot M_{Fe}}{\rho_{Fe} \cdot (1 - \epsilon_{Fe})} \quad (\text{A.2.3})$$

The porosity of magnetite, wüstite and iron can be calculated as a function of the hematite porosity by rearranging formula A.2.3. Sintering is assumed not to take place.

$$\epsilon_{mt} = 1 - \frac{2}{3} \cdot \frac{\rho_{hm}}{\rho_{mt}} \cdot \frac{M_{mt}}{M_{hm}} \cdot (1 - \epsilon_{hm}) \quad (\text{A.2.4})$$

$$\epsilon_{wu} = 1 - 2 \cdot \frac{\rho_{hm}}{\rho_{wu}} \cdot \frac{M_{wu}}{M_{hm}} \cdot (1 - \epsilon_{hm}) \quad (\text{A.2.5})$$

$$\epsilon_{Fe} = 1 - 2 \cdot \frac{\rho_{hm}}{\rho_{Fe}} \cdot \frac{M_{Fe}}{M_{hm}} \cdot (1 - \epsilon_{hm}) \quad (\text{A.2.6})$$

For $\epsilon_{hm}=0$, the porosity of magnetite, wüstite and iron are calculated to 2.2%, 17.3% and 53.4%, respectively.

The following densities and molecular weights were used:

Density (g/cm ³):	hm:5.24, mt:5.18, wu:5.7, Fe: 7.86
Molecular weight (mole/g):	hm:159.69, mt:231.54, wu:71.85, Fe:55.85

The molecular weight of stoichiometric FeO (71.85 mole/g) was applied, instead of the molecular weight of wüstite (Fe_{1-y}O). Depending on y, the molecular weight of wüstite is less than M_{FeO}. This implies that $\epsilon_{wu} > 17.3\%$.

However, the volume of a particle is not constant during reduction. During the reduction of hematite to magnetite the particle volume increases, implying that the magnetite porosity is higher than 2.2%, which was calculated for $\rho_{hm}=0$. Later the volume decreases during metallization due to sintering.

Appendix A.3

Experimental results from the prereduction experiments

The tables A.3.1a and b give a brief summary of the contents in the tables A.3.2 - A.3.15. Tables A.3.2 - A.3.15 present the wet chemical analyses, Fe^{tot} , Fe^{2+} and Fe^{met} (by weight%), and the calculated amount of Fe^{3+} , for each sample. Parallel analyses are reported. Parallels were carried out mainly because the first analysis was believed to be a little out of the range. The output of material in percentage of input weight in each single experiment is also reported in the tables.

The following abbreviations have been used;

Fe^{tot} :	total iron
Fe^{met} :	metallic iron
RO:	oxidizing potential of the reduction gas, defined by formula 2.21 in section 2.3.
OX:	degree of oxidation of solids
Sum	Σ , sum of metallic iron and iron oxides
A	the output of reduced material collected in the sample container in weight% of input
B	relative output

OX is calculated according to formula 5.2 in section 5.1. The formulas below are also applied. The sum (formula A.3.2) is too high when Fe^{2+} is contained in $Fe_{1-y}O$ (wu), since $M_{wu} < M_{FeO}$.

$$Fe^{3+} = Fe^{tot} - (Fe^{2+} + Fe^{met}) \quad (A.3.1)$$

$$\Sigma (\%) = Fe^{met} (\%) + \frac{M_{FeO}}{M_{Fe}} \cdot Fe^{2+} (\%) + \frac{M_{hm}}{M_{Fe}} \cdot \frac{1}{2} \cdot Fe^{3+} (\%) \quad (A.3.2)$$

$$B = A \cdot \frac{Fe^{tot}(\text{reduced sample})}{Fe_o^{tot}(\text{prior reduction})} \quad (A.3.3)$$

M_{Fe}	=	Molecular weight of iron = 55.85 g/mole
M_{FeO}	=	" of FeO (stoichiometric wüstite) = 71.85 g/mole
M_{hm}	=	" of hematite = 159.69 g/mole

Negative values for Fe^{3+} in the tables A.3.8 and A.3.11 indicate that the sum, $Fe^{met} + Fe^{2+}$, exceeds the analysis of Fe^{tot} . Mean values of the chemical analyses have been used to calculate the mean degree of oxidation in section 5.6.

The prereduction results for preoxidized Sydvaranger magnetite are presented in the tables A.3.2 - A.3.8 and the prereduction results for the natural hematite concentrates are presented in the tables A.3.9 - A.3.15. The experimental conditions for the results in each of these tables are given in the tables A.3.1a and A.3.1b for preoxidized magnetite and natural hematites, respectively. The same results are also presented in figures in chapter 5 and x in the tables A.3.1a and A.3.1b is the abscissa in the figures referred to.

Table A.3.1a A guide to find the experimental results for the preoxidized Sydvaranger magnetite.

Tables in A.3	pre-ox.-temp	Prereduction conditions				Figures in chapter 5	
		Temp. (°C)	RO (%)	Time (s)	H ₂ ^o (%)	results	rel. output
A.3.2		760	50	x	35	5.29, 5.30	5.50
A.3.3		760	20	x	35	5.29, 5.31	5.51
A.3.4		x	50	20	35	5.32	5.52
A.3.5		x	20	20	35	5.32	5.53
A.3.6		760	50	20	x	5.33	
A.3.7	x	760	50	20/60	35	5.34	
A.3.8	x	760	20	20/60	35	5.34	

Table A.3.1b A guide to find the experimental results for the natural hematite concentrates

Tables in A.3	Prereduction conditions				Figures in chapter 5	
	Temp. (°C)	RO (%)	Time (s)	H ₂ ^o (%)	prereduction results	relative output
A.3.9	760	50	x	35	5.35, 5.36	5.50
A.3.10	760	35	x	35	5.37, 5.38	
A.3.11	760	20	x	35	5.39, 5.40, 5.41	5.51
A.3.12	x	50	20	35	5.42	5.52
A.3.13	x	20	20	35	5.43	5.53
A.3.14	760	50	20	x	5.44	
A.3.15	760	20	20	x	5.45	

Table A.3.2 Results from the prereduction experiments at 760°C with preoxidized Sydvaranger magnetite.
Reduction gas: 50%RO, 35%H₂ (inlet gas)

sample	Pre-ox. temp. (°C)	Red. time (s)	Chemical analyses (%)				OX (%)	Sum (%)	Output (weight%)	
			Fe ^{tot}	Fe ²⁺	Fe ^{met}	Fe ³⁺			A	B
S1	799	0	69.5	0.0	0.0	69.5	100.0	99.4		100.0
S112	"	12	71.3	19.2	0.3	51.8	90.6	99.1	84.8	87.0
S13	"	20	72.2	27.0	0.3	44.9	87.1	99.2	80.8	83.9
				28.7		43.2	86.3	99.0		
S113	"	35	73.4	38.6	0.2	34.6	82.2	99.3	78.0	82.4
S14	"	60	75.1	52.0	0.2	22.9	76.7	99.8	60.4	65.3
				56.6		18.3	74.6	99.2		
S8	1244	0	68.6	0.0	0.0	68.6	100.0	98.1		100.0
S812	"	12	71.0	16.6	0.3	54.1	91.8	99.0	82.0	84.9
S83	"	20	70.8	22.3	0.4	48.1	88.9	97.9	76.0	78.4
				22.8		47.6	88.7	97.8		
S813	"	35	72.6	31.2	0.3	41.1	85.3	99.2	72.0	76.2
S84	"	60	73.3	41.5	0.2	31.6	80.9	98.8	57.2	61.1
				43.7		29.4	79.9	98.5		

Table A.3.3 Results from the prereduction experiments at 760°C with preoxidized Sydvaranger magnetite.
Reduction gas: 20%RO, 35%H₂ (inlet)

sample	Pre-ox. temp. (°C)	Red. time (s)	Chemical analyses (%)				OX (%)	Sum (%)	Output (weight%)	
			Fe ^{tot}	Fe ²⁺	Fe ^{met}	Fe ³⁺			A	B
S1	799	0	69.5	0.0	0.0	69.5	100.0	99.4	-	100.0
S115	"	12	73.2	31.7	0.8	40.7	84.5	99.8	-	-
S11-2	"	20	76.0	58.6	2.1	15.3	71.5	99.4	72.8	79.6
				59.1		14.8	71.3	99.3		
S116	"	35	76.9	69.7	2.6	4.6	66.4	98.8	59.0	65.3
			76.3		1.0	4.0	67.5	98.4		
S12	"	60	80.6	56.9	20.6	3.1	50.9	98.2	8.8	10.2
				59.9		0.1	49.7	97.8		
S8	1244	0	68.6	0.0	0.0	68.6	100.0	98.1	-	100.0
S815	"	12	72.3	30.1	0.6	41.6	85.3	98.8	-	-
S81	"	20	75.0	50.2	1.6	23.2	75.6	99.3	76.0	83.1
					1.7	23.2	75.5	99.3		
S816	"	35	75.7	54.3	3.4	18.0	71.6	99.0	64.0	70.6
S82	"	60	77.5	66.1	9.8	1.6	58.9	97.1	48.0	54.2
				63.4		4.3	60.1	97.5		
				59.3		8.4	61.8	98.1		

Table A.3.4 Experimental results after 20s prereduction of preoxidized Sydvaranger magnetite.
Reduction gas: **50%RO**, 35% H_2 (inlet)

Reduced sample	Pre-ox. temp. (°C)	Red. temp. (°C)	Chemical analyses (%)				OX (%)	Sum (%)	Output (weight%)	
			Fe ^{tot}	Fe ²⁺	Fe ^{met}	Fe ³⁺			A	B
S19	799	700	72.2	21.6	0.0	50.6	90.0	100.1	80.0	83.1
S110	"	730	73.0	25.4	0.0	47.6	88.4	100.7	82.8	87.0
S13	"	760	72.2	28.7	0.3	43.2	86.3	99.0	80.8	83.9
				27.0		44.9	87.1	99.2		
S18	"	800	72.8	35.7	0.0	37.1	83.7	99.0	80.0	83.8
S111	"	850	74.7	45.0	0.0	29.7	79.9	100.4	66.8	71.8
S89	1244	700	71.0	18.4	0.0	52.6	91.4	98.9	76.0	78.7
S810	"	730	71.6	21.0	0.0	50.6	90.2	99.4	64.8	67.6
S83	"	760	70.8	22.8	0.4	47.6	88.7	97.8	76.0	78.4
				22.3		48.1	88.9	97.9		
S88	"	800	72.6	29.0	0.0	43.6	86.7	99.6	71.2	75.4
S811	"	850	72.6	35.9	0.2	36.5	83.2	98.6	—	—
				45.4		27.0	78.9	97.2		
				26.3		46.1	87.6	99.9		

Table A.3.5 Experimental results after 20s prereduction of preoxidized Sydvaranger magnetite.
Reduction gas: **20%RO**, 35% H_2 (inlet)

Reduced sample	Pre-ox. temp. (°C)	Red. temp. (°C)	Chemical analyses (%)				OX (%)	Sum (%)	Output (weight%)	
			Fe ^{tot}	Fe ²⁺	Fe ^{met}	Fe ³⁺			A	B
S11-2	799	760	76.0	59.1	2.1	14.8	71.3	99.3	72.8	79.6
				58.6		15.3	71.5	99.4		
S117	"	800	76.0	64.1	2.5	9.4	68.6	98.4	72.0	78.7
S118	"	850	76.1	69.3	2.3	4.5	66.6	97.9		
					2.1	4.5	66.8	97.9		
S81	1244	760	75.0	50.2	1.6	23.2	75.6	99.3	76.0	83.1
					1.7	23.2	75.5	99.3		
S817	"	800	75.0	56.1	1.3	17.6	73.3	98.6	72.0	78.7
S818	"	850	75.2	56.9	2.2	16.1	71.9	98.4	48.8	53.5

Table A.3.6 Experimental results after 20s prereduction at 760°C for preoxidized Sydvaranger magnetite. Reduction gas: 50%RO, CO is substituted by H₂

Reduced sample	Pre-ox. temp. (°C)	Gas inlet H ₂ (%)	Chemical analyses (%)				OX (%)	Sum (%)	Output (weight%)	
			Fe ^{tot}	Fe ²⁺	Fe ^{met}	Fe ³⁺			A	B
S114	799	0	71.6	18.2	0.3	53.1	91.1	99.6	84.0	86.5
S15	"	15	71.9	26.0	0.0	45.9	87.9	99.1	82.0	84.8
S17	"	25	71.9	26.6	0.0	45.3	87.7	99.0	76.0	78.6
S13	"	35	72.2	28.7	0.3	43.2	86.3	99.0	80.8	83.9
				27.0		44.9	87.1	99.2		
S16	"	45	72.4	29.0	0.0	43.4	86.6	99.4	79.2	82.5
S814	1244	0	69.9	11.1	0.2	58.6	94.4	98.3	86.0	87.6
S85	"	15	71.7	21.0	0.0	50.7	90.2	99.5	79.2	82.8
S87	"	25	71.2	21.7	0.0	49.5	89.8	98.7	78.4	81.4
S83	"	35	70.8	22.8	0.4	47.6	88.7	97.8	76.0	78.4
				22.3		48.1	88.9	97.9		
S86	"	45	71.8	23.7	0.0	48.1	89.0	99.3	75.2	78.7

Table A.3.7 Effect of preoxidation temperature for Sydvaranger magnetite on the prereduction results.
Reduction conditions: 760°C, 50%RO, 35%H₂ (inlet)

Reduced sample	Pre-ox. temp. (°C)	Red. time (s)	Chemical analyses (%)				OX (%)	Sum (%)	Output (weight%)	
			Fe ^{tot}	Fe ²⁺	Fe ^{met}	Fe ³⁺			A	B
S13	799	20	72.2	27.0	0.3	44.9	87.1	99.2	80.8	83.9
				28.7			43.2	86.3		
S33	1002	"	71.4	24.1	0.3	47.0	88.3	98.5	82.0	84.3
				25.4			45.7	87.7		
S53	1104	"	72.3	25.6	0.2	46.5	87.9	99.6	79.6	83.1
				27.1			45.0	87.2		
S63	1150	"	71.0	21.7	0.3	49.0	89.4	98.3	76.8	79.5
				22.2			48.5	89.2		
S73	1195	"	71.3	21.4	0.2	49.7	89.7	98.8	77.6	80.6
				23.1			48.0	88.9		
S83	1244	"	70.8	22.3	0.4	48.1	88.9	97.9	76.0	78.4
				22.8			47.6	88.7		
S14	799	60	75.1	52.0	0.2	22.9	76.7	99.8	60.4	65.3
S54	1104	"	74.2	52.0	0.2	22.0	76.4	98.5	62.0	66.5
				54.7			19.3	75.2		
S84	1244	"	73.3	41.5	0.2	31.6	80.9	98.8	57.2	61.1
				43.7			29.4	79.9		

Table A.3.8 Effect of preoxidation temperature for Sydvaranger magnetite on the prereluction results.
Reduction conditions: 760°C, 20%RO, 35%H₂ (inlet)

Reduced sample	Pre-ox. temp. (°C)	Red time (s)	Chemical analyses (%)				OX (%)	Sum (%)	Output (weight%)	
			Fe ^{tot}	Fe ²⁺	Fe ^{met}	Fe ³⁺			A	B
S11-2	799	20	76.0	58.6	2.1	15.3	71.5	99.4	72.8	79.6
				59.1		14.8	71.3	99.3		
S21-2	900	"	74.9	55.3	2.0	17.6	72.7	98.3	66.8	71.9
				59.0		13.9	71.1	97.7		
S31-2	1002	"	75.8	55.1	3.0	17.7	71.8	99.2	80.8	88.3
				55.6	3.0	17.2	71.6	99.1		
S31-3	1002	"	74.6	54.1	0.9	19.6	74.6	98.5	65.2	70.1
				53.3		20.4	75.0	98.6		
S41-2	1050	"	75.3	55.5	1.6	18.2	73.3	99.0	63.6	69.0
				55.6		18.1	73.3	99.0		
S51-2	1104	"	75.8	55.6	1.6	18.6	73.4	99.7	78.0	85.4
				58.6		15.6	72.1	99.3		
S61	1150	"	75.4	50.2	2.1	23.1	75.0	99.7	77.6	85.3
				51.7		21.6	74.4	99.5		
				49.0		24.3	75.6	99.9		
S71	1195	"	75.4	50.2	1.0	24.2	76.5	100.2	79.2	87.1
				51.0		23.4	76.1	100.1		
S81	1244	"	75.0	50.2	1.6	23.2	75.6	99.3	76.0	83.1
					1.7	23.2	75.5	99.3		
S12	799	60	80.6	56.9	20.6	3.1	50.9	98.2	8.8	10.2
S22	900	"		59.9		0.1	49.7	97.8	8.0	9.2
			80.2	56.1	23.0	1.1	48.0	96.7		
S32	1002	"		59.3		-2.1	46.7	99.3	9.5	11.1
			81.1	55.6	23.3	2.2	48.4	98.0		
S42	1050	"		58.2		-0.4	47.3	98.2	10.6	12.3
			80.4	57.0	21.1	2.3	50.1	97.7		
S52	1104	"		61.0		-1.7	48.5	99.6	15.5	17.9
			79.8	60.6	17.1	2.1	53.3	98.1		
S62	1150	"		63.3		-0.6	52.1	98.5	28.0	31.8
			78.0	68.6	8.9	0.5	59.3	97.9		
S72	1195	"		66.4		1.8	59.1	97.8	19.6	22.4
			78.3	68.4	9.2	0.7	59.1	98.2		
S82	1244	"		63.2		5.9	61.3	98.9	48.0	54.2
				58.7		10.4	63.3	99.6		
			77.5	66.1	9.8	1.6	58.9	97.1		
			59.3		8.4	61.8	98.1			
			63.4		4.3	60.1	97.5			

Table A.3.9 Results from the prereduction experiments with natural hematites at 760°C.
Reduction gas: 50%RO, 35%H₂ (inlet)

Sample ₁ and run	Red. time (s)	Chemical analyses (%)				OX (%)	Sum (%)	Output (weight%)	
		Fe ^{tot}	Fe ²⁺	Fe ^{met}	Fe ³⁺			A	B
CCL-0	0	64.6	4.6	0.0	60.0	97.6	91.7		100.0
CCL5012	12	67.7	15.8	0.3	51.6	91.8	94.4	84.0	88.0
CCL5020	20	67.1	24.5	0.4	42.2	87.2	92.2	79.2	82.3
		64.4			39.5	86.7	88.4		79.0
CCL5035	35	69.7	30.2	0.3	39.2	85.1	95.2	78.0	84.2
CCL5060	60	69.7	43.6	0.4	25.7	78.6	93.3	70.0	75.6
GUL-0	0	69.6	0.3	0.0	69.3	99.9	99.5		100.0
GUL5012	12	71.8	22.2	0.3	49.3	89.3	99.4	79.2	81.7
GUL5020	20	72.2	29.8	0.4	42.0	85.7	98.8	68.0	70.5
GUL5035	35	72.7	31.6	0.2	40.9	85.2	99.3	68.8	71.9
		72.6			40.8	85.2	99.2		71.8
GUL5060	60	73.4	40.1	0.8	32.5	80.7	98.9	44.0	46.4
LIL-0	0	70.0	0.4	0.0	69.6	99.8	100.0		100.0
LIL5012	12	72.1	22.9	0.3	48.9	89.0	99.7	72.0	74.2
LIL5020	20	72.3	29.5	0.2	42.6	86.1	99.1	60.0	62.0
LIL5035	35	72.7	31.9	0.2	40.6	85.1	99.3	56.8	59.0
LIL5060	60	74.1	43.1	0.5	30.5	79.9	99.5	18.2	19.3
MBA-0	0	69.9	0.9	0.0	69.0	99.6	99.8		100.0
MBA5012	12	71.4	19.7	0.2	51.5	90.5	99.2	68.0	69.5
MBA5020	20	71.8	28.1	0.3	43.4	86.5	98.5	65.6	67.4
MBA5035	35	72.9	34.7	0.3	37.9	83.7	99.1	54.4	56.7
		71.5			36.5	83.4	97.1		60.2
MBA5060	60	73.3	46.1	0.4	26.8	78.5	98.1	23.6	24.8
MBL-0	0	69.5	0.1	0.0	69.4	100.0	99.3		100.0
MBL5012	12	72.0	21.6	0.3	50.1	89.6	99.7	61.6	63.8
MBL5020	20	72.8	31.6	0.2	41.0	85.3	99.5	42.4	44.4
MBL5035	35	74.5	42.1	0.2	32.2	80.9	100.4	28.9	
			42.0		32.3	80.9	100.4		
MBL5060	60	74.2	55.1	0.3	18.8	74.8	98.1	19.1	20.4
RHP-0	0	66.9	1.7	0.0	65.2	99.2	95.4		100.0
RHP5012	12	68.6	13.3	0.3	55.0	93.1	96.0	88.0	90.2
RHP5020		68.9	24.5	0.3	44.1	87.7	94.9	76.0	81.8
RHP Y	"	70.1	22.6	0.3	47.2	88.8	96.9	82.0	85.9
RHP F	"	69.6	23.2	0.3	46.1	88.5	96.1	78.0	81.1
RHP G	"	69.8	22.9	0.4	46.5	88.5	96.3	"	81.4
RHP X	"	69.4	23.5	0.3	45.6	88.3	95.7	"	80.9
RHP5035	35	70.0	32.6	0.3	37.1	84.0	95.3	72.8	76.2
		69.6			36.7	84.0	94.7		78.4
RHP5060	60	71.0	43.8	0.4	26.8	78.9	95.1	66.8	70.9

1) Referring to footnote in table A.3.14

Table A.3.10 Results from the prereduction experiments with natural hematites at 760°C.
Reduction gas: 35%RO, 35%H₂ (inlet)

Sample and run	Red. time (s)	Chemical analyses (%)				OX (%)	Sum (%)	Output (weight%)	
		Fe ^{tot}	Fe ²⁺	Fe ^{met}	Fe ³⁺			A	B
CCL-0	0	64.6	4.6	0.0	60.0	97.6	91.7		100.0
CCL7612	12	66.7	17.8	0.0	48.9	91.1	92.8		
CCL7620	20	67.7	28.6	0.0	39.1	85.9	92.7	58.4	61.2
CCL7635	35	70.0	43.5	0.0	26.5	79.3	93.8	48.0	52.0
CCL7660	60	71.2	51.0	0.0	20.2	76.1	94.5	44.3	48.8
GUL-0	0	69.6	0.3	0.0	69.3	99.9	99.5		100.0
GUL7612	12	72.0	27.8	0.0	44.2	87.1	99.0	65.6	67.9
GUL7620	20	72.4	34.8	0.0	37.6	84.0	98.5	51.3	53.4
GUL7635	35	73.7	45.6	0.0	28.1	79.4	98.8	41.1	43.5
GUL7660	60	75.1	54.6	0.0	20.5	75.8	99.5	35.0	37.8
LIL-0	0	70.0	0.4	0.0	69.6	99.8	100.0		100.0
LIL7612	12	72.0	27.1	0.0	44.9	87.5	99.1	66.0	67.9
LIL7620	20	72.8	34.3	0.0	38.5	84.3	99.2	50.3	52.3
LIL7635	35	73.8	44.6	0.0	29.2	79.9	99.1	37.7	39.7
LIL7660	60	75.0	54.7	0.0	20.3	75.7	99.4	30.2	32.4
MBA-0	0	69.9	0.9	0.0	69.0	99.6	99.8		100.0
MBA7612	12	71.3	23.2	0.0	48.1	89.2	98.6	49.2	50.2
MBA7620	20	72.8	35.6	0.0	37.2	83.7	99.0	33.4	34.8
MBA7635	35	73.9	49.6	0.0	24.3	77.6	98.5	23.8	25.2
MBA7660	60	75.1	60.4	0.0	14.7	73.2	98.7	14.8	15.9
MBL-0	0	69.5	0.1	0.0	69.4	100.0	99.3		100.0
MBL7612	12	71.8	25.0	0.0	46.8	88.4	99.1	57.3	59.2
MBL7620	20	74.7	52.9	0.3	21.5	76.0	99.1	44.0	47.3
		75.4	49.8		25.3	77.6	100.5		47.7
MBL7635	35	76.0	62.0	0.3	13.7	72.4	99.6	33.3	36.4
MBL7660	60	76.4	66.7	0.6	9.1	70.1	99.4	22.2	24.4
RHP-0	0	66.9	1.7	0.0	65.2	99.2	95.4		100.0
RHP7612	12	68.1	19.2	0.0	48.9	90.6	94.6	75.3	76.7
RHP7620	20	70.0	30.7	0.0	39.3	85.4	95.7	71.2	74.5
RHP7635	35	70.8	45.8	0.0	25.0	78.4	94.7	69.6	73.7
RHP7660	60	72.1	56.1	0.0	16.0	74.1	95.0	48.4	52.2

Table A.3.11 Results from the prereduction experiments at 760°C.
Reduction gas: 20%RO, 35%H₂ (inlet)

1) Sample and run	Red. time (s)	Chemical analyses (%)				OX (%)	Sum (%)	Output (weight%)	
		Fe ^{tot}	Fe ²⁺	Fe ^{met}	Fe ³⁺			A	B
CCL-0	0	64.6	4.6	0.0	60.0	97.6	91.7		100.0
CCL2012	12	67.7	27.6	0.6	39.5	85.5	92.6	83.2	87.2
CCL2020	20	69.2	40.7	1.8	26.7	77.8	92.3	88.0	94.3
		71.3		2.4	28.2	77.6	95.2		97.1
CCL2030	30	71.1	53.8	1.7	15.6	72.4	93.2	72.0	79.2
CCL2040	40	72.8	57.9	4.6	10.3	67.2	93.8	67.2	75.7
			55.9		12.3	68.1	94.1		
CCL2050	50	69.5	49.7	6.1	13.7	67.4	89.6	28.6	30.8
		70.4	48.9		15.4	68.2	91.0		31.2
CCL2060	60	73.6	48.9	11.0	13.7	62.9	93.5	18.4	21.0
			46.4		16.2	64.0	93.9		
GUL-0	0	69.6	0.3	0.0	69.3	99.9	99.5		100.0
GUL2012	12	73.8	37.7	0.6	35.5	82.2	99.9	74.0	78.5
GUL2020	20	74.8	48.9	0.4	25.5	77.7	99.8	72.0	77.4
GUL2030	30	75.5	59.4	0.8	15.3	72.7	99.1	60.8	66.0
GUL2040-2	40	76.6	60.7	1.8	14.1	71.2	100.0	63.2	69.6
GUL O	"	75.8	66.1	1.0	8.7	69.6	98.5	59.6	64.9
GUL A	"	76.3	62.6	1.6	12.1	70.6	99.4	58.6	64.2
GUL H	"	75.9	69.4	1.4	5.1	67.7	98.0	"	63.9
GUL I	"	75.6	60.0	1.5	14.1	71.6	98.8	"	63.7
GUL2050-2	50	76.5	64.3	3.1	9.1	67.9	98.8	62.0	68.1
GUL2060-2	60	77.5	64.0	5.7	7.8	65.1	99.2	49.2	54.8
LIL-0	0	70.0	0.4	0.0	69.6	99.8	100.0		100.0
LIL2012	12	73.6	37.6	0.3	35.7	82.6	99.7	76.0	79.9
LIL2020	20	74.8	48.7	0.4	25.7	77.8	99.8	68.0	72.7
LIL2030	30	76.1	57.7	1.4	17.0	72.9	99.9	60.0	65.2
LIL2040-2	40	76.8	61.1	3.6	12.1	68.8	99.5	62.0	68.0
			58.4		14.8	70.0	99.9		
LIL2050-2	50	77.0	63.2	3.1	10.7	68.6	99.7	52.0	57.2
LIL2060-2	60	77.6	63.8	5.2	8.6	65.9	99.6	45.2	50.1
MBA-0	0	69.9	0.9	0.0	69.0	99.6	99.8		100.0
MBA2012	12	72.4	31.8	0.7	39.9	84.4	98.7	68.0	70.4
MBA2020	20	73.9	46.7	0.6	26.6	78.1	98.7	64.0	67.7
MBA2030	30	75.4	58.3	1.1	16.0	72.8	99.0	56.0	60.4
MBA2040-2	40	77.3	64.1	2.5	10.7	69.1	100.3	36.7	40.6
MBA2050	50	76.7	65.6	6.1	5.0	63.5	97.6	25.8	28.3
MBA2060	60	77.1	64.0	11.6	1.5	57.3	96.1	11.3	12.5
MBL-0	0	69.5	0.1	0.0	69.4	100.0	99.3		100.0
MBL2012	12	73.8	40.1	0.8	32.9	80.8	99.4	54.7	58.1
MBL2020	20	75.5	59.7	0.8	15.0	72.6	99.0	40.0	43.5
			59.8		14.9	72.5	99.0		
MBL2030	30	77.5	68.3	5.9	3.3	63.0	98.5	31.4	35.0
			69.3		2.3	62.6	98.3		
MBL2040-2	40	79.0	63.2	13.9	1.9	55.7	97.9	25.5	29.0
			61.5		3.6	56.5	98.2		
			69.7		-4.6	53.0	103.6		
MBL2050	50	80.7	61.0	18.9	0.8	51.4	98.5	20.0	23.2
MBL2060	60	81.8	55.8	25.5	0.5	46.1	98.0	12.7	14.9
RHP-0	0	66.9	1.7	0.0	65.2	99.2	95.4		100.0
RHP2012	12	69.8	27.6	0.3	41.9	86.4	95.7	84.0	87.6
RHP2020	20	71.3	44.0	0.4	26.9	78.9	95.5	78.4	83.6
RHP2030	30	73.1	54.8	0.7	17.6	74.1	96.4	84.0	91.8
RHP2040	40	73.0	60.1	2.4	10.5	69.3	94.7	74.0	80.7
RHP2050	50	73.4	61.5	5.5	6.4	64.6	93.8	63.2	69.3
RHP2060	60	73.1	59.7	7.4	6.0	62.7	92.8	36.8	40.2

1) Parallels from the same run: GUL A, GUL H, GUL I. Different runs: GUL O, GUL2040-2

Table A.3.12 Experimental results after 20s prereduction of the natural hematites.
Reduction gas: 50%RO, 35%H₂ (inlet)

Sample ¹ and run	Red. temp (°C)	Chemical analyses (%)				OX (%)	Sum (%)	Output (weight%)	
		Fe ^{tot}	Fe ²⁺	Fe ^{met}	Fe ³⁺			A	B
CCL7050	700	67.4	19.3	0.0	48.1	90.5	93.6	84.0	87.6
		68.7			49.4	90.6	95.5		89.3
CCL5020	760	67.1	24.5	0.4	42.2	87.2	92.2	79.2	82.3
		64.4			39.5	86.7	88.4		79.0
CCL8550	850	69.8	34.5	0.0	35.3	83.5	94.8	74.0	80.0
		67.5			33.0	83.0	91.6		77.3
GUL7050	700	72.0	23.3	0.0	48.7	89.2	99.6	77.2	79.9
GUL7350	730	72.0	26.2	0.0	45.8	87.9	99.2	75.6	78.2
GUL5020	760	72.2	29.8	0.4	42.0	85.7	98.8	68.0	70.5
GUL8050	800	72.3	31.6	0.0	40.7	85.4	98.8	71.2	74.0
GUL8550	850	73.1	34.9	0.0	38.2	84.1	99.5	64.6	67.8
LIL7050	700	72.2	23.9	0.0	48.3	89.0	99.8	60.8	62.7
LIL5020	760	72.3	29.5	0.2	42.6	86.1	99.1	60.0	62.0
LIL8550	850	73.7	34.9	0.0	38.8	84.2	100.4	59.2	62.3
MBA7050	700	72.3	21.1	0.0	51.2	90.3	100.3	66.4	68.7
MBA5020	760	71.8	28.1	0.3	43.4	86.5	98.5	65.6	67.4
MBA8550	850	72.1	34.3	0.0	37.8	84.1	98.2	54.4	56.1
MBL7050	700	73.3	23.4	0.0	49.9	89.4	101.4	62.0	65.4
MBL7350	730	73.4	27.0	0.0	46.4	87.7	101.1	57.2	60.4
MBL5020	760	72.8	31.6	0.2	41.0	85.3	99.5	42.4	44.4
MBL8050	800	74.1	37.5	0.2	36.4	82.9	100.5	44.0	46.9
MBL8550	850	74.4	41.2	0.0	33.2	81.5	100.5	47.6	51.0
RHP7050	700	68.8	17.5	0.0	51.3	91.5	95.9	82.0	84.3
RHP7350	730		20.3		48.5	90.2	95.5		
		69.1	20.0	0.0	49.1	90.4	95.9	81.2	83.9
			17.7		51.4	91.5	96.3		
			19.3		49.8	90.7	96.0		
RHP5020		68.9	24.5	0.3	44.1	87.7	94.9	76.0	81.8
RHP Y	760	70.1	22.6	0.3	47.2	88.8	96.9	82.0	85.9
RHP F	760	69.6	23.2	0.3	46.1	88.5	96.1	78.0	81.1
RHP G	760	69.8	22.9	0.4	46.5	88.5	96.3	"	81.4
RHP X	760	69.4	23.5	0.3	45.6	88.3	95.7	"	80.9
RHP8050	800	69.8	31.1	0.0	38.7	85.1	95.3	76.0	79.3
RHP8550	850	71.1	37.7	0.0	33.4	82.3	96.3	76.0	80.0
			39.5		31.6	81.5	96.0		

1) Referring to footnote in table A.3.14

Table A.3.13 Experimental results after 20s prereduction of natural hematites.
Reduction gas: **20%RO**, 35% H_2 (inlet)

Sample and run	Red. temp. ($^{\circ}C$)	Chemical analyses (%)				OX (%)	Sum (%)	Output (weight%)	
		Fe^{tot}	Fe^{2+}	Fe^{met}	Fe^{3+}			A	B
CCL2020	760	69.2	40.7	1.8	26.7	77.8	92.3	88.0	94.3
		71.3		2.4	28.2	77.6	95.2		97.1
CCL8020	800	71.5	46.7	0.9	23.9	77.0	95.1	76.0	84.1
		70.7			23.1	76.7	94.0		83.2
CCL8520	850	72.9	54.4	1.1	17.4	73.6	96.0	56.8	64.1
GUL2020	760	74.8	48.9	0.4	25.5	77.7	99.8	72.0	77.4
GUL8020	800	74.4	51.3	0.6	22.5	76.2	98.8	68.4	73.1
GUL8520	850	75.6	59.0	0.8	15.8	72.9	99.3	50.0	54.3
LIL2020	760	74.8	48.7	0.4	25.7	77.8	99.8	68.0	72.7
LIL8020	800	74.7	51.8	0.6	22.3	76.1	99.1	51.0	54.4
LIL8520	850	75.3	57.8	0.6	16.9	73.6	99.1	46.0	49.5
MBA2020	760	73.9	46.7	0.6	26.6	78.1	98.7	64.0	67.7
MBA8020	800	74.1	54.0	0.9	19.2	74.5	97.8	44.0	46.6
MBA8520	850	75.0	59.2	1.6	14.2	71.6	98.1	12.0	12.9
MBL2020	760	75.5	59.7	0.8	15.0	72.6	99.0	40.0	43.5
MBL8020	800	75.7	64.3	2.8	8.6	68.0	97.8	19.4	21.1
MBL8520	850	76.7	65.5	5.9	5.3	63.8	97.7	16.2	17.9
RHP2020	760	71.3	44.0	0.4	26.9	78.9	95.5	78.4	83.6
RHP8020	800	71.5	50.8	0.8	19.9	75.2	94.6	76.0	81.2
RHP8520	850	72.9	60.8	1.5	10.6	70.1	94.9	50.0	54.5

Table A.3.14 Experimental results after 20s prereduction of the natural hematites at 760°C.
Reduction gas; **50%RO**, CO is substituted by H₂

1) Sample and run	H ₂ ^o (%)	Chemical analyses (%)				OX (%)	Sum (%)	Output (weight%)	
		Fe ^{tot}	Fe ²⁺	Fe ^{met}	Fe ³⁺			A	B
CCL5020	35	67.1	24.5	0.4	42.2	87.2	92.2	79.2	82.3
		64.4			39.5	86.7	88.4		79.0
GUL1	0	71.5	25.0	0.3	46.2	87.9	98.5	72.0	74.0
			24.0		47.2	88.4	98.7		
GUL2	15	72.3	24.3	0.3	47.7	88.4	99.8	76.0	78.9
GUL4	25	72.1	26.9	0.0	45.2	87.6	99.2	72.0	74.6
GUL5020	35	72.2	29.8	0.4	42.0	85.7	98.8	68.0	70.5
GUL3	45	71.3	28.8	0.2	42.3	86.3	97.7	70.0	71.7
			28.6		42.5	86.3	97.8		
LIL5020	35	72.3	29.5	0.2	42.6	86.1	99.1	60.0	62.0
MBA5020	35	71.8	28.1	0.3	43.4	86.5	98.5	65.6	67.4
MBL1	0	71.3	17.9	0.3	53.1	91.2	99.2	56.6	58.1
			17.4		53.6	91.4	99.3		
MBL2	15	73.1	24.8	0.0	48.3	88.7	101.0	46.0	48.4
MBL4	25	72.6	27.7	0.0	44.9	87.3	99.8	58.0	60.6
MBL5020	35	72.8	31.6	0.2	41.0	85.3	99.5	42.4	44.4
MBL3	45	73.0	30.8	0.0	42.2	85.9	100.0	56.0	58.8
RHP1	0	68.8	15.2	0.3	53.3	92.2	96.1	80.0	82.3
RHP2	15	68.2	21.0	0.0	47.2	89.7	94.5	88.0	89.7
RHP4	25	69.6	23.6	0.0	46.0	88.7	96.1	78.0	81.1
RHP5020	35	68.9	24.5	0.3	44.1	87.7	94.9	76.0	81.8
RHP Y	35	70.1	22.6	0.3	47.2	88.8	96.9	82.0	85.9
RHP F	35	69.6	23.2	0.3	46.1	88.5	96.1	78.0	81.1
RHP G	35	69.8	22.9	0.4	46.5	88.5	96.3	"	81.4
RHP X	35	69.4	23.5	0.3	45.6	88.3	95.7	"	80.9
RHP3	45	68.5	24.3	0.2	44.0	87.9	94.4	78.4	80.3
			24.0		44.3	88.0	94.4		

- 1) Parallel samples from the same run: RHP F, RHP G, RHP X
Parallel samples from different runs: RHP Y, RHP5020

Table A.3.15 Experimental results after 20s prereduction of the natural hematites at 760°C.
Reduction gas: 20%RO, H₂ substitutes CO

Sample and run	H ₂ ^o (%)	Chemical analyses (%)				OX (%)	Sum (%)	Output (weight%)	
		Fe ^{tot}	Fe ²⁺	Fe ^{met}	Fe ³⁺			A	B
CCL5	0	67.2	21.5	0.3	45.4	88.9	92.9	82.8	86.3
		67.4	21.5		45.6	88.9	92.9		86.4
CCL2020	35	69.2	40.7	1.8	26.7	77.8	92.3	88.0	94.3
		71.3		2.4	28.2	77.6	95.2		97.1
GUL5	0	72.1	32.4	0.2	39.5	84.7	98.4	76.0	78.7
GUL6	15	73.3	39.0	0.6	33.7	81.4	99.0	72.0	75.8
GUL2020	35	74.8	48.9	0.4	25.5	77.7	99.8	72.0	77.4
GUL8	45	74.4	50.0	0.6	23.8	76.8	98.9	67.6	72.3
LIL5	0	72.8	32.0	0.5	40.3	84.7	99.3	68.0	70.7
LIL2020	35	74.8	48.7	0.4	25.7	77.8	99.8	68.0	72.7
MBA5	0	71.4	24.5	0.4	46.5	88.0	98.4	56.8	58.0
MBA2020	35	73.9	46.7	0.6	26.6	78.1	98.7	64.0	67.7
MBL5	0	72.1	26.1	0.5	45.5	87.2	99.1	37.0	38.4
MBL6	15	73.5	39.2	1.0	33.3	80.9	99.0	34.0	36.0
MBL2020	35	75.5	59.7	0.8	15.0	72.6	99.0	40.0	43.5
			59.8		14.9	72.5	99.0		
MBL8	45	75.1	58.5	1.1	15.5	72.6	98.5	48.0	51.9
RHP5	0	68.8	22.3	0.3	46.2	88.8	95.0	84.0	86.4
RHP6	15	69.8	32.0	0.6	37.2	83.9	94.9	72.0	75.1
RHP7	25	69.8	36.2	0.8	32.8	81.6	94.3	78.0	81.4
RHP2020	35	71.3	44.0	0.4	26.9	78.9	95.5	78.4	83.6
RHP8	45	71.1	42.0	1.0	28.1	78.9	95.2	69.0	73.3

Appendix A.4
Degree of oxidation with magnetite corrections

Table A.4 Mean degree of oxidation with corrections for magnetite contents according to formula 5.65. Short terms for the natural hematite concentrates are given in section 4.2.

Temp. (°C)	RO (%)	H ₂ ^o (%)	Time (s)	Corrected degree of oxidation ¹ (%)					
				CCL	GUL	LIL	MBA	MBL	RHP
760	20	35	0	100.0	100.0	100.0	100.0	100.0	100.0
			12	84.6	82.1	82.5	84.2	80.8	86.2
			20	74.7	77.5	77.6	77.7	72.5	78.0
			30	67.9	72.5	72.6	72.1	62.7	72.8
			40	61.9	69.9	69.0	68.3	54.9	67.6
			50	62.1	67.7	68.3	62.5	51.2	62.5
			60	56.6	64.8	65.5	56.0	45.9	60.4
760	35	35	12	91.7	87.1	87.4	89.2	88.4	90.7
			20	85.1	83.9	84.2	83.5	76.7	85.1
			35	76.7	79.3	79.7	77.2	72.3	77.5
			60	72.7	75.6	75.5	72.6	70.0	72.8
760	50	35	12	92.6	89.3	89.0	90.6	89.6	93.5
			20	86.4	85.6	86.1	86.4	85.2	88.3
			35	84.1	85.2	85.0	83.3	80.9	83.6
			60	75.8	80.6	79.8	78.1	74.8	78.0
760	20	0	20	88.9	84.7	84.6	88.0	87.2	88.7
		15	-	81.3	-	-	80.8	83.4	
		25	-	-	-	-	-	81.0	
		35	74.7	77.5	77.6	77.7	72.5	78.0	
		45	-	76.6	-	-	72.5	78.1	
760	50	0	20	-	88.1	-	-	91.3	92.5
		15	-	88.4	-	-	88.7	89.8	
		25	-	87.5	-	-	87.3	88.7	
		35	86.4	85.6	86.1	86.4	85.2	88.3	
		45	-	86.3	-	-	85.9	87.9	
760	20	35	20	74.7	77.5	77.6	77.7	72.5	78.0
800			73.6	76.0	75.9	73.9	67.9	74.1	
850			69.5	72.7	73.4	70.9	63.7	68.6	
700	50	35	20	91.0	89.2	89.0	90.3	89.4	91.0
730			-	87.9	-	-	87.7	91.0	
760			86.5	85.6	86.1	86.4	85.2	88.3	
800			-	85.4	-	-	82.8	84.8	
850			81.7	84.0	84.1	84.0	81.5	81.3	

1) Mean values of parallel chemical analyses were applied in formula 5.65.